AlGaN/GaN MBE 2DEG Heterostructures: Interplay between Surface-, Interface- and Device-Properties

Von der Fakultät für Elektrotechnik und Informationstechnik
der Rheinisch-Westfälischen Technischen Hochschule Aachen
zur Erlangung des akademischen Grades
eines Doktors der Ingenieurwissenschaften genehmigte Dissertation

vorgelegt von
Diplom-Ingenieur

Martin Kočan
aus Bratislava, Slowakei

Berichter: Universitätsprofessor Dr. H. Lüth
Universitätsprofessor Dr.-Ing. R. Waser

Tag der mündlichen Prüfung: 16. Juli 2003

Contents

Chapter 1

Introduction

In the semiconductor technology the leading role is still played by silicon, with its well stabilized CMOS process. All integrated circuits and chips are practically developed on silicon basis. In the last decades also III-V semiconductors gained more and more importance, conquering well established positions in important niches. As-based (AlGaInAs) and P-based (AlGaInP) systems are successfully used for optoelectronic applications in the infrared, red and yellow range, as well as for high frequency devices.
There are many areas where conventional III-V semiconductors cannot be used. Short wavelength light emitters are required for full color displays, laser printers, high density information storage, and under water communication. High power and high temperature transistors are needed for automobile engines, future advanced power distribution systems, all electric vehicles and avionics. Si and conventional III-V semiconductors are not suitable for designing and fabricating optoelectronic devices in the violet and blue region of the spectrum. Their band gaps are not sufficiently large. GaAs based electronic devices can not be used at high temperatures. III-nitrides are particularly suitable for applications in these areas. The band gaps of III-nitrides are large and direct. The band gap values vary from 0.7 eV for InN, 3.4 eV for GaN and 6.2 eV for AlN for wurtzite semiconductors (fig. 1.1, 2.1). Due to their wide band gaps and strong bond strength, they can be used for violet, blue and green light emitting devices and for high temperature transistors.
In the last 10 years we assisted impressive development of the nitride semiconductor technology, where major achievements have been the fabrication of high brightness blue light emitting devices (LEDs) and laser diodes [1–3]. In 1993 Nakamura succeeded in producing a blue LED using an InGaN/AlGaN double heterostructure, whose 1 cd light intensity is comparable with the one of an AlGaAs LED. The following intense work has led to the brightest visible LEDs available today concerning the blue part of the spectrum (6 cd). As far as blue LEDs were developed the interest of the research moved to blue lasers. A blue laser, having a wavelength shorter than the lasers that are used nowadays, could greatly increase the storage capability of CD-ROM and DVD discs, which are actually widely used to store electronic data.

Besides optoelectronic applications, nitride heterostructures play an important role in AlGaN/GaN based RF-high power high frequency High Electron Mobility Transistor (HEMT) devices [4, 5], that are expected to be used in earth bound transmitter stations for satellite communication. Specially for high power applications the GaN-based material enables high temperature operation, reduced cooling, high frequency operation (10 GHz), high saturation electron velocity (2.7×10^7 cm/s), a larger breakdown electric field (3 MV/cm), allowing high drain-source bias voltage, a high power density of an AlGaN/GaN HEMT over 11 W/mm, a larger conduction band discontinuity between GaN and AlGaN and the presence of polarization fields that allow a large two dimensional electron gas (2DEG) concentration to be confined, as opposed to by remote doping induced 2DEG as in AlGaAs/GaAs modulation doped heterostructures and gate induced inversion in silicon Metal Oxide Semiconductor Field Effect Transistors (MOSFETs).

In semiconductor technology and device physics the development of semiconductor devices and the related process technology was intimately related to fundamental investigations in surface and interface science. A recent great acknowledgment of this important interplay was the Nobel Prize in Physics 2000 to Herbert Kroemer, who uses to say: "By increasing miniaturization in semiconductor device technology, the interface itself becomes the device" [6].
For group III-nitrides with wurtzite structure the presence of fixed polarization interface charges yields new challenges in order to understand and control Schottky barrier heights, band offsets and 2D confinement in heterostructure field effect transistors. The Fermi energy E_F at the semiconductor surface relative to the semiconductor band edge

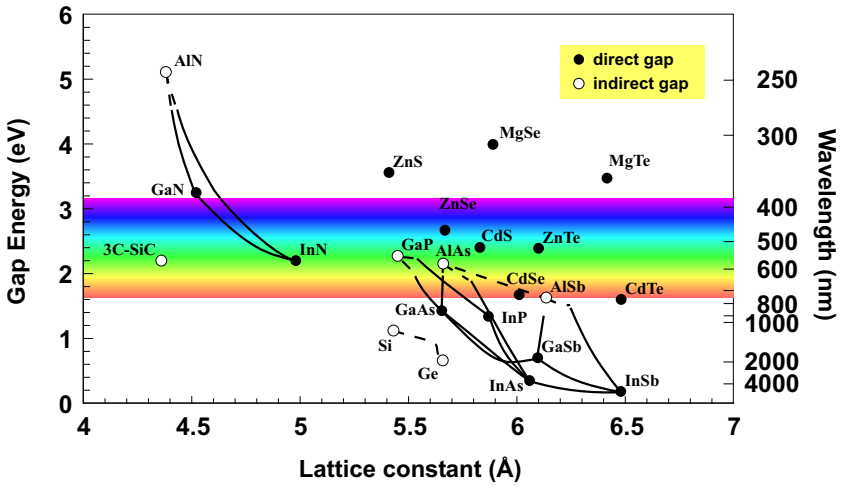

Figure 1.1: Bandgaps of the most important elementary and binary semiconductors versus their lattice parameter. For group III-nitrides the values of cubic polytypes are shown.

(conduction band edge for n-type and valence band edge for p-type), *i.e.* the surface potential, has fundamental importance as well as technological relevance, especially for the performance of planar unipolar transistors (MOSFET, HEMTs). The application of wurtzite nitride heterostructures to advanced optical and electronic devices requires an understanding of the electronic properties of their surface and interfaces and also their interplay with the polarization charges at the heterojunctions, which characterize the wurtzite III-N heterostructures as compared with the classical zincblende III-V ones.

The aim of this work has been to perform growth optimization of III-nitrides on different substrates (SiC and Si) by Molecular Beam Epitaxy in order to grow an AlGaN/GaN HEMT structure and to study surface and interface electronic properties which form the knowledge basis for understanding and improving the performance of AlGaN/GaN HEMTs. The present work is divided into eight parts.

The second chapter introduces the main properties of III-nitride semiconductors, in particular the crystal structure, polarization fields present in nitrides, formation of a 2DEG and electron transport in a AlGaN/GaN heterostructure. Furthermore the growth of nitrides on various substrates is discussed and the most common growth techniques are presented. Surface and interface electronic properties with particular attention to Schottky barrier heights, band offsets and performance of HEMT devices are discussed in the last section.

The third chapter is focused on experimental methods employed to characterize the grown samples. A deep analysis of them would be too long, so the reader is pleased to refer to specific publications for more detailed and complete explanations. We only highlight the properties of such methods that make them useful for our work.

A short description of the used experimental apparatus at the Institut für Schichten und Grenzflächen in Forschungszentrum Jülich is presented in the fourth chapter, in particular attention to the Molecular Beam Epitaxy system and Hall measurement setup which was improved and developed within the present work.

Chapter four deals with the theoretical study of AlGaN/GaN heterostructures by means of Schrödinger-Poisson self consistent calculations. We studied the role of the polarization charge on the 2DEG formation, the influence of the structure parameters as thickness, Al content and doping in the AlGaN barrier on the 2DEG concentration and the interrelation of the surface potential with the electronic properties of the AlGaN/GaN heterostructure, in particular with the concentration of the 2DEG at the interface.

The experimental results are shown in the sixth chapter. The procedure of AlGaN/GaN growth optimization on SiC and Si substrates is reported. In the last section of this part we focused on the surface and interface properties in AlGaN and GaN structures. The influence of a thin silicon nitride passivation layer on the surface potential was also considered.

The last two chapters, presented in English and in German language, summarize the main obtained results and an outlook for possible developments is presented.

Chapter 2

Nitrides

2.1 Nitrides Properties

2.1.1 Physical Properties

In contrast to cubic III-V semiconductors like GaAs and InP with zincblende structure, the thermodynamically stable phase of InN, GaN and AlN is the hexagonal wurtzite structure (α-phase), with the space group $P6_3mc$. In this phase III-Nitride materials form a continuous alloy system (InGaN, InAlN, AlGaN) whose direct optical bandgaps range from 0.7 eV for α-InN[1] and 3.4 for α-GaN to 6.2 eV for α-AlN (fig. 2.1). The wurtzite structure consists of alternating biatomic close-packed (0001) planes of Ga and N pairs stacked in an ABABAB sequence (fig. 2.2). Atoms in the first and third layers are directly aligned with each other.

Beside the α-phase, a metastable β-phase with zincblende structure exists (space group $F\overline{4}3$m) (fig. 2.2). The zincblende structure of GaN can be stabilized in epitaxial films. The stacking sequence for the (111) close-packed planes in this structure is ABCABC.
Because the α- and β-phases of group III-nitrides only differ in the stacking sequence of nitrogen and metal atom planes, the coexistence of hexagonal and cubic phases is possible in epitaxial layers, for example due to stacking faults.

The hexagonal crystal structure of group III-nitrides can be described by the edge length a_0 of the basal hexagon, the height c_0 of the hexagonal prism and an internal parameter u defined as the anion-cation bond length along the (0001) axis. Because of the different cations and ionic radii (Al^{3+}: 0.39 Å, Ga^{3+}: 0.47 Å, In^{3+}: 0.79 Å) InN, GaN and AlN have different lattice constants, bandgaps and binding energies as shown in table 2.1.

Both wurtzite and zincblende structures have polar axes (lack of inversion symmetry). In particular, the bonds in the $\langle 0001 \rangle$ direction for wurtzite and $\langle 111 \rangle$ direction for zincblende are all faced by nitrogen in the same direction and by the cation in the opposite.

[1] The band gap of InN has not been fi rmly established; the value reported is from reference [7].

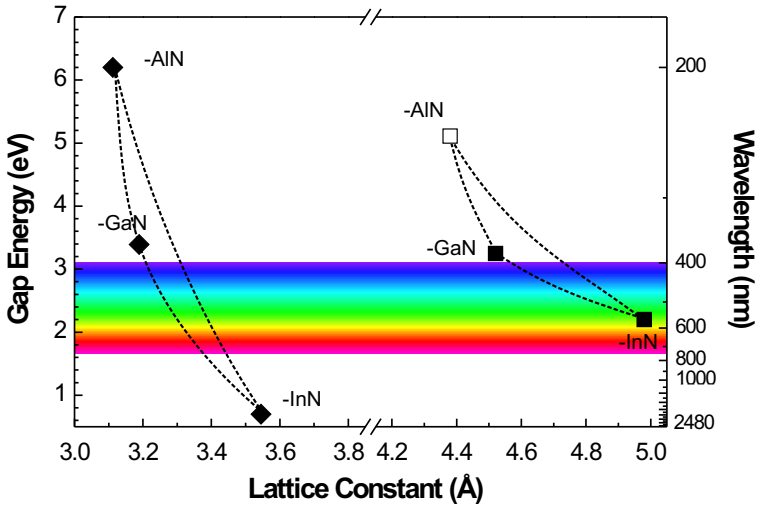

Figure 2.1: Energy gaps and lattice constants for III-N semiconductors with wurzite (α-phase) and zincblende (β-phase) structures.

Both bulk and surface properties can depend significantly on whether the surface is faced by nitrogen or metal atoms.
Among III-nitrides, GaN is certainly the most investigated one, since it is always the basis material to start growing heterostructures. The most common growth direction of hexagonal GaN is normal to the {0001} basal plane, where the atoms are arranged in bilayers consisting of two closely spaced hexagonal layers, one with cations and the other with anions, so that the bilayers have polar faces. The group III-nitrides lack an inversion plane perpendicular to the c-axis, thus, crystal surfaces have either a group III element (Al, Ga, or In) polarity (designated (0001)) or a N-polarity (designated $(000\bar{1})$) (fig. 2.3) [16]. Ga-faced conventionally means Ga on the top position of the {0001} bilayer, correspond-

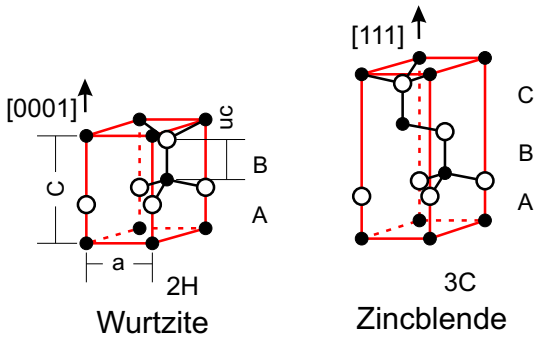

Figure 2.2: Stick and ball stacking model of crystal with zincblende structure along the [111] direction (left) and with wurtzite structure along the [0001] direction (right).

	AlN	GaN	InN	SiC	GaAs	Si
lattice constant a_0 (Å)	3.112	3.189	3.54	3.081	5.65	5.43
lattice constant c_0 (Å)	4.982	5.185	5.705			
internal parameter u	0.380	0.376	0.377			
energy gap E_g(300K) (eV)	6.2	3.39	0.7	3.1	1.43	1.1
dielectric constant ϵ_r	8.5	8.9	15.3	9.6	12.5	11.8
effective mass (m_e)	0.48	0.20	0.11	0.65	0.067	0.91
				0.25		0.19
electron mobility (bulk)	300	440	70-250	$<$400	6000	1350
at 300K (cm^2/Vs)						
optical phonon energy (meV)		91.2		95	33.2	62.9
elastic constant C_{13} [1)]	$108^{(a)}$	$103^{(a)}$	$92^{(a)}$			
	$120^{(b)}$	$70^{(b)}$	$121^{(b)}$			
elastic constant C_{33} [1)]	$373^{(a)}$	$405^{(a)}$	$224^{(a)}$			
	$395^{(b)}$	$379^{(b)}$	$182^{(b)}$			
piezoelectric constant e_{31} (C/m^2)	-0.60[2)]	-0.49[2)]	-0.57[2)]			
	-0.58[3)]	-0.36[4)]				
		-0.33[5)]				
	-0.38[6)]	-0.32[6)]				
piezoelectric constant e_{33} (C/m^2)	1.46[2)]	0.73[2)]	0.97[2)]			
	1.55[3)]	1.00[4)]				
		0.65[5)]				
	1.29[6)]	0.63[6)]				

Table 2.1: Material parameters for III-nitrides and other semiconductors of interest (SiC is considered in its 6H polytype). (a) and (b) correspond to theoretical and experimental values, respectively. All the data are from [8] and [9], except [1)] [10], [2)] [11], [3)] [12], [4)] [13], [5)] [14], [6)] [15].

ing to [0001] polarity. Ga-faced does not mean Ga-terminated; termination should only be used to describe a surface property, while following this terminology a Ga-faced material can be Ga-terminated or N-terminated as well. It is important to note that the (0001) and $(000\bar{1})$ surfaces of GaN are inequivalent (by convention, the [0001] direction is given by a vector pointing from a Ga to a nearest neighbor N-atom) along the longitudinal bond [10].
Some properties of GaN make it very attractive for device applications. High thermal conductivity (about four times higher than that of GaAs) and high breakdown field allow this

Characteristic	AlGaAs/InGaAs	AlGaN/GaN
2DEG electron mobility at T $= 300°$K (cm^2/Vs)	8500	2000
Saturated (peak) electron velocity ($\times 10^7$ cm/s)	1.3 (2.1)	1.3 (2.7)
Critical breakdown field (MV/cm)	0.4	3.0
Thermal conductivity (W/cmK)	0.5	> 1.5

Table 2.2: Transport properties of GaAs- and GaN-based 2DEG structures.

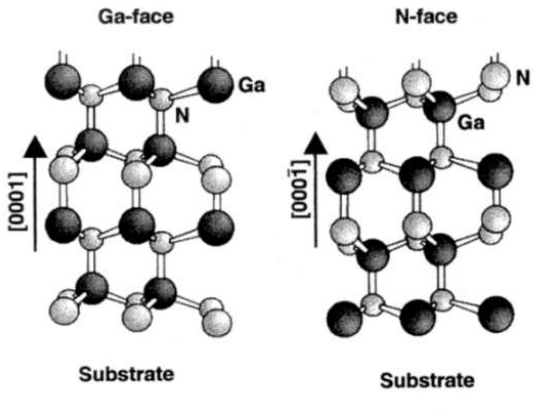

Figure 2.3: Structure of the N-face and Ga-face GaN.

material to withstand high power levels, and excellent electron-transport properties (particularly a high saturation velocity) enable it to operate at high frequencies (see table 2.2). The peak drift velocity reaches in AlGaN/GaN higher values (2.7×10^7 cm/s) than in AlGaAs/InGaAs (2.1×10^7 cm/s) since an electric field is able to accelerate the electrons up to higher field values before scattering due to optical phonons occurs. In fact the optical phonon energy is much higher in GaN (91.2 meV) than in GaAs (33.2 meV).

2.1.2 Symmetry and Polarization of III-Nitrides

Certain crystal types exhibit an electrical polarization called *spontaneous polarization* [17, 18]. The word *spontaneous* means that the polarization has *non*-zero value in absence of an external electric field; this is a physical property described by a vector, $\mathbf{P}_{\mathrm{SP}}$. The spontaneous polarization must be distinguished from the induced polarization which results when a dielectric is placed in an electric field.

If a stress σ is applied to certain crystals they develop an electric moment which magnitude is proportional to the applied stress. This is known as the direct *piezoelectric effect* and the general relationship between the piezoelectric polarization, the vector $\mathbf{P}_{\mathrm{PE}}$, and the second-rank stress tensor, σ_{ij}, is given by $\mathbf{P}^i_{\mathrm{PE}}$=$d_{ijk}\sigma_{jk}$. The d_{ijk} are the *piezoelectric moduli*; they form a third-rank tensor [18].

In the following we briefly discuss the polarization issue; as a physical property of a crystal, in relation with the symmetry properties of the semiconductor crystal structures of interest here.

Unlike for most III-V semiconductor compounds with zincblende crystal structure, the nitride equilibrium crystal structure is the hexagonal wurtzite type. The two crystal structures are compared in fig. 2.4. Neumann's principle states that the symmetry elements of any physical property of a crystal must include the symmetry elements of the point group of the crystal. A spontaneous polarization, a physical property described by a vector

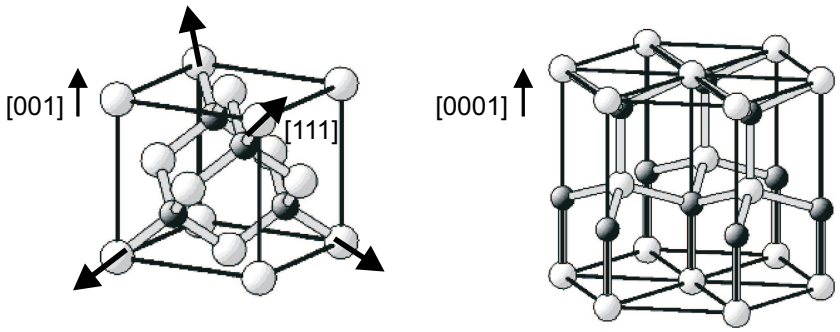

Figure 2.4: Cubic zincblende and hexagonal wurtzite-type of structure. Sum of the microscopic dipoles result in zero spontaneous polarization (zincblende) and in non-zero spontaneous polarization (wurtzite structure).

with a fixed orientation in the crystal, can therefore occur only in those crystals (also known as pyroelectric crystals) in which there is at least one direction (a vector) that remains invariant under all the symmetry operations of the crystal. These is the case only for rotation through any angle about the vector and mirroring in any plane containing the vector. Any kind of inversion, through a centre of symmetry or through the presence of a n-fold inversion axis (rotation followed by inversion through a given point on the axis) as well as multiple rotation axis are symmetric elements not compatible with a spontaneous polarization in the crystal. It follows that
(i) pyroelectric crystal can not have a centre of symmetry, and
(ii) pyroelectric crystals either have no rotation axis, or have a single rotation axis that is not an inversion axis.

According to the point group symmetry, both zincblende (crystal class $\overline{4}3m$) and wurtzite (class $6mm$) are non-centrosymmetrical. The wurtzite, with its unique 6-fold symmetry axis and mirror planes containing it, satisfies both requirements and can therefore have a spontaneous polarization which is parallel to the polar axis (c-axis). This is not true for zincblende, which, besides four polar three-fold rotation axis (the [111] equivalent direction), possesses also four-fold inversion axis (the [001] equivalent directions) (fig. 2.4). Thus a spontaneous polarization can definitely not occur in zincblende crystals.

The piezoelectric effect is described by a third-rank tensor and is restricted merely to non-centrosymmetric classes. As maybe derived from the form of the piezoelectric moduli, in particular from its non-zero components, in zincblende symmetry crystals a piezoelectric polarization appears [18].

From the symmetry requirements above the following statement holds: all pyroelectric substances are also piezoelectric. The inverse is not true, of course.

The macroscopic electric polarization of a crystal is often defined as the dipole of a unit cell. Indeed, such a dipole is not well defined, since it depends up on the choice of the

unit cell: contributions that result from charge transfer between the unit cell, across the cell boundary, have to be taken into account, in order to get a result for the polarization which is independent of the choice of the cell, as Martin has pointed out [19]. For example by referring to the two possible choices of zincblende unit cell shown in the left part of fig. 2.4 and with the crude approximation of assigning equal positive and negative point charges to the cation and anion lattice sites, respectively, it is a simple exercise to show that the calculated dipoles of the two unit cells are different. While it is zero for the standard cubic unit cell on bottom, it is different for zero for the hexagonal one shown on top.

A detailed discussion of the macroscopic polarization in crystalline dielectrics is presented by [20]. One of the main concepts is that the polarization $\mathbf{P}_{\mathrm{SP}}$ of a pyroelectric (or analogous of a ferroelectric) can not be measured as an intrinsic equilibrium property: the physical observables are only the variations of the polarization ΔP, which are indeed measured as bulk material properties in several circumstances. The differential concept is a basic one also for a theoretical formulation as well. The first quantum-mechanical calculation of the spontaneous polarization of a crystal has dealt with wurtzite BeO [21].

Since non-polar structures of this material do not exist, which can be taken as the reference for a differential method of computation, a fictitious zincblende BeO (zero polarization) has been used to this aim and the spontaneous polarization of the wurtzite (real) material has been defined with the respect to the reference structure. The actual calculation was performed in a supercell geometry, where wurtzite and zincblence slabs coexist, and ΔP was evaluated upon determining the interface charge which piles up at the domain boundaries. In agreement with symmetry arguments a *non vanishing* spontaneous polarization was obtained for the *ideal* wurtzite structure.

In a pictorial representation of this quantum mechanical result, the dipol can be understood in terms of a polarization of the electronic charge. In the wurtzite structure atoms of opposite electronegativity lie above each other along the symmetry axis and the charge displacement gives rise to a dipole along the same axis. On the other hand, the highest symmetry of the zincblende structure causes a cancellation of these contributions along the four [111] equivalent directions. An atomic relaxation in the wurtzite structure (non ideal wurtzite) due to Coulomb forces acting differently along c-axis on the different tetrahedral bonds (fig. 2.4, right) enhances this effect. Accordingly, a higher calculated macroscopic polarization results from the internal crystallographic distortion (P_3^{SP}=1.5$\times 10^{-2}$ C/m^2 at the equilibrium lattice parameters in BeO, *i.e.* 2/3 larger than for the ideal BeO) [21].

An equivalent technique based on the Berry-phase approach was applied by Bernardini *et al.* to the evaluation of the spontaneous polarization, the dynamical Born charges, and the piezoelectric constants of the III-V nitrides AlN, GaN and InN [11]. In this modern theory the difference in polarization between two states of a system (infinite periodical crystal) is calculated through a geometric quantum phase approach. Also in this case the zincblende structure is taken as a reference state with zero polarization. The piezoelectric constants are found to be up to ten times larger than in conventional III-V and II-VI semiconductor compounds, and comparable to those of ZnO. Further

properties at variance with those of conventional III-V compounds are the sign of the piezioelectric constants (positive as in II-VI compounds) and the very large spontaneous polarization. This important theoretical work has therefore predicted the presence of huge built-in electric field in wurtzite III-V nitride heterostructures which originate from heterointerface discontinuities of the macroscopic bulk polarization of the nitrides.

Wurtzite is the structure with the highest symmetry compatible with the existence of spontaneous polarization (fig. 2.4) and the piezoelectric tensor of wurtzite has three independent non-vanishing components. Therefore polarization in III-nitrides system will have both a spontaneous and a piezoelectric component.
In the absence of external electric fields, the total macroscopic polarization **P** of a solid is the sum of the spontaneous polarization $\mathbf{P}_{\mathrm{SP}}$ in the equilibrium lattice and the strain-induced or piezoelectric polarization $\mathbf{P}_{\mathrm{PE}}$.

Here polarization along the [0001] axis is considered, because this is the direction along which $\mathbf{P}_{\mathrm{SP}}$ occurs. The sign of the spontaneous polarization is determined by the polarity and turns out to be opposite to the [0001] direction. The piezoelectric polarization along the c-axis can be calculated using the piezoelectric coefficients e_{33} and e_{13} as

$$P_{PE_3} = e_{33}\varepsilon_3 + e_{31}(\varepsilon_1 + \varepsilon_2) \tag{2.1}$$

where $\varepsilon_3 = (c - c_0)/c_0$ is the strain along the c-axis, $\varepsilon_1 = \varepsilon_2 = (a - a_0)/a_0$ is the in-plain strain (which is assumed to be isotropic), a_0 and c_0 are the equilibrium values of the lattice parameters.
The third independent component of the piezoelectric tensor (e_{15}) is related to the polarization induced by shear strain and is not of interest for heteroepitaxial layers grown in the [0001] direction, in absence of external applied forces. For an hexagonal structure, the relation between the lattice constants is given by

$$\frac{c - c_0}{c_0} = -2\,\frac{C_{13}}{C_{33}}\,\frac{a - a_0}{a_0} \tag{2.2}$$

where C_{13} and C_{33} are the elastic constants (table 2.1).
Using equations (2.1) and (2.2) the amount of piezoelectric polarization in the direction of the c-axis can be determined by

$$P_{PE_3} = 2\,\frac{a - a_0}{a_0}\left(e_{31} - e_{33}\frac{C_{13}}{C_{33}}\right). \tag{2.3}$$

Equation (2.3) is valid in the linear regime for small strain values. It defines the piezoelectric tensor through the change in polarization induced by variations of lattice constants a and c only. From a microscopic point of view, a strain parallel or perpendicular to the c axis produces an internal displacement of the metal sublattice with respect to the nitrogen

ones, *i.e.*, a variation of the parameter u of the wurtzite structure. Therefore the spatial distribution of the polarization charges changes in comparison with the unstrained state and a piezoelectric contribution P_{PE} to the macroscopic polarization P must be considered. The calculated values of the piezoelectric constants in GaN, InN, and AlN are up to ten times larger than in GaAs based crystals and the sign is opposite to other III-V compounds. The value of the piezoelectric polarization is increasing with the strain and, for crystals or epitaxial layers under the same strain, it is increasing from GaN to InN and AlN.

The spontaneous polarization P_{SP} of the group-III nitrides was calculated by Bernardini *et al.* [11] and it is found to be negative: $-0.081\ (\mathrm{C/m^2})$ for AlN, $-0.029\ (\mathrm{C/m^2})$ for GaN and $-0.032\ (\mathrm{C/m^2})$ for InN, as resumed in fig. 2.5.

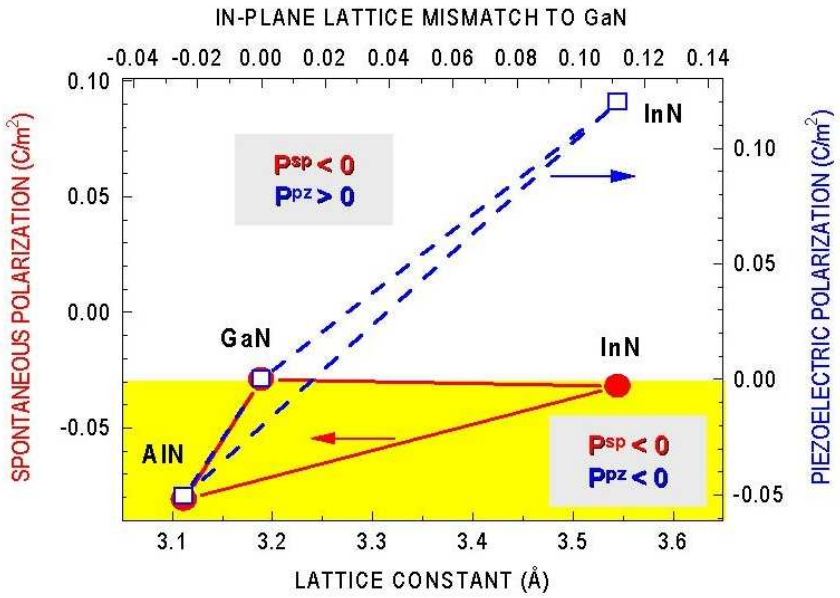

Figure 2.5: Spontaneous (*filled circles*) and piezoelectric (*open squares*) polarizations for the binary III-N compounds. The piezoelectric polarization is calculated for a pseudomorphic epitaxial layer on a GaN substrate, with the assumption of biaxial strain in the basal plane. The spontaneous polarization values are taken from [11].

For the $\mathrm{Al_xGa_{1-x}N}$ alloy it results:

$$\left(e_{31} - e_{33}\frac{C_{13}}{C_{33}}\right) < 0 \tag{2.4}$$

the relation which is satisfied over the whole range of x compositions. Therefore, from eq. (2.3) it follows that the piezoelectric polarization is negative for tensile and positive for

compressive strained $\mathrm{Al_XGa_{1-X}N}$ films, respectively. As a consequence, the orientation of the piezoelectric polarization is parallel to the spontaneous polarization in the case of tensile strain and antiparallel in the case of compressively strained $\mathrm{Al_XGa_{1-X}N}$ layers. From this point on $\mathbf{P}_{\mathrm{SP}}$ and $\mathbf{P}_{\mathrm{PE}}$ will be the polarizations considered along the c-axis. Associated with the divergence of the polarization, a polarization induced charged density is given as

$$\rho_p = -\nabla \cdot \mathbf{P} \tag{2.5}$$

For homogeneous top/bottom pairs layer **P** is constant in the bulk and has a discontinuity at the interface where a fixed polarization charge density σ is found. It can be calculated over an area ΔS through the theorem of divergency as:

$$\sigma \Delta S = \int_V \rho_p dv = -\int_V \nabla \cdot \mathbf{P} dv = -\int_\Sigma \mathbf{P} \cdot \mathrm{ds}\hat{\mathbf{n}} = \left(|\mathrm{P_{top}}| - |\mathrm{P_{bottom}}|\right) \Delta S \tag{2.6}$$

where the cylindrical surface Σ, enclosing the volume V, is formed by two surfaces ΔS just above and below the interface, as shown in fig. 2.6.

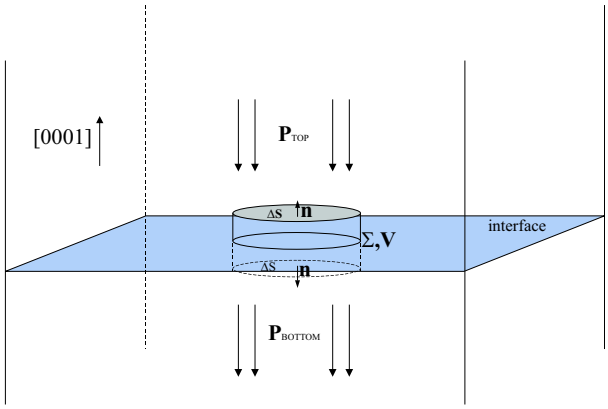

Figure 2.6: The close surface Σ enclosing the volume V can be used to calculate σ (charge density at the interface) through the theorem of divergency.

O'Clock, Duffy [13] and Tsubouchi [12] determined piezoelectric constants of GaN and AlN by measuring the electromechanical coupling coefficients of thin epitaxial layers grown on sapphire. In addition, piezoelectric constants of GaN, InN, AlN of BN crystals have been calculated by Bernardini *et al.* [11] and Shimada *et al.* [15] using the Berry approach to polarization in solids. The calculated and measured results by different groups for e_{33}(AlN) and e_{31}(GaN) are in good agreement, but the values of e_{31}(AlN) and e_{33}(GaN) differ by approximately 30%. Changes in e_{31} and e_{33} with the strain are attributed to the fact that the piezoelectric constans are significantly influenced by the internal strain component (changes in *u*) and depend on structural parameter of the unit cell

(changing with the lattice constants), which leads to a non-linear piezoelectric polarization at higher strains in pseudomorphic $\mathrm{Al_XGa_{1-X}N}$/GaN heterostructures. The nonlinearity of piezoelectric constants caused by strain leads to a negligible change of the piezoelectric polarization induced sheet charge of about 2% [22].

In order to determine the polarization induced sheet charge located at $\mathrm{Al_XGa_{1-X}N}$/GaN interface, following linear interpolations for $\mathrm{Al_XGa_{1-X}N}$ were used:
piezoelectric constants:

$$e_{ij}(x) = [e_{ij}(AlN) - e_{ij}(GaN)] \cdot x + e_{ij}(GaN) \tag{2.7}$$

lattice constants:

$$a_0(x) = (-0.077 \cdot x + 3.189) \tag{2.8}$$

$$c_0(x) = (-0.203 \cdot x + 5.189) \tag{2.9}$$

elastic constants:

$$C_{13}(x) = (5 \cdot x + 103)\ GPa \tag{2.10}$$

$$C_{33}(x) = (-32 \cdot x + 405)\ GPa \tag{2.11}$$

and the spontaneous polarization:

$$P_{SP}(x) = (-0.052 \cdot x - 0.029)\ \frac{C}{m^2}. \tag{2.12}$$

For the typical barrier $\mathrm{Al_XGa_{1-X}N}$ thickness of 300$\pm$50 Å the macroscopic strain relaxation was first observed for alloy compositions of $x = 0.38 \pm 0.03$. The degree of relaxation increases linearly with increasing the Al concentration for higher values of x. To calculate the reduction of the piezoelectric polarization and the polarization induced sheet charge due to the strain relaxation, the measured degree of relaxation was approximated by

$$r(x) = \begin{cases} 0 & 0 \le x < 0.38 \\ 3.5 \cdot x - 1.33 & 0.38 \le x < 0.67, \text{for d(AlGaN)} \approx 300 \\ 1 & 0.67 < x \le 1 \end{cases} \tag{2.13}$$

The piezoelectric polarization for partially relaxed barriers can be determined using the measured lattice constants (eq. (2.2)) or from the measured degree of relaxation

$$P_{PE}(x) = 2[r(x) - 1] \cdot \left\{ \frac{a_0(x) - a(GaN)}{a_0(x)} \right\} \times \left\{ e_{31}(x) - e_{33}(x) \cdot \frac{C_{13}(x)}{C_{33}(x)} \right\} \tag{2.14}$$

For a barrier with fixed alloy composition, the piezoelectric polarization induced sheet charge decreases linearly with increasing degree of relaxation. The maximum of the piezoelectric polarization induced sheet charge is limited by strain relaxation. The bound sheet

charge induced by only piezoelectric polarization σ/e_{PE} of AlGaN barriers with different degrees of relaxation is shown in fig. 2.7 (left). The maximum sheet charge caused by piezoelectric polarization of strained 300 Å thick barrier was calculated using the approximation of measured degree of relaxation $r(x)$ (eq. (2.13)) to be 9.26×10^{12} cm^{-2} reached at $x = 0.38$.

The calculated total bound sheet charge $(\sigma/e)_{\mathrm{PE+SP}}$ at the AlGaN/GaN interface is displayed in fig. 2.7 (right) as a function of Al concentration and different degrees of relaxation of the barrier. It is important to note that due to the difference in spontaneous polarization in AlGaN and GaN layers, the sheet charge does not drop to zero for an unstrained barrier. For barriers where the degree of relaxation can be described by $r(x)$, the polarization induced sheet charge is found to reach 2.38×10^{13} cm^{-2} at an alloy composition of 53%. For Al concentrations higher than 67%, the sheet charge is further increased up to 3.25×10^{13} cm^{-2}, even if the barrier is completely relaxed, caused by the increase of spontaneous polarization of the AlGaN layer with increasing Al composition.

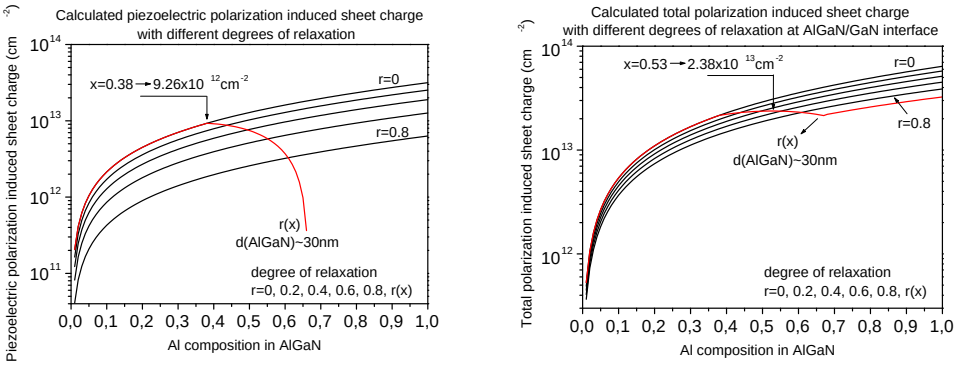

Figure 2.7: Calculated piezoelectric (left) and total (right) polarization induced sheet charge versus Al composition in AlGaN barrier at AlGaN/GaN interface displayed as a function of degree of relaxation.

2.1.3 Heterostructure and 2-dimensional Electron Gas

A combination of two different semiconductors with different band gaps grown on each other is called a heterostructure. $\mathrm{Al_XGa_{1-X}As}$, $\mathrm{Al_XGa_{1-X}N}$ are examples for wide-bandgap semiconductor (I) and GaAs, GaN for narrow-bandgap semiconductor (II) (fig. 2.8 (top)). Assuming to put in contact the two semiconductors, then two interface parameters for evaluating the band scheme are of interest:

- band gap discontinuity between valence ΔE_V and conduction band ΔE_C
- the band bending due to the built-in potential

Because of the different length and field scale it is possible by the theoretical treatment to clearly distinguish the description of band discontinuities from the influence of the band bending due to the built-in potential.

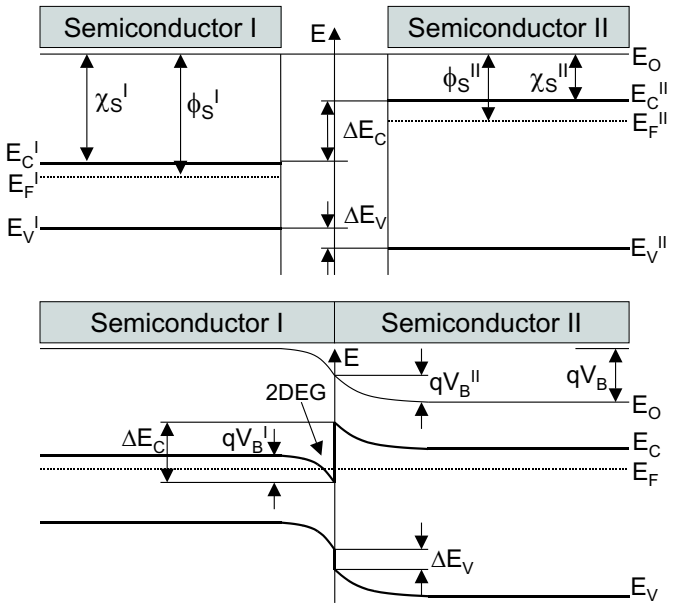

Figure 2.8: Band scheme of a lightly n-doped narrow-gap semiconductor (I) and a moderately/heavily n-doped wide-gap semiconductor (II) before (top) and after contact (bottom). In thermal equilibrium (bottom), the electrons are confined in the triangular quantum well of the narrow-gap semiconductor (I) and form a two dimensional electron gas (2DEG). E_C is the conduction band minimum, E_V the valence band maximum, E_F the Fermi level, ϕ_S the semiconductor work function, χ_S the electron affinity and V_B the built-in voltage.

The band discontinuity is determined by high electrostatic potential gradients acting on the carriers on the length scale of some atomic interplanar spacing. The energies and forces are very important at this point and the electric fields are equal to the atomic fields ($\gtrsim 10^8$ V/cm). Since semiconductor (I) has a smaller gap than semiconductor (II), there are regions in the gap of (II) where the continuum of bulk valence- and conduction-band states of (I) leak into the gap of semiconductor (II) (fig. 2.9 (a)). Thus, in limited energy range in the upper and lower parts of the gap of semiconductor (II) there exist continua of Virtual Induced Gap States (VIGS) derived from the bands (wave functions) of both semiconductors (I) and (II) [23].
Any electronic state in the gap of a semiconductor, including VIGS, is necessarily a mixture of valence- and conduction-band states. The closer the state is to valence-band edge, the more valence character it has. Nevertheless it always includes a certain admixture of conduction-band wave function. The crossover point (also branching point or neutrality

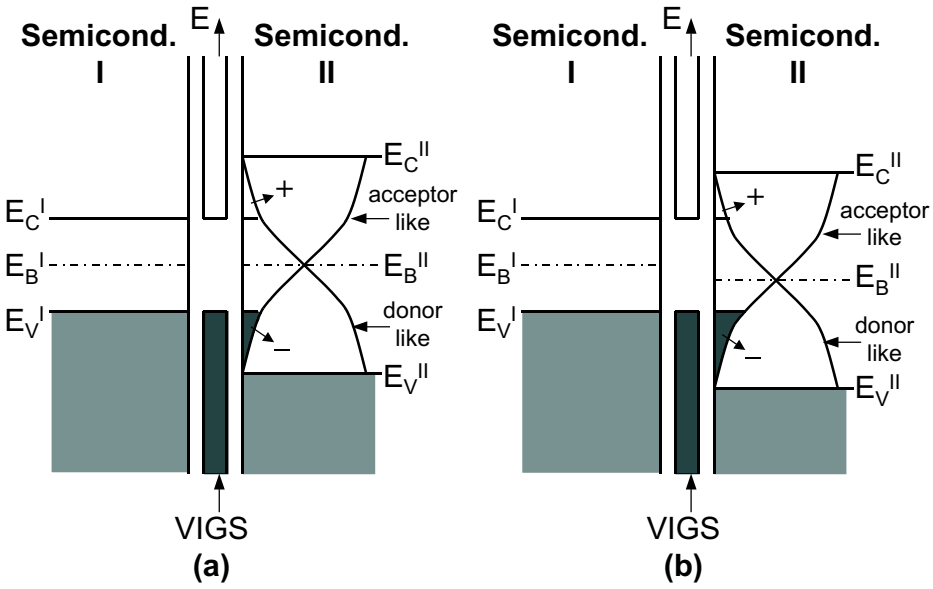

Figure 2.9: Schematic explanation of the formation of a semiconductor heterostructure in terms of Virtual Induced Gap States (VIGS) model. The band schemes of two semiconductors are plotted with conduction-band edge E_C and valence-band edge E_V. The matching of the two band schemes, *i.e.* the band off-sets, are determined by charge neutrality within the VIGS.
(a) The branching energies E_B^I and E_B^{II} coincide and charge neutrality in VIGS is achieved.
(b) The branching energies E_B^I and E_B^{II} does not coincide and the charge in the VIGS is not balanced.

level) E_B occurs where the gap states have equal valence and conduction character, i.e. where a net donor-like band behavior (lower part of the gap) changes into a net acceptor like behavior (upper part of the gap). The occupation of a state in the gap leads to a local excess of electronic charge in proportion to its degree of conduction character (tab. 2.3).

When the Fermi level E_{F} lies close to the branching point E_{B} of the VIGS, overall charge compensation occurs. In the situation shown in fig. 2.9 (b), where the branching points E_B^I and E_B^{II} of the two semiconductors do not match, the negative charge carried by the VIGS below E_B^{II} exceeds (due their weak conduction character) the tiny positive charge in the interface states in the upper half of the gap. This positive charge is, of

Gap state character	empty	occupied
valence (donor-like)	positive (+)	neutral (0)
conduction (acceptor-like)	neutral (0)	negative (-)

Table 2.3: The charge character of occupied and empty VIGS.

course, due to the fact that these predominantly acceptor-type states nonetheless have a small amount of valence character, which carries positive charge if the state is not occupied. It is obvious that both the positive and the negative interface charge residing in the VIGS is compensated when the branching points E_B^I and E_B^{II} in the two materials are aligned (fig. 2.9 (a)). For energetic reasons, the condition of zero interface dipole therefore requires alignment of the branching energies E_B. For an ideal semiconductor heterostructure the alignment of the branching points E_B^I and E_B^{II} in the two semiconductors directly yields the valence-band offset (fig. 2.9 (a)) as

$$\Delta E_V = (E_B^I - E_V^I) - (E_B^{II} - E_V^{II}) \tag{2.15}$$

The built-in potential is due to free charges in the material, for example arising from dopant atoms, that accumulate in the lowest energetic states, creating together with the ionized dopants a space charge zone. The potential, which overlaps the effective crystal potential, is determined by the interface position of the Fermi level and extends on a length scale that depends on the bulk doping of the two semiconductors (via the Poisson equation). Such a length scale, of the order of the Debye length, can be as long as thousand Å for doping of the order of 10^{16} cm^{-3}, and as short as $10 - 100$ Å for doping up to 10^{20} cm^{-3}. The electric fields are similar to the those which are spread over space charge in a P-N junction (10^5 V/cm).
The situation displayed in figure 2.8 (bottom) shows a depletion region of fixed ionized donor atoms spread in the wide-gap semiconductor near the interface due to the accumulation of donor dopant electrons in the narrow-gap semiconductor, which form a two dimensional electron gas (2DEG).

Let us now focus on semiconductor heterostructures where a thick GaN layer is grown on thin $\mathrm{Al_XGa_{1-X}N}$ layer. This thin $\mathrm{Al_XGa_{1-X}N}$ layer is grown on a GaN buffer layer and is therefore under tensile strain. In this special case the piezoelectric and the spontaneous polarizations point in the same direction and the value of the total polarization is:

$$P = P_{PE} + P_{SP} \tag{2.16}$$

Because the values of the piezoelectric constants and spontaneous polarization increase from GaN to AlN, the total polarization of a strained (or even unstrained) $\mathrm{Al_XGa_{1-X}N}$ layer is larger than that of a relaxed GaN buffer layer $[|P(Al_XGa_{1-X}N)| \geq |P(GaN)|]$ and therefore a positive polarization charge is present at the lower AlGaN/GaN interface for Ga-face structure (fig. 2.10 (left)) and at the upper GaN/AlGaN interface for the N-face structure (fig. 2.10 (right)) (eq. (2.6)) [22]. Electrons tend to compensate this positive polarization charge resulting in the formation of a 2DEG, assuming that the triangular quantum well at the AlGaN/GaN interface will drop below the Fermi level E_F. In analogy, a negative polarization sheet charge density can cause an accumulation of holes at the interface, if the valence band edge of the AlGaN/GaN heterostructure crosses the Fermi level. In fact, the spontaneous and piezoelectric polarization is large enough to produce 2DEGs

with high electron concentration even without intentionally doping the barrier, as opposed to by remote doping induced 2DEG as in AlGaAs/GaAs modulation doped heterostructures (tab. 2.2).

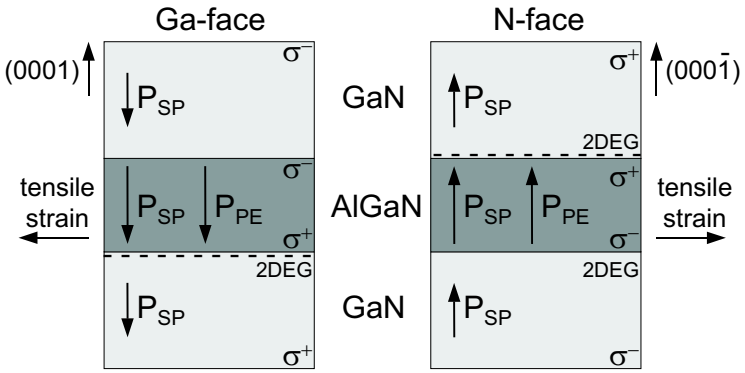

Figure 2.10: Spontaneous, piezoelectric polarization bound interface charges and 2DEGs in pseudomorphic $\mathrm{GaN/Al_XGa_{1-X}N/GaN}$ heterostructures with Ga-face (left) and N-face (right).

2.1.4 Electron Transport in III-V Nitrides

At the AlGaN/GaN interface a quite large conduction band discontinuity, up to 2.4 eV for AlN/GaN, together with the band bending induced by charge transfer across the junction leads (for a growth in the $[0001]$ direction) to the formation of a quantum well on the side of GaN. The electron confinement in the quantum well leads to a high carrier density depending on the position of the Fermi level and so on the doping.
The eigenvalues of electrons along the normal to the surface are quantized due to the confinement in the quantum well. Parallel to the interface the assumption of a free electron gas, described by Bloch waves, still holds. Therefore this case is described as that of a two dimensional electron gas. The eigenvalues of the electrons in a 2DEG are given by means of:

$$E_i^{2D} = \frac{\hbar^2}{2m_x^*} \cdot k_x^2 + \frac{\hbar^2}{2m_y^*} \cdot k_y^2 + E_i \,. \tag{2.17}$$

E_i can be calculated numerically by solving the Schrödinger and Poisson equations. The approximation of a symmetrical triangular potential is often sufficient for a qualitative treatment [24]. The eigenfunctions are given by the Airy-functions.
The existence of a 2DEG has significant consequences on the electronic transport along the interface. In a 3 dimensional non degenerate semiconductor the transport properties are calculated by solving the Boltzmann equation for elastic scattering under the assumption,

that the relaxation time τ_m is averaged through the temperature dependent energy distribution. A 2DEG can be treated as a degenerate semiconductor: only the electrons near the Fermi edge contribute to the transport and so τ_m has to be calculated just at $E = E_F$. This different energy dependence leads to a different temperature behavior as in the 3 dimensional case. In addition to this the Fermi impulse becomes dependent on the carrier concentration $k_F = \sqrt{2\pi n_s}$, that determines the quantity of initial and final states, which are available for scattering processes.
One experimental evidence of the existence of a 2DEG is gained by temperature dependent Hall effect measurements. For this purpose it is necessary to consider the different possible scattering mechanisms and their importance for the mobility of the electrons. We present now the most important of these mechanisms for the group III - nitrides. The 2DEG mobility as well as for some cases also the 3D mobility for non degenerate semiconductor are listed. For a more precise treatment see [25].
The different scattering mechanisms limit the electron mobility in different ways, but their effects can be treated as independent of each other. The effective mobility can then be determined in first approximation by the Matthiensen rule:

$$\frac{1}{\mu_{tot}} = \sum_i \frac{1}{\mu_i} \,. \tag{2.18}$$

Lattice (Phonon) Scattering
Atoms in a crystal lattice vibrate around their equilibrium positions. These fluctuations, which become bigger with the temperature, act as non periodic potential perturbations against the electron movement. The electrons interact with this distorted potential and exchange energy and impulse with the lattice atoms. The impulse exchange leads to a scattering of the electrons. The lattice vibrations freeze out at low temperatures. Phonon scattering plays an important role for temperatures higher than 80 K. Three most important phonon scattering processes are deformation potential acoustic, piezoelectric acoustic and polar optical.

Polar Optical Phonon Scattering
For the optical branch the atoms in the elementary cell move in opposite direction. In a polar crystal this is connected with an oscillating dipole moment. Since the energy of polar-optical phonons in GaN have such large energy ($E_0 = 90.5$ meV) compared to the energy separation between subbands, one must take a large number of subbands into account when calculating their effects, so the problem changes from two-dimensional to a three-dimensional. This corresponds to the fact that electrons which absorb an optical photon gain so much energy that they can be scattered completely out of the confining potential and into the bulk. Thus in calculating the optical phonon limited mobility, a variational principle method [26] can be used. It is possible to extract an analytical solution

for the mobility [27]:

$$\mu_{opt}^{3D} = \mu_{opt}^{2D} \propto e^{E_0/kT} \left[1 - \frac{5kT}{E_g}\right] \tag{2.19}$$

where E_g is the band gap energy of GaN. This mechanism gives the principal limitation to the mobility for temperatures above 200 K.

Acoustic Phonon Scattering
The acoustic branch describes the dispersion free spread of acoustic waves. In modulation doped heterostructures, although the movement of the electrons is confined to a thin layer of perhaps 100 Å near the interface, it is usually assumed that acoustic phonons can propagate freely in all three dimensions. Within the acoustic branch, the electrons in a polar crystal can interact either electrostatically through the piezoelectric interaction or through the deformation potential. The temperature dependence of confined electrons with three-dimensional acoustic phonons due to screened deformation potential scattering is given by [28]

$$\mu_{DP}^{3D} \propto T^{-3/2}, \qquad \mu_{DP}^{2D} \propto T^{-1} \cdot n_s^{1/2} \,. \tag{2.20}$$

The mobility limited by the screened piezoelectric mode scattering is given by

$$\mu_{piezo}^{3D} \propto T^{-1/2}, \qquad \mu_{piezo}^{2D} \propto T^{-1} \cdot n_s^{-1/2} \,. \tag{2.21}$$

The acoustic phonon scattering rates are linear functions of temperature. This approximation is true at temperatures at which the thermal energy is greater than the acoustic phonon energy. At lower temperatures the above expressions will overestimate acoustic phonon contributions to the total scattering rate [29]. However, since temperature independent processes, such as Coulomb scattering, tend to dominate the low temperature mobility, the deviations of the acoustic phonon scattering rate from linearity will have little effect on the total mobility.

Defect Scattering
Changes in the perfect periodicity of the lattice lead to local potential changes and so to a scattering of the electrons.

Ionized Impurity Scattering
Also the incorporation of impurities lead to a deviation of the electrons in the crystal. Particularly strong is the interaction with the Coulomb potential of the ionized impurities, which is dominant at low temperatures. In an AlGaN/GaN modulation doped heterostructure, we consider two different types of ionized impurity scattering. The first type is scattering by *residual ionized impurities* in the GaN. In bulk semiconductors, the ionized impurities occupy the same region of space as the conduction electrons, making a Coulomb

scattering very efficient process. Of course, the electrostatic interaction between an ionized donor and a conduction electron is somewhat screened by other conduction electrons. However, in order to achieve the high electron concentrations needed for efficient screening, the crystal must itself be highly doped, leading to higher concentrations of ionized impurity centers and effectively negating any beneficial screening effects. The second type is scattering by the *ionized donors* in the AlGaN barrier left behind the conduction electrons. Since the electric field of ionized centers drop off as the distance squared, this type of scattering is much less effective in limiting the electron mobility. This contribution can be neglected for concentrations up to 10^{15} cm^{-3} for spacers in the AlGaN barrier less than few hundred Å.
Assuming the impurities screening (Thomas-Fermi screening) the mobilities can be expressed as following:

$$\mu_{ii}^{3D} \propto \frac{T^{1/2}}{N_i}, \qquad \mu_{ii}^{2D} \propto \frac{n_s^{3/2}}{N_i} \tag{2.22}$$

where N_i is the concentration of ionized impurities. Coulomb scattering rates has been performed in a temperature independent approximation for 2DEGs, assuming that all scattering events involve electrons at the Fermi level [30]. At temperatures above 100 K, when the Fermi level starts to shift upward, the approximation is no longer valid. At such temperatures the mobility is limited by phonon scattering.

Alloy Disorder Scattering
In the alloys the statistical distribution of the elements leads to local potential fluctuations. The height of the scattering potential can be assumed as the difference of the energy gaps of the two different binary compounds. The importance of this kind of scattering mechanism depends on the degree of disorder in the crystal, *i.e.* on the frequency of the appearance of the single constituents. This is taken in consideration through a factor $x(1-x)$, where x is the atomic concentration of one of the constituents:

$$\mu_{alloy}^{3D} \propto \frac{1}{x(1-x)T^{1/2}}, \qquad \mu_{alloy}^{2D} \propto \frac{1}{x(1-x)n_s^{1/2}}\,. \tag{2.23}$$

The wave function for the 2DEG penetrate trough the interface into the $Al_XGa_{1-X}N$ alloy, thus cause alloy disorder scattering, which does not show any temperature dependence for the 2DEG case.

Dislocation Scattering
Commonly observed extended defects in GaN(0001) include stacking faults, stacking disorder, related Shockley and Frank partial dislocations, inversion domains and threading dislocations (TDs) [31]. The stacking disorder and partial dislocations usually occur in the region in immediate adjacency to the substrate and are associated with the growth of

a disordered low temperature nucleation layer [32]. Inversion domains are normally associated with nitrogen polar domains that have grown either through the free surface of an Ga-polar film or are overgrown by Ga-polar material. The TDs have typical total densities in the range $10^8 - 10^{10}$ cm^{-2} as a result of the substantial GaN film-substrate chemical and lattice mismatch [33]. There are two different predominantly observed TDs: pure edge, with Burgers vectors in the family $\frac{1}{3} < \overline{2}110 >$ and [0001] line directions; mixed character, with Burgers vectors in the family $\frac{1}{3} < \overline{2}113 >$ and line directions inclined $\sim 10^\circ$ from [0001] towards the Burger vector. Pure screw TDs, with line direction [0001], represent a small fraction ($\sim 0.1 - 1\ \%$) of the total density of TDs [31].
TDs in the group III-nitrides behave as non-radiative recombination centers, have energy levels in the forbidden energy gap, act as charged scattering centers in doped materials and provide a leakage current pathways. The highly dislocated wurtzite crystal can be pictured as hexagonal columns rotated relatively to each other by a small angle, with inserted atomic planes to fill the space between the columns [34, 35]. This is a consequence of the coalescence of slightly misoriented GaN high temperature islands [36]. Grain boundaries between prisms as in poly-crystalline material would require arrays of dislocations along the interface between two prisms.
Pure screw and mixed dislocations decrease with distance from the substrate-buffer interface [37]. Edge dislocations with mainly vertical orientation thread to the epilayer surface. The charged vertical dislocation lines form space charge around and cause scattering of electrons and reducing the mobility. Additional mobility reduction occurs in the buffer region due to scattering at screw dislocations, point defects and stacking faults. Empty traps are electrically neutral, while each filled trap carries one electronic charge. The negatively charged dislocation lines act as Coulomb scattering centers [38, 39]. The influence of scattering at charged dislocation lines on the mobility, compared to the lattice and ionized impurity scattering, becomes significant at threading dislocation densities above 10^9 cm^{-2} [39].
At low growth temperatures the formation of "V-defect" can occur. The V-defects consist of six $\{10\overline{1}1\}$ family planes and form an inverted hexagonal pyramid. They always form at TDs, with higher propensity for formation at mixed character TDs, but they also form at pure edge TDs [40, 41]. Wu *et al.* attributed the formation of V-defects to a kinetically limited growth process in which the surface depression associated with a TD assists in the formation of $\{10\overline{1}1\}$ facets [41].

Vertical devices are unaffected by the scattering of electrons at threading dislocation lines due to the repulsive band bending around dislocations and the directional dependence of the dislocation scattering. This may explain the observed performance of LEDs and lasers in the presence of high dislocation densities [39]. On other hand V-defects are important sources of reverse leakage in diodes and light scattering centers for laser structures. For HEMTs the V-defects usually form during the last grown AlGaN layer and can concentrate electric fields at ohmic source-drain and Schottky gate contacts.

The mobility in 2DEG inhibited by dislocation scattering only is given by

$$\mu_{disl}^{2D} = \frac{e \cdot \tau_{disl}^{2D}}{m^*}, \tag{2.24}$$

where m^* is the effective mass of GaN material multiplied by mass of an electron, e elementary charge of an electron and τ_{disl}^{2D} the 2D dislocation scattering time. The dependence of mobility on 2DEG sheet density n_s and dislocation density N_{disl} is given by

$$\mu_{disl}^{2D} \propto \frac{n_s^{3/2}}{N_{disl}}. \tag{2.25}$$

The theory of scattering by charged dislocations lines in AlGaN/GaN 2DEG developed by Jena *et al.* [33] shows that for dislocation density of 10^{10} cm^{-2} and carrier densities in the $10^{12} - 10^{13}$ cm^{-2} range, maximum 2DEG mobilities will be in the $10^3 - 10^4$ cm^2/Vs range. A reduction in the dislocation density to $\sim 10^8$ cm^{-2} in AlGaN/GaN HEMTs has resulted in record high mobilities at low temperatures [42, 43]. The novel method of lateral epitaxial overgrowth (LEO) is promising candidate for reducing the density of dislocations in the nitrides [44].

Interface Scattering

In a quasi two dimensional electron gas the charge transport takes place along the interface between two semiconductors. The interface roughness produces an additional deviation from the periodical lattice and so can substantially reduce the mobility of a 2DEG. Theoretical calculations were performed on AlGaN/GaN wurtzite and zincblende heterostructures in order to determine the scattering processes that limit the electron mobility by Oberhuber *et al.* [45]. At room temperature (RT), the mobility is dominated by polar optical phonon scattering. For higher sheet electron densities in the 2DEG the remote donor (impurity) and piezoacoustic scattering processes (which dominate at lower sheet densities) are effectively screened and the electrons are pushed closer to the interface. Depending on the interface quality, this can decrease the mobility significantly due to the increase of interface roughness scattering. For perfect interfaces, mobility of 2000 cm^2/Vs at RT is predicted, which is markedly higher than theoretically estimated [46] and measured [47, 48]. Antoszewski *et al.* [49] confirmed that depleting the electrons from the 2DEG channel by applying negative gate voltage the electron screening is less effective and consequently strong influence of Coulomb scattering reveals. Increasing the negative gate bias, the maximum mobility shifts towards higher temperatures with a simultaneous and dramatic decrease of the maximum mobility. The effect of the surface roughness on the mobility is expressed by

$$\mu_{SR}^{2D} = \frac{e \cdot \tau_{SR}^{2D}}{m^*}, \tag{2.26}$$

where the relaxation time is given by

$$\frac{1}{\tau_{SR}^{2D}} = \pi m^* \left[\Delta\Lambda e^2(0.5n_s + N_{DEPL})/\varepsilon_s)\right]^2/\hbar^3. \tag{2.27}$$

Δ and Λ are the root-mean-square deviation of the interface and the correlation length, respectively, ε_s is the dielectric constant, n_s the 2D electron concentration, N_{DEPL} is the charge density per unit area in the depletion layer and m^* the effective mass of an electron. For $Al_{0.25}Ga_{0.75}N$/GaN and for the 2DEG densities below $7-8\times10^{12}$ cm^{-2}, the mobility is limited by interface charge scattering with the scattering reducing as the 2DEG density increases due to increased screening. For the 2DEG densities above $7-8\times10^{12}$ cm^{-2}, the mobility decreases with increasing n_s resulting from increased interface roughness scattering as a result of the shift of the 2DEG towards the interface.

Dipole Scattering

Dipole scattering is dominant scattering mechanism at low temperatures and is absent in AlGaAs/GaAs HEMTs and Si metal-oxid-semiconductor field effect transistor (MOSFET). The 2DEGs in III-V nitride modulation doped heterostructures (MDHs) have a fundamentally new origin. The 2DEG in such heterostructures can be entirely polarization induced, as opposed to by remote doping as in AlGaAs/GaAs MDHs and gate induced inversion in Si-MOSFETs. In fact the spontaneous and piezoelectric polarization is large enough to produce 2DEGs without intentionally doping the barrier.

Because of strong polarization along the c-axis of the wurtzite nitride compounds and due to fluctuations of a perfectly periodic structure in the AlGaN alloy, a random distribution of microscopic dipoles in AlN and GaN regions of the alloy scatters the electrons in 2DEG [50].

The mobility inhibited by dipole scattering alone

$$\mu_{dipole}^{2D} = \frac{e\cdot\tau_{dipole}^{2D}}{m^*}, \tag{2.28}$$

was evaluated for different alloy compositions by Jena *et al.* [50]. An expected increase in mobility with the increase in the binary nature of the alloy barrier was observed. The intrinsic low temperature mobility limit in the $x=0.1-0.4$ range (which is typical of state of the art III-V nitride HEMTs) is in the $2-4\times10^5$ cm^2/Vs range. It is well worth noticing that this is much lower than the record low temperature mobilities ($\sim 10^7$ cm^2/Vs) of AlGaAs/GaAs modulation doped heterostructures and an order of magnitude higher than the record high mobilities in the AlGaN/GaN HEMTs observed (51700 cm^2/Vs) [43, 51]. The lateral epitaxial overgrowth promise to reduce the dislocation densities in the nitrides [44]. The effects of dipole scattering will be the next hurdle overcome in pushing the mobilities higher. Digital alloy growth is suggested as a technique to reduce the severity of dipole scattering. By growing either purely Al or

purely Ga layers, we use periodicity to overcome the scattering originating from the random nature of the alloy. However, digital alloy growth suffers from interdiffusion of atoms in the growth process, so dipole scattering can not be completely eliminated by this method.

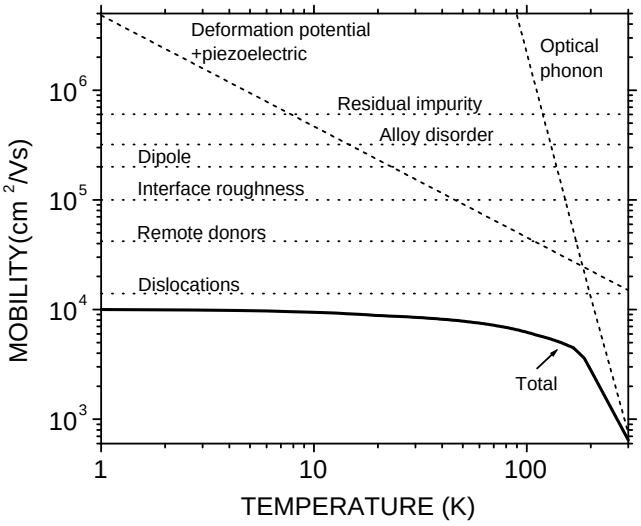

Figure 2.11: Theoretical temperature dependence of electron mobility in a $Al_{0.15}Ga_{0.85}N$/GaN modulation doped heterostructure. All curves are calculated mobilities (see text). The 2DEG density for this case is 1.6×10^{12} cm^{-2}, the concentration of residual ionized impurities in the GaN is 4×10^{15} cm^{-3}, the remote donor concentration in AlGaN barrier 10^{18} cm^{-3} and the dislocation density 10^9 cm^{-2}.

The interaction of electrons with charged impurity centers is dominant mechanism responsible for the scattering of free electrons at low temperatures in doped high quality bulk semiconductors. In order to reduce this interaction and increase the low temperature mobility, it was proposed that the carriers can be separated from the parent donors by growing modulation doped heterostructures. The figure 2.11 shows the estimated total mobility and calculated component mobilities of the electrons in an $Al_{0.15}Ga_{0.85}N$/GaN structure with no spacer, residual ionized impurity concentration of $N_{GaN} = 4 \times 10^{15}$ cm^{-2} and remote donor concentration of $N_{AlGaN} = 10^{18}$ cm^{-2} as a function of temperature from 1 to 300 K [30]. All Coulomb contributions were calculated in a temperature independent approximation, so the contribution to the mobility from all types of ionic impurities appear as straight lines.
At low temperatures, the electron mobility is dominated mainly by dislocation scat-

tering [33] assuming a dislocation density $N_{disl} = 10^9$ cm^{-2} and interactions with the Coulomb field of the remote donors [30]. The dipole scattering is calculated according to the study of Jena *et al.* [50] for $x = 0.15$ in $Al_XGa_{1-X}N$. The calculation of interface roughness scattering is taken from Ref. [49]. The scattering due to the interface charge was neglected. Starting at about 50 K, acoustic phonon scattering would become the main mechanism limiting the mobility through both deformation potential and piezoelectric scattering, if a spacer layer will be used in order to reduce the remote donor scattering and the dislocation density will be decreased to $\sim 10^8$ cm^{-2} in order to reduce the dislocation scattering. The strengths of both, deformation potential and piezoelectric scattering, are roughly equal. The exact temperature dependence at which acoustic phonon scattering becomes dominant will depend on the remote donor concentration as well as the spacer width and alloy composition of the $Al_XGa_{1-X}N$ layer [30]. As one would expect, at temperatures above 170 K, the mobility is limited by polar optical phonon scattering. As can be seen from the figure 2.11 the mobility saturates at roughly 10^4 cm^2/Vs.
Increase of low temperature mobility can be achieved by reducing the dislocation densities. This is nowadays possible by lateral epitaxial overgrowth [44]. Using wide spacers, the remote donor contribution can be made negligible even for concentrations up to 10^{20} cm^{-3}. The effects of dipole scattering can be removed by growing binary semiconductor as a barrier, either purely Ga or purely Al, with suggested digital alloy growth technique. Alloy disorder can be made less severe either by changing the Al fraction of the $Al_XGa_{1-X}N$ or by reducing the electron density which can be accomplished by growing wider spacers or reducing the remote doping concentration. By optimizing these parameters, the inherent mobility of a $Al_XGa_{1-X}N$/GaN modulation doped heterostructure can theoretically be increased to almost 6×10^6 cm^2/Vs neglecting interface roughness scattering. It should be noted however, that obtaining such mobilities puts very stringent requirements on the purity of the GaN layer. The residual charged impurity concentration must be less than 10^{13} cm^{-3}. The quality of the grown layers has to be very high with dislocation densities below $\sim 10^7$ cm^{-2}. The dipole scattering can be neglected by growing AlN barriers.

2.1.5 Principle of HEMT Device

The modern epitaxy techniques for growing high quality semiconductor layers enables to grow very fast, low noise High Electron Mobility Transistors (HEMTs) for high frequency application (20-100 GHz). The HEMT devices are the next stage development of Metal Semiconductor Field Effect Transistor (MESFET) used especially for radar application and satellite communication.
The epitaxial growth of wide-gap AlGaN semiconductor on a thick GaN undoped buffer layer leads to a heterostructure which can be used for HEMT devices. Such AlGaN/GaN HEMT structure is displayed in the fig. 2.12a. The HEMT is also controlled through

a Schottky barrier underneath the gate electrode as the MESFET. But the n-channel is built by a 2DEG at the AlGaN/GaN interface with typical electron concentrations of 1×10^{13} cm^{-2}. Conventional material systems based on AlGaAs/GaAs layer structure lead to a electron concentration in the 2DEG of 2×10^{12} cm^{-2}. The high electron concentration is separated from the ionized donors, so high mobilities and low noise operation are reached. Drain and source contacts have to be prepared such that under the metal overlayers a good ohmic contact to the 2DEG at the interface can be established.

In thermal equilibrium, the band scheme along an intersection normal to the layers below the gate electrode appears as in fig. 2.12b. When positive drain voltage is applied, the potential drop along the source-drain connection leads, of course, to a variation of the band scheme in fig. 2.12b parallel to the AlGaN/GaN interface. Depending on the local potential, the accumulation layer is more or less emptied of electrons; the position of the Fermi level E_F with respect to the band edges varies along the current channel. Transistor action is possible since an additionally applied gate voltage shifts the Fermi level in the gate metal with respect to its value deep in the undoped GaN layer (fig. 2.12b). Because of strong Schottky depletion layer just below the metal gate electrode (donors in the AlGaN layer having been emptied), most of the voltage drop occurs across this AlGaN layer, thus establishing a quasi-insulating barrier between gate electrode and 2DEG. The action of this Schottky barrier is similar to that of the SiO_2 layer in a Metal Oxide Semiconductor FET (MOSFET). Depending on the gate voltage, the triangular potential well at the interface is raised or lowered in energy and the accumulation layer is emptied (fig. 2.12c) or filled (fig. 2.12b). This changes the carrier density of the 2DEG and switches the drain-source current. For large enough gate bias, the depletion region penetrates into the 2DEG region, 2DEG concentrations become negligible and the current channel is pinched off. The corresponding relative gate voltage is called threshold voltage.

The amplification of the transistor is based on the control of low gate currents that switch much higher drain-source currents. Assuming a simplified model with the gate length L and gate width W the gate capacitance is given by

$$C_g = \varepsilon_s \varepsilon_o \frac{LW}{d_{AlGaN}}, \tag{2.29}$$

where ε_s is the dielectric constant of the semiconductor, ε_o the dielectric constant of the vacuum and d_{AlGaN} the thickness of the AlGaN layer below the gate electrode. The charge density en_S in the 2DEG is induced by the gate voltage V_g, thus enables to write for the gate capacity in linear approximation

$$C_g = \frac{dQ}{dV_g} \approx \frac{e \cdot n_S}{V_g - V_{BI}} \cdot LW, \tag{2.30}$$

where V_{BI} is the built-in voltage at zero external gate bias. For normal performance the drain-source voltage is so high that the electrons in the channel move with saturation

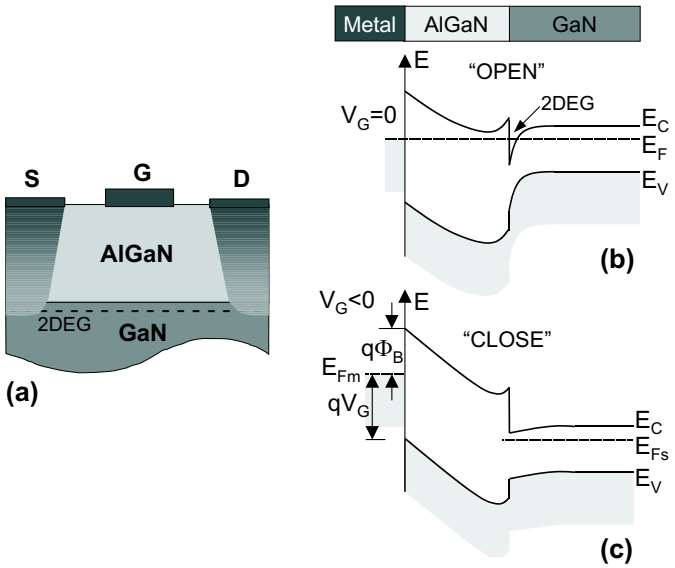

Figure 2.12: Schematic structure (a) and electronic band scheme perpendicular to the wafer surface underneath the gate electrode of an AlGaN/GaN HEMT device (b,c). The conductive channel is formed by 2DEG. The band schemes are under zero gate voltage, in thermal equilibrium, (b) and under negative gate bias (c). E_C is the conduction band minimum, E_V the valence band maximum, E_{Fm} the Fermi level in metal, E_{Fs} the Fermi level in the semiconductor, $q\Phi_B$ the Schottky barrier hight and V_G the gate voltage.

velocity v_s ($\sim 10^7$ cm/s) independent of drain voltage. The drain-source current can be written as

$$I_{DS} \approx e n_S v_s W. \tag{2.31}$$

Evaluating the n_S from the equation (2.30) and inserting it into the eq. (2.31) nearly linear dependence on the gate voltage is reached in the simple model

$$I_{DS} \approx \frac{1}{L} C_g v_s \left(V_g - V_{BI}\right). \tag{2.32}$$

Important parameter describing the performance of HEMT is the transconductance g_m which defines the change of drain-source current I_{DS} with the change of the gate voltage V_g at constant drain-source voltage V_{DS}:

$$g_m = \left(\frac{\partial I_{DS}}{\partial V_g}\right)_{V_{DS}} \approx \frac{1}{L} C_g v_s = e v_s \frac{dn_S}{dV_g} W. \tag{2.33}$$

The transconductance depends on the influence of electron concentration on the gate voltage. The relation between the transconductance and the capacity defines, according to eq. (2.33), the transit time τ for an electron to pass under the gate

$$f_m = \frac{1}{\tau} = \frac{v_s}{L} = \frac{g_m}{C_g}, \tag{2.34}$$

where f_m is the maximal frequency. For gate lengths in the order of 1 μm and saturation velocities v_s around 10^7 cm/s transit times of about 10 ps are reached. This makes the HEMT extremely interesting for microwave applications. To improve the high frequency properties, the capacity should be as low as possible and the transconductance as high as possible.

2.2 Nitride Growth

2.2.1 Substrates for III-Nitride based Heteroepitaxy

For an epitaxial process the best choice is to perform the growth of the semiconductor on a substrate made of the same material (*homoepitaxy*). The process to synthesize bulk GaN is quite complex, because of the very high melting point of GaN (2800°C). At this high temperature, the vapor equilibrium pressure of N_2 is very high and high pressures are needed (2000 bar) to let incorporate N and finally grow GaN. The trend is to grow very thick ($\sim 100\ \mu$m) layers by Hydride Vapor Phase Epitaxy (HVPE) and to use them as "quasi" substrates. Because the bulk gallium nitride crystals are not commercially available, most researchers have relied on *heteroepitaxy*, which is crystal growth on substrates of another material, for device fabrication. The substrate should satisfy the following requirements:

- be available in a minimum size of two inches, in large quantities and at an acceptable price.
- have physical properties concerning crystal structure and thermal expansion coefficients similar to the epilayer in order to reduce the density of defects propagating from the interface between the substrate and the epilayer towards the top of the structure. These defects, like microscopic fault lines, can degrade the performance of the semiconductor device which has to be realized.
- exhibit atomic flat surfaces.
- be stable under the influence of nitrogen radicals at temperature around 800°C for MBE[2] and 1100°C for MOCVD[3].

Most often, the lattice constant mismatch has been the primary criteria for determining the suitability of a material as a substrate for GaN epitaxy. In practice, properties including the material's crystal structure, surface finish, composition, reactivity, chemical, thermal and electrical properties, are also important in determining its suitability as a substrate, as these greatly influence the resulting properties of the epitaxial layer, sometimes in unexpected ways. The substrate determines the crystal orientation, polarity, polytype, the surface morphology, strain and the defect concentration of the GaN film. Thus, the substrate properties may ultimately determine whether the device achieves its optimal performance.

[2]Molecular Beam Epitaxy
[3]Metal Organic Chemical Vapour Deposition

Substrate property	Consequence
Lateral (a-lattice constant) mismatch	High misfit (primarily edge) dislocation densities causing: device leakage currents, short minority lifetimes; reduced thermal conductivity; rapid impurity diffusion pathways
Vertical (c-lattice constant) mismatch	Antiphase boundaries, inversion domain boundaries
Surface steps in non--isomorphic substrates	Double positioning boundaries (stacking mismatch boundaries)
Coefficient of thermal expansion mismatch	Thermally induced stress in the film and substrate; cracks formation in the film and substrate
Low thermal conductivity	Poor heat dissipation
Different chemical composition than the epitaxial film	Contamination of the film by elements from the substrate; electronic interface states created by dangling bonds; poor wetting of the substrate by the growing film
Non-polar surface	Mixed polarity in the epitaxial film; inversion domains

Table 2.4: Problems commonly encountered with the heteroepitaxy.

The influence of the substrate on the polarity and polarization of the group III nitride epitaxial layer is particulary important. The chemical reactivity and the conditions required for good quality epitaxy depend on the polarity of the crystal. In many cases, the substrate controls the crystal polarity, the magnitude and sign (tensile or compressive) of the strain incorporated into the epitaxial layers, and thereby the extend of the polarization effect. Considerable variations are possible using a variety of epitaxial growth techniques, as evidenced from the case of sapphire, where epitaxial GaN films of either polarity can be controllably produced. Nevertheless, the choice of substrate does provide limits on what can be done in subsequent processing.

Thus far, the vast majority of substrate studies produces [0001] oriented GaN. This orientation is generally the most favorable for growing smooth films. However, interest in GaN epitaxial layers with other orientations is increasing to eliminate the polarization effects. Such effects can be deleterious for some optoelectronic devices, causing red shifts in emission. In addition, piezoelectric effects in quantum wells can cause a spatial separation of electrons and holes, thereby decreasing the recombination efficiency [52].

Problems arising from heteroepitaxy are summarized in table 2.4 [53]. The misfit and threading dislocation densities in broad area of epitaxially deposited GaN on foreign substrates such as sapphire and silicon carbide are typically between 10^8 and 10^{10} cm^{-2}, compared to densities of essentially zero for silicon homoepitaxy, or 10^2 and 10^4 cm^{-2} for gallium arsenide homoepitaxy [54]. Other crystalline defects commonly observed in GaN heteroepitaxial layers include inversion domain boundaries and stacking faults [55, 56]. Such defects create non-radiative recombination centers, introduce energy states into the band gap and reduce minority carrier lifetimes. Impurities diffuse more rapidly along

	GaN	AlN	6H-SiC	Al_2O_3	Si
lattice parameter a(100) (Å)	3.189	3.11	3.08	4.73	5.43
lattice parameter a(111) (Å)				2.679	3.84
lattice parameter c (Å)	5.186	4.98	15.12	12.99	
thermal conductivity λ (W/cm K)	1.3	2.85	3.0-3.8	0.5	1-1.5
thermal expansion coeffi cient $\alpha_{\parallel}(10^{-6}\ \mathrm{K}^{-1})$	5.59	4.2	4.2	7.5	2.59
lattice mismatch GaN/substrate	-	+2.4%	+3.5%	-16%	-17%
thermal mismatch GaN/substrate	-	+25%	+25%	-34%	+54%

Table 2.5: Physical properties of the GaN, AlN, 6H-SiC, Al_2O_3, Si(111). All values are taken from [67].

threading dislocations than in bulk material, causing a non-uniform impurity distribution and degrading pn junction abruptness [57]. Because of the high piezoelectric constants of GaN, the local strain surrounding threading dislocations causes submicron scale variations in the electrical potential and electric field in comparison to the bulk material [58]. Such defects are typically non-uniformly distributed, thus the electrical and luminescence properties of the material are non-uniform as well. Defects increase the device threshold voltage and reverse bias leakage currents, deplete sheet charge carriers concentrations in heterostructure field effect transistor and reduce the charge carrier mobility and thermal conductivity. These detrimental effects will prevent more complex or large area (necessary for high power) GaN devices from achieving their optimal performance.

Regardless of the choice of substrate, many of its shortcomings such as its crystal quality or poor bonding characteristics with GaN can be ameliorated through an appropriate surface preparation such as nitridation, deposition of low-temperature (LT) AlN or GaN buffer layer, multiple intervening LT buffer layers [59], epitaxial lateral overgrowth [60], pendeoepitaxy [61] and other techniques [62–64]. Through a variety of such techniques, GaN layers with dislocation densities as low as 10^7 cm^{-2} have been produced.

Despite this success, even lower defect densities are necessary for more sophisticated devices operating at more extreme conditions of temperature, voltages and current densities. Thus, substrate capable of supporting better quality GaN epitaxial layers will still be needed for realizing the full potential of GaN-based devices.

The most common substrates for nitride growth are silicon carbide (SiC) and sapphire (Al_2O_3), but also silicon (Si) is getting nowadays more and more importance. Their properties are shown in table 2.5 in comparison with AlN and GaN. Wurtzite GaN and zincblende GaN has been grown also on gallium arsenide GaAs(111) and GaAs(001), respectively [65, 66]. The choice of the substrate depends not only on physical properties but also on the above described criteria (see table 2.6).

Sapphire

Sapphire has the space group of $R\overline{3}c$ and is mainly composed of ionic bonds. The single crystal can be described by both rhombohedral unit cells and hexagonal unit cell [68].

	SiC	Al_2O_3	Si
Advantages of the substrate	-low lattice mismatch to GaN -conductive -high thermal conductivity	-widely available -high stability at high temperature -easy to clean -quite cheap	-cheap -widely available -possibility of integration with Si microelectronics -available in conductive and insulating forms
Disadvantages of the substrate	-expensive -high micropipes and screw density	-high lattice mismatch to GaN -insulating -low thermal conductivity	-high lattice mismatch to GaN -high thermal mismatch to GaN

Table 2.6: Advantages and disadvantages of possible substrates for the nitride growth.

Sapphire, single crystal aluminium oxide, was the original substrate used in Maruskas and Tietjen's pioneering study of GaN epitaxy by HVPE in 1969 [69], and it remains the most commonly employed substrate for GaN epitaxy. The large lattice constant mismatch (+16%) of sapphire with GaN leads to high dislocation density (10^{10} cm^{-2}) in the GaN epitaxial film [54]. These high defect densities reduce the charge carrier mobility, reduce the minority carrier life time and decrease the thermal conductivity, all of which degrade device performance. Sapphire's coefficient of thermal expansion is greater than GaN (+34%), thus, producing biaxial compressive stress in the layer as it cooled from the deposition temperature. For thick films, the stress can cause both the film and the substrate to crack [70]. The thermal conductivity of sapphire is low (about 0.25 W/cm K at 100°C), thus, it is relatively poor at dissipating heat compared to other substrate materials and can not be used for power applications. The cleavage planes of epitaxial GaN layer are not parallel to those of sapphire, making laser facet formation difficult. Sapphire is electrically insulating, thus, all electrical contacts must be made to the front side of the device, reducing the area available for devices and complicating device fabrication. In addition, there is evidence that oxygen from the sapphire causes unintentional doping in the GaN layer, raising its background electron concentration [71].

One of the reasons sapphire has been so successful as a substrate for GaN epitaxy is simply that much more research has gone into developing procedures for producing good quality films on it compared to other substrates. The sapphire is grown mainly with MOCVD technique thanks to its ability to withstand high temperatures ($T_{melting} = 2030°C$). The large lattice constant mismatch between GaN and sapphire causes the film to be completely relaxed (not strained) essentially from the beginning of the growth. Consequently, the defect density at the film/substrate interface is very high. The detrimental effect of sapphire's large lattice constant mismatch must be ameliorated by a sophisticated processing scheme. First, the substrate surface is treated to remove the surface contaminants, remnant polishing damage, and to produce a step and terrace surface

structure. Second, the substrate is nitridated to alter the wetting characteristics of the deposited layers. Third, a thin buffer layer of either GaN or AlN (usually 10-100 nm thick) is deposited at a LT (usually $500 - 550°$C for MOCVD and $400°$C for MBE) and annealed to produce a surface ready for final epitaxial growth. There can be many variations in process conditions of each of these steps.

Control of the polarity of GaN films is critical in epitaxy. Generally for GaN on c-plane sapphire, smooth high quality films grown by MOCVD and HVPE are Ga-polarity [72–74]. In contrast to most researchers, Sumiya *et al.* [75] was able to produce N-polarity films by MOCVD. The polarity of GaN films on c-plane sapphire grown by MBE can be controlled by the buffer layer employed. A HT ($> 770°$C) GaN buffer layer produces N-polarity films, while a HT ($> 900°$C) AlN buffer produces Ga-polarity films [72, 76]. Generally, Ga-polarity GaN is preferable for obtaining smooth GaN films hence abrupt interfaces and heterojunctions.

Silicon carbide

Silicon carbide exists in more than 250 polytypes-one-dimensional variations of the stacking sequence of close packed biatomic planes [77]. The basic unit of the structure for all polytypes is a covalently bonded tetraedron of C atoms with a Si atom at its center or visa versa, *i.e.* either SiC_4 or CSi_4. The two most important polytypes as substrates for GaN epitaxy, 6H- and 4H-SiC, have stacking sequence ABCACBA and ABACA, respectivelly. Their bandgaps at liquid helium temperature are 3.02 eV (6H-SiC) and 3.27 eV (4H-SiC), and they belongs to the same space group $P6_3mc$ as wurtzite GaN.

Silicon carbide (both the 4H- and 6H-polytype) has several advantages over sapphire for GaN epitaxy, including a smaller lattice constant mismatch (3.5%) for (0001) oriented films, and a much higher thermal conductivity (3.8 W/cm K) (tab. 2.5). Conductive substrates available, making electrical contacts to the backside of the substrate possible, thereby simplifying the device structure compared to sapphire substrates. The crystal planes in epitaxial GaN parallel to those of the SiC substrate, making facets formation by cleaving easier. It is available with both carbon and silicon polarities, potentially making control of the GaN film polarity easier. However, most studies have been on Si-polarities substrates.

SiC does have its disadvantages. Gallium nitride epitaxy directly on SiC is problematic, due to poor wetting between these materials [78]. This can be remedied by using an AlN or $Al_XGa_{1-X}N$ buffer layer, but such layers increase the resistance between the device and the substrate. Even though the lattice constant mismatch for SiC is smaller than that for sapphire, it is still sufficiently large to cause a large density of defects to form in the GaN layers. Surface roughness of SiC as received from the vendors is one order of magnitude (1 nm RMS) higher than that for sapphire (0.1 nm RMS). 10-100 micropipes for cm^2 range, screw dislocations with dislocation density of 10^3-10^4 cm^{-2} [79] and also remnants subsurface polishing damage are sources of defects, which may propagate into the GaN epitaxial layer and degrade device performance. Preparing smooth silicon car-

bide surfaces is difficult and can enhance the price of a 2 inch wafer up to 2000 Euro. SiC's thermal expansion coefficient is less than that of AlN and GaN, thus, the films are typically under biaxial tension at room temperature. SiC can be realized in insulating and conducting type (n, p) and its use for nitrides allows several applications (fig. 2.13). Recently interest in semi-insulating SiC has developed, as it is the preferred substrate for both SiC- and AlGaN-based power microwave devices. Typical electrical properties of commercial SiC are summarized in table 2.7. Currently single crystal SiC is produced by relatively few manufactures.

Conductivity type	Impurity	Carrier concentration range (cm^{-3})	Resistivity range ($\Omega \cdot$ cm)
N	N	10^{15} to 10^{19}	0.01-0.10
P	Al	10^{15} to 10^{19}	1-10
Semi-insulating			10^{5}

Table 2.7: Conductivity types, impurities and resistivities of commercial 4H- and 6H-SiC wafers.

The many studies of GaN epitaxy on SiC substrates can be divided into three areas: substrate preparation, nucleation and growth. Substrate preparation studies have focused on methods of producing cleaner, more ordered SiC surface. This is done to enhance nucleation and to minimize defects in the final epitaxial layer. Nucleation studies have considered the effects of the temperature, substrate polarity, and the effects of process condition (temperature, III/V ratio, etc.) on the growth mode and deposit morphology of the initially deposited AlN or GaN. Growth studies look at the cumulative effects of surface preparation and nucleation on the film quality and stress in the film.

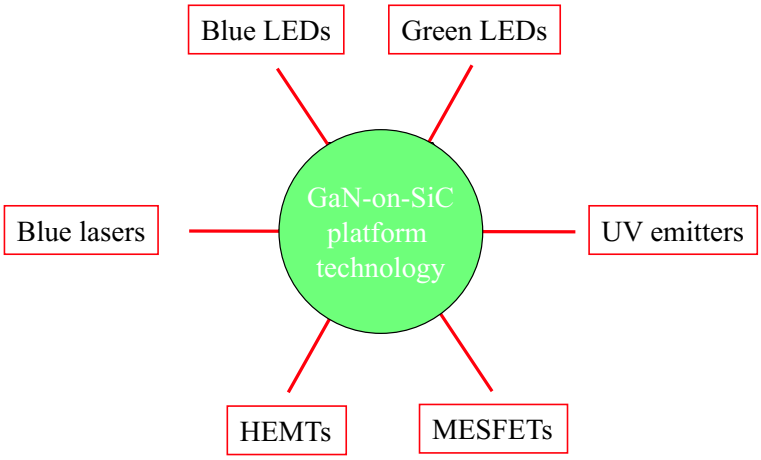

Figure 2.13: Possible applications of nitrides grown on SiC.

Although the smaller lattice constant mismatch suggest SiC should produce better GaN films than sapphire, the best GaN films on both substrates are similar quality. Early, it was recognized that one factor limiting the quality of GaN films on SiC substrates may be poor surface finish (roughness) of SiC substrates as received from vendors. Sapphire can be prepared with surface having one tenth the roughness of SiC. Producing SiC with comparable surface smoothness has proved difficult due to its extreme hardness and high chemical stability. Typically, as received SiC substrates have surface scratches and subsurface crystal damage, remnants of the polishing procedure. An example of the surface scratches on 6H-SiC substrate in shown in figure 6.6 in subsection 6.2.1. In addition to the scratches, there is a very little order to the surface structure of as received substrates; the surface may terminate on any step position A, B, C. Defects generated at the surface may propagate into the epitaxial structure and, hence, degrade the film quality.

To remove this damage from the 6H-SiC surface, and to produce a more uniform step and terrace structure, several methods have been examined including oxidation of the SiC to form SiO_2 which is subsequently removed by hydrofluoric acid [80]; etching in HCl+H_2 [81]; ion etching [82]; or most commonly, HT ($> 1500°$C) etching in hydrogen [83, 84]. Hydrogen etching removes all scratches and on axis 6H-SiC substrates produces an ordered surface of steps one full (1.5 nm) unit cell high, which presumably all terminate on the same stacking position [85].

The nucleation behavior of GaN and AlN on 6H-SiC substrates are significantly different. Aluminium nitride nucleates at both HT and LT. In contrast, GaN only nucleates on 6H-SiC at LTs ($< 800°$C), in random, three-dimensional island growth.

At high deposition temperatures ($> 800°$C), AlN nucleates in two-dimensional manner, resulting in complete surface coverage after the deposition of very little material. The AlN is truly epitaxial, without the high density of defects at the film/substrate interface seen with AlN/sapphire. It helps reduce the direct mismatch of $\sim$3.4% between GaN and 6H-SiC, and promotes wetting of the substrate surface.

As an alternative to pure AlN, $\mathrm{Al_XGa_{1-X}N}$ buffer layers have also been considered as the later has smaller lattice mismatch to GaN and can be electricaly conductive. The $\mathrm{Al_XGa_{1-X}N}$ buffer layer provides a mean of changing the relative lattice mismatch between the substrate and upper GaN layer. This is another control of the GaN film quality. Lin and Cheng [86] found the GaN quality improved with an $\mathrm{Al_{0.08}Ga_{0.92}N}$ buffer layer grown by low-pressure MOCVD. The deposited GaN epitaxial layer had a mobility and carrier concentration of 612 cm^2/Vs and 1.3×10^{17} cm^{-3} (at 300 K), respectively, and the FWHM of the X-ray (0002) rocking curve was 145 arcsec for 1.3 μm GaN.

Due to the smaller thermal expansion coefficient for SiC than for wurtzite GaN, the final GaN films on SiC typically are under stress, but both the magnitude and the sign of the strain vary considerably with process condition. Typically, GaN epitaxial layers on SiC are highly strained, with the average value of biaxial stress ranging up to 1 GPa. The

large lattice mismatch together with the considerable differences in the thermal expansion coefficient between GaN film and SiC, lead to a large extended defects density of 10^9 to 10^{10} cm^{-2}. Optical and Raman spectroscopy studies of MOCVD-grown and MBE-grown GaN on SiC confirm they are under tensile stress, while those on sapphire substrates are under compression [87]. This suggests that the mismatch of the thermal expansion coefficient is the dominant factor determining the stress in GaN films on the SiC substrate.

Polarity control could be a key advantage of SiC compared to sapphire if a single polarity is produced on a specific substrate. For sapphire without a proper nitridation and buffer layer, films of mixed polarity may be deposited. The electrical polarity of the GaN/SiC interface plays a central role in determining the quality of the GaN material for optoelectronic applications.

The polarity of the SiC substrate strongly influences the surface morphology and crystal quality of the epitaxial GaN films. Electronic structure calculation for the (0001) interface indicates that the stronger bonds are at the Si/N interface and at the C/Ga interface [88] and therefore Si-terminated SiC substrate should produce a Ga-terminated (0001) GaN epilayer. Ren and Dow [89] analyzed the lattice matching of the SiC with GaN using tight-binding model of the electronic structure. They argued that the GaN grown on a C-terminated SiC (0001) substrate has a local microscopic lattice mismatch of 6%, while in contrast, GaN grown on the Si-terminated surface has a local lattice mismatch $< 3\%$ by theoretical calculation.

Although the polarity of GaN on SiC has been studied by a number of techniques, many experimental results in the literature are in conflict. The above theoretical arguments is considered as ”standard framework”, where Ga-face GaN grows on Si-face SiC and N-face GaN on C-face SiC [16]. With a few exceptions such as the work of Asaki and Matsuoka [90], where they concluded that the epitaxial GaN layers on $(0001)_{Si}$ and $(0001)_C$ SiC were terminated with N and Ga, respectively, most results are consistent with ”standard framework”.

Silicon

Silicon is an attractive substrate for GaN-based devices because of its physical properties, crystal quality, doping capability, thermal stability, low cost and well known Si technology (fig. 2.14). The crystal perfection is better than any other substrate material used for GaN epitaxy and its surface could be prepared with extremely smooth finishes. To date, the quality of GaN epitaxial layers on silicon has been much poorer than that on sapphire or silicon carbide, due to large lattice constant (-17%) and thermal expansion coefficient (+54%) mismatch, and the tendency of silicon to form an amorphous silicon nitride layer when exposed to reactive nitrogen sources. Nevertheless, GaN devices have been already demonstrated on Si substrates including LEDs and HEMTs [67, 91].

Si has a diamond-lattice structure with the space group of $Fd\overline{3}m$, which belongs to the cubic-crystal family. It can be presented as two interpenetrating fcc sublattices with one

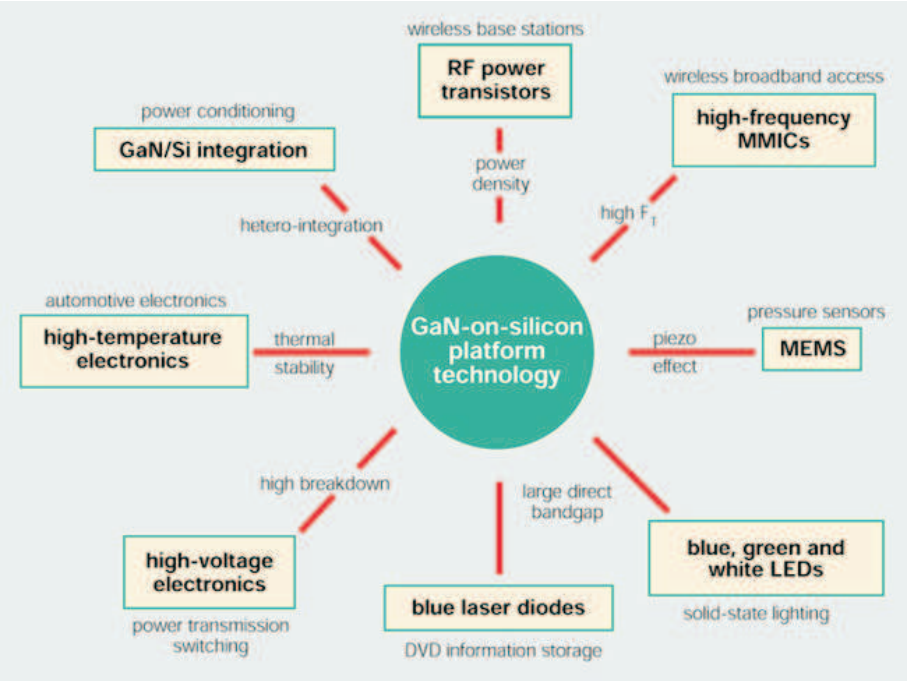

Figure 2.14: Possible applications of nitrides grown on Si(111) [92].

sublattice displaced from the other by one quarter of the distance along a body diagonal of the cube (*i.e.* displacement of $a\sqrt{3}/4$, where $a = 0.543$ nm). Each atom is surrounded by four equidistant nearest neighbors that lie at the corners of tetrahedron. The physical properties are listed in table 2.6.

Both zincblende and wurtzite GaN epilayers have been grown on the Si(001) by MBE [93], MOCVD [94] or HVPE [95]. The GaN films directly on Si(001) are phase mixed [93] or wurtzite phase only [96]. Due to the large lattice mismatch, it is difficult to grow pure zincblende phase GaN directly on Si(001). Furthermore, an amorphous Si_XN_Y layer may form at the GaN/Si interface due to the reaction of atomic nitrogen and Si atoms introducing a phase mixture [97]. Buffer layers are typically deposited first on the Si substrate to enhance wetting, reduce the reactivity of the substrate and to provide a better lattice constant match between the film and substrate. A thick layer of 3C-SiC produced by CVD or a thin layer prepared by direct carbonization is commonly used to eliminate this amorphous layer and promote zincblende growth. The utilization of other buffer layers, such as AlN or $Al_XGa_{1-X}N$ [94] resulted in the wurtzite phase growth.

Si(111) is generally the preferred substrate for GaN epitaxy. The quality of GaN layers on these substrates has been significantly improved and the devices such as field-effect transistors [98], Schottky-barrier ultraviolet detectors [99] and blue LEDs [100] have been

achieved in the past few years.

Large difference in lattice constant (-17%) and the strength of the Si-N bond results in a high dislocation density of $\sim 10^{10}\mathrm{cm}^{-2}$ comparable to GaN on sapphire [91]. To overcome this problem different buffer layers such as AlAs [101], GaAs [102], AlN [102–104], LT GaN [105] and ZnO [106] have been tested for Si(111) substrates. The choice of buffer layer is still an open problem, and the quality of deposited GaN epilayers may strongly depend on the buffer layer properties. In addition, to avoid formation of silicon nitride, it is common in MBE to initiate the growth of AlN buffer layer by exposing the Si substrate to the flux of aluminium for short time and subsequently nitridation is set on [102, 103]. These techniques helps suppress the formation of silicon nitride at the interface and result into a 2D growth mode of wurtzite GaN [107]. In MOCVD growth, HT AlN buffer layer is much better than LT one to produce 2D growth for GaN epitaxy [108].

The greater thermal expansion coefficient of GaN as compared to that of Si ($5.6 \times 10^{-6}\,\mathrm{K}^{-1}$ versus $2.6 \times 10^{-6}\,\mathrm{K}^{-1}$) (+54%) puts the film in tension, hence crack may be generated in GaN during the cool-down cycle as shown in fig. 2.15 of GaN($1\ \mu$m)/AlN(100 nm) heterostructure grown on Si(111) in our MBE system. GaN layers exceeding about $1\ \mu\mathrm{m}$ of thickness show usually cracks when grown on Si(111) [109].

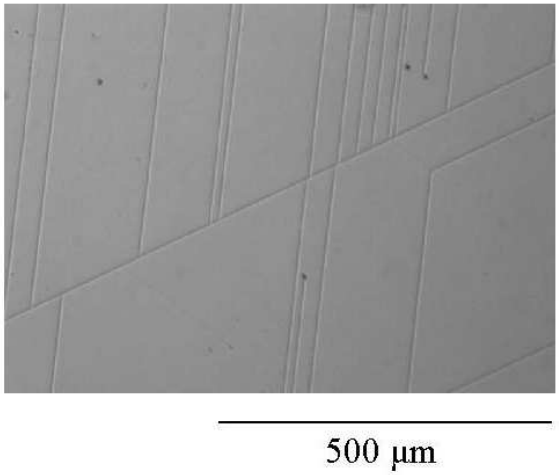

Figure 2.15: Cracks formed on the sample ED157 [GaN($1\mu m$)/AlN(100 nm)/Si(111)] grown in our MBE system.

There are three equivalent primary crack directions along $[11\bar{2}0]$, $[\bar{1}2\bar{1}0]$ and $[\bar{2}110]$. The resulting cleavage planes are $(1\bar{1}00)$, $(10\bar{1}0)$ and $(01\bar{1}0)$ respectively [91]. The epitaxial relationship is GaN(0001) on Si(111). Since the primary cleavage planes of Si are of type {111} with $< 110 >$ cleavage directions, GaN and Si have always a common cleavage direction, e.g. $[11\bar{2}0]$GaN and $[\bar{1}10]$Si [91] (fig. 2.16). The critical thickness at

which cracking occurs depends on the growth technique because the stress in GaN layers grown on Si(111) is proportional in first approximation to the difference between the growth temperature and room temperature [110]:

$$\sigma_{th} = \Delta\alpha_{th}(T_g - T_r) \tag{2.35}$$

where:

σ_{th}	is the thermal stress,
$\Delta\alpha_{th} = \alpha_{th}(GaN) - \alpha_{th}(Si(111))$	the difference between thermal expansion coefficients,
T_g	the growth temperature and
T_r	the room temperature.

Using an AlN buffer layer deposited at low temperatures such as 700°C, or an intermediate layer consisting of AlN and AlGaN at high temperature (1100°C) [105], or a thick AlN to GaN graded buffer layer [111], or using AlN/GaN supperlattice [112], or step graded $\mathrm{Al_XGa_{1-X}N}$ [113], the crack problem could be reduced. Nikishin *et al.* [102] reported a biaxial stress of ~ 160 MPa and an in-plane stress +0.09% for GaN epilayers deposited by MBE between 0.4 to 2.2 μm. Marchand *et al.* [111] confirmed that the thickness of AlN buffer layer will change the sign of stress (tensile or compressive) in AlN and stress magnitude in GaN epilayer. With MBE growth technique it has been possible to grow crack-free GaN layers (up to 3 μm) thicker than with MOCVD due to the lower growth temperature [114]. However the critical thickness at which cracking occurs

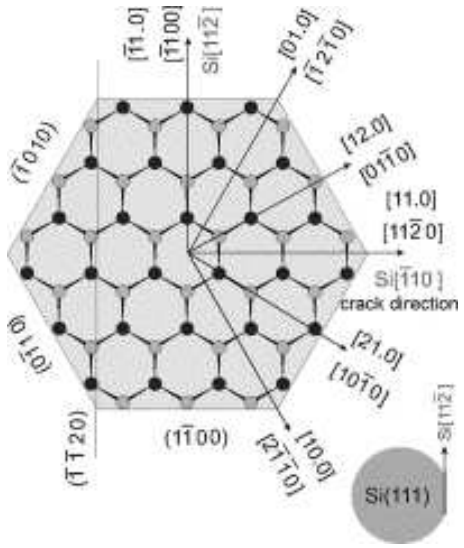

Figure 2.16: Cleavage directions of a GaN grown on Si(111) [91].

depends not only on the growth temperature, but also on the quality of the buffer layer. The complex mechanism underling the formation of cracks in GaN grown on Si(111) is still not fully understood. A very recent work from Krost *et al.* [67] gives an outlook of recent developments and on the techniques employed to avoid the cracking problem.

Zhao *et al.* [115] determined that the GaN grown on an AlN buffer layer by MOCVD had Ga-polarity. Hellman [16] concluded that GaN grown on an AlN buffer layer on Si(111) was Ga faced and GaN grown directly on Si(111) was N faced according to the "standard framework".

Nevertheless III-nitrides growth on Si promise many advantages compared to other substrates, especially possible integration with Si microelectronics. Its application will be a common procedure in industry (*i.e.* NITRONEX) only when a large request from the market will overcome the extra cost required for a successful growth.

GaN substrates

Gallium nitride itself is the best choice as a substrate for GaN epitaxy and device fabrication, as it eliminates all problems associated with heteroepitaxy. Homoepitaxy offers better control of crystal polarity, dopant concentration, stress, zero or very low thermal expansion coefficient and lattice constant mismatch, and no need of buffer layers or nitridation compared to heteroepitaxy on silicon, sapphire or silicon carbide substrates. Although there are several techniques for producing bulk GaN crystals including growth by vapor phase transport [116], growth from supercritical fluids [117] and growth from sodium fluxes [118], only high pressure growth from solutions and hydride vapor phase epitaxy have produced large area crystals. Already some bulk crystals and free-standing epitaxial HVPE GaN crystals are commercially available. Should bulk GaN wafers become available, future growth of III-nitrides on current substrates will be omitted.

2.2.2 MBE

Molecular Beam Epitaxy (MBE) is a versatile technique for growing thin epitaxial structures made of semiconductors, metals or insulators. In MBE, thin films crystallize via reactions between thermal-energy molecular or atomic beams of the constituent elements and a substrate surface which is maintained at an elevated temperature in ultrahigh vacuum (UHV) as schematically shown in fig. 2.17. The composition of the grown epilayer and its doping level depend on the relative arrival rates of the constituent elements and dopants, which in turn depend on the evaporation rates of the appropriate sources. The typical growth rate of 5-10 nm/min is low enough that surface migration of the impinging species on the growing surface is ensured, consequently the surface of the grown film is very smooth.

Simple mechanical shutters in front of the beam sources are used to interrupt the fluxes, *i.e.* to start and stop the deposition and doping. Changes in composition and doping can

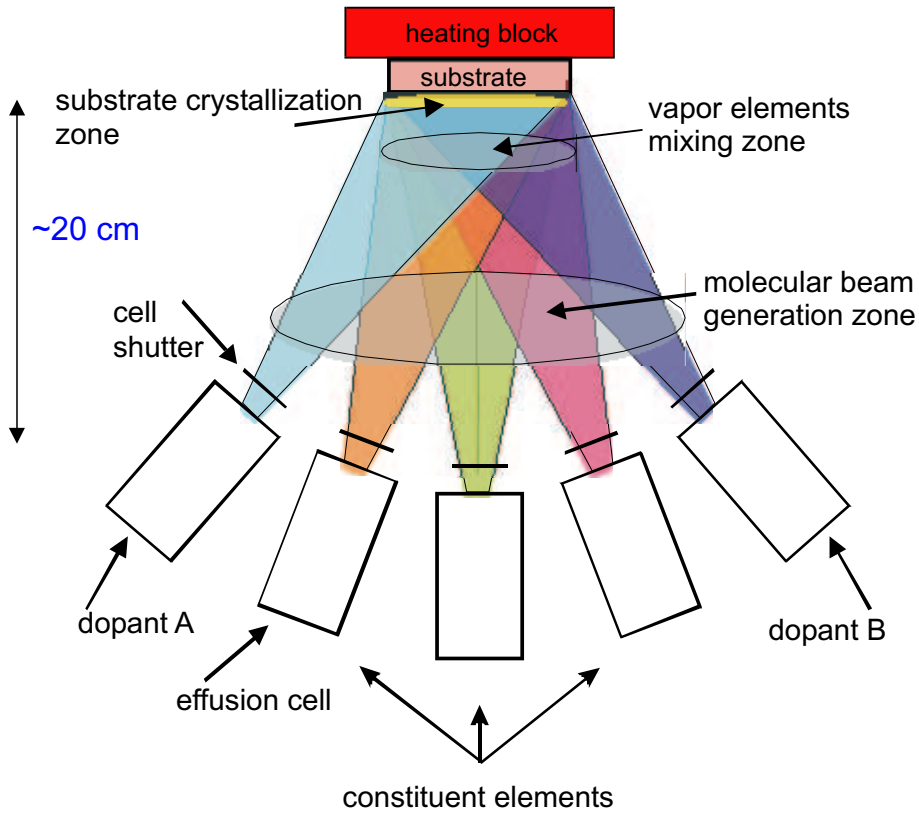

Figure 2.17: Schematic description of a MBE chamber.

thus be abrupt on an atomic scale.

A peculiar characteristic which distinguishes MBE from other deposition techniques is its significantly more precise control of the beam fluxes and growth conditions. Because of vacuum deposition, MBE growth is carried out under conditions far from thermodynamic equilibrium and is governed mainly by the kinetics of the surface process occurring when the impinging beams react with the outermost atomic layers of the substrate crystal. MBE has also an other unique advantage: the direct control of the epitaxy. Being realized in UHV environment it may be controlled in situ by surface sensitive diagnostic methods such as Reflection High Energy Electron Diffraction (RHEED), Auger Electron Spectroscopy (AES), or ellipsometry.
For nitride growth, the effusion of the metal atoms (Ga, In, Al) and dopants (Si, Mg) from conventional Knudsen effusion cells has to be combined with a source for nitrogen radicals. Nitrogen at room temperature is an inert gas and not very reactive, because of the triple bond between the two nitrogen atoms. The dissociation of one molecule into

reactive nitrogen atoms requires a relatively high amount of energy:

$$946.04\,\mathrm{kJ}\cdot\mathrm{mol}^{-1} + \mathrm{N}_2 \rightarrow 2\mathrm{N}.$$

Under the influence of a plasma at reduced pressure, a significant dissociation of the nitrogen molecules takes place. Atomic nitrogen is chemically very active at room temperature and bonds with many metals (Hg, Zn, Cd, Mg) creating various nitrides. Therefore group III-nitrides can be grown by plasma assisted molecular beam epitaxy, where the plasma induced fragmentation of nitrogen molecules is combined with the evaporation of metal atoms from effusion cells.
The growth is carried out in the molecular flow regime, where the transport of atoms or molecules in both thermal beams from the effusion cells as well as the beam of activated nitrogen from the plasma source occurs in a collisionless manner. The admissible value of the total pressure of the residual gas to preserve the molecular flow regime in the vacuum reactor can be estimated to be in the order of 10^{-4} mbar [119]. A much lower pressure (10^{-11} mbar) is required in order to preserve the sample from contaminations.
The nitrogen ions created by the plasma sources are poorly confined and reach the substrate because of the pressure difference between the plasma cell and the MBE chamber and perhaps due to attraction by negatively charged substrate. Nitrogen radicals leaving the RF plasma source have energies in the region of 2 eV so radiation damage, that in GaN has an estimated threshold energy of 24 eV, can be neglected [10].
More technical details about MBE can be found in section 4.1, where our experimental apparatus is described.

2.2.3 MOCVD

The growth of Group III-nitrides by MOCVD entails the transport of gas phase organometallic precursors, hydrides for the nitrogen source ($\mathrm{N}_x\mathrm{H}_y$) and transport gases to a heated substrate on which the precursors are pyrolyzed and the nitride film deposited (fig. 2.18). The underlying chemical mechanism is complex, involving a combination of gas phase and surface reactions and still remain poorly characterized. This technique has the advantage of large area growth capability, good conformal step coverage and precise control of epitaxial deposition.
The deposition of epitaxial MN (M = In, Ga, Al) by MOCVD has traditionally been carried out using mixtures of trimethyl-indium, -gallium, -aluminium ($\mathrm{Me}_3\mathrm{M}$) and ammonia (NH_3). The high thermal stability of NH_3, although still low compared to N_2, is one reason for the use of high substrate temperatures, typically above $900°$C for GaN and AlN. The high growth temperature and thus high nitrogen vapour pressure lead to problem of nitrogen loss from the MN film and to carbon contamination from the decomposition of the organic during metalorganic pyrolysis. The loss of nitrogen can be alleviated by the use of high V/III gas ratios during the deposition (e.g. $> 2000 : 1$). A development of MOCVD,

very effective in reducing dislocations, is the “Lateral Epitaxial Overgrowth” (LEO). This technique consists of partially masking of a substrate with SiO_2 and subsequently regrowth over it. The dislocation density at the surface of the overgrown film ($10^4 - 10^5$ cm^{-2}) is reduced by at least three orders of magnitude relative to that of conventional GaN films (10^8 cm^{-2}).

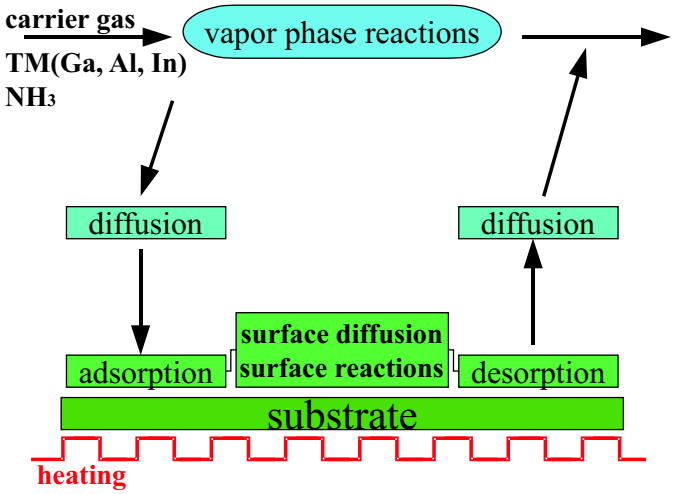

Figure 2.18: The principle of a MOCVD.

2.3 Surface and Interface Electronic Properties

Surface and interface electronic properties play an important role for AlGaN/GaN HEMT devices. For group III-Nitrides with wurtzite structure the presence of fixed polarization interface charges yields new challenges in order to understand and control Schottky barrier heights, band offsets and 2D confinement in heterostructure field effect transistors. The surface properties have significant impact on the formation and concentration of the 2DEG at the AlGaN/GaN heterointerface. In real devices using the passivation layer the performance is stabilized. Passivation layer protects the surface of a semiconductor structure from outer influences, which can degrade the device activity. All these properties form the knowledge basis for understanding and improving the performance of AlGaN/GaN HEMTs (fig. 2.19) and will be mentioned in this section. Surface states were investigated and discussed in more detail in section 6.4 and subsection 5.2.2.

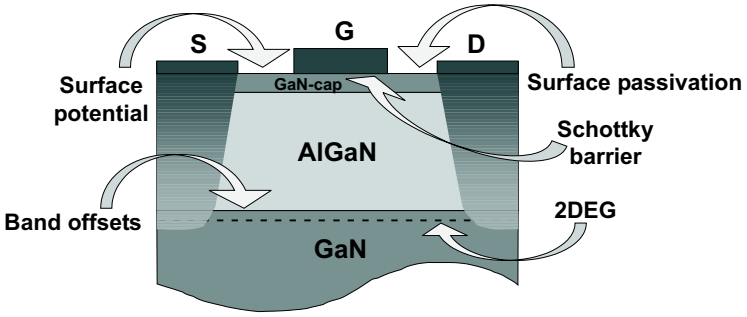

Figure 2.19: Properties forming the knowledge basis for understanding and improving the performance of AlGaN/GaN HEMTs.

2.3.1 Band Offsets at SiC/AlN, SiC/GaN and GaN/AlGaN Heterostructures

The valence band offset (VBO) has been determined by XPS at the 6H-SiC/AlN, 6H-SiC/GaN and AlN/GaN heterointerfaces within our group [120]. Fig. 2.20 summarizes the experimental results with a schematic view of the energy band scheme both at the heterojunctions and at the surface. The two heterojunctions with the SiC substrate are of interest, in particular, for device growth on conductive substrates. While the AlN nucleation layer represents an electrical isolation to the substrate, this is not the case for a GaN nucleation layer. In fact, the almost vanishing conduction band offset for the SiC/GaN heterojunction allows electron transfer from and into the substrate. This is of interest when the conducting SiC substrate is used as back contact to devices on top, as e.g. in laser diodes.

The AlN on GaN and the reverse heterojunctions have also been studied. Due to scattering of the measured data a range is given for the VBO from 0.15 to 0.4 eV. Considering

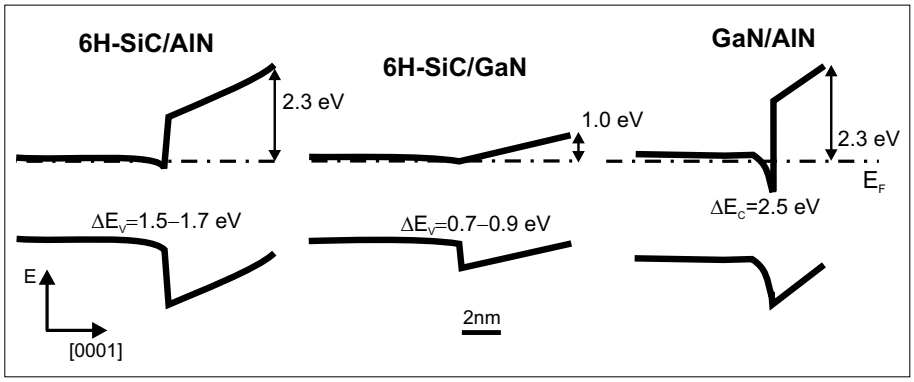

Figure 2.20: Schematic plots of the band scheme at the studied heterojunctions: the band offsets and the surface Fermi level pinning positions are those derived from the XPS experiments.

that the band gap difference between AlN and GaN amounts to 2.8 eV, our results indicate 10% of the band gap discontinuity falling into the valence band and consequently 90% into the conduction band. This large conduction band offset is of importance for the confinement of electrons at GaN/AlGaN 2DEG heterostructures and is one of the reasons for the very high sheet concentrations measured in the channel (see subsection 6.2.6 and section 5.2).

The apparent dependence of the experimental VBO on the overlayer thickness, due to the presence of the strong polarization fields, has also been pointed out, in view of a correct VBO determination by XPS [120]. In fact, electric fields are expected in the ultrathin overlayer with consequent bending of the overlayer band scheme. Since the VBO determination by XPS is based on the measurement of the binding energy difference between a core level in the substrate and one in the overlayer, the shift in the overlayer core level due to the electric field causes an apparent dependence of the VBO on the overlayer thickness.

Furthermore, a comparison of the experimental XPS data with self consistent calculations of the band scheme, in particular close to the $n-$6H-SiC/2H-AlN heterojunction, clarifies the interplay of charged AlN surface states.

In the model, electronic surface states (SS) are accounted for in a simplified way, by considering a uniform distribution in the AlN gap. The energy position of the AlN gap states is between 2.5 and 4.5 eV above the AlN VBM, according to the surface state energies calculated for a (1×1) ideal surface [121]; their charge neutrality level is assumed to be at an energy in the mid of the surface density of states (SDOS). The resulting band scheme has been calculated for a surface density of states in the range between 10^{12} and 10^{16} cm^{-2}eV^{-1}. Fig. 2.21 (a) shows the surface state effect for an intermediate SDOS (3×10^{13} cm^{-2}eV^{-1}). At increasing AlN thickness the SS carry an increasing positive charge, which partially compensates the negative surface polarization charge. As a consequence the electric field intensity decreases with the AlN thickness. For the lowest SDOS

an increase of the overlayer thickness empties the surface states, but their positive charge is too small to screen the field in the AlN, which therefore maintains the strength predicted by theory.

In fig. 2.21 (b) the experimental results (symbols) are compared with the model. In the model, each core level signal, from the overlayer (Al-2p) and from the substrate (C-1s), is obtained for a certain thickness by adding several discrete gaussian components, whose intensity decays exponentially from the overlayer surface and whose energy position shifts according to the band bending, as in fig. 2.21 (a). The centroid energy difference as a function of the AlN thickness is then plotted as a continuous line in case of a pseudomorphic overlayer. If relaxation has occurred, then the piezo-component of the field is lacking and the dashed line is calculated. A quantitative agreement is found for a SDOS of 3×10^{13} cm^{-2}eV^{-1}.

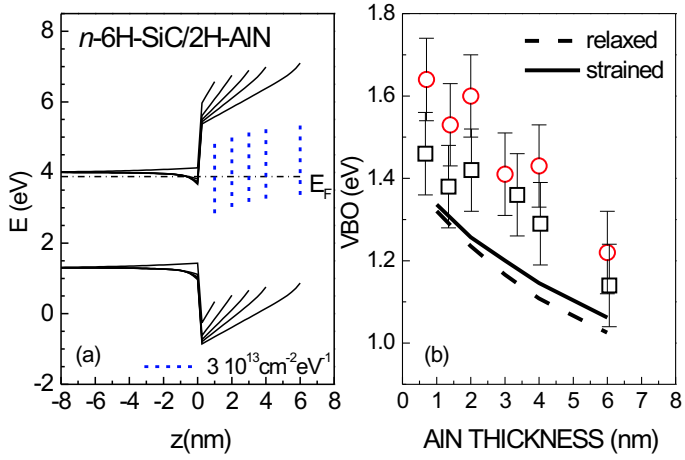

Figure 2.21: (a) Tight Binding self consistent calculation of a *relaxed* AlN/SiC heterostructure as a function of the overlayer thickness taking into account a constant density of surface states SDOS=3×10^{13} cm^{-2}eV^{-1} (sketched with a vertical dashed line). (b) VBO as a function of the AlN overlayer thickness: experimental XPS data determined from different runs (symbols) compared with the model (see text) for a pseudomorphic and relaxed overlayer (continuous and dashed line, respectively).

2.3.2 Schottky Barrier Height at Pt/GaN Ga- and N-face interfaces

The study of the Schottky barrier height (SBH), in particular its dependence on the polarity of the GaN, provides a further example of new aspects for the electronic properties at wurtzite nitride heterojunctions, due to the presence of polarization charges.

In contrast to earlier assumptions, where the Schottky barrier height at metal/semiconductor junctions is determined by the difference in metal and semiconductor work functions (Schottky model [122]), the MIGS (metal induced gap states) -model

of Heine [123], Tersoff [124] and refined by Mönch [125] meanwhile allows in simple cases a quantitative understanding and even prediction of Schottky barrier heights. More details about the models are shown in section 3.7.

In a recent study Karrer *et al.* [126] investigated the Schottky barrier heights of Pt on MBE grown n-type GaN surfaces of different polarity (Ga-face with internal polarization in GaN directed away from the Pt/GaN interface, N-face with internal polarization directed to the Pt/GaN interface). On the Ga-face the measured Schottky barrier height $\phi_{exp}(\mathrm{Ga-face}) = 1.1$ eV nearly matches the expected value from the MIGS model, taking also into account charge transfer at the interface in terms of electronegativity differences between Pt and the semiconductor (fig. 2.22). For the N-face polarity of GaN with positive polarization charge Q_{pol} at the interface (internal polarization directed to interface) the measured Schottky barrier height $\phi_{exp}(\mathrm{N-face}) = 0.9$ eV differs significantly from the MIGS model curve (fig. 2.22).

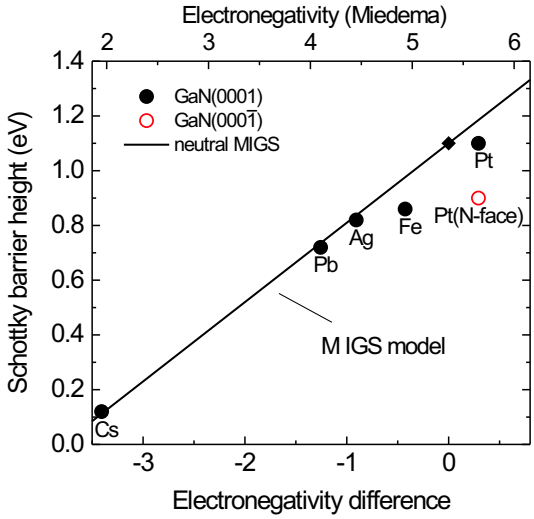

Figure 2.22: Barrier heights of laterally homogeneous GaN Schottky contacts as a function of the metal and the GaN electronegativity difference. The MIGS line is drawn after $\phi_{Bn} = \phi_{bp} + S_X(X_m - X_s)$ with $\phi_{bp} = 1.1$ eV and $S_X = 0.29$ eV/Miedema-unit, derived from a charge neutrality condition, which does not take into account the polarization charge close to the GaN surface (after Ref. [127]).

This deviation can be quantitatively explained by adding the polarization charge Q_{pol} to the interface charge balance in addition to the charges residing in the MIGS Q_{MIGS}, the space charge depletion layer Q_{sc} and the metal (Pt) Q_m [128],

$$Q_{pol} + Q_{MIGS} + Q_{sc} + Q_m = 0. \tag{2.36}$$

The decrease of 0.33 eV in ϕ_{Bn} was calculated with respect to the standard MIGS model, that is in very good agreement with the experimental finding of 0.28 eV.

A similar increase of ϕ_{Bn} with respect to the MIGS model curve in fig. 2.22, but not found in the experiment, would be expected for the Pt/Ga-face Schottky barrier (as well as for the other metals Cs, Pb, Ag and Fe in fig. 2.22), since for the Ga-face polarity negative polarization charge $-Q_{pol}$ has to be taken into account in the total interface charge balance as well. A qualitative explanation might be, that reconstruction models of GaN(0001) [129] suggest the presence of a metallic Ga double layer which might effectively screen the polarization induced interface charge Q_{pol} and the "refined" MIGS-model of Mönch [125, 127] holds as is seen in the experimental results (fig. 2.22)

2.3.3 Impact of surface states on AlGaN/GaN HFET performance

GaN based HFETs are tremendous interest in application requiring high power at microwave frequencies. Their development has been the result of improving structural quality with regard to unintentional impurity concentrations of GaN and AlGaN layers. The main obstacle to progress is the control of the trap densities in the bulk and surface of the material. The surface trapping effects significantly impact the problem of drain current collapse. The surface states are essential to improve the performance of high power device and are unavoidable in this material system due to the strong polarization fields [43, 130–132].

The power of an HEMT device is lowered due to the reduction of maximum drain current, called as current collapse, clearly seen in DC $I_{DS} - V_{DS}$ characteristic [133–137] (fig. 2.23 (left)). The positive charge of the donor-like surface states beside the polarization charges play an important role in formation of high sheet electron concentration at AlGaN/GaN interface [43, 130–132]. The fact, that the current collapse occurs when a negative gate voltage is applied to the device, suggest that electrons coming from the gate electrode are responsible for the current collapse. The mechanism of the current collapse can be explained as follows:

1. During the negative gate bias, electrons flowing out of the gate electrode are captured by the free surface states at the area between gate and drain electrodes as shown in figure 2.23 (right).

2. Electrons captured by the surface states cause a virtual gate due to the reduction of the amount of net positive charge at the surface in donor-like states [133], causing a decrease in the drain-source current I_{DS} and transconductance g_m. The parameter that now determines the drain current from the device is the potential on the virtual gate.

Possible reason of the current collapse are (i) deep levels in the barrier layer under the gate metal, (ii) deep levels in the interface and/or in the buffer GaN layer, and (iii) surface states. However, the threshold voltage did not change by the gate bias stress. This

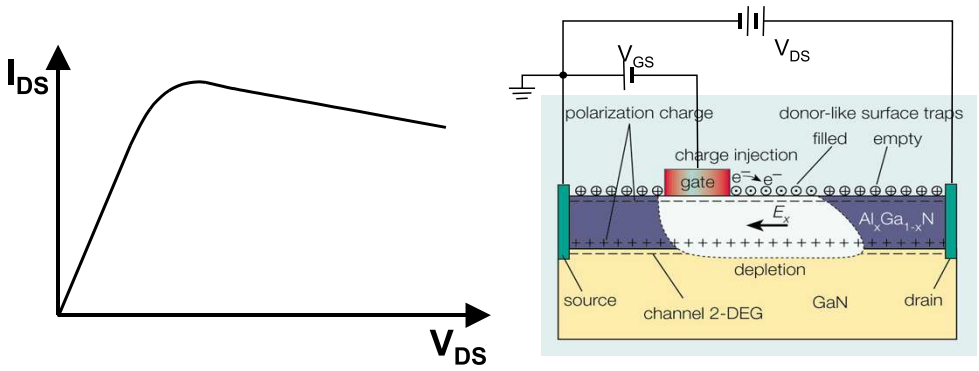

Figure 2.23: Negative biased gate leads to trapping of electrons in the surface states and formation of the virtual gate in the region between gate and drain (right). Consequently the drain-source current is reduced (left), the current collapse effect occurs.

indicates that contribution of the deep levels in the barrier layer under the gate and in the interface/buffer layer is not significant [138].

To restore the drain-source current I_{DS} to its value the net positive charge on the surface must be restored and virtual gate must become forward biased. This can be done in two ways: (i) Electrons trapped in the surface states are removed if the gate voltage is forward biased with respect to the source and drain. (ii) Incident photons of energy greater than GaN bandgap induce the formation of electron hole pairs in the GaN channel. The holes are pulled to the surface by electric field in the AlGaN. The accumulation of holes at the surface forward biases the surface, thus eliminate the virtual gate.

The surface passivation prevents the formation of the virtual gate on the surface of the device in the gate drain access region and thus reduces the effect of the current collapse. Possible mechanism which prevents the current collapse: (i) The passivant makes the surface donors inaccessible to electrons leaking from the gate metal. (ii) The process of depositing silicon nitride passivant causes Si to incorporate as a shallow donor at the AlGaN surface in sufficiently large quantities to replace the surface donor.
If the AlGaN/passivant interface or bulk of the passivant contains charge trapping sites, then electrons leaking from the gate metal under the influence of large electric fields present during high power operation can get trapped. This trapped negative charge can cause a negatively charged virtual gate to develop in a manner similar to that on an unpassivated surface. This can negatively impact long time stability and reliability of the device characteristic and performance.

Chapter 3

Experimental Methods

3.1 Auger Electron Spectroscopy

Auger Electron Spectroscopy (AES) is a standard analysis technique in surface and interface physics. It is used predominantly to check the cleanliness of a freshly prepared surface under UHV conditions. Other important fields of application include studies of film growth and surface chemical composition.

AES is an electron core-level spectroscopy, in which the excitation process is induced by a primary electron beam from an electron gun. The Auger process results in secondary electrons of relatively sharply defined energy, which are analysed and detected by a standard electron analyzer.

AES is surface sensitive because of the limited escape depth of electrons and the typical probing depths are in the range $10 \div 30$ Å.

The principle of the Auger process is explained in fig. 3.1. The primary electron produces an initial hole ionization of a core level (K or L shell). The electronic structure of the ionized atom rearranges such that the deep initial hole in the core level is filled by an electron originating from an energetically higher-lying shell. This transition may be accompanied by the emission of a characteristic X-ray photon, or alternatively the deexcitation process may be a radiationless Auger transition, in which the energy gained by the electron that "falls" into the deeper atomic level is transfered to another electron of the same or a different shell. This latter electron is then emitted with a characteristic Auger energy, thereby leaving the atom in a double-ionized state (two holes).

Since the emitted Auger electron carries a well-defined kinetic energy that is directly related to differences in core-level energies, measurement of this energy can be used to identify the particular atom. Chemical element analysis is then possible with an high surface sensitivity.

In a simple one electron picture the kinetic energy of the outgoing Auger electron would be given by the difference between the corresponding core-level energies:

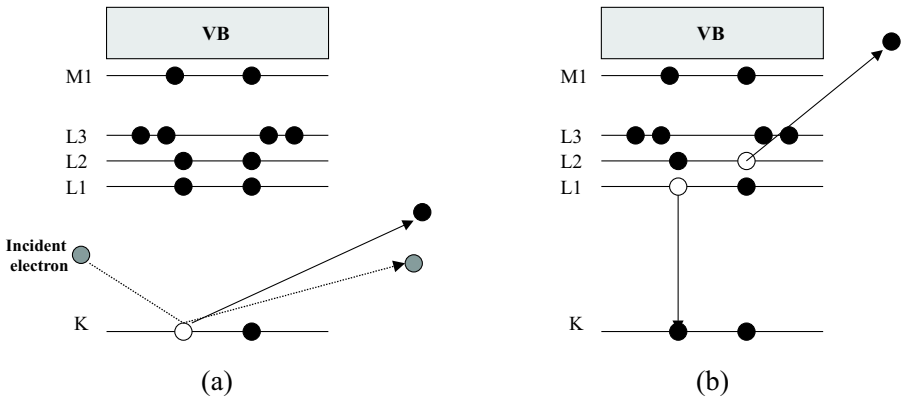

Figure 3.1: Explanation of the Auger process on the basis of atomic level schemes. A primary electron produces an initial hole in a core level (a). Another electron is deexcited from a higher shell and the deexcitation energy is then transferred to a third electron, which leaves the system as an Auger electron (b).

$E_{kin} = E_K - E_{L_1} - E_{L_2}$.

The standard equipment for AES consists of an electron gun, which produces the primary electron beam with a typical energy of 2000 to 5000 eV. The most commonly used energy analysers for Auger electrons are Cylindrical Mirror Analysers (CMA) where the electron gun is integrated into the CMA on its central axis. Because of the small Auger signals AES is usually carried out in the derivative mode to suppress the large background of true secondary electrons [139].

3.2 Low Energy Electron Diffraction

In almost every surface-physics laboratory Low Energy Electron Diffraction (LEED) is used as the standard technique to check the crystallographic quality of a surface, prepared either as a clean surface, or in connection with ordered adsorbate overlayers. In this experiment a beam of electrons with a primary energy between 50 and 300 eV is incident on the surface and the elastically backscattered electrons give rise to diffraction (or Bragg) spots that are imaged on a phosphorous screen.

To understand the essential features of such an experiment, kinematic theory is sufficient. We can first consider the general case where a plane wave with wave vector **k** is incident on a crystal lattice described by the base vectors **a**, **b**, **c** and is elastically scattered by it. We define the scattering vector $\mathbf{\Delta k} = \mathbf{k} - \mathbf{k}'$, where $\mathbf{k}'$ is the wave vector of the diffracted wave and $|\mathbf{k}| = |\mathbf{k}'|$ because we assumed elastic scattering . A constructive interference in the diffracted wave occurs only if the scattering vector is one of the reciprocal lattice vectors $\mathbf{K}_{hkl}$, that is:

$$\mathbf{\Delta k} = \mathbf{K}_{hkl} = h\mathbf{a}^* + k\mathbf{b}^* + l\mathbf{c}^*, \tag{3.1}$$

where $\mathbf{a}^*$, $\mathbf{b}^*$, $\mathbf{c}^*$ are base vectors of the reciprocal lattice. The condition (3.1) is called "Laue condition" for constructive interference in crystal diffraction. A simple geometrical interpretation, known as "Ewald diagram" is illustrated in fig. 3.2.

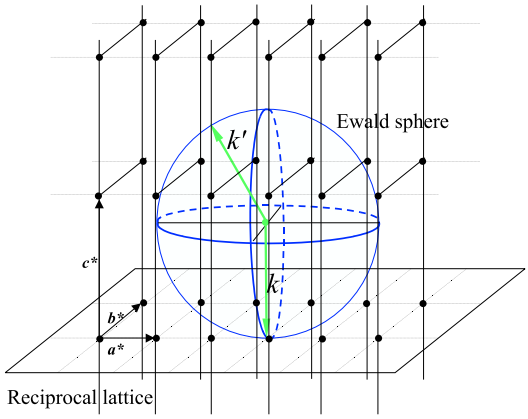

Figure 3.2: Ewald diagram describing the diffraction from a three dimensional crystal lattice. The Laue condition is fulfi lled when the surface of the sphere touches a point of the reciprocal lattice.

If we draw a sphere of radius $\mathrm{k} = |\mathbf{k}|$ about the origin of the wave vector **k** of the incident radiation, where **k** is taken to end on a point of the reciprocal lattice, then wherever the sphere intersects any other point of the reciprocal lattice constructive interference is observed. From the Laue condition we infer that constructive interference is associated with particular vectors $\mathbf{K}_{hkl}$ and can not be easily realized in a real experiment.

Assuming that 2θ is the angle between $\mathbf{k}$ and $\mathbf{k}'$ equation (3.1) can be rewritten in the form:

$$|\mathbf{\Delta k}| = 2k\sin\theta = |\mathbf{K}(hkl)| = \frac{2\pi}{d_{hkl}} \tag{3.2}$$

and reduces to the familiar Bragg law for constructive interference by reflection from planar arrays (hkl) in the real lattice:

$$2d_{hkl}\sin\theta = \lambda, \tag{3.3}$$

where d_{hkl} is the interplanar spacing. In the case of electrons the de Broglie wavelength λ can be easily calculated from their energy E by:

$$\lambda = \sqrt{\frac{h^2}{2mE}}, \tag{3.4}$$

where m is the electron rest mass, and for a typical energy of 100 eV it is about 1 Å, so the same order of magnitude as interatomic separation. Furthermore at such energies the mean free path of electrons in a solid is about $5-10$Å and the diffraction process is restricted to the first atomic layers. We can approximate the electron to be scattered only by the surface layer and so we can consider a two dimensional lattice, letting the base vector $\mathbf{c} \to \infty$. Correspondingly the reciprocal lattice vector $\mathbf{c}^* \to 0$, which means that the discrete points parallel to $\mathbf{c}^*$ in the reciprocal lattice come closer and closer, finally coalescing to form lines, or rods as they are usually called (fig. 3.3). Now the Laue condition is fulfilled for the points in which the rods cross the sphere. Experimentally this condition is much easier to be achieved because for each value of k (radius of the Ewald sphere) some rod is crossing the sphere and a spot is obtained in the diffraction pattern [140].

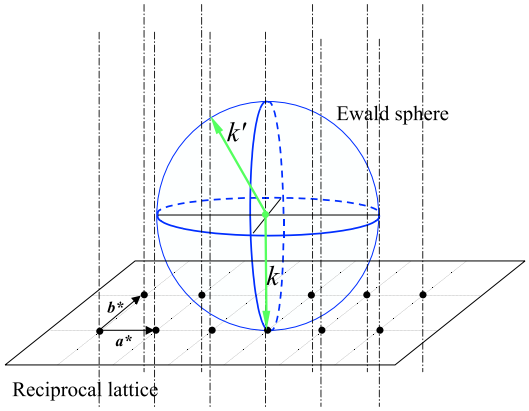

Figure 3.3: Ewald diagram describing the diffraction from a surface. The reciprocal lattice can be described by parallel rods intersecting the Ewald sphere.

3.3 Atomic Force Microscopy

Atomic Force Microscopy (AFM) technique allows the analysis of surface topography of a wide range of solid materials (conducting, insulating, magnetic) on nm scale. The basic principle is simple: a tip (in our case a Si_3N_4 with typical curvature radius of 10-15 nm and opening angle of about $20°$) is brought very near to the surface to be analyzed and undergoes attractive or repulsive forces. This causes the deflection of the cantilever on which the tip is located and the deflection is revealed by an optical amplification system: a laser beam pointing on the cantilever is reflected towards four photodiodes in a cross configuration and the movement of the tip is so detected (fig. 3.4).

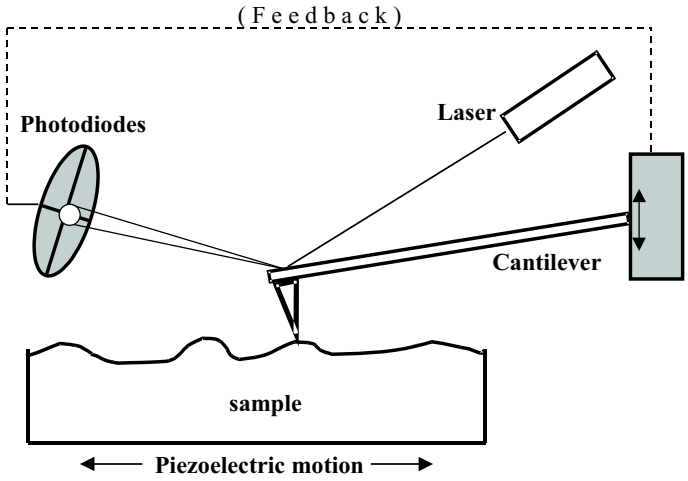

Figure 3.4: Schematic description of the AFM operation principle.

A feedback system keeps the tip-sample interaction constant and is monitored while the sample is scanned. By correlating, point-by-point, the feedback system's status with scanner motions, an image of the sample emerges. It is possible to operate with the AFM in different ways; one of them is the so called *contact mode*, in which the tip-sample forces are maintained at a constant level and the tip "rides" across the surface, like a profilometer (usually the sample is moved and the tip is fixed). In *tapping mode* AFM the tip oscillates and its natural resonance frequency is shifted by the tip-sample force, the shifting being proportional to the second derivative of the potential. The shift is then converted in a topographical image of the surface. The introduction of lock-in amplification techniques allows a more stable detection, filtering out the thermal noise.

The forces acting between the tip and the surface are of different nature and play a specific role in the overall interaction especially in respect with the tip-sample distance (fig. 3.5). The first interaction is encountered only by probes which are in *tapping mode*. A damping air film is developed when an oscillating probe comes to within $10\ \mu\mathrm{m}$ of

the sample surface (Fluid Film Damping). At this distance, air is squeezed between the probe and the surface during each downstroke of the probe. Conversely, as the probe rebounds upward, a partial vacuum results. This pumping effect dampens probe motion and may lead to false engagement of the surface. If the boundary is passed, however, the phenomenon disappears.

The second interaction encountered is the electrostatic force zone beginning at $0.1 - 1\ \mu\mathrm{m}$, and may be either attractive or repulsive depending on the material.

Surface tension effects result from the presence of condensed water vapor at the surface, and begin at $10 - 100$ nm over it. This is an attractive force that can pull a tip down toward the sample surface strong enough to indent some material. Usually *tapping mode* is employed to alleviate surface tension attraction (the oscillating tip allows it to break free of the water layer).

At the angstrom level above the surface Van Der Waals forces cause a weak attraction between atoms in the tip and sample, while they are said to "contact" when their respective atoms encounter each other generating coulombic forces. At this level electron shells from atoms on both tip and sample repulse one another, preventing further intrusion by one material into the other. Pressure exerted beyond this level leads to mechanical distortion of one or both materials and the tip may be damaged.

The image of the sample surface collected by the AFM device is affected by some limitations, because the actual "sharpness" of a tip directly influences its ability to resolve

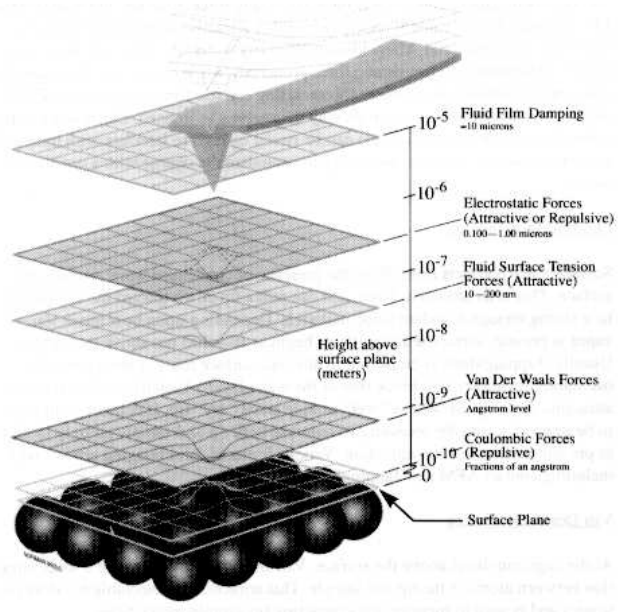

Figure 3.5: Representation of the interactions between the AFM scanning tip and the sample surface.

surface features. Moreover certain tip defects (e.g. double-pointed and cracked tips) produce predictable defects in the image. To understand how tip-sample geometry affects the quality of an image, it is useful ti think on the nanometric scale of tip sample interactions. One obvious surface limitation (deep fissures) is represented in fig. 3.6a. In the case the tip is not long enough, or thin enough, to reach the bottom of a recess. Although the edges would be imaged here, each square recess would be misrepresented as a wedged trench. Moreover the edge of the tip present an angled aspect to the wall of the sample and cannot detect any angles steeper than itself. The other half of the tip-sample relationship is the tip. Just as certain surface geometry has a direct influence on the accuracy of the image data, the geometry of the tip (the quality of its sharpness, size and shape) has a direct influence. Consider a Si_3N_4 tip having a radius R as it encounters a series of parallel, rod-shaped features of radius r (fig. 3.6b). Depending upon the value of R, the scanning tip will resolve separation between the rods of varying defects. As R increases, the ability of the tip to perceive the radius r and separation of features decreases.

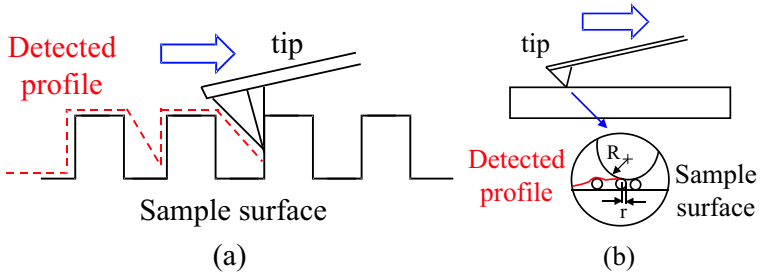

Figure 3.6: Errors deriving from surface geometry (a) and tip geometry (b) during AFM characterization.

3.4 X-Ray Diffraction

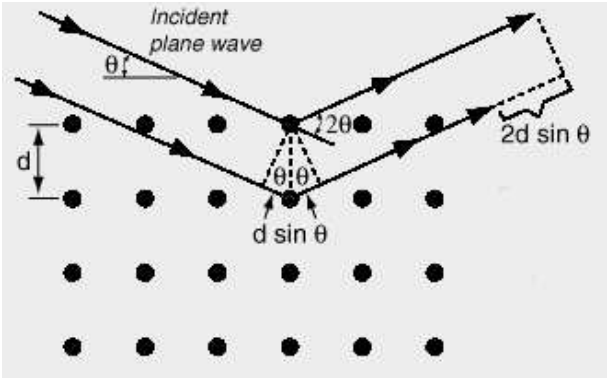

Figure 3.7: Diffraction of X-rays by a crystal.

X-Ray diffraction (XRD) is a very versatile method used to determine not only the structure of epilayers but also the composition of a ternary compound or the stress in heteroepitaxial films. Diffraction is due essentially to the existence of certain phase relations. It is well known that two rays are completely in phase whenever their path lengths differ by either zero or a whole number of wavelengths. Differences in the path length of various rays arise quite naturally when we consider how a crystal diffract X-rays. Figure 3.7 shows the diffraction of a beam of parallel and monochromatic X-rays of wavelength λ is incident on a crystal at an angle θ, the so called Bragg angle, which is measured between the direction of the incident beam and the crystal plane under consideration. The interaction with the first of these planes produces a reflected component at the specular reflection angle θ, which is rather weak if the X-rays are deeply penetrating. For the second and all subsequent planes, there are similar components of reflected energy at the specular angle θ. It can be seen from fig.3.7 that the additional path of the lower ray compared to the upper ray is $2d\sin\theta$. Consequently all reflected components can interfere constructively in phase if this distance is a multiple of the wavelength. This condition for efficient specular reflection is called Bragg's law

$$2d\sin\theta = n\lambda,$$

where n is an integer. Since the atomic arrangement is the same in all the planes under consideration, the Bragg diffraction condition depends on the spacing of the planes, but is independent of the atomic arrangement within each plane. Since $\sin\theta$ cannot exceed unity, the basic condition $n\lambda < 2d$ must be satisfied to obtain any diffraction. For a spacing between planes in the order of 3 Å, λ cannot exceed 6 Å. On the other hand if λ is much smaller than d, the diffraction angles are too small to be conveniently measured. Experimentally by using X-rays of known wavelength λ and measuring θ one can determine through Bragg's law the spacing d of the planes in a crystal [119].

Following the conventional definitions ω is the angle between the incident beam and the sample, while 2θ is the angle between the incident and diffracted beams, as shown in fig. 3.8. In a so called $\theta - 2\theta$ scan the analyzer slowly rotate with a velocity that is two times the one of the sample so that ω is always equal to θ. In this case only regions of the sample having a constant lattice spacing d_θ contribute to the diffracted reflexes. This kind of measurement is important for example to distinguish in the a $Al_XGa_{1-X}N$ ternary compound a possible segregation of the single binary components, which have a different d_θ, or to detect wether the structure is strained. In the ω-scan the angle 2θ is maintained constant and just the angle ω is changed. Now contributions to the reflex come just from sample regions which have a well defined lattice spacing, determined by the angle 2θ. The variation of ω makes visible the tilt of different crystalline grains. If the measurement is performed with wide open detector, the full width at half maximum (FWHM) of the curve obtained (the so called "rocking curve") is an often used quantity for evaluating the structural quality of epitaxial layers [141].

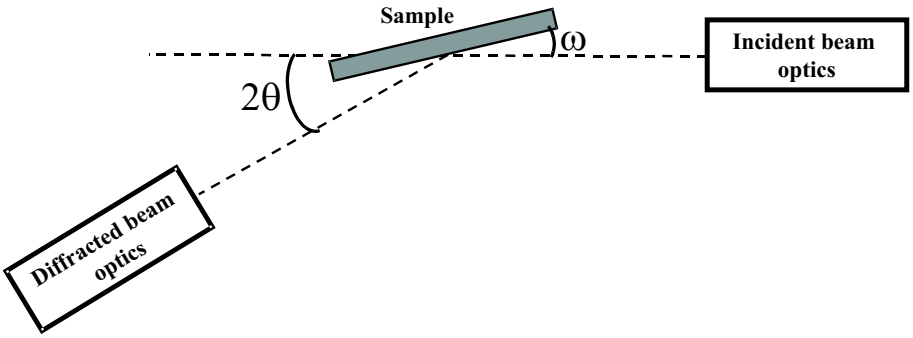

Figure 3.8: Schematic setup of a XRD measurement system.

3.5 Secondary Ions Mass Spectroscopy

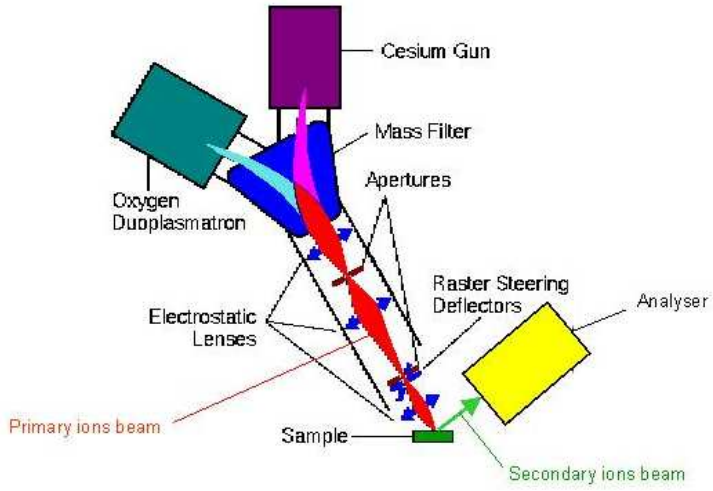

Figure 3.9: Schematic description of a SIMS equipment.

In Secondary Ions Mass Spectroscopy (SIMS) a primary ion beam (e.g. Cs^+ or O_2^+) with a typical energy between 1 and 30 keV is incident on the studied sample. Due to the transferred impact energy neutral atoms, molecules and ions (secondary ions) are emitted from the surface and they can be analyzed by a mass spectrometer (usually a quadrupole) (fig. 3.9).
SIMS is a destructive technique because the sample surface is slowly sputtered away. The sputter yield is the ratio between the number of sputtered atoms and impinging primary ions, and typically fall in a range from 5 and 15. The measured mass spectrum then yields information about the chemical composition of the surface. If high primary-beam currents are used, an high rate of emission of secondary ions is obtained and considerable quantities of material are removed, allowing a layer by layer analysis of the substrate, *i.e.* a depth profiling of impurities and chemical composition. High sputtering rates are obtained by primary ions current densities of 10^{-5} to 10^{-3} A/cm^2 but a limit is given by the depth resolution since mass signals from several atomic layers can be mixed, causing sharp profiles to be smeared out. In practice the sputtering rate must be carefully adjusted in order to combine the optimum depth resolution with the required high erosion speed. Sputter typical rates are between $0.5 - 5$ nm/s. SIMS can reach sensitivity up to 1 part per million (ppm) and is so suitable to detect possible contaminations and impurities in grown layers, while is difficult to use it to get information in the "percent" region, e.g. to study the stoichiometry of compounds.

3.6 X-ray Photoelectron Spectroscopy

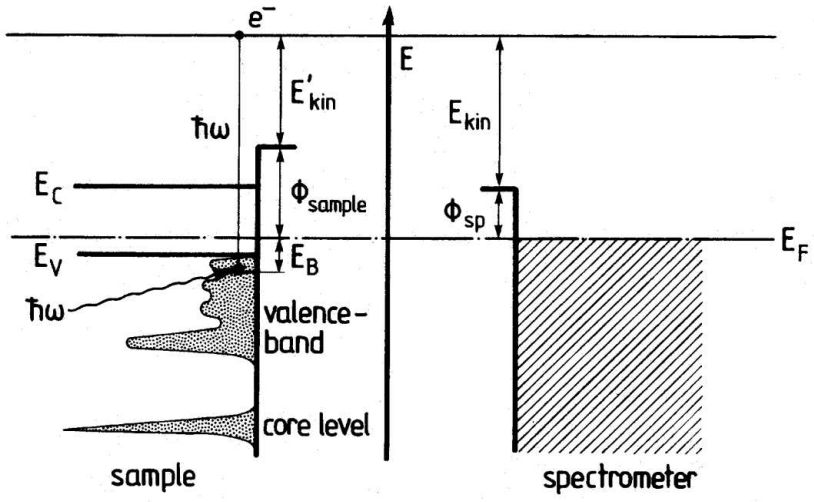

Figure 3.10: Schematic representation of the processes occurring in photoemission spectroscopy

The photoeletric effect, for the interpretation of which Einstein was awarded with the Nobel price, makes possible the spectroscopy of the occupied electron states in solid state samples. An incident monoenergetic radiation (energy $\hbar\omega$) causes the emission of electrons from the solid into vacuum; an energy analyzer allows the spectroscopy of their kinetic energy E_{kin}. The original binding energy E_B with respect to the vacuum can be extracted considering the energy conservation principle:

$$E_{kin} = \hbar\omega - E_B \; . \tag{3.5}$$

The obtained energetic spectra contain information about the electronic structure and the chemical environment of the measured material.
The wavelength of the used light sources leads to the differentiation in: x-ray photoelectron spectroscopy (XPS) and ultraviolet photoelectron spectroscopy (UPS). A schematic representation of the processes occurring in a photoelectron spectroscopy measurement is shown in fig. 3.10. An introductory and a more deep description of the method is presented in ref. [142] and [143].
For a treatment of the photoelectron spectroscopy physical effect one often resorts to an approximation, the so called three-step model [144]. It assumes the excitation of an electron, by the photon, from an occupied initial state to an empty final state (step 1) followed by ballistic transport to the surface (step 2) and transmission across the surface (step 3). In this model every step is treated as independent on the others. This means that the probability for the photoemission process results from the product of the three probabilities for the single steps.

Optical Excitation

The absorption of a photon causes excitation of a system consisting of N electrons described by an initial state wave function Ψ^i going to a final state with Ψ^f. The intensity of a photoelectron signal is determined by the transition probability or photoelectric cross section σ from the initial Ψ^i to the final Ψ^f state under the influence of the incident electromagnetic wave:

$$\mathbf{A}(\mathbf{r},t) = \mathbf{e}A_0 e^{[i(\mathbf{k}\cdot\mathbf{r}-\omega t)]}, \tag{3.6}$$

where $\mathbf{e}$ is a unit vector in the direction of the light polarization, A_0 the amplitude and $\mathbf{k}$ the wave vector. Within the semiclassical approximation, the transition probability is then proportional to the squared matrix element:

$$|M_{if}|^2 = \hbar^2 A_0^2 | < \Psi_f | \sum_{j=1}^{N} e^{(i\mathbf{k}\cdot\mathbf{r})} \mathbf{e}\cdot\nabla_j | \Psi_i > |^2, \tag{3.7}$$

where the summation and integration runs over the N electrons and their respective coordinates. It is further assumed that the radiation wavelength λ is large compared to the atomic dimensions. Then the eq. (3.7) simplifies to the "dipole approximation":

$$|M_{if}|^2 = \hbar^2 A_0^2 \sum_{i,f} |\mathbf{e} < \Psi_f | \sum_{j=1}^{N} \nabla_j | \Psi_i > |^2. \tag{3.8}$$

The most often used approximation for further treatment starts from one-electron picture for the photoemission process and from the assumption that the primary excitation is rapid with respect to the relaxation of the remaining electrons, which is called the "sudden approximation". The one-electron treatment leads straightforward to the request of energy and impulse conservation for the photoemitted electron:

$$E_f = E_i + \hbar\omega, \tag{3.9}$$

$$\mathbf{k}_f = \mathbf{k}_i + \mathbf{G}_B. \tag{3.10}$$

Analog to the optical absorption, the transition probability for electrons coming from the valence band is proportional to the joint density of states for occupied valence band states and empty conduction band states having an energy distance equal to the one of the photon.

Transport to the Surface

During their transport to the surface the electrons are scattered by plasmons, phonons, electrons and holes. These inelastic processes result in a background of secondary electrons, exponentially decreasing in the direction of low binding energy. The whole scattering can be described by means of a phenomenological quantity: the escape depth λ. This

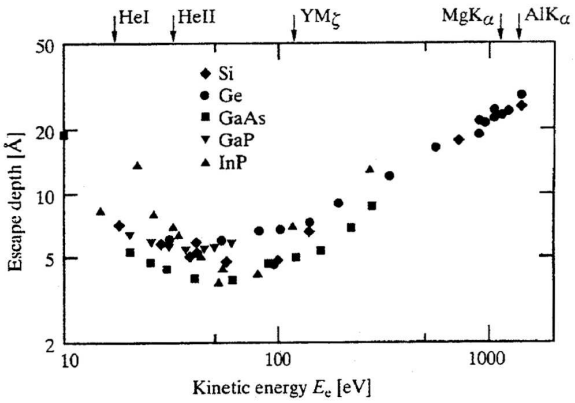

Figure 3.11: Dependence of the photoelectron escape depth on the kinetic energy [143]. The energies of different typical radiation sources are also given.

gives the number of the electrons, $I(E,d)$, generated at a depth d that reach the surface by means of the relation:

$$I(E,d) = I_0(E)e^{-d/(\lambda\cos\alpha)}, \tag{3.11}$$

where α is the angle formed from the outgoing direction to the surface normal. The escape depth depends strongly on the kinetic energy of the electrons, whereas the material specific influences can be neglected in most cases [145]. In fig. 3.11 the universal curve for λ is reported.

Transmission across the Surface
In the last step the electrons are emitted from the solid. During this process they experience a further energy loss equal to the work function of the material. The broken symmetry perpendicular to the surface has as a consequence that only the parallel component of the wave vector is conserved, *modulo* a vector of the reciprocal surface lattice. The resulting conservation equations are:

$$E_B = \hbar\omega - E_{kin} - e\cdot\Phi, \tag{3.12}$$
$$\mathbf{k}_{i\|} = \mathbf{k}_{ex\|} - \mathbf{G}_{B\|} - \mathbf{G}_S, \tag{3.13}$$

where $e\cdot\Phi$ is the work function for the material, and $\mathbf{G}_S$ a vector in the reciprocal space of the surface lattice.

3.6.1 Core Levels and Valence Band Spectra

Core Levels
The core level electrons are localized at the corresponding atomic nuclei, and their energy depends on the the nucleus charge and on the screening of the other core level electrons.

So their position is characteristic for the specific atom. The core level energy depends also in a weaker way on the screening of the valence electrons. For example the bond to a more electronegative atom attracts electrons away and so the lower screening of the nucleus shifts all the atomic core levels to higher binding energies.
The creation of a photoelectron leaves a hole in the solid. The remaining electrons relax to screen the hole and the resulting relaxation energy is the kinetic energy of the emitted electron. Therefore the lifetime of the hole determines the energetic width of the core level emission though the Heisenberg uncertainty principle. The expected form of the peak is therefore a Lorentzian. Experimentally the distribution in energy of the incoming photons, the limited resolution of the analyzer, the possible inhomogeneous band bending/Fermi level pinning and fluctuations in the binding state lead to a broadening of the measured peak. The influence of the first two effects can be described with a gaussian energy distribution. The resulting form of the peak can be well described by a Voigt function, e.g. a convolution of a Lorentz profile with a Gaussian distribution:

$$I_{Voigt}(E) = \frac{\int_{-\infty}^{+\infty} \frac{e^{-x^2}}{a_3^2+\left[\left(\frac{E-E_0}{a_2}\right)^2-x\right]^2}dx}{\int_{-\infty}^{+\infty} \frac{e^{-x^2}}{a_3^2+x^2}dx} \,. \tag{3.14}$$

Valence Band
We saw in the third step of the previously presented model that $k_\perp$ conservation can no more be assumed, as a consequence of the presence of the surface. In reality both indirect and direct transitions contribute in general to the spectrum of the valence band energetic region with different weights. The indirect transitions are demonstrated to be more probable with increasing photon energy, for example going from UPS to XPS [146, 147]. The modulation due to the distribution of the final states can be therefore neglected. Supposing to be in the indirect transition scheme, the signal extracted by angle resolved photoelectron spectroscopy has the energetic dependence of a one dimensional density of states:

$$j(E,\phi,\theta) \sim \frac{1}{\pi}\left(\frac{dE_{V,\mathbf{k}_\parallel}}{dk_\perp}\right)^{-1} \,. \tag{3.15}$$

Integration over all the possible wave vector (integration over the acceptance angle) gives then a picture of the three dimensional density of state in the valence band. For the XPS an acceptance angle of the detector larger than some degrees leads already to an integration in k over the first Brillouin zone. Therefore in our experimental condition we obtain information on the whole density of states of the valence band. The location of the valence band maximum can be achieved by fitting the XPS data in the region around the maximum with an instrumentally broadened density of states. The convolution with a lorentzian profile and a gaussian function (in analogy to what was stated before for the core levels) can be

simplified by using just a gaussian. The width of this experimental gaussian and the position of the Fermi level of the system is normally derived from a calibration measurement on a metal. Often a linear decrease is already a satisfying model for the leading edge of the theoretical valence band density.

3.6.2 Determination of the Valence Band Offset

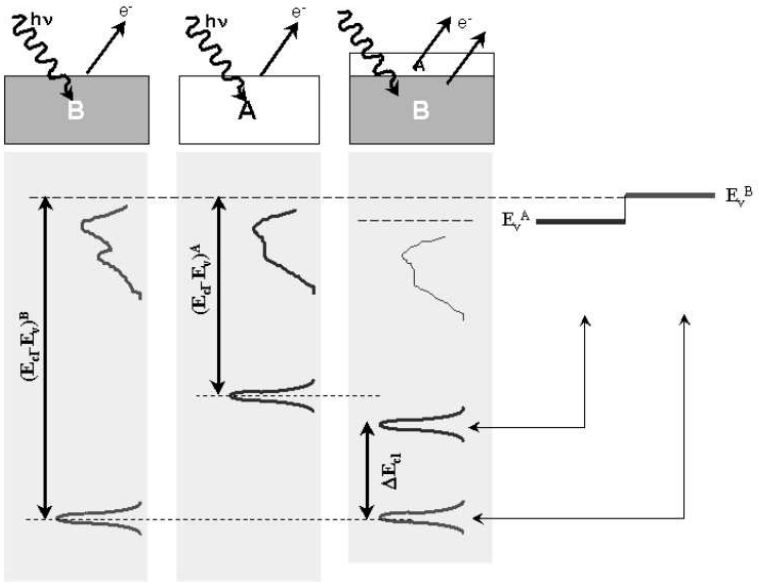

Figure 3.12: Schematic representation of the measurement of the valence band offset at an interface by means of photoemission spectroscopy.

Figure 3.12 shows the basic principle for the measurement of the band offset by means of photoelectron spectroscopy. Supposing a thin overlayer ($1-2$ nm) of a material A on a thick substrate of material B, the incident radiation causes core level emissions from both sides of the interface. Two core levels have to be chosen, that can be assigned only to one specific side of the interface and that are representative for the volume bonds of the respective material. Their positions measured at the actual interface shift rigidly together with the respective maximum of the valence band and so they can furnish the information about the band alignment at the junction. This has to be accomplished by the measurement, on thick layers, of the distance of the typical core level chosen to the valence band maximum for each material. The VBO results then from this relation:

$$\Delta E_V = (E_V^A - E_{CL}^A) - (E_V^B - E_{CL}^B) + \Delta E_{CL}^{A,B} \; . \tag{3.16}$$

The position of the core levels can be determined very precisely using the standard line form analysis already presented, for the valence band attention must be paid to the even-

tual presence of surface states giving some contribution to the measured DOS (see subsection 6.4.1). The maximum precision obtainable in the determination of the VBO with this technique is 60 meV [148, 149]. Optical methods and transport measurements offer potentially more precise determination, but XPS is less sensitive to measurements errors, because of the simultaneous check of morphology and of possible chemical reactions or incorporation of impurities at the interface.

3.7 Capacitance-Voltage Measurements

This section shows how the net doping density in a semiconductor can be obtained from measurements of the capacitance associated with the band bending region of a metal Schottky contact, which is known as the depletion capacitance. Using the depletion approximation the depletion capacitance can be determined for a contact on a semiconductor with an arbitrary non-uniform doping profile and the local voltage derivative of the capacitance is given by the local doping density at the edge of the depletion region.

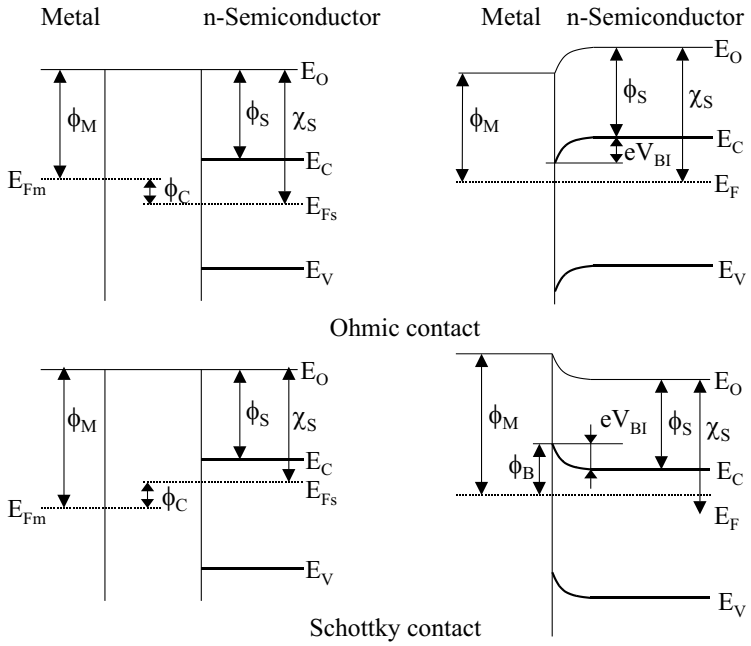

Figure 3.13: Energy band diagram of ohmic (top) and Schottky contact (bottom). Thermal equilibrium of the metal and semiconductor (left) and of the metal-semiconductor junction brought into contact (right). (ϕ_C is the contact potential energy.)

In order to use the properties of semiconductors in semiconductor devices, the metal-semiconductor interface introduces the junction between the semiconductor and the outside circuit. The current is linearly dependent from the voltage for an ohmic contact, where the work function of semiconductor is greater than the work function of a metal ($\phi_{\mathrm{S}} > \phi_{\mathrm{M}}$) (fig. 3.13 (top)). The metal ϕ_{M} and semiconductor ϕ_{S} work function is defined as a energy required to remove an electron from the metal Fermi level and semiconductor Fermi level to the vacuum level, respectively. Non-linear resistivity across the metal-semiconductor junction is reached, if the work function of semiconductor is smaller than the work function of a metal ($\phi_{\mathrm{s}} < \phi_{\mathrm{m}}$) (fig. 3.13 (bottom)). According to the Schottky model [150] the energy band diagram is constructed by reference to the vacuum level

(defined as the energy of an electron at rest outside the material) using the material properties of work function of the metal ϕ_{M} and electron affinity of the semiconductor χ_{S}, defined as the energy required to remove an electron from the semiconductor band edge to the vacuum level. These properties are assumed to be constant in a given material right up to the interface and it is further assumed that the vacuum level is continuous across the interface. When the two materials are brought into contact, the matching of the Fermi levels invariably causes charge flow from one side to the other. The thermal equilibrium is reached and the Fermi levels in the metal and semiconductor must be coincident and these conditions result in a band diagram for the interface shown in figure 3.13 (right bottom). A dipole layer is formed at the interface due to the flow of electrons from the semiconductor to the metal. For a n-semiconductor a depleted region is built with a positive space charge of ionized donors and a depletion width x_d. In the metal a neutralizing negative charge in the form of free electrons is accumulated at the contact over a distance x_m which is the free carrier screening length in the metal (fig. 3.14). Since the electron concentration in the metal is much greater than the doping density in the semiconductor $x_m \ll x_d$ and it can be assumed that the potential difference across the metal at the contact (V_M) is negligibly small compared to that in the semiconductor (V_S). We can therefore write the total zero bias band bending, or built-in voltage as

$$eV_{BI} \approx eV_S = \phi_M - \chi_S - (E_C - E_F)$$

that is

$$eV_{BI} = \phi_B - (E_C - E_F)\,. \tag{3.17}$$

The determination of the Schottky barrier height ϕ_B as difference of the metal work function ϕ_{M} and electron affinity of the semiconductor χ_{S} ($\phi_B = \phi_{\mathrm{M}} - \chi_{\mathrm{S}}$) is a very ideal approximation to the measured barrier height at metal-semiconductor interface [23].

In reality the charge neutrality at the interface is not only modified by space charge in the semiconductor and the charge in the metal, but also by a dipole arising from an intrabond charge transfer at the interface. When the metal atoms come into close contact with the semiconductor surface, they will form chemical bonds whose strength will depend on the nature of partners. The surface state distribution at the semiconductor surface will be changed. The states at the metal-semiconductor interface are called Metal Induced Gap States (MIGS). Additionally, charge will flow from one side to the other due to the formation of the bonds. This may be described by the formation of a dipole layer of atomic dimensions ($\sim 1 - 2$ Å).

The theory of MIGS was pointed out by Heine [123], that assumes metal (Bloch) wave function tails leaking into the semiconductor in the energy range in which the conduction band of the metal overlaps the forbidden band of the semiconductor. Continuum of states (MIGS) formed within the gap of semiconductor are a mixture of valence and conduction band states. The so-called charge neutrality level, CNL, or branching point, E_B, separates the donor-like from acceptor-like character of the states. The position

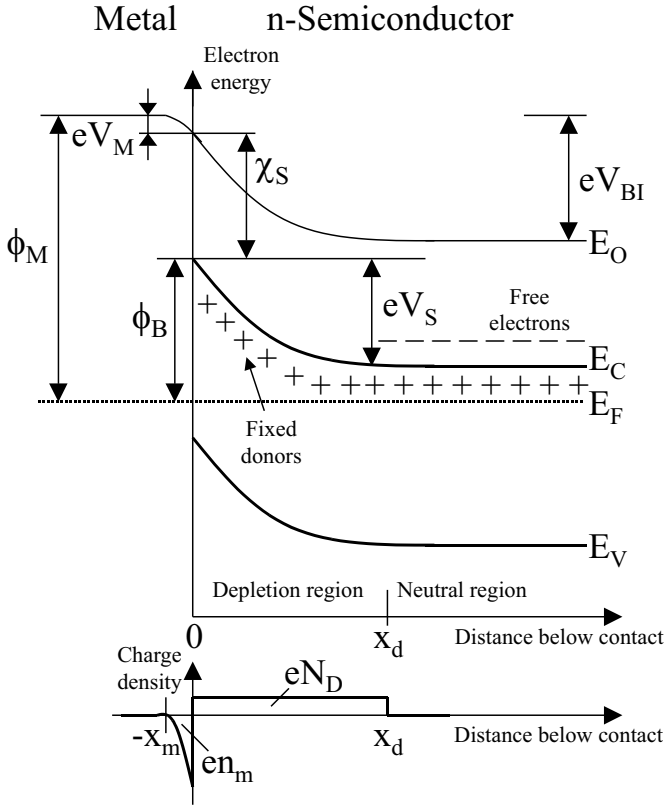

Figure 3.14: Energy band diagram of a metal-semiconductor Schottky barrier and associated charge density profi le for uniformly doped material. The diagram is constructed assuming the vacuum level is continuous across the interface.

of CNL depends from the 3D band structure of a real crystal. The calculation of CNL was done by Tersoff [151–154] and is based on summation over bulk states. If the Fermi level lies in the energetic range of the more donor-like states, *i.e.* below CNL, ionized (empty) donors build up a large positive interface charge. On other hand, if E_F is above CNL this leads to ionized (occupied) acceptor states and a negative interface charge.

The band bending across the depletion layer of n-type semiconductor is defined by the sum of the built-in voltage of the Schottky contact (eq. (3.17)) and the bias voltage, so the depletion layer width can be calculated from the charge density $\rho(x)$ using the Poisson's equation. The electrostatic potential $\psi(x)$ at any point is given by

$$\frac{d^2\psi(x)}{dx^2} = -\frac{\rho(x)}{\varepsilon_r \varepsilon_o}, \tag{3.18}$$

where ε_r is the dielectric constant of the material and ε_o the dielectric constant of the vacuum. At large distances from the contact, outside the depletion layer, the charge

density and band banding is zero, so the electric field $E = -\frac{d\psi}{dx}$ is zero, hence the potential is constant $\psi(x) = \psi_n$ for $x > x_d$ and $\psi(x) = \psi_m$ for $x < -x_m$.

For $0 < x < x_d$ the charge density $\rho(x)$ is equal to eN_D, where e is the elementary charge and the N_D the doping density of the semiconductor. The Poisson's equation is expressed by

$$\frac{dE(x)}{dx} = \frac{\rho(x)}{\varepsilon_s \varepsilon_o} = \frac{eN_D}{\varepsilon_s \varepsilon_o}, \tag{3.19}$$

where ε_s is the dielectric constant of the semiconductor. Furthermore the integration

$$\int_{E(x)}^{0} dE(x) = \frac{eN_D}{\varepsilon_s \varepsilon_o} \cdot \int_{x}^{x_d} dx \tag{3.20}$$

results into the electric field intensity dependent from the depth x

$$E(x) = -\frac{eN_D}{\varepsilon_s \varepsilon_o} \cdot (x_d - x) \tag{3.21}$$

in the range of $0 < x < x_d$. The maximal intensity of the electric field is reached at the interface and is given by

$$E_{MAX}(x = 0) = -\frac{eN_D}{\varepsilon_s \varepsilon_o} \cdot x_d. \tag{3.22}$$

The electrostatic potential can be calculated from the following equation

$$\frac{d\psi}{dx} = -E(x). \tag{3.23}$$

Integrating the previous equation we can write

$$\int_{\psi(x)}^{\psi_n} d\psi = -\int_{x}^{x_d} E(x)dx \tag{3.24}$$

and using the equation 3.21, the solution for the electrostatic potential is expressed as

$$\psi(x) = -\frac{eN_D}{2\ \varepsilon_s \varepsilon_o} (x_d - x)^2 + \psi_n \tag{3.25}$$

in the range of $0 < x < x_d$.

For the range of $-x_m < x < 0$ the charge density $\rho(x)$ is equal to en_m, where n_m is the free electron concentration of an accumulation layer in metal. Analogous to equation (3.19) the Poisson equation in the metal can be written as

$$\frac{dE(x)}{dx} = \frac{\rho(x)}{\varepsilon_m \varepsilon_o} = \frac{en_m}{\varepsilon_m \varepsilon_o}, \tag{3.26}$$

where ε_m is the dielectric constant of the metal. The depth dependent electric field intensity can be calculated by integration,

$$\int_0^{E(x)} dE(x) = -\frac{en_m}{\varepsilon_m \varepsilon_o} \cdot \int_{-x_m}^{x} dx, \tag{3.27}$$

and finally given by

$$E(x) = -\frac{en_m}{\varepsilon_m \varepsilon_o} \cdot (x + x_m)\,. \tag{3.28}$$

The maximal intensity of electric field is reached at the interface and is given by

$$E_{MAX}(x = 0) = -\frac{en_m}{\varepsilon_m \varepsilon_o} \cdot x_m. \tag{3.29}$$

The electrostatic potential can be calculated from the equation (3.23) and integrating,

$$\int_{\psi_m}^{\psi(x)} d\psi = -\int_{x_m}^{x} E(x)dx, \tag{3.30}$$

we get the final expression for the electrostatic potential in the accumulated layer of metal

$$\psi(x) = \frac{en_m}{2\ \varepsilon_m \varepsilon_o} (x + x_m)^2 + \psi_m \tag{3.31}$$

in the range of $-x_m < x < 0$. The built-in potential, V_{BI}, spread across the metal-semiconductor interface in thermal equilibrium can be calculated by

$$V_{BI} = \psi_n - \psi_m = \frac{eN_D}{2\ \varepsilon_s \varepsilon_o} x_d^2 + \frac{en_m}{2\ \varepsilon_m \varepsilon_o} x_m^2 \approx \frac{eN_D}{2\ \varepsilon_s \varepsilon_o} x_d^2 \tag{3.32}$$

assuming the depletion depth region in the semiconductor much greater than the accumulation layer in the metal ($x_m \ll x_d$). The depletion space charge x_d can be then given by

$$x_d = \sqrt{\frac{2\ \varepsilon_s \varepsilon_o}{eN_D} \cdot V_{BI}}. \tag{3.33}$$

In general the band bending V is the sum of the built-in voltage V_{BI} and the applied bias V_A. A forward bias has the opposite sense to V_{BI} and serves to reduce the overall band bending, $V = V_{BI} - V_A$. The reverse bias increases the total band bending, $V = V_{BI} + V_A$.

The capacitance across the depletion space charge is given by

$$C = \frac{dQ}{dV} = eNA \cdot \frac{dx}{dV} \implies \frac{dV}{dx} = \frac{eNA}{C}, \tag{3.34}$$

where N is the doping concentration and A the Schottky contact area. The differential capacity due to voltage is expressed as

$$\frac{dC}{dV} = \varepsilon_r \varepsilon_o \, A \cdot \frac{d(1/x)}{dV} \implies \frac{dV}{dx} = -\frac{\varepsilon_r \varepsilon_o \, A}{x^2} \cdot \left(\frac{dC}{dV}\right)^{-1}. \tag{3.35}$$

Comparing the two equations (3.34) and (3.35) we get the doping concentration profile

$$N(x) = -\frac{\varepsilon_r \varepsilon_o C}{e \, x^2} \cdot \left(\frac{dC}{dV}\right)^{-1} = -\frac{C^3}{e \, \varepsilon_r \varepsilon_o \, A^2} \cdot \left(\frac{dC}{dV}\right)^{-1}. \tag{3.36}$$

This equation shows how $N(x)$ can be obtained from the local slope of the $C(V)$ curve, with corresponding depth being obtained from mean value of C using the equation

$$C = A \cdot \frac{dQ}{dV} = \frac{\varepsilon_r \varepsilon_o \, A}{x}. \tag{3.37}$$

3.8 Magnetotransport Measurement

Hall effect measurement is nowadays standard process to electrically characterize a semiconductor [155]. The majority carrier type concentration and mobility in semiconductor can be determined. In this section the Hall effect for electrons and holes as charge carriers is described.

We can consider a rectangular shaped sample of single carrier type conduction with four contacts in the edges. An electric field $\mathbf{E}_z$ is applied resulting to a current flow $\mathbf{J}_z$ through the sample from the side A to B. According to the picture displayed in the figure 3.15 the electrons are going from right to left and the holes in opposite direction. Uniform magnetic induction $\mathbf{B}_x$ perpendicular to the current flow is also applied. Electrons and holes flowing in the semiconductor will experience a Lorentz-force bending their trajectories, and they will build up on one side of the sample. An electric field starts to form which counteract the Lorentz-force. After short time equilibrium is reached and no current is flowing in the x-direction $I_x = 0$. The counteract voltage is so called "Hall voltage", $V_H = V_C - V_D$. For developing a simple expression for the Hall voltage we assume in the Drude relaxation approximation that all the conduction carriers have the same drift velocity $\mathbf{v}_d$ and the same relaxation time τ_c. If a hole or an electron is moving in magnetic field a Lorentz-force has influence on them:

$$\mathbf{F} = q \cdot (\mathbf{v}_d \times \mathbf{B}) \tag{3.38}$$

where q is the elementary charge; q=-e for electrons and q=+e for holes.

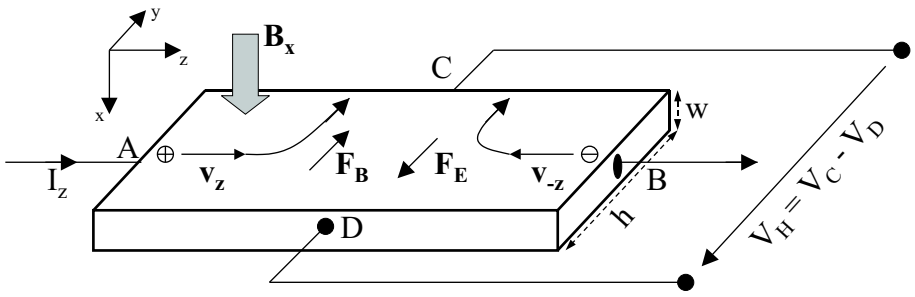

Figure 3.15: Sign convention and terminology for a rectangular Hall sample.

The evaluation of the electron and hole concentration follows on the right and left side, respectively.

The Lorentz-force for holes and electrons is given by:

Holes	**Electrons**	
$\mathbf{F}_B = e \cdot (\mathbf{v}_z \times \mathbf{B}_x) \equiv \mathbf{F}_y$	$\mathbf{F}_B = -e \cdot (\mathbf{v}_{-z} \times \mathbf{B}_x) \equiv \mathbf{F}_y.$	(3.39)

The amplitude of the Lorentz-force can be determined as:

$$\begin{aligned} |\mathbf{F}_B| &= |e \cdot (\mathbf{v}_z \times \mathbf{B}_x)| & |\mathbf{F}_B| &= |-e \cdot (\mathbf{v}_{-z} \times \mathbf{B}_x)| \\ &= ev_z B_x & &= ev_z B_x. \end{aligned} \tag{3.40}$$

The vector of this force has the same direction for both carrier types. The carriers are attracted to the side C, where they cause an electric field, which opposes the force of magnetic field. The force caused by this electric field is expressed by:

$$\begin{aligned} \mathbf{F}_E &= q \cdot \mathbf{E}_{-y} = -q \cdot \mathbf{E}_y & \mathbf{F}_E &= q \cdot \mathbf{E}_y = \\ &= -e \cdot \mathbf{E}_y \equiv \mathbf{F}_{-y} & &= -e \cdot \mathbf{E}_y \equiv \mathbf{F}_{-y}. \end{aligned} \tag{3.41}$$

$$|\mathbf{F}_E| = |-e \cdot \mathbf{E}_y| = e \cdot E_y \tag{3.42}$$

In steady state the whole force is equal zero,

$$\begin{aligned} F_B + F_E = ev_z B_x + e \cdot E_y = 0 \\ \Rightarrow ev_z B_x = -e \cdot E_y \end{aligned} \tag{3.43}$$

Expressing the drift velocity using the current density equation $\mathbf{J}_z = qp\mathbf{v}_z = ep\mathbf{v}_z$, $J_z = |\mathbf{J}_z| = epv_z$ for holes and $\mathbf{J}_z = qn\mathbf{v}_{-z} = -en\mathbf{v}_{-z} = en\mathbf{v}_z$, $J_z = |\mathbf{J}_z| = envz$ for electrons, where p and n is the bulk hole and bulk electron concentration, respectively, we get

$$\begin{aligned} \tfrac{J_z}{en_H} B_x &= -E_y \\ \Rightarrow R_H = \tfrac{1}{en_H} = \tfrac{-E_y}{J_z B_x} &= \tfrac{V_C - V_D}{J_z B_x h} = \tfrac{V_H}{J_z B_x h} = \tfrac{hw}{I_z} \tfrac{V_H}{B_x h} = \tfrac{w}{I_z} \tfrac{V_H}{B_x}, \end{aligned} \tag{3.44}$$

where n_H could be either n or p, R_H is the Hall factor, $V_H = V_C - V_D$ the Hall voltage, h the layer width, w the conductive layer thickness and $J_z = I_z/hw$ the current density. If the Hall voltage is positive, $V_H > 0$, then the conduction is caused by holes ($n_H = p$) and if negative, $V_H < 0$, then the conduction is caused by electrons ($n_H = n$).

If the conductivity σ is known then the Hall mobility can be determined by following expression:

$$\begin{aligned} \mu_n &= \tfrac{\sigma_n}{en} \qquad \text{for N} - \text{type and} \\ \mu_p &= \tfrac{\sigma_p}{ep} \qquad \text{for P} - \text{type semiconductor.} \end{aligned} \tag{3.45}$$

3.8.1 Van der Pauw Hall Measurement

According to the work of L. J. van der Pauw [156] it is possible to measure the specific resistivity and the Hall effect on an arbitrary shaped sample. Special preparation of a sample is not necessary. The measured sample has to fulfill following requirements:

- the contacts are positioned on the sample edge
- the contacts are small compared to the sample size
- the thickness of the sample is constant
- the surface introduces a uninterrupted coherent area

According to the contact's numeration shown in fig. 3.16 the Van der Pauw resistivity can be defined as:

$$R_{2134} = \frac{U_{34}}{I_{21}}, \tag{3.46}$$

where contact point 2 means I_+, 1 I_-, 3 U_+ and 4 U_-. The current flows trough the contacts 2 and 1, and the voltage is measured between 3 and 4. The conductivity can be defined by:

$$\sigma = \frac{ln2}{\pi w}\frac{2}{R_{2134}+R_{3241}}\left[f\left(\frac{R_{2134}}{R_{3241}}\right)\right]^{-1}, \tag{3.47}$$

where f is a correction factor for geometrical asymmetry and not for material anisotropy or inhomogeneity. It is a function of the symmetry factor Q, defined as ratio of the resistivities for two pairs with a common contact:

$$Q = \frac{R_{2134}}{R_{3241}}. \tag{3.48}$$

For a square 'ideal' sample $Q = 1$. Good sample preparation will routinely achieve a value for Q less than 1.2, although values of Q up to 1.5 will still yield sensible measurements. Values $Q > 1.5$ are usually a result of badly defined VdP patterns, non-Ohmic contacts or anisotropic samples. Bar or bridged shaped specimens might be more suitable for anisotropic samples. Rectangular samples will of course have values of $Q > 1$ and for these samples the symmetry factor cannot be used to monitor sample quality.

f is normally obtained by reference to graphs. However, if the asymmetry is not too large ($Q < 10$), the following approximation can be used:

$$f = 1 - 0.34657 \cdot A - 0.09236 \cdot A^2, \tag{3.49}$$

where

$$A = \left[\frac{Q-1}{Q+1}\right]^2. \tag{3.50}$$

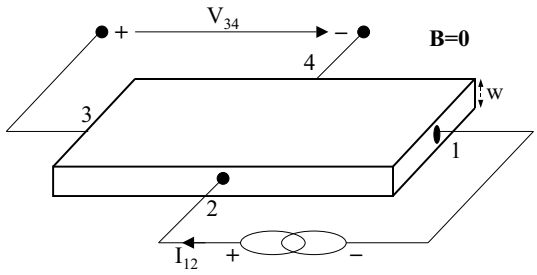

Figure 3.16: Van der Pauw arrangement for measuring the conductivity of an arbitrary shaped sample.

To exclude the non-symmetry of the sample it is useful to average the conductivity by including the remaining two contacts permutations and also reversing the current for all four permutations. Then

$$\begin{aligned}\frac{1}{\sigma} = \rho = \frac{\pi w}{ln2} \cdot \frac{1}{8}\{(R_{2134} - R_{1234} + R_{3241} - R_{2341})f_A + \\ +(R_{4312} - R_{3412} + R_{1423} - R_{4123})f_B\},\end{aligned} \tag{3.51}$$

where ρ is the resistivity, correction factors $f_A(A_A)$ and $f_B(A_B)$ are given by the equation (3.49), and $A_A(Q_A)$ and $A_B(Q_B)$ by equation (3.50). The symmetry factors Q_A and Q_B can be determined by reversing the current as

$$Q_A = \frac{R_{2134} - R_{1234}}{R_{3241} - R_{2341}},\ Q_B = \frac{R_{4312} - R_{3412}}{R_{1423} - R_{4123}} \tag{3.52}$$

For the Hall effect measurement the current flows through the sample and on the remaining two contacts the Hall voltage is measured (fig. 3.17). To minimize the magneto-resistive and other effects it is useful to average over the current and magnetic field polarities. Ideally the Hall voltage is zero, if no magnetic field is applied. In reality due to the inhomogeneous sample, this voltage is non-zero. According this considerations following magneto-resistivities for different current polarity and magnetic field can be defined:

$$\begin{aligned}R_1^{B+} &= \tfrac{1}{2} \cdot \{(R_{4213}(B+) - R_{4213}(0) + R_{2431}(B+) - R_{2431}(0)\} \\ R_2^{B+} &= \tfrac{1}{2} \cdot \{(R_{1324}(B+) - R_{1324}(0) + R_{3142}(B+) - R_{3142}(0)\} \\ R_1^{B-} &= \tfrac{1}{2} \cdot \{(R_{4213}(B-) - R_{4213}(0) + R_{2431}(B-) - R_{2431}(0)\} \\ R_2^{B-} &= \tfrac{1}{2} \cdot \{(R_{1324}(B-) - R_{1324}(0) + R_{3142}(B-) - R_{3142}(0)\}\end{aligned} \tag{3.53}$$

Averaging through magnetic field polarities we get the final magneto-resistivity:

$$R_\phi = \frac{R_{B+}+R_{B-}}{2} = \frac{1}{2}\{\frac{R_1^{B+}+R_2^{B+}}{2} + \frac{-R_1^{B-}-R_2^{B-}}{2}\}$$

$$= \frac{1}{4}\{R_1^{B+} + R_2^{B+} - R_1^{B-} - R_2^{B-}\}$$

$$\begin{aligned} = \frac{1}{8}\{&R_{4213}(B+) - R_{4213}(0) + R_{2431}(B+) - R_{2431}(0) + \\ &+R_{1324}(B+) - R_{1324}(0) + R_{3142}(B+) - R_{3142}(0) - \\ &-R_{4213}(B-) + R_{4213}(0) - R_{2431}(B-) + R_{2431}(0) - \\ &-R_{1324}(B-) + R_{1324}(0) - R_{3142}(B-) + R_{3142}(0)\} \end{aligned} \tag{3.54}$$

$$\begin{aligned} = \frac{1}{8}\{&R_{4213}(B+) - R_{4213}(B-) \ + \ R_{2431}(B+) - R_{2431}(B-) + \\ &+R_{1324}(B+) - R_{1324}(B-) \ + \ R_{3142}(B+) - R_{3142}(B-)\} \end{aligned}$$

According to the equation (3.44) the carrier concentration can be calculated by

$$n_H = \frac{1}{e}\frac{B}{w}\frac{1}{R_\phi}, \tag{3.55}$$

where n_H can be 3D hole concentration, p, for P-type conductivity semiconductor, if $R_{B+} - R_{B-} > 0$ or 3D electron concentration, n, for N-type conductivity semiconductor, if $R_{B+} - R_{B-} < 0$ assuming the measurement geometry $(I_+, I_-, U_+, U_-, B_+, B_-)$ as shown in figure 3.17.

Finally the carrier Hall mobility can be determined by

$$\mu_H = \frac{\sigma}{e \cdot n_H} \tag{3.56}$$

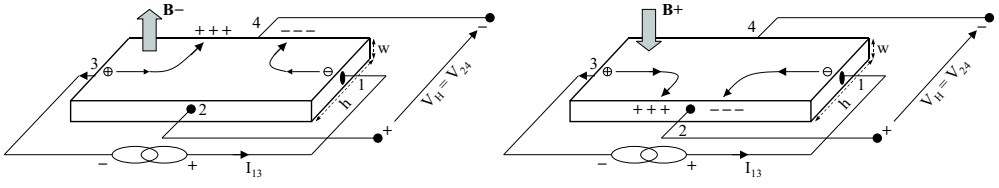

Figure 3.17: Van der Pauw arrangement for measuring the Hall factor of an arbitrary shaped sample. If $R_{B+} - R_{B-} > 0$ then the semiconductor is P-type and if $R_{B+} - R_{B-} < 0$ then the semiconductor is N-type, assuming single type conductivity semiconductor.

Let us consider the effects of inhomogeneity in the sample. Departures from the uniform current distribution which we assumed above can arise in various ways. Perhaps the

simplest example concerns the effect of band bending at a surface or, in the case of epitaxial films, of an interface as a result of charge in the surface states or in deep states in the substrate. The simplicity follows from the fact that the current flow is still parallel to the surface and we can derive general expressions for the effective Hall coefficient and Hall mobility in terms of parallel conducting slabs within each the current flows uniformly. These expressions can readily be applied to the analysis of either positive or negative band bending (i.e. depletion or accumulation).

Consider the two-component conductor shown in fig. 3.18. From the equations (3.44) and

$$\sigma = \frac{J_z}{E_z} \tag{3.57}$$

we can write:

$$R_H \sigma^2 = \frac{-E_y}{E_z^2} \frac{J_z}{B_x} \tag{3.58}$$

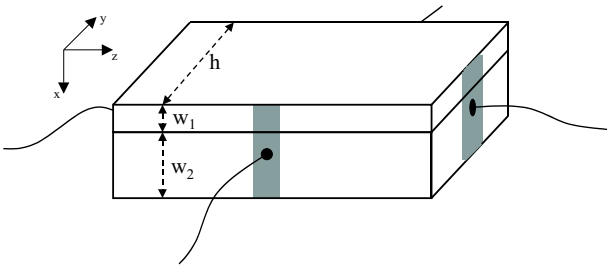

Figure 3.18: Non-uniform sample in the form of two parallel slabs with different thickness, carrier density and mobility. Current flow is everywhere parallel to z direction and is uniform within the individual slabs.

Applying this separately to the two parallel conductors of thickness w_1 and w_2, and to the whole sample gives following results

$$R_{H_1}\sigma_1^2 = \frac{-E_y}{E_z^2}\frac{I_{z1}}{hw_1 B_x} \quad R_{H_2}\sigma_2^2 = \frac{-E_y}{E_z^2}\frac{I_{z2}}{hw_2 B_x} \tag{3.59}$$

$$R_H \sigma^2 = \frac{-E_y}{E_z^2} \frac{I_{z1} + I_{z2}}{h(w_1 + w_2) B_x} \tag{3.60}$$

Further the Hall factor can be expressed by simple derivation:

$$R_H \sigma^2 = \frac{R_{H_1}\sigma_1^2 w_1 + R_{H_2}\sigma_2^2 w_2}{w_1 + w_2} \tag{3.61}$$

Similarly

$$\sigma_1 = \frac{J_{z1}}{E_z} \quad \sigma_2 = \frac{J_{z2}}{E_z} \tag{3.62}$$

$$\sigma = \frac{J_z}{E_z} = \frac{I_z}{hwE_z} = \frac{I_{z1} + I_{z2}}{hwE_z} = \frac{\sigma_1 w_1 + \sigma_2 w_2}{w_1 + w_2}. \tag{3.63}$$

So, finally we obtain an expression for the apparent Hall coefficient for the composite material:

$$R_H = \frac{R_{H_1}\sigma_1^2 w_1 + R_{H_2}\sigma_2^2 w_2}{\sigma^2(w_1 + w_2)} = \frac{w_1 + w_2}{e}\frac{\mu_1^2 n_1 w_1 + \mu_2^2 n_2 w_2}{(\mu_1 n_1 w_1 + \mu_2 n_2 w_2)^2}, \tag{3.64}$$

where the n_1 and n_2 are bulk carrier concentrations, μ_1 and μ_2 the mobilities of the first and second conductive channel, respectively.

In the same formulation, the apparent conductivity σ and Hall mobility μ_H are given by:

$$\sigma = \frac{\sigma_1 w_1 + \sigma_2 w_2}{w_1 + w_2} = e \cdot \frac{\mu_1 n_1 w_1 + \mu_2 n_2 w_2}{w_1 + w_2}, \tag{3.65}$$

$$\mu_H = R_H \sigma = \frac{1}{en_H} e n_H \mu_H = \frac{\mu_1^2 n_1 w_1 + \mu_2^2 n_2 w_2}{(\mu_1 n_1 w_1 + \mu_2 n_2 w_2)}. \tag{3.66}$$

Finally the carrier concentration can be derived from equation (3.64):

$$n_H = \frac{1}{eR_H} = \frac{1}{w_1 + w_2}\frac{(\mu_1 n_1 w_1 + \mu_2 n_2 w_2)^2}{\mu_1^2 n_1 w_1 + \mu_2^2 n_2 w_2}, \tag{3.67}$$

If two conductive layers consist of mixed conductivity channels, electron and hole, the electron concentration has to be assumed negative in above equations because the Hall factor for electrons is negative (see section 3.8).

Chapter 4

Experimental Apparatus

4.1 MBE System

The MBE growth chamber consists of a stainless steel pot, connected in series through metal sealed gate valves to the analysis chamber on one side and a load lock introduction chamber on the other. The sample is mounted on a Molibdenum sample holder and inserted in the small introduction chamber, which is evacuated by means of a turbomolecular pump. A pressure lower than 1×10^{-7} mbar is reached usually in one hour (pumping speed 370 l/s). In this pressure range a quick transfer of the sample-holder in the MBE growth chamber does not influence the basis pressure of the epitaxy chamber ($\sim 10^{-11}$ mbar). The

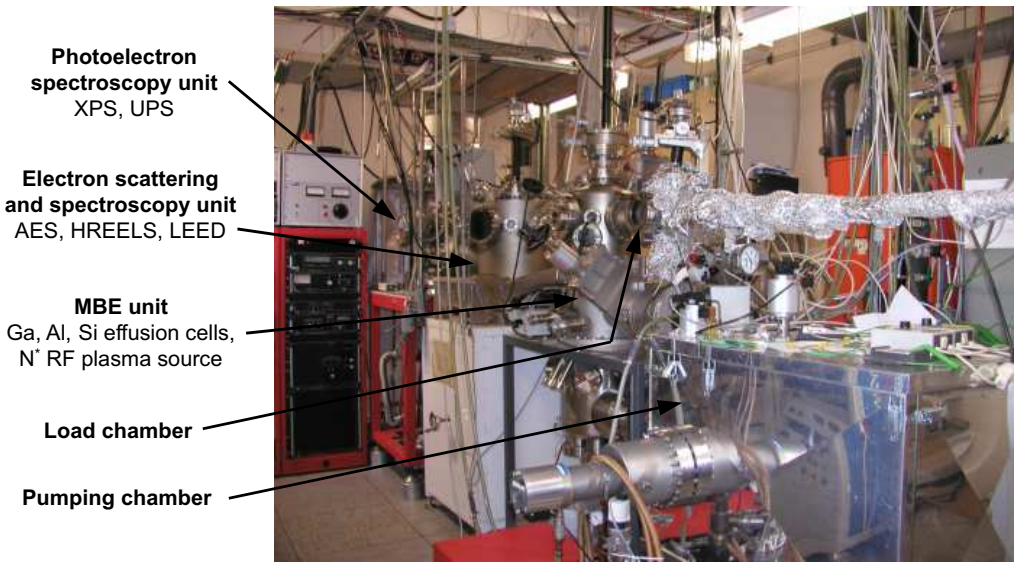

Figure 4.1: Picture of the MBE apparatus at the Institut für Schichten und Grenzflächen (ISG-1) of Forschungszentrum Jülich, used for the III-Nitride layer growth.

UHV base pressure is reached by means of a turbomolecular pump with 1000 l/s pumping speed, connected directly to the middle portion of the chamber, and by means of a pumping unit implemented with an ion pump (400 l/s), a cryo pump and a small turbo pump. During the nitride epitaxy the pressure reaches values up to 1.5×10^{-5} mbar at a flux of nitrogen of 1 sccm. The chamber has also a cryoshroud system, which is filled with liquid nitrogen during growth, to trap the impurities coming from the hot cell surroundings. A further cryoshroud surrounds a titanium sublimation pump, which is efficiently used to quickly reduce the chamber pressure after the epitaxy, thanks to its getter action.
The chamber is equipped with four 63CF flanges which have their axis focused on a point, where the sample surface is located during the epitaxy. On three of these ports standard effusion Knudsen cells are mounted for the evaporation of gallium, aluminum and silicon and the fourth flange is dedicated to the plasma source, which provides the nitrogen radicals necessary for the reaction.
The impingement rate I_A (number of atoms or molecules impinging on the sample per unit area) of the molecular beam at the central point of a substrate axially mounted in front of the cell can be determined, in first approximation, by the equation:

$$I_A = 1.118 \times 10^{22} \frac{pA}{r^2\sqrt{MT}} \quad \text{(molecules cm}^{-2}\text{s}^{-1}\text{)} \tag{4.1}$$

where A is the orifice area of the cell, p the equilibrium vapor pressure[1] in Torr of the effusing species at the cell temperature T, r is the distance of the substrate from the orifice and M the atomic mass of the evaporated species (all quantities in cgs units) [119]. Practically, a calibration of the system is necessary to determine the rate and the stoichiometry of the growth.

The particle (atoms or molecules) flux is determined by the temperature of the melted material in the crucible: experimentally the cell temperatures were measured with W-Re thermocouples and controlled by Eurotherms. The stand-by temperatures were kept well above the melting point of the materials, that are $30°$C for Ga and $660°$C for Al because a frequent solidification of the materials can give rise to cracks in the pyrolitic boron nitride crucibles (pBN). The beam equivalent pressure (BEP) was checked by means of a movable ion gauge, that can be placed at the sample growth position. As a matter of experience, the Ga flux should be checked after each or every two long epitaxy runs in the first weeks after refilling of the crucibles and becomes slowly more stable with the operation time. The purity of the materials used to charge the cells was 7N for gallium and 6N for aluminum.

As source for the creation of reactive nitrogen we had at disposal a radio frequency (RF) plasma source UNI-Bulb^{TM} from EPI Inc. It consists of a LC circuit matching unit that is operated by a RF generator working at 13.56 $(\pm 0.005\%)$ MHz, with powers between 0 and 600 W. For the epitaxial growth nitrogen is used with 6.0 purity, then further

[1] A table of vapor pressure vs temperature of many elements and molecules can be fi nd on: www.applied-epi.com

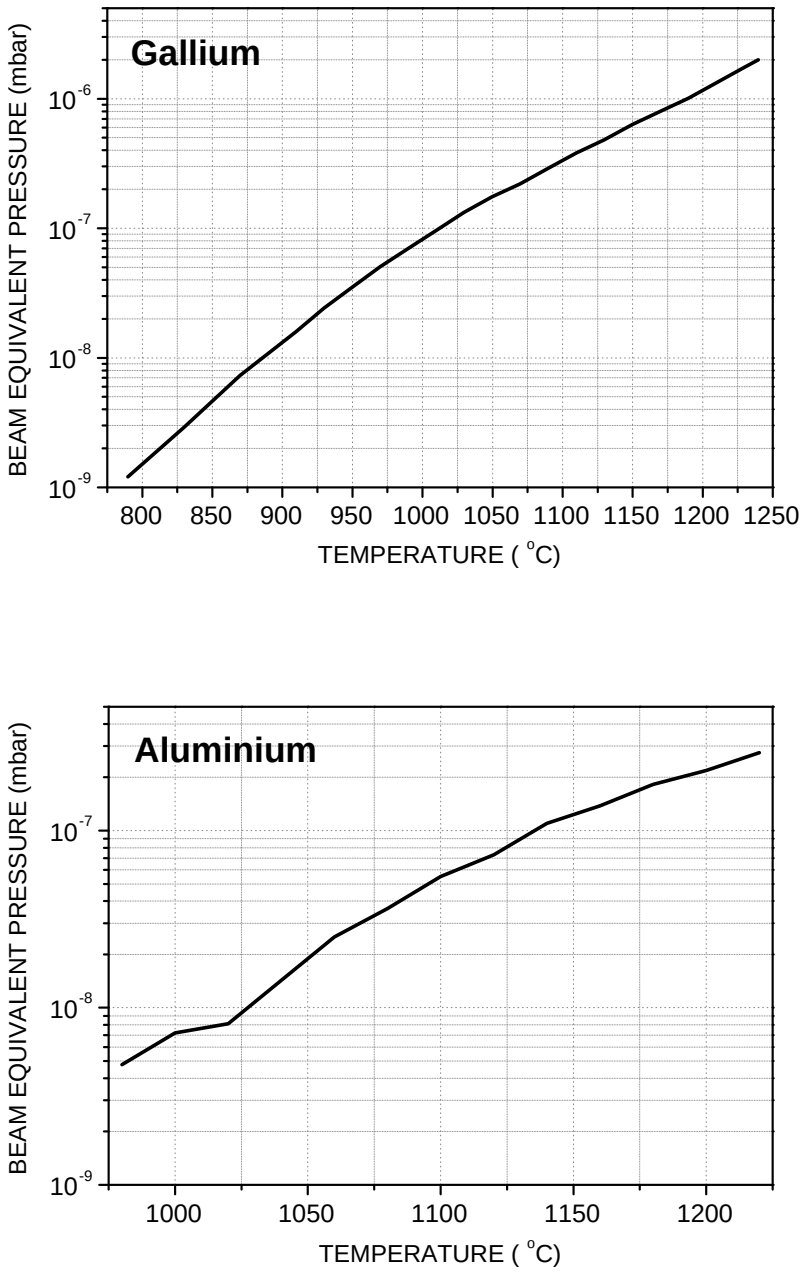

Figure 4.2: Beam equivalent pressure (BEP) of the gallium (top) and aluminium (bottom) effusion cells as a function of temperature.

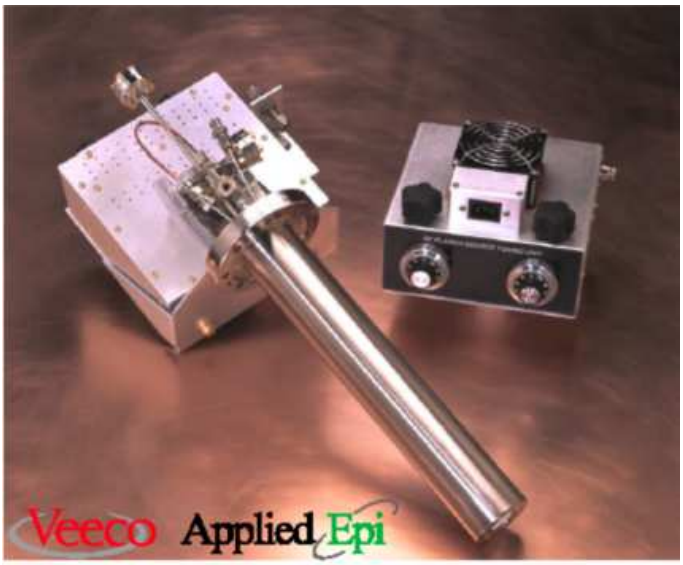

Figure 4.3: The Epi UNI-Bulb^{TM} plasma source.

purified to a still lower level by a commercial filter. The nitrogen flux is controlled by a mass flow controller (MKS Inc.). The plasma is created inside a pBN cylinder with a hole in the direction of the sample. This cylinder is located inside the water cooled copper coil of the LC circuit, that is coupled in the outside part of the cell to the variable capacitors. This makes possible to couple the oscillating LC circuit to different plasma conditions (different gas flux and/or power). The ignition and stability of the plasma is optically checked by controlling the intensity of the yellow light coming out from a view port. The spectral analysis of the outcoming light was not performed but we referred to the work in Ref. [157].
A calibration of the sample surface temperature was performed by means of an optical pyrometer for different voltages applied to the heating resistance. In the region of temperatures used during the growth the error is $\pm 30°$C. The inhomogenity of the temperature distribution at the sample surface was found to be $\sim 10°$C.

4.2 In- and ex-situ Analysis System

Connected in series to the MBE chamber there are two other UHV chambers, separated by valves. The first one is pumped by means of an ion pump with titan sublimator and contains a High Resolution Electron Energy Loss Spectroscopy (HREELS, not used in this work), a Low Energy Electron Diffraction (LEED), and an Auger Electron Spectroscopy (AES) systems. The AES spectra are recorded by means of a Cylindrical Mirror Analyzer (CMA) using a primary energy of the exciting electrons of 2 KeV in a normal geometry. The acquisition of the first derivative of the signal is achieved using a lock-in amplifier. The LEED system is characterized by a three grids optics and it is possible to acquire the patterns projected on the fluorescent screen with a digital camera.
In the second analysis chamber it is possible to perform photoelectron spectroscopy by means of X-ray Photoelectron Spectroscopy (XPS).
For XPS the radiation is obtained from an Al anode, the Al-K_α line (1486.6 eV) is then selected by a monochromator. The X-ray anode is usually operated at 28 mA and 13 V, to obtain a sufficient signal also at the higher resolution ($\Delta E = 0.45$ eV).
The emitted photoelectrons are analyzed in energy using a CHA (Concentric Hemispherical Analyzer). A three stages manipulator allows the rotation of the sample to achieve, for example, a different surface sensitivity, but has as consequence a consistent reduction of the signal intensity.

For the morphological analysis of the samples an atomic force microscope (AFM) MMAFM-2^{TM} by Veeco Inc. controlled by the dedicated Nanoscope^{TM} software was used. The electrical characterization was performed with an Hall effect equipment in the temperature range of 4.2 to 300 K and magnetic field variable between $+0.5$ and -0.5 Tesla. More detailed description is shown in subsection 4.2.1
Thanks to collaborations within the Institute we could investigate grown samples using also Rutherford Back-Scattering (RBS), X-ray Diffraction (XRD), Secondary Ions Mass Spectroscopy (SIMS) and Transmission Electron Microscopy (TEM).

4.2.1 Hall Measurement Experimental Setup

The Hall measurements were performed in the Low Temperature Hall measurement system[2] in Magnet laboratory (fig. 4.4). The measurement scheme is shown in figure 4.5. A personal computer is used for controlling the electronic devices in measurement cycle and collecting the measured data. The Hall measurement is done in the temperature range from 4 K to 300 K with a magnetic field of 0.5 T. The low temperature is reached using the ^{4}He-overflow cryostat, which consists of three chambers: sample, helium and isolation chamber, as displayed in figure 4.6.

The sample chamber can be used for measurement of two Hall-bar or van der Pauw

[2]TTH - Tief Temperatur Hall Messplatz

Figure 4.4: Low Temperature Hall measurement system in Magnet laboratory.

samples. The lower part is placed in helium chamber, which is filled with liquid Helium from a barrel through a Helium pipe. The liquid Helium evaporates and colds the walls of the sample chamber. The Helium gas is then pumped out using a rotary vane pump. The isolation chamber serves to thermally isolate the sample and helium chamber from the outside environment. Using a rotary vane pump, it is possible to reach a vacuum of 10^{-3} mbar.

After the sample is built into the cryostat and before the cooling is started, the air in the sample chamber can be pumped out and replaced with a ^{4}He gas from He-backward's pipe. The ^{4}He gas serves as a contact gas at low temperatures.

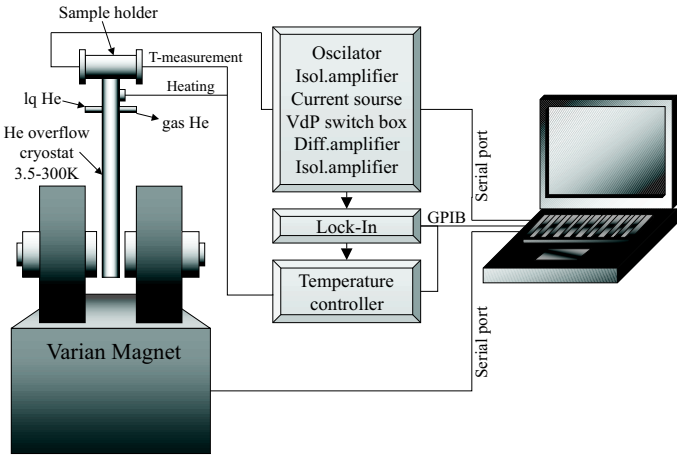

Figure 4.5: Low temperature Hall measurement setup.

The sample is electrically, but not thermally isolated from the copper sample holder and is held by four golden-copper springs, which are used also as contacts (fig. 4.7). The wires are varnish-isolated copper wires and are placed in a steel pipe to be protected.

The temperature is measured using a Platin temperature sensor (PT100), which provides accurate temperature measurement in the region from 30 K to 300 K. The lowest temperature reached in the overflow cryostat is 4.2 K. The temperature can be stabilized using the Lake-Shore Temperature Controller 331 in the range of 4-90 K. The cooling flux of liquid He is set to be constant. The power of a heating resistor is controlled by the difference between the desired and measured temperature. The proportional (P), derivative (D) and integral (I) parameters of the control loop vary for different temperature range. The PID control algorithm calculates control output based on temperature setpoint and feedback from the control sensor. The PID parameters are the key point for fast stabilization of the desired temperature. Above 100 K the stabilizing of the temperature is impossible due to the low heating power of the resistance and due to the slow system.

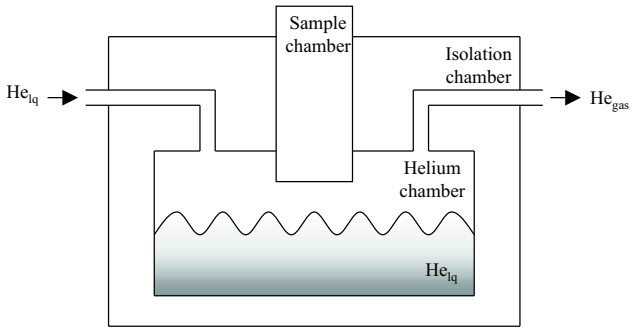

Figure 4.6: ^{4}He-overfbw cryostat consists of three chambers.

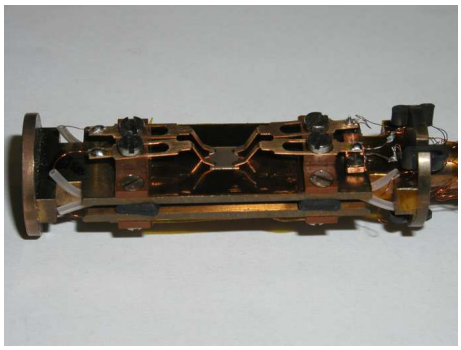

Figure 4.7: Sample holder for the Hall measurement.

The magnet is a current-coil water cooled Varian Magnet. The magnetic induction can be changed from 0 to 0.6 T. The calibration of the magnet was done using a Hall probe and the calibration curve is shown in figure 4.8. During the measurement magnetic field of 0.5 T is used. The poles of the magnet surround the cryostat and produce a homogeneous magnetic field in the sample chamber. Changing the current polarity in the coil, the polarity of the magnetic induction is changed.

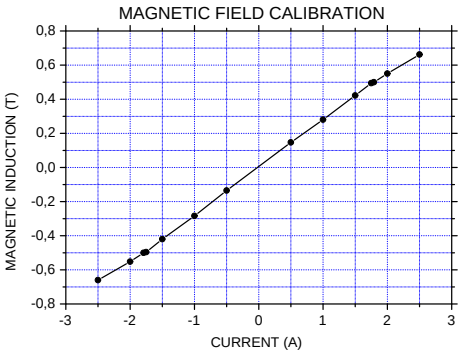

Figure 4.8: Magnetic fi eld calibration of the Varian Magnet.

The measurement cycle is shown in the figure 4.9 and consist of a oscillator (OSC), current source (I-Drive), van der Pauw switch box (VdP switch box)[3] and Lock-In amplifier Dynatrac 501. The Hall measurement can be performed either as direct (DC) or alternated circuit (AC). In order to exclude the noise influences during the measurement, it is useful to perform AC measurement. The direct or alternated (0-120 Hz) voltage (0-1 V) from an oscillator is joined to an input of the isolation amplifier (Input ISO Amp), where

[3]OSC, I-Drive, switch box, isolation and differential amplifi ers were built in Elektronik Werkstatt, ISG-1, FZ Jülich by Mr. Ralph Otto

it is amplified by factor of 10. The inner measurement circuit is optically coupled in the isolation amplifier with the outside electronic circuit. The galvanic connection between inner and outside electronic circuit is interrupted in this way and the noise signals are suppressed. Furthermore the signal is coming into the current source (V-I convertor), where various current amplitudes ($n \times 10^{-x}$ A for $n \times 0.1$ V input voltage, where $0 \leq n \leq 10$ and x=3, 4,..8) according to the resistance load can be adjusted. Various measurement configurations controlled by a self developed software package in the PC (described in the subsection 3.8.1) can be set using relays in the Switch box. The measured signal from the sample is amplified by a differential amplifier with a gain of: 1, 10, 100, 200 or 500. Subsequently the signal is coupled optically to the outside electronic circuit through output isolation amplifier (Output ISO Amp) and by factor 10 amplified. Finally the amplitude and the phase of the voltage signal regarding the reference oscillator signal is measured in the Lock-In amplifier.

One measurement cycle from 4 K to the room temperature including the cooling down takes approximately 6 hours.

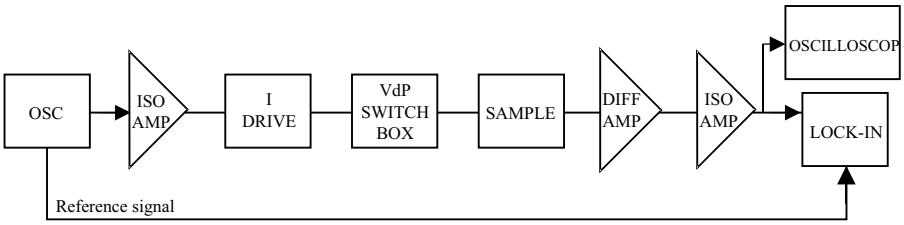

Figure 4.9: Hall measurement circuit scheme.

The maximal error of the magnetic field is $\pm 3\%$. The non-accuracy of the measured data due to the capacity of the used BNC wires lies below 3%. However a low frequency of 39 Hz of the alternated signal was used. The error measurement of the current source, Lock-In and other amplifiers is 2%. The total accuracy of the Hall measurement setup can be estimated to 5%.

4.2.2 Hall Measurement Control using a PC

Before the Hall measurements on the samples could be performed, it was necessary to realize a program algorithm of the Hall measurement using a personal computer. The program has been written within LabVIEW version 5.1. LabVIEW (Laboratory Virtual Instrument Engineering Workbench) is a development environment based on the graphical programming language G. LabVIEW is integrated fully for communication with hardware such as GPIB, VXI, PXI, RS-232, RS-485, and plug-in data acquisition boards. This subsection deals with the description of the realized program.

The user program window for the Hall measurement is shown in figure A.1. The program enables to perform multiple (automatic) or single Hall measurements of two built samples, A and B, with van der Pauw contact's geometry and to evaluate conductivity, bulk or sheet carrier concentration and carrier mobility. The measurement by itself includes two sets of measurements: conductivity measurement (without magnetic field, $B = 0$), which consists of 8 measured values according to applied connection configurations (see subsection 3.8.1) and Hall factor measurement (with magnetic field, $B \neq 0$) consisting also of 8 readings. The measured carrier concentrations and mobilities for each temperature are plotted in a graph and saved to a file together with all partial measurement results.

The electronic devices necessary for the measurement procedure (described in the previous subsection) are controlled by the computer using an IEEE-488 interface, which complies with the IEEE-488.2 - 1987 standard and serial interface, commonly referred to as an RS-232C interface, which is a standard of the Electronics Industries Association (EIA). The communication with the switch-box and magnet is performed through RS-232 interface, and the communication of the Lock-In and temperature controller through IEEE-488. The electronic devices are asked by addressed commands and queries to perform specific operation. The commands and queries with description for each device are listed in the appendix A.1.

A short description of the controlled devices follows. In the switch box, current source poles (I+, I-) and measured voltage poles (U+, U-) can be connected to the contacts of the sample A or B. The amplitude of the current flowing through the sample, attenuation and gain of the differential amplifier can be also chosen. If the switch box does not respond, a reset can initialize the switch box into the initial status.

The voltage of the sample is measured with Lock-In Dynatrac 501 regarding the frequency of the reference oscillator signal. The user has the possibility to choose the sensitivity range, time constant and the phase shift. Unfortunately the device does not have automatic sensitivity range function. Therefore the auto-range function was included in the program. Because of time delays, using of fixed sensitivity range is recommended. In this case the user has to check if measured value is not in overload. Overload is signaled by lighting up of an indicator. The calculated resistivity and the phase of the signal is displayed. The resistivity is given by the measured voltage and set current ($R_{ijkl} = U_{kl}/I_{ij}$, where indexes i, j, k, l correspond to the van der Pauw sample contacts) assuming the adjusted gain of the differential and isolation amplifiers.

Fixed magnetic field induction of 0.5 T is used for the Hall measurement. Reverse B-, forward B+ and zero magnetic field can be set through PC.

The temperature is measured by the Lake-Shore Temperature Controller 331 and the value is displayed. For the temperature control, the desired temperature have to be defined and the temperature controller adjusted to Tune mode. The PID parameters of the control loop for certain temperature range have to be inserted through the front panel of the Temperature controller.

More detailed description of using the program is in the appendix A.2.

Chapter 5

Band Scheme Modelling

5.1 Self-consistent Algorithm

To study the band scheme of semiconductors in the middle of the Brillouin zone theoretically following is assumed: one electron approximation, interaction between electrons is neglected, the periodic potential of the solid is approximated by effective mass. To include the influence of an electronic charge a self-consistent solution of Schrödinger and Poisson equation has to be used. The following describes the self-consistent solution of Schrödinger and Poisson equation.

First approximation of the potential energy in real heterostructure is a rectangular quantum well. In reality its behavior is modified by an electrostatic potential, which results from non-zero charge density in quantum well.
Calculation algorithm of the potential profile, quantized energy levels and wave functions of electrons is shown in fig. 5.1. After the input parameters are defined, as effective mass, doping concentration, temperature etc., the input potential energy $V_o(x)$ is set as conduction band minimum profile given by conduction band offset of both semiconductors with zero charge density.

Following one-dimensional Schrödinger equation for this potential is calculated:

$$-\frac{\hbar^2}{2}\frac{d}{dx}\left(\frac{1}{m^*(x)}\frac{d}{dx}\right)\cdot\psi(x)+V(x)\cdot\psi(x)=E\cdot\psi(x), \tag{5.1}$$

where $\psi(x)$ is the wave function, $V(x)$ the potential energy, E the energy of an electron, $\hbar$ the Planck′s constant divided by 2π and m^* the effective mass of a electron. The solution of Schrödinger equation are quantized bound energy states E_n and corresponding wave functions $\psi_n(x)$, which can be used to calculate charge density distribution. The electron concentration $n(x)$ is given by following equation:

$$n(x)=\sum_{k=1}^{m}\psi_k^*(x)\psi_k(x)n_k, \tag{5.2}$$

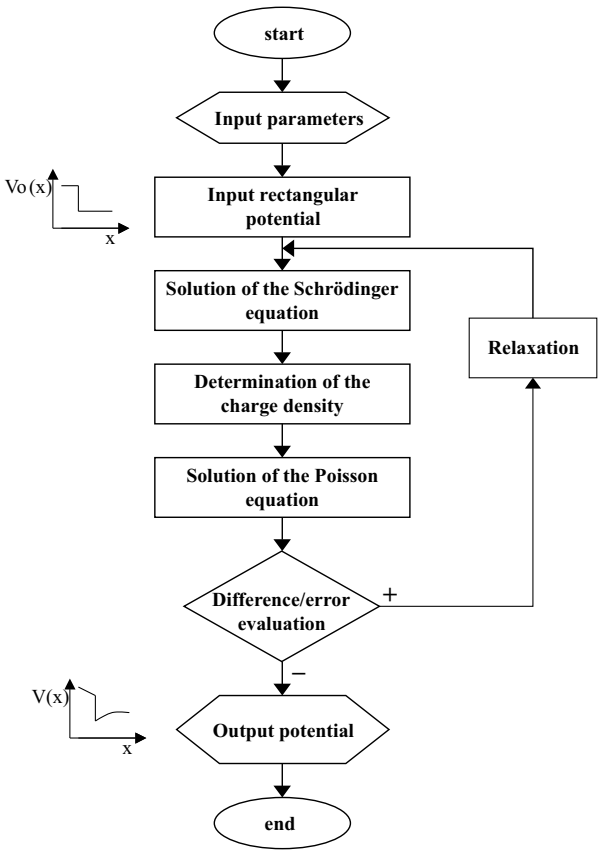

Figure 5.1: Self-consistent algorithm of solving Schrödinger and Poisson equation.

where m is the number of bound states and n_k the electron occupation for each state.

The calculated free electron $n(x)$ and hole $p(x)$ carrier concentration, ionized donor $N_D^+(x)$ and ionized acceptor concentration $N_A^-(x)$ are used to calculate the electrostatic potential $\phi(x)$ from the Poisson equation:

$$\frac{d}{dx}\left(\varepsilon_s(x)\frac{d}{dx}\right)\cdot\phi(x) = \frac{-q\cdot[p(x)-n(x)+N_D^+(x)-N_A^-(x)]}{\varepsilon_0}, \tag{5.3}$$

where ε_s is the dielectric constant. In a quantum well of arbitrary potential energy profile, the potential energy V is related to the electrostatic potential ϕ as follows:

$$V(x) = -q\cdot\phi(x) + \Delta E_c(x), \tag{5.4}$$

where $\Delta E_c(x)$ is conduction band discontinuity. The result is a new potential energy $V(x)$, that is used as a new input into the Schrödinger equation. The solution of Schrödinger and Poisson equation is started again. The iterative calculation is terminated when the difference between two subsequent potentials is smaller than a certain error

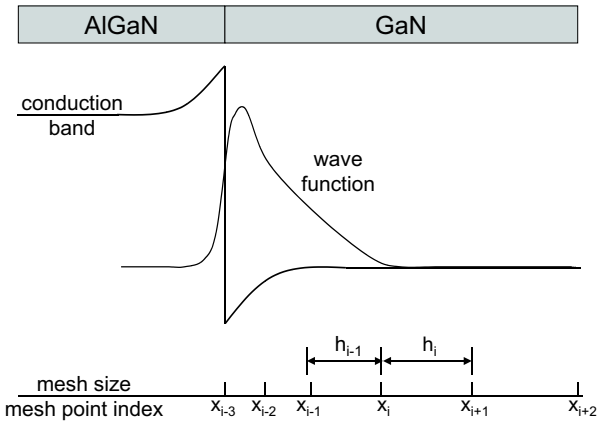

Figure 5.2: Band diagram of a single heterojunction AlGaN/GaN and its bounded state wave function (top) and discretization of the potential using a nonuniform mesh (bottom).

value. In most cases difference of 10^{-5} eV is enough to reach satisfied results.

Schrödinger and Poisson equation are second grade differential equations, which can not be calculated analytically, but numerically. There are several numerical methods which can be used: finite difference, finite elements, transfer matrix, variation method, shooting method. Band scheme simulation shown in this work uses finite difference method. Real space is divided into nonuniform discrete mesh points according to fig. 5.2.

Discretisation of the Schrödinger equation

In order to solve the Schrödinger equation numerically we may discretise the equation (5.1) by using three-point difference scheme as shown in fig. 5.2. The derivation in eq. (5.1) is replaced by difference with a nonuniform step h_i:

$$\frac{d}{dx}\cdot\left(\frac{1}{m^*(x_i)}\frac{d\psi(x_i)}{dx}\right)=\frac{\frac{\psi'(x_{i+\frac{1}{2}})}{m^*(x_{i+\frac{1}{2}})}-\frac{\psi'(x_{i-\frac{1}{2}})}{m^*(x_{i-\frac{1}{2}})}}{\frac{h_i+h_{i-1}}{2}} \tag{5.5}$$

$$\frac{1}{m^*(x_{i+\frac{1}{2}})}\cdot\frac{d\psi(x_{i+\frac{1}{2}})}{dx}=\frac{1}{m^*(x_{i+\frac{1}{2}})}\cdot\frac{\psi(x_{i+1})-\psi(x_i)}{h_i} \tag{5.6}$$

$$\frac{1}{m^*(x_{i-\frac{1}{2}})}\cdot\frac{d\psi(x_{i-\frac{1}{2}})}{dx}=\frac{1}{m^*(x_{i-\frac{1}{2}})}\cdot\frac{\psi(x_i)-\psi(x_{i-1})}{h_{i-1}} \tag{5.7}$$

Inserting the equations (5.6) and (5.7) into the (5.5) we get

$$\frac{d}{dx}\left(\frac{1}{m^*(x_i)}\frac{d\psi(x_i)}{dx}\right)=\frac{2}{h_i+h_{i-1}}\cdot\left(\frac{\psi(x_{i+1})-\psi(x_i)}{m^*(x_{i+\frac{1}{2}})\cdot h_i}+\frac{\psi(x_i)-\psi(x_{i-1})}{m^*(x_{i-\frac{1}{2}})\cdot h_{i-1}}\right) \tag{5.8}$$

This equation (5.8) is further inserted into the Schrödinger equation (5.1) and we get discretised Schrödinger equation:

$$-\frac{\hbar^2}{h_{i-1}+h_i}\cdot\left(\frac{\psi(x_{i+1})-\psi(x_i)}{h_i\cdot m^*(x_{i+\frac{1}{2}})}-\frac{\psi(x_i)-\psi(x_{i-1})}{h_{i-1}\cdot m^*(x_{i-\frac{1}{2}})}\right)+V(x_i)\cdot\psi(x_i)=E\cdot\psi(x_i) \quad (5.9)$$

The border points $\psi(x_1)$, $\psi(x_N)$ have to fill the boundary condition. The number N represents the number of mesh points. For $N-2$ points, we get $N-2$ equations, that can be expressed as matrix equation:

$$H_{i-1,j-1}\cdot\psi(x_i)=E\cdot\psi(x_i), \quad (5.10)$$

which shows the solution of the eigenvectors

$$\psi(x_i)=\begin{pmatrix}\psi(x_2)\\ \psi(x_3)\\ .\\ .\\ \psi(x_{N-1})\end{pmatrix}$$

and eigenvalues E. The Hamiltonian $H_{i-1,j-1}$ is a tridiagonal nonsymmetric matrix (N-2)×(N-2), where the number $i-1$ and $j-1$ is the number of row and column, respectively. Numbers i and j can have $2,3..N-1$ values.

$$H_{i-1,j-1}=\begin{cases}-\frac{\hbar^2}{h_i+h_{i-1}}\cdot\frac{1}{m^*(x_{i-\frac{1}{2}})}\frac{1}{h_{i-1}} & \text{if i}+1=\text{j (next}-\text{left diagonal)},\\ \frac{\hbar^2}{h_i+h_{i-1}}\cdot\left(\frac{1}{m^*(x_{i+\frac{1}{2}})}\frac{1}{h_i}+\frac{1}{m^*(x_{i-\frac{1}{2}})}\frac{1}{h_{i-1}}\right)+V(x_i) & \text{if i}=\text{j (main diagonal)},\\ -\frac{\hbar^2}{h_i+h_{i-1}}\cdot\frac{1}{m^*(x_{i+\frac{1}{2}})}\frac{1}{h_i} & \text{if i}-1=\text{j (next}-\text{right diagonal)},\\ 0 & \text{otherwise.}\end{cases}$$

The index i identifies the grid on the one-dimensional mesh (fig. 5.2). Half-integer index implies a point midway between the grid points ($m^*(x_{i+\frac{1}{2}})\approx\frac{m^*(x_i)+m^*(x_{i+1})}{2}$), and h_i is the mesh size between adjacent points x_i and x_{i+1}. The matrix H is symmetric only if the mesh spacings h_i are all uniform.

Discretisation of the Poisson equation

Solving the Poisson equation numerically using the finite difference method, the derivation in eq. (5.3) is replaced by difference using three-point difference scheme as shown in fig. 5.2:

$$\frac{d}{dx}\cdot\left(\varepsilon_r(x_i)\frac{d\phi(x_i)}{dx}\right)=\frac{\varepsilon_r(x_{i+\frac{1}{2}})\cdot\phi'(x_{i+\frac{1}{2}})-\varepsilon_r(x_{i-\frac{1}{2}})\cdot\phi'(x_{i-\frac{1}{2}})}{\frac{h_i+h_{i-1}}{2}} \quad (5.11)$$

$$\varepsilon_r(x_{i+\frac{1}{2}}) \cdot \frac{d\phi(x_{i+\frac{1}{2}})}{dx} = \varepsilon_r(x_{i+\frac{1}{2}}) \cdot \frac{\phi(x_{i+1}) - \phi(x_i)}{h_i} \tag{5.12}$$

$$\varepsilon_r(x_{i-\frac{1}{2}}) \cdot \frac{d\phi(x_{i-\frac{1}{2}})}{dx} = \varepsilon_r(x_{i-\frac{1}{2}}) \cdot \frac{\phi(x_i) - \phi(x_{i-1})}{h_{i-1}} \tag{5.13}$$

Inserting the equations (5.12) and (5.13) into the (5.11) we get:

$$\frac{d}{dx}\left(\varepsilon_r(x_i)\frac{d\phi(x_i)}{dx}\right) = \frac{2}{h_i + h_{i-1}}\left(\frac{\phi(x_{i+1}) - \phi(x_i)}{\frac{h_i}{\varepsilon_r(x_{i+\frac{1}{2}})}} - \frac{\phi(x_i) - \phi(x_{i-1})}{\frac{h_{i-1}}{\varepsilon_r(x_{i-\frac{1}{2}})}}\right) \tag{5.14}$$

After inserting this equation (5.14) into the Poisson equation (5.3) we get discrete Poisson equation:

$$\begin{aligned}\frac{2}{h_i+h_{i-1}}\left[\frac{\phi(x_{i-1})}{\frac{h_{i-1}}{\varepsilon_r(x_{i-\frac{1}{2}})}} - \left(\frac{\phi(x_i)}{\frac{h_{i-1}}{\varepsilon_r(x_{i-\frac{1}{2}})}} + \frac{\phi(x_i)}{\frac{h_i}{\varepsilon_r(x_{i+\frac{1}{2}})}}\right) + \frac{\phi(x_{i+1})}{\frac{h_i}{\varepsilon_r(x_{i+\frac{1}{2}})}}\right] + \\ + \frac{e}{\varepsilon_O}\left[N_D^+(x_i) - N_A^-(x_i) + p(x_i) - n(x_i)\right] = 0\end{aligned} \tag{5.15}$$

First and last point of the one-dimensional mesh, $\phi(x_1)$ and $\phi(x_N)$, have to fill the boundary condition. The discrete Poisson equation can be expressed in matrix equation:

$$A_{i-1,j-1} \cdot \phi(x_i) = B_i, \tag{5.16}$$

where $B_i = \frac{e}{\varepsilon_O}\left[N_D^+(x_i) - N_A^-(x_i) + p(x_i) - n(x_i)\right]$ and

$$A_{i-1,j-1} = \begin{cases} \frac{2}{h_i+h_{i-1}} \cdot \frac{\varepsilon_r(x_{i-\frac{1}{2}})}{h_{i-1}} & \text{if i} + 1 = \text{j (next} - \text{left diagonal)}, \\ -\frac{2}{h_i+h_{i-1}} \cdot \left(\frac{\varepsilon_r(x_{i-\frac{1}{2}})}{h_{i-1}} + \frac{\varepsilon_r(x_{i+\frac{1}{2}})}{h_i}\right) & \text{if i} = \text{j (main diagonal)}, \\ \frac{2}{h_i+h_{i-1}} \cdot \frac{\varepsilon_r(x_{i+\frac{1}{2}})}{h_i} & \text{if i} - 1 = \text{j (next} - \text{right diagonal)}, \\ 0 & \text{otherwise.} \end{cases}$$

$A_{i-1,j-1}$ is a tridiagonal nonsymmetric matrix, where the number $i-1$ and $j-1$ is the number of row and column, respectively. Numbers i and j can have $2, 3..N-1$ values.

5.2 Modelling of 2DEG AlGaN/GaN Heterostructures

This section describes band scheme properties of Ga-face AlGaN/GaN heterostructures as derived by application of a Schrödinger-Poisson solver [158] under electrical neutrality at temperature of 300 K. We focused on the calculated two dimensional electron concentration confined at the AlGaN/GaN interface, which is an important parameter for HEMT applications. In particular, the issue of polarization charge and the role played by surface states which is modelled by Fermi level pinning at the surface is emphasized. Furthermore, the influence of the thickness, Al alloy composition and the doping in AlGaN barrier is discussed.

5.2.1 Polarization Charge Issue

The dramatic effect of the polarization charge on the 2DEG formation at $\mathrm{Al_{0.1}Ga_{0.9}N/GaN}$ interface is shown in the self-consistent calculations [158] of the conduction band edge and of the electron concentration in fig. 5.3 (left) and has been pointed out by several authors [22, 159, 160]. The Ga-face polarity is assumed in the calculation, therefore a positive polarization charge is present at the AlGaN/GaN interface (fig. 5.3 (left-up)). The MBE nitride heterostructures grown on Si-face 6H-SiC(0001) always with Ga on top of the bilayer (Ga-face polarity), due to energetically favorable Si-N bond at the $\mathrm{SiC(0001)_{Si}/AlN}$. The calculated polarization induced sheet charges are added to the structure at layer boundaries as fixed charges (fully ionized donors (positive) and acceptors (negative)). The thickness of these layers has to be as small as possible. In our calculation we used 1 Å. A background doping of 10^{17} cm^{-3} has been assumed in the whole heterostructure corresponding to the typical unintentional n-doping experimentally observed (subsection 6.2.5). Without the polarization and without the modulation doping, no quantum well is formed at the heterojunction and no electron confinement results. In fact, the surface band bending induces an electron depletion region extending from the surface beyond the $\mathrm{Al_XGa_{1-X}N/GaN}$ interface. If the polarization is introduced into the calculation, as a fixed interface charge, the electron energy close to the interface is reduced due to the attractive potential of the polarization charges: a triangular quantum well is formed on the GaN side which crosses the Fermi energy and therefore electrons are strongly confined in a quasi-2D electron gas. The calculated electron sheet concentration in the potential well for the quite low Al content $x = 0.1$ is $n_s = 1.9 \times 10^{12}$ cm^{-2}.

Fig. 5.3 (right) shows analogous results for a modulation doped structure, with a doping level in the $\mathrm{Al_{0.1}Ga_{0.9}N}$ barrier of $n = 5 \times 10^{18}\ \mathrm{cm^{-3}}$ and the same background concentration of 10^{17} cm^{-3} for the bulk GaN. In this modulation doped structure, of course, a 2DEG is formed at the interface also without polarization. The polarization charge causes an increase of the electron concentration in the 2DEG, which amounts to $n_s = 3.8 \times 10^{12}\ \mathrm{cm^{-2}}$; on the other hand, the electron distribution is seen to leak into the barrier region, which is not desired for optimized device structures. In fact, alloy scatter-

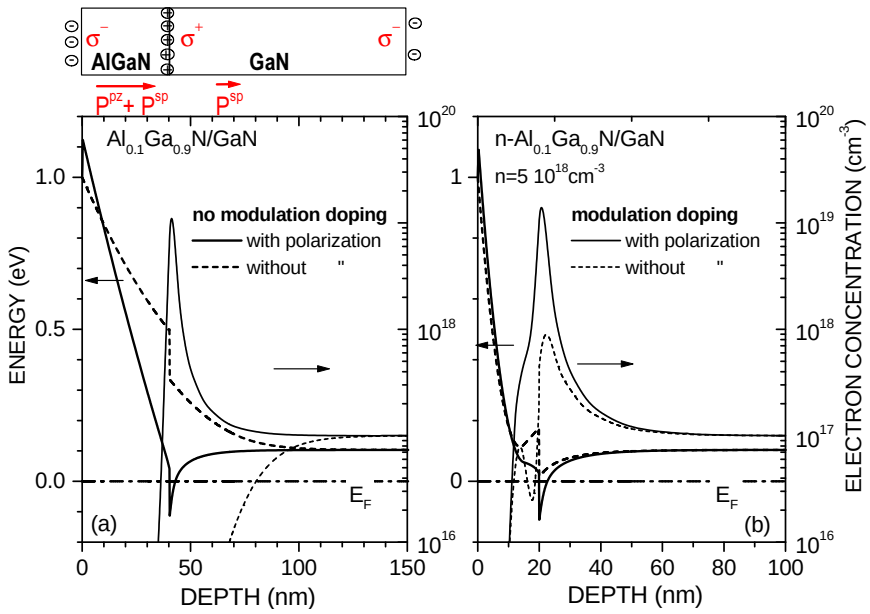

Figure 5.3: Self-consistent Schrödinger-Poisson calculation for an $Al_{0.1}Ga_{0.9}N$/GaN pseudomorphic heterostructure with and without modulation doping. The conduction band edge profile is shown (left scale) together with the electron concentration (right scale) along the undoped (left) and doped $n = 5 \times 10^{18}$ cm^{-3} (right) AlGaN/GaN heterostructure.

ing as well as interface scattering will be increased due to roughness. Further drawbacks for HEMT applications are associated with the doping of the $Al_XGa_{1-X}N$ barrier, as compared with undoped structures: the gate leakage current increases, the pinch-off voltage is higher and more noise is expected due to the deep donors in $Al_XGa_{1-X}N$. These are the reasons why many groups prefer non-modulation doped nitride HEMT structures [161]. In table 2.2 a comparison between the main characteristics of $Al_XGa_{1-X}As/In_XGa_{1-X}As$ and $Al_XGa_{1-X}N/GaN$ 2DEG structures is reported.

5.2.2 Surface States

The effect of the surface Fermi level pinning is discussed in this subsection. Self-consistent calculations [158] of the conduction band edge and of the electron concentration along $Al_XGa_{1-X}N$/GaN heterostructures are shown in fig. 5.4. The Ga-face polarity is assumed in the calculation, therefore a positive polarization charge is present at the AlGaN/GaN interface, which induces the formation of a 2DEG at the interface without need of modulation doping. A background doping of 10^{17} cm^{-3} has been assumed in the whole heterostructure corresponding to the typical unintentional n-doping experimentally observed. For low Al concentrations in the barrier (fig. 5.4(a)) and without E_F pinning, no quantum well is formed at the heterojunction and no electron confinement results. If the Fermi level

position, as derived from the experiments described in subsection 6.4.1, is introduced as a surface boundary condition into the calculation, then a triangular quantum well is formed on the GaN side, which crosses the Fermi level energy and therefore electrons are strongly confined in a quasi-2D electron gas. The calculated electron sheet concentration in the potential well for the quite low Al content $x = 0.1$ is $n_S = 1.9 \times 10^{12}$ cm^{-2}. In the case of an AlN barrier (fig. 5.4(c)) the effect of introducing the Fermi level pinning at the surface is less dramatic, however with an increase in the 2DEG concentration from 1.1 to 1.5×10^{13} cm^{-2} corresponds anyhow to a 27% more charge in the 2DEG channel. The n_S increase of one order of magnitude by increasing the Al content is due to the increase of the spontaneous polarization charge at the interface (subsection 5.2.1, 5.2.3).

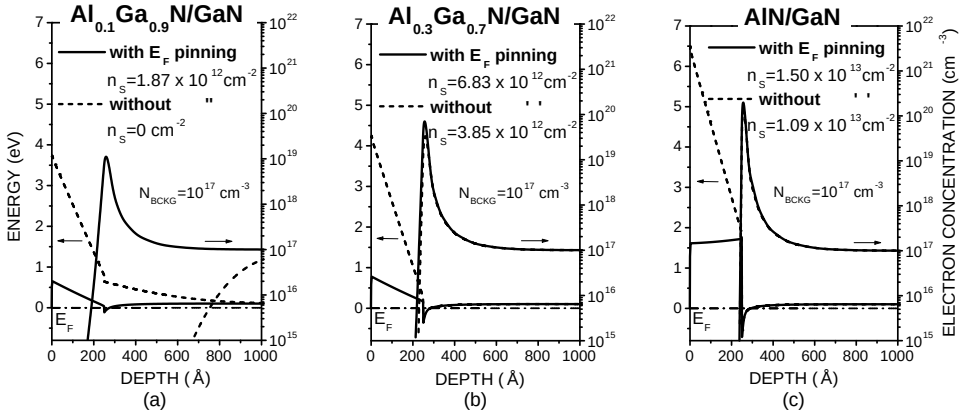

Figure 5.4: Self-consistent Schrödinger-Poisson calculation for $\mathrm{Al_XGa_{1-X}N}$/GaN 2DEG heterostructures, (a) x=0.1, (b) x=0.3 pseudomorphic layers and (c) x=1. The conduction band edge profi le is shown (left scale) together with the electron concentration (right scale) along the structure. Two cases are shown in each panel: without (red line) and with surface Fermi level pinning (blue line). Always a homogeneous background doping of 10^{17} cm^{-3} is considered in the whole structure.

These calculations together with the experimental results on the electronic properties of AlGaN surfaces (subsection 6.4.1) give some insight in the origin of the 2DEG in unintentionally doped AlGaN/GaN heterostructures: we believe that an important role is played by electrically active surface states of the AlGaN, which are responsible for the surface Fermi level pinning discussed in subsection 6.4.1 and which have also been postulated by Smorchkova *et al.* [162]. In absence of electronic gap states, the conduction band edge in the barrier due to the strong polarization field hits the surface at $E_C - E_F = 3.7$ eV, 4.2 eV and 6.4 eV for $x = 0.1$, 0.3 and 1, respectively. The lower value found in the experiment corresponds to a lower electric field in the barrier and therefore to a positive charge at the surface which partially screens the negative

polarization charge. This positive charge in donor-like surface states arises from a transfer of electrons into the structure and therefore into the 2DEG (fig. 5.5). In the Schrödinger-Poisson model this effect is described by the surface boundary condition and provides the high electron concentration in the 2DEG channel.

A continuous trend is observed in going from low to high x values, namely the surface potential gets higher, but also the conduction band offset increases and therefore the quantum well shifts more and more below E_F. A consequence is the 2DEG concentration becoming less sensitive to surface conditions by increasing the Al concentration. On the other hand, at low barrier concentrations ($x \leq 0.3$) a dramatic effect is expected if the surface electron properties change (different energy position of the surface Fermi level): large instability of the 2DEG in AlGaN/GaN heterostructures (the active layer of nitride based High Electron Mobility Transistors) are expected in absence of modulation doping, that have actually been observed by several groups.

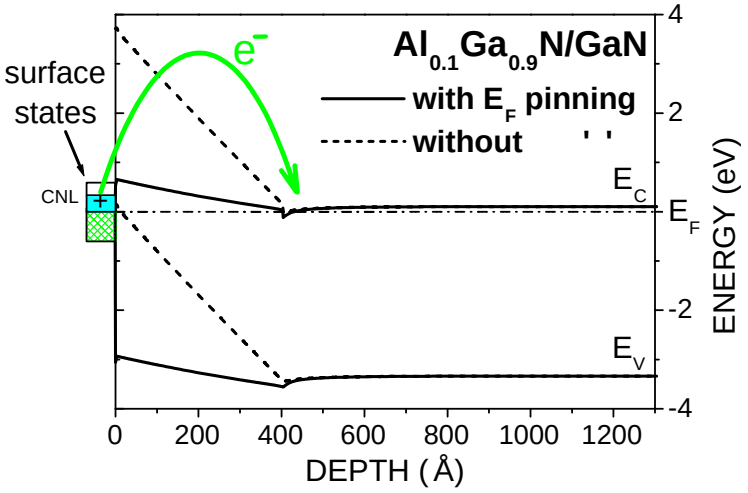

Figure 5.5: Band scheme simulation of an $\mathrm{Al_{0.1}Ga_{0.9}N/GaN}$ heterostructure with and without Fermi level pinning at the surface. The positive charge at the surface corresponds to electrons, which are transferred from surface states into the 2DEG. In the Schrödinger-Poisson model this effect is described by the surface boundary condition and provides the high electron concentration in the 2DEG channel. CNL means charge neutrality level (also crossover point or branching point E_B) where the gap states have equal valence and conduction character [23].

5.2.3 AlGaN Barrier Thickness and Al Alloy Composition

With the aim of optimizing AlGaN/GaN heterostructures, the variation of two structure parameters has been considered in the following: the Al concentration, x, and the thickness, d, of the barrier. The electron sheet concentration in the 2DEG region, n_S, has been calculated by integrating the square modulus of the electron wave functions in the quantum well region.

The Al composition and the thickness of the $\mathrm{Al_XGa_{1-X}N}$ barrier varies from the value $x = 0.1, 0.2, 0.3$ to 0.4 and $d_{\mathrm{AlGaN}} = 20,\ 40$ to 60 nm, respectively. Strained AlGaN layer on GaN are assumed in the band scheme calculation. The 60 nm thick barrier has been considered up to the Al concentration of 20%, because the critical thickness of strained AlGaN on GaN for higher x decreases. Figure 5.6 shows the conduction band minimum profile (top) and the electron concentration profile (bottom) of a AlGaN/GaN heterostructure. A background electron concentration of 1×10^{17} cm^{-3} is assumed. The Fermi level pinning at the surface measured by XPS (subsection 6.4.1) is introduced as a boundary condition into the calculation. Higher electron concentrations n_S are obtained by increasing the Al composition, due to the increase of the polarization charge at the interface. The effect of the barrier thickness on n_S is less significant. The n_S slightly increases with increasing barrier thickness, because the conduction band minimum of the triangular quantum well slides down through the Fermi level and more electrons are confined in the triangular quantum well.

Further the band scheme simulation of GaN cap(5 nm)/AlGaN/GaN heterostructure is presented. The simulated structure is the same as previously discussed, moreover, there is an additional 5 nm thick GaN cap layer inserted on top of the AlGaN/GaN layers. The GaN cap layer is useful for preparing ohmic contacts in HEMT device technology. The smaller Schottky barrier on GaN layer compared to AlGaN improves the quasi-ohmic behavior of the contacts. The figure 5.7 shows the conduction band minimum profile (top) and the electron concentration profile (bottom) of a GaN/AlGaN/GaN heterostructure. The n_S increases also with increasing Al composition in the $\mathrm{Al_XGa_{1-X}N}$ barrier as for AlGaN/GaN structure without GaN cap discussed above. The influence of the barrier is also less significant. In this simulation we show the influence of the GaN cap on the calculated sheet electron concentration in 2DEG, n_S. The results are summarized in the figure 5.8. In presence of a 5 nm thick GaN cap layer on top of the AlGaN/GaN heterostructure, slightly lower n_S is obtained. The surface donor-like states of GaN provide less electrons into the 2DEG than those of AlGaN. Additionally, the high negative polarization charge present at the top of the AlGaN barrier is not partially compensated by the positive charge of the surface states as for AlGaN/GaN layer structure.

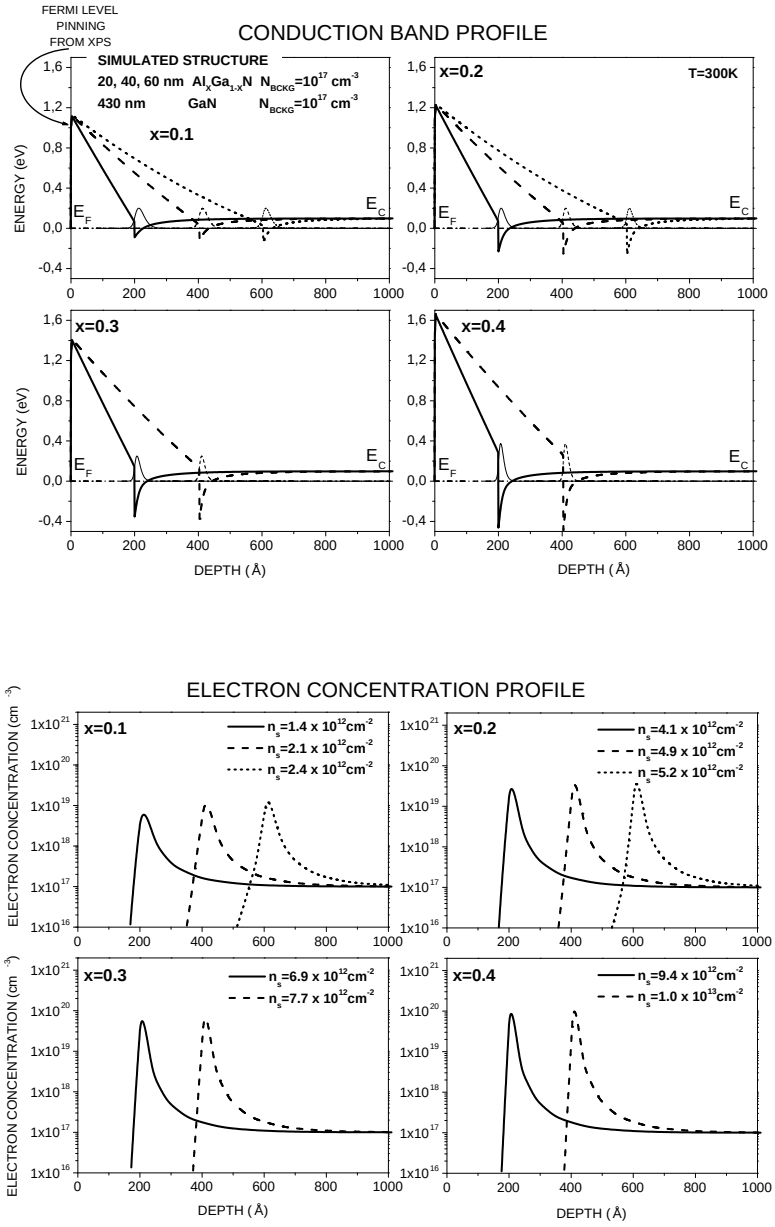

Figure 5.6: Band scheme simulation of an $\mathrm{Al_XGa_{1-X}N/GaN}$ heterostructure with various Al concentrations (x=0.1, 0.2, 0.3, 0.4) and barrier thickness ($d = 20,\ 40,\ 60$ nm). The conduction band minimum E_C with the probability function $|\psi_1|^2$ of the first discrete energy state in the triangular quantum well (top) and electron concentration profile (bottom) are displayed. The concentration in 2DEG is shown in the legend for all calculations.

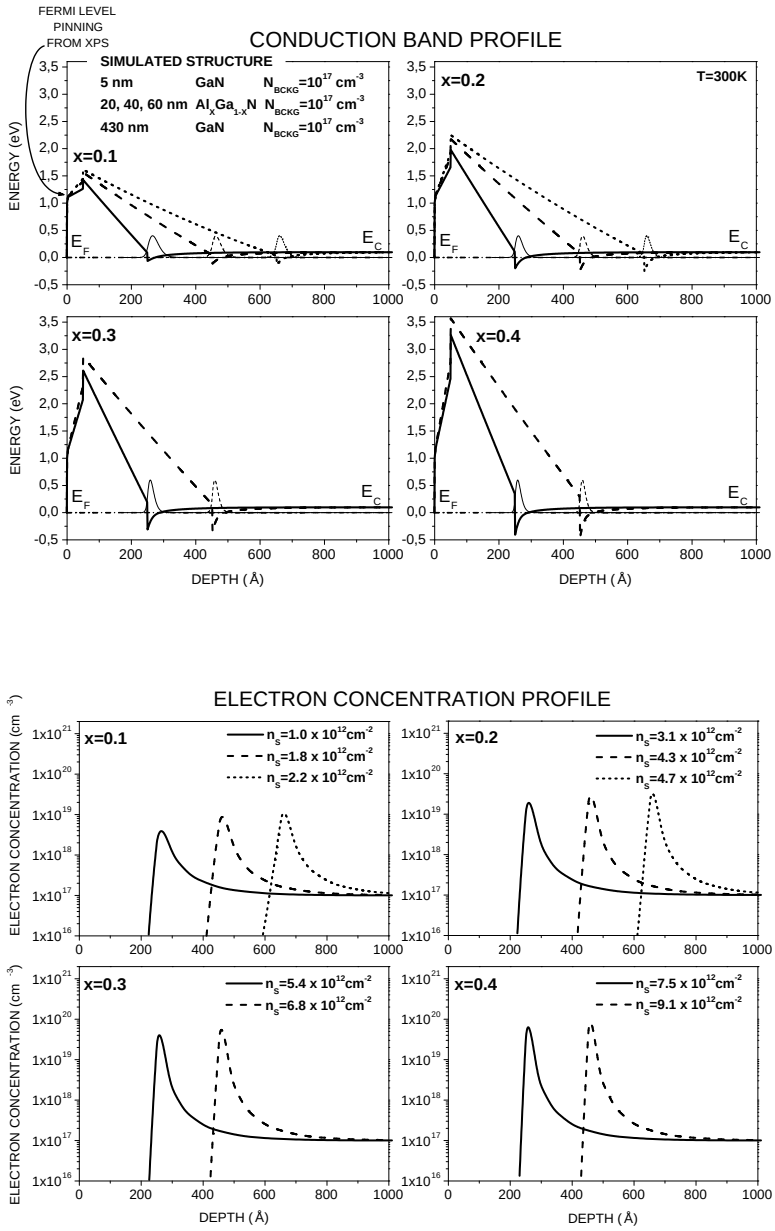

Figure 5.7: Band scheme simulation of a $\mathrm{GaNcap/Al_XGa_{1-X}N/GaN}$ heterostructure with various Al concentrations (x=0.1, 0.2, 0.3, 0.4) and barrier thickness ($d = 20$, 40, 60 nm). The conduction band minimum E_C with the probability function $|\psi_1|^2$ of the first discrete energy state in the triangular quantum well (top) and electron concentration profile (bottom) are displayed. For all calculations the concentration in 2DEG is shown in the legend.

For HEMT high power applications the conductivity σ (eq. (5.17)) of the channel should be as high as possible for the purpose of reaching high current densities. In order to satisfy this demand the electron concentration and the mobility of the 2DEG have to be high in agreement with the conductivity definition:

$$\sigma = e \cdot \mu \cdot n, \tag{5.17}$$

where e is the elementary charge, μ electron mobility and n the electron concentration. According to the simulations, to reach high sheet electron concentration in the 2DEG, it is necessary to grow AlGaN layers with high Al content, x between 0.25-0.40. On other hand, higher values of x reduce the critical thickness of the barrier layer and relaxation may occur. A critical AlGaN thickness of about 70 nm has been estimated for $x = 0.22$ from Hall effect experiments [163]. Additionally, high Al composition causes high polarization charge at the interface and consequently lower mobility due to the interface scattering. Smorchkova $et\ al.$ [162] have grown $\mathrm{Al_{0.09}Ga_{0.91}N/GaN}$ heterostructures with two-dimensional electron gas density of $2.23 \times 10^{12}\ \mathrm{cm^{-2}}$ and electron mobility of 51700 cm^2/Vs at the temperature of 13 K.

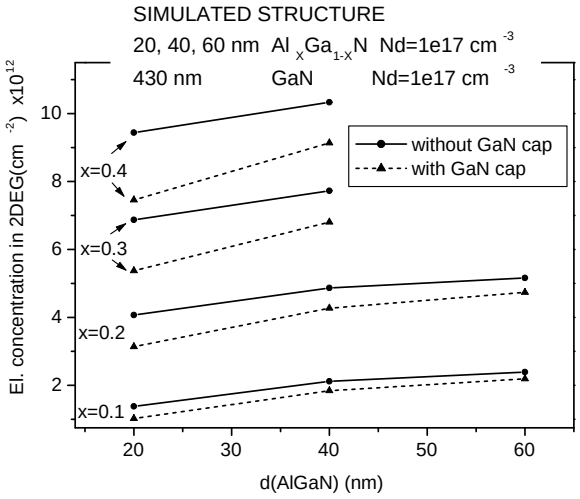

Figure 5.8: $\mathrm{n_{2DEG}}$ comparison between $\mathrm{Al_XGa_{1-X}N/GaN}$ heterostructure with and without GaN cap for various Al composition (x=0.1, 0.2, 0.3, 0.4) and barrier thickness ($d = 20, 40, 60$ nm) calculated using band scheme simulation.

5.2.4 Doped AlGaN/GaN Heterostructures

The modulation doped HEMT structures based on GaAs material system exhibit in average one order lower electron concentrations than III-nitride layers. The nitrides 2DEG

structures do not need to be even doped. Here we present the band scheme simulation using self-consistent Schrödinger-Poisson equation calculation of $Al_{0.18}Ga_{0.82}N$/GaN 2DEG heterostructure for various doping densities in the barrier: 2×10^{18}, 5×10^{18}, 1×10^{19} cm^{-3}. Thickness of 21 nm for the whole barrier is assumed. To increase the mobility of electrons in the 2DEG channel through minimizing the scattering on ionized donors at the interface, a undoped AlGaN layer with the thickness of 5 nm is inserted between the doped AlGaN and undoped GaN. For undoped layers a background concentration of 10^{17} cm^{-3} is assumed. Fermi level pinning at the surface measured by XPS of as grown $Al_XGa_{1-X}N$ layers (subsection 6.4.1) is introduced as a boundary condition. The result of the simulation is shown in the figure 5.9. The calculated conduction band minimum and the free electron concentration of the three structures are displayed. Higher doping causes the sliding of the conduction band minimum towards to Fermi level energy and higher electron densities in the 2DEG. At high doping densities of 10^{19} cm^{-3} a parallel channel starts to form in the AlGaN barrier. The increase of free electron concentration in the barrier region is clearly seen in the figure 5.9. If the barrier would be thicker, a parallel channel with free electron concentration equal the doping will be created. The higher conductivity in the barrier would lead to higher gate leakage current, higher pinch-off voltage and worse high frequency properties of HEMT devices.

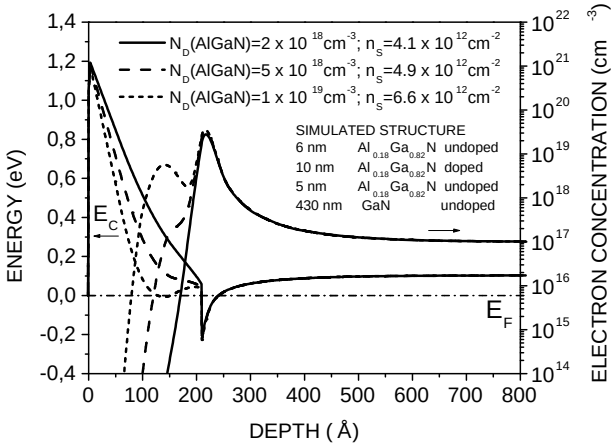

Figure 5.9: Band scheme simulation of a modulation doped $Al_{0.18}Ga_{0.82}N/GaN$ heterostructure with three different doping densities: 2×10^{18}, 5×10^{18}, 1×10^{19} cm^{-3}. The conduction band minimum profile (left scale) and free electron concentration profile (right scale) are displayed. A background electron concentration of 10^{17} cm^{-3} is assumed in undoped layers. The concentration in 2DEG is shown in the legend for all calculations.

Chapter 6

Experimental Results

6.1 Epitaxial Growth of III-N Layers

6.1.1 Growth Rate Determination

In the growth of GaN three regions are usually defined. The growth diagram shown in fig. 6.1 depicts the Ga flux conditions and substrate temperatures that define these growth regimes at a constant N flux corresponding to a growth rate of 15.2 nm/min under Nitrogen limited growth conditions. As reported in ref. [164] films grown with streaky RHEED patterns that exhibit Ga droplets characterize the "**Ga-droplet**" regime. These films are observed at low temperatures and high Ga fluxes (Ga/N$\gg$1). Excess Ga accumulates on the surface during growth in the form of large droplets $\sim 5-20$ μm in diameter and the growth rate is determined by the N flux. The surface of GaN films presents spiral hillocks usually associated with screw dislocations [165].

Films grown with streaky RHEED patterns that do not have Ga droplets are observed at higher temperatures and intermediate Ga fluxes (Ga/N$\geq$1). This phase is usually referred as "**intermediate**" regime. In this case excess Ga forms a steady-state, incomplete, monolayer or bilayer of metallic Ga on the surface without the formation of Ga droplets but also with a growth rate determined by the N flux.

Finally the "**N-stable**" regime, characterized by films having spotty RHEED patterns, is observed at low Ga fluxes for a wide range of substrate temperatures (Ga/N$<$1). Films grown in the N-stable regime are Ga deficient, with growth rate limited by the available Ga flux. The growth rate is always determined by the lower of both fluxes (N or Ga) [166].

A systematic growth calibration was necessary to determine the optimum parameters for different growth processes. All samples reported in this section were grown on 6H n-SiC (0001) Si-face substrates, supplied by CREE Research Inc. After the usual cleaning with acetone and propanol the substrates were etched for 10 min in HF 10% and ultrasonics to remove the oxide passivation layer, dipped in deionized water and rapidly

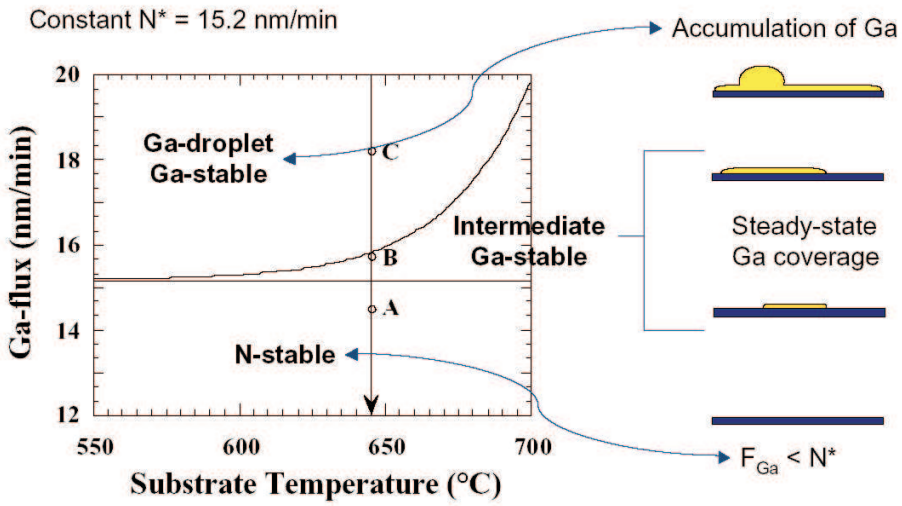

Figure 6.1: Growth regime diagram depending on the Ga-flux and substrate temperature at constant N-flux of 15.2 sccm taken from Ref. [164].

built in vacuum on the sample holder.

The first step was the growth of a 100 nm thick AlN buffer layer, necessary to reduce the mismatch between SiC and GaN, with the following parameters: $\mathrm{BEP_{Al}} = 1.4 \times 10^{-7}$ mbar , N flux $= 1$ sccm, RF power $= 350$ W and $\mathrm{T_{SUB}} = 770°\mathrm{C}$.

Then a series of 7 samples was grown increasing the Ga flux from 0.5×10^{-7} mbar to 6.0×10^{-7} mbar (tab. 6.1). A Nitrogen flux of 1 sccm (standard cubic centimeter) and a RF power of 450 W were chosen for the N-supply. The substrate temperature was $763°\mathrm{C}$ and the growth time 1 hour and 35 minutes.

Sample	$\mathrm{BEP_{Ga}}$ (mbar)
ED136	0.5×10^{-7}
ED134	1.0×10^{-7}
ED135	1.5×10^{-7}
ED131	2.5×10^{-7}
ED132	4.0×10^{-7}
ED130	5.0×10^{-7}
ED133	6.0×10^{-7}

Table 6.1: Samples grown for the growth rate determination with different Ga fluxes at a constant N flux and substrate temperature. The growth parameters of all samples are listed in appendix B.

In order to determine the GaN growth rate we measured the thickness of the samples with a thickness profiler (Dektak) taking the side of the samples covered by the

sample-holder (where no growth occurs) as a reference for zero. We found a rate of about 5.1 nm/min in the Ga-droplet region, as shown in fig. 6.2. As can be clearly seen the "intermediate" region is obtained for Ga fluxes around 2×10^{-7} mbar.

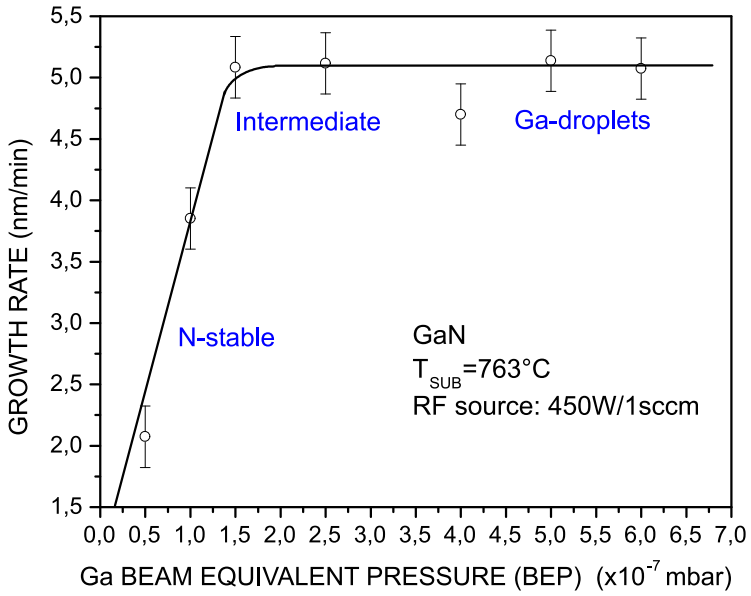

Figure 6.2: GaN growth rate for different Gallium beam equivalent pressures. The N flux was 1 sccm and the RF power 450 W.

A preliminary surface analysis was performed with an optical microscope (fig. 6.3). In the sample grown under Ga-intermediate conditions (ED131) circular structures can be seen: we associated them to the first stage of Ga droplet formation. Similar structures are also recognized in a sample grown under more Ga-rich conditions (ED132), but the magnified picture clearly evidences the formation of Ga droplets in this case.

All the samples were analyzed by AFM to get information about the surface quality. In figure 6.4 four samples grown with different Ga fluxes are compared.

The surface morphology of GaN layers grown under N-rich conditions (ED134) is quite rough with deep pits and has a quite high root mean square (RMS) roughness. This can be explained by assuming that in N-rich conditions big regions of the surface are terminated with N atoms, as proposed by Ambacher [10]. This atoms are then bonded on the underlying Ga atoms just with one bond, the remaining three dangling bonds per atom significantly reduce the Ga adatom surface mobility. The reason for this is the high number of Ga-N bonds which must be partially broken and reformed in order for surface diffusion to occur. Under Ga-rich conditions the layers show, between the Ga droplets, a drastic improvement of their structural quality and a lower surface roughness. In this case, in fact, the adatoms have a larger diffusion length and so they can move relatively freely until the incorporation at a step edge occurs.

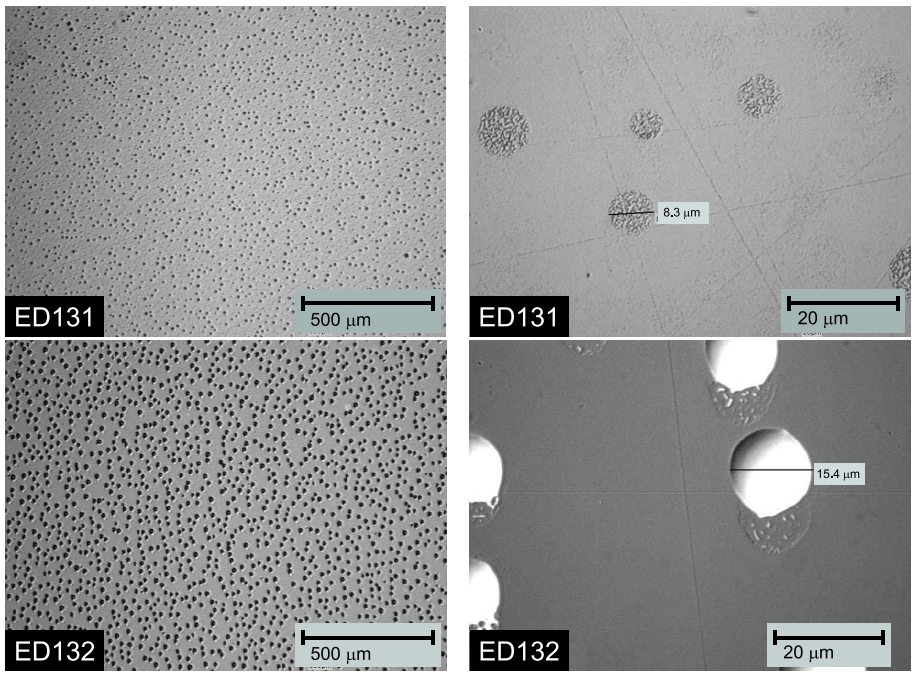

Figure 6.3: Optical microscope picture of ED131 and ED132 samples captured with two different magnifications. The circular "rougher" structures in ED131 are supposed to be the first stage for the formation of droplets. ED132 grown with a higher Ga flux shows formation of real droplets.

The lowest surface roughness was observed in ED132: the RMS is only 0.7 nm on a scan area of 5×5 μm^2 and is comparable with the best values reported in the literature [167]. The hexagonal spirals observed are associated with threading screw dislocations reaching the surface [165]. On the other hand the large Ga droplets present on the surface are a problem for the realization of electronic devices. Ga fluxes between 2 and 2.5×10^{-7} mbar seem to represent the best compromise. The number of dislocations is lower than in the other two regimes. Dislocations are defects of the crystal structure which introduce trap-energy levels between the minimum of the conduction band and the maximum of the valence band of GaN. These traps can collect electrons and reduce the sheet charge concentration of the 2DEG at the interface AlGaN/GaN and so they reduce the current density between source and drain of a HEMT electronic device. In the N-stable region the pits visible on the surface of GaN are associated with threading dislocations with both edge and screw character [165], while in the Ga-rich region spirals are usually connected to pure screw dislocations which seem to be more problematic because they increase the reverse bias leakage current as measured by scanning current-voltage microscopy (SIVM) study of GaN films grown by nitrogen plasma assisted MBE on GaN templates prepared by hydride vapor phase epitaxy [168].

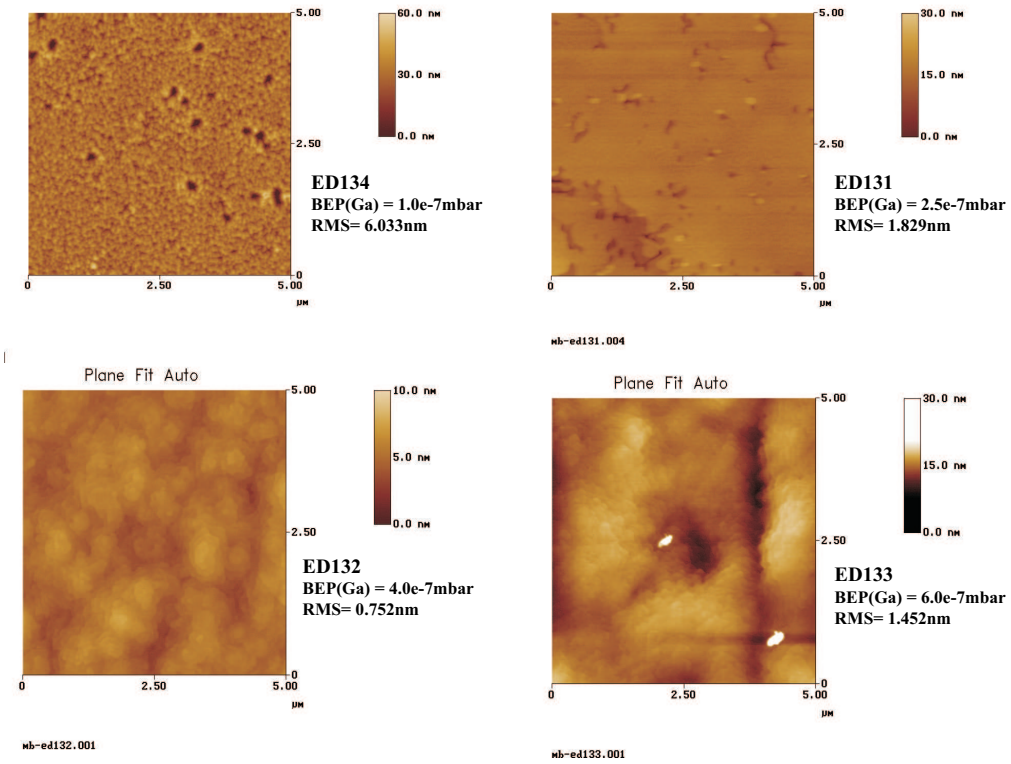

Figure 6.4: Comparison of the surface morphologies of GaN layers grown with different Ga fluxes.

6.1.2 Determination of $Al_XGa_{1-X}N$ Alloy Composition

A series of 6 samples was grown in order to determine the Al concentration *x* in $Al_XGa_{1-X}N$ layers grown with different Al fluxes. All layers were 100-150 nm thick and were grown on Si(111) substrates (only ED137 was grown on SiC). The beam equivalent pressure (BEP) of the metal flux (Ga+Al) was chosen to be 2.5×10^{-7}mbar, the same metal component as for the best GaN sample (ED131). The samples reported in the table 6.2 were grown either directly on the substrate (ED137, ED138, ED150) or with a 100 nm thick AlN buffer (ED151, ED153, ED155). The substrate temperature was 763°C, the Nitrogen flux 1 sccm and the RF power 450 W. The composition of the $Al_XGa_{1-X}N$ was determined by Rutherford Back Scattering (RBS). The measurement error assigned to the Al concentration is $\pm 8\%$.

The linear fit reported in fig. 6.5 was thereafter used to grow $Al_XGa_{1-X}N$ layers with the desired Al concentration.

Sample	BEP(Al)/BEP(Ga) ($\times 10^{-7}$mbar)	Al concentration in the $Al_XGa_{1-X}N$
ED137	$0.45/2.05$	30%
ED138	$0.35/2.15$	23%
ED150	$0.25/2.25$	12%
ED151	$0.5/2.0$	40%
ED153	$0.2/2.3$	11%
ED155	$0.8/1.7$	58%

Table 6.2: Fluxes used for the growth of $Al_XGa_{1-X}N$ samples and Aluminium concentration resulting from RBS measurements.

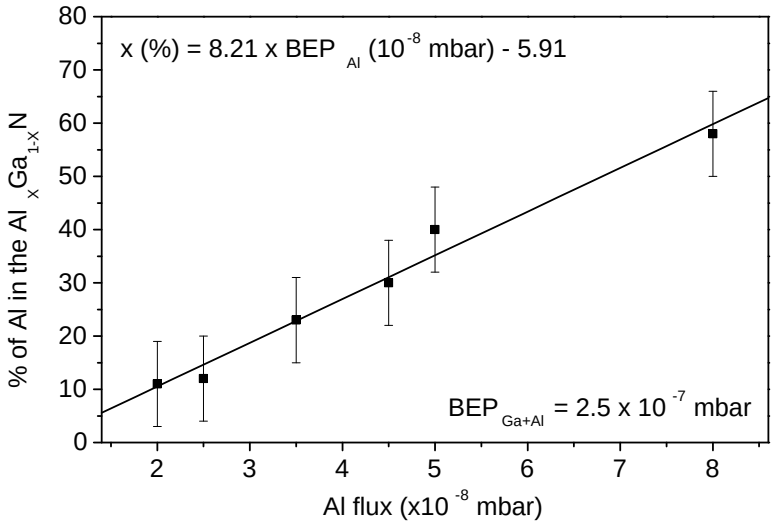

Figure 6.5: Al concentration in $Al_XGa_{1-X}N$ grown with different Al fluxes measured by RBS. The linear fit was thereafter used to grow layers with the desired composition.

6.2 Growth Optimization of Nitrides on SiC Substrate

6.2.1 Substrate Preparation

For the growth of the 2DEG structures insulating 6H-SiC (0001) Si-face substrates from Sterling Semiconductor Inc. were chosen. They show a much flatter surface than the substrates from Cree Research Inc., which have lot of scratches on the surface. This is extremely important for the further epitaxial growth, because surface imperfections or impurities can be nucleation centers for dislocations (fig. 6.6).

Insulating SiC substrates were not used for the growth optimization due to their extremely high cost. Their high resistivity ($> 10^5$ Ω·cm) allows straightforward Hall effect characterization, which instead is a problem for layers grown on the CREE conductive substrates - the presence of a parallel conduction channel through the substrate makes quite difficult the interpretation of Hall data. Anyway, it should be pointed out here, that the crystallographic quality of these insulating substrates is still not good enough to ensure optimum epitaxy, as was verified by XRD. The substrates are sold as "research grade" product by the delivering company.

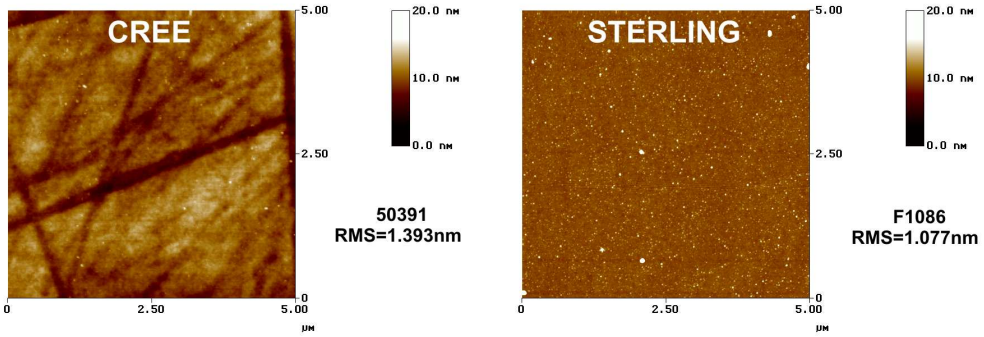

Figure 6.6: Surface morphology of Cree substrate (left) and Sterling substrate (right) on 5×5 μm^2 scanning area measured by AFM. The substrate from Cree Research Inc. perform rough surface with many scratches, the substrates from Sterling Semiconductor Inc. are flatter.

The substrates can not be used for the growth "as received" (as suggested by the company), because oxide is present at the surface, as verified by AES and it is not easily removed by the standard cleaning procedure (wet chemical cleaning and anneling at ~ 700°C in UHV). As reported in literature the oxide can be more efficiently removed by annealing the sample at temperature above 900°C [169]. Unfortunately the maximum temperature that could be reached with our sample holder was 800°C, and therefore an alternative procedure was adopted. The samples were first degreased with acetone (3 min) and propanol (3 min) then cleaned in ultrasonics with a solution of HF 50% (2 min) and rapidly put into the vacuum system. Annealing for at least 10 hours at 550°C follows.

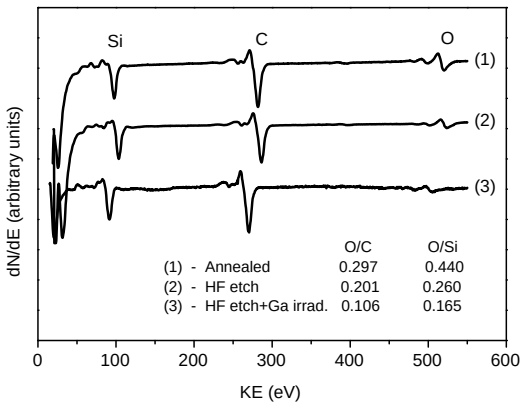

Figure 6.7: Comparison between Auger spectra of SiC substrates cleaned in different ways (see text). The ratio between the peaks of silicon and oxygen and between carbon and oxygen is also shown.

The temperature was then increased to 770°C and the samples were exposed to a Ga flux. At this temperature the reaction product GaO_2, and excess Ga evaporate, leaving a clean SiC surface [167, 170]. Different Ga-exposure times were considered and the amount of O on the surface was checked by AES. The optimum procedure was found to be a cycle, repeated three times, as follows: 3 min Ga irradiation (BEP$= 3 \times 10^{-7}$ mbar, $T_{SUB} = 770°C$), 10 min annealing at 790°C.

In fig. 6.7 the Auger spectra of three samples, one cleaned with the described procedure (3), one etched in HF and annealed ($550°C$ for 10 h, $790°C$ for 15 min) (2), one only annealed ($550°C$ for 10 h, $790°C$ for 15 min) (1) are compared. The signal of oxygen, though not completely suppressed, was strongly reduced in the sample etched and exposed to Ga. A LEED analysis (fig. 6.8) confirmed a quite clean surface showing a (1×1) reconstruction with sharp spots.

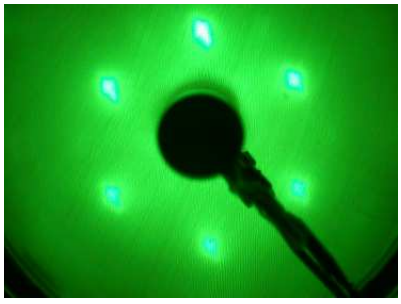

Figure 6.8: LEED image of a SiC substrate after the cleaning procedure.

6.2.2 Nucleation and Buffer Layer Growth

The first step towards the growth of a 2DEG structure on insulating SiC (Sterling) substrate was the optimization of each single layer composing it. We started from the AlN nucleation layer (100 nm of thickness) . We have grown two samples with the same parameters ($T_{SUB} = 770°C$, RF power=350 W, N flux=1 sccm [157]) but different Al fluxes (1.4×10^{-7} mbar for ED191 and 1.0×10^{-7} mbar for ED194). A first inspection was performed at the optical microscope as shown in fig. 6.9: many Al droplets can be seen on ED191, indicating a too high metal flux, while on ED194 only few of them are present and only in some area of the sample. AFM also confirmed this trend (fig. 6.10): the RMS roughness, though low in both samples, is still lower in ED194. The parameters used for ED194 were thereafter used for the growth of the AlN buffer.

The next step was the optimization of the GaN growth. A GaN layer ($1\ \mu$m of thickness) was grown on the optimized AlN buffer described before, and two different Ga fluxes were considered (1.9×10^{-7} mbar for ED195, 2.2×10^{-7} mbar for ED196), by referring to the calibration performed on n-SiC (section 6.1.1). The other parameters were chosen to be: $T_{SUB} = 763°C$, RF power=450 W, N flux=1 sccm [157]. The surface of ED195, with no droplets and pits deeper than 50 nm (fig. 6.11), indicates Ga poor growth conditions

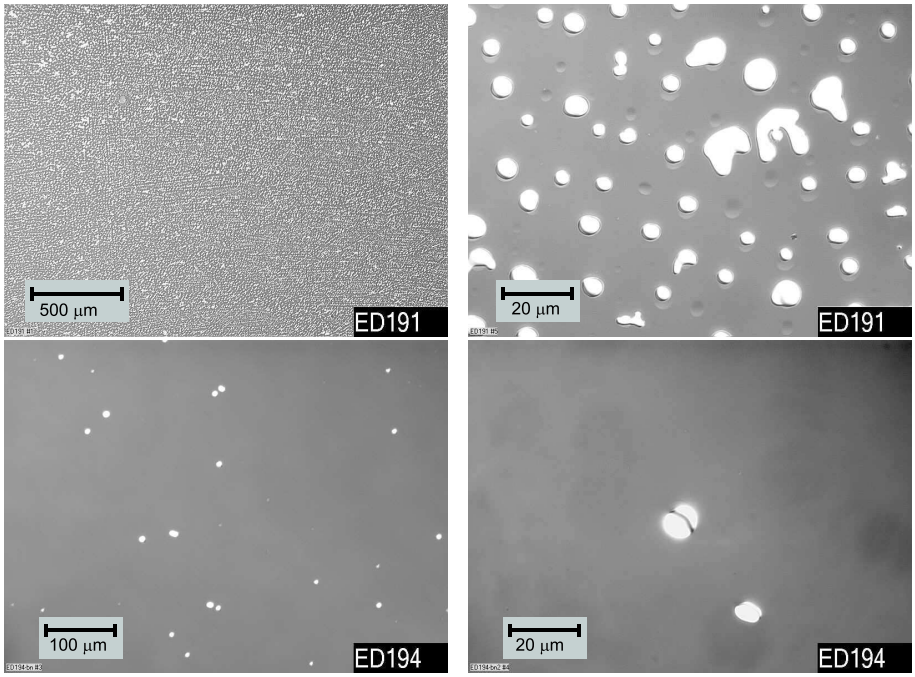

Figure 6.9: Optical microscope pictures of AlN nucleation layers grown on i-SiC substrate, ED191 and ED194, obtained with two different magnifi cations. Many Al droplets can be recognized on ED191, while few of them are present on ED194.

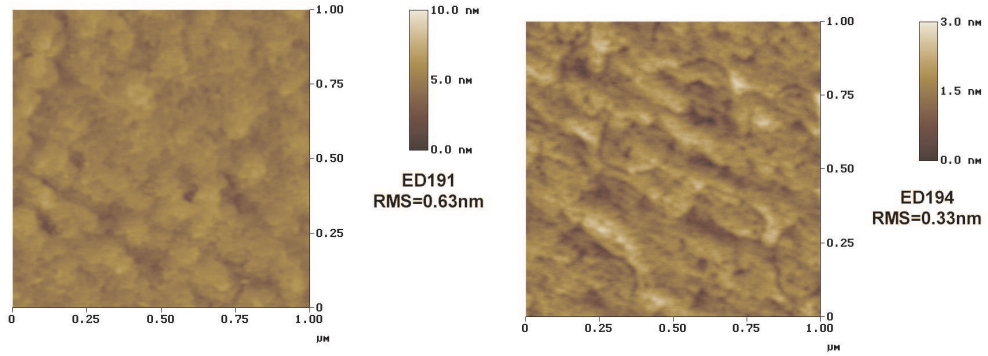

Figure 6.10: $1 \times 1\ \mu m^2$ AFM picture of ED191 and ED194. Notice that the color scales are different.

(Ga/N flux ≤ 1) [165]. On ED196 instead many droplets were observed on the surface, indicating Ga rich conditions (Ga/N flux > 1). They were effectively removed by etching the sample in HCl for 4 min prior to perform the AFM characterization. This sample (fig. 6.11) resulted to be much flatter than ED195, with terraces at the surface and only with some small pit interspersed. These pits can be correlated to the presence of threading dislocations [165] and by counting them is possible to have an estimate of their number: $\sim 2 \times 10^9$ cm^{-2} for the sample ED196.

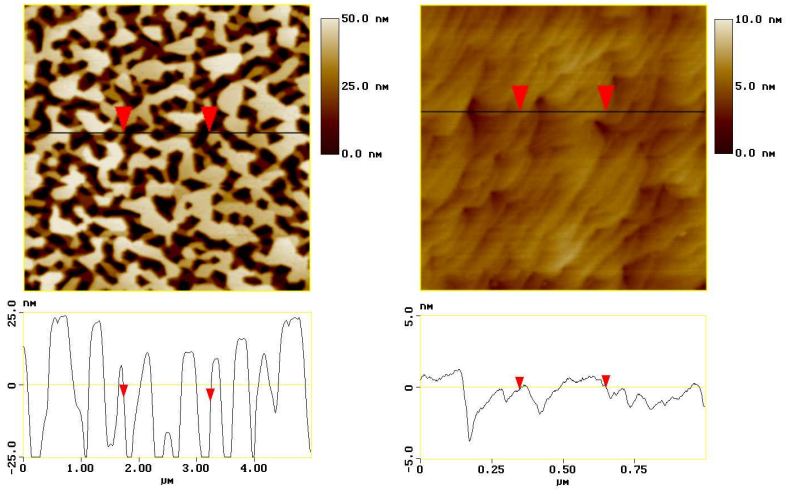

Figure 6.11: AFM picture and cross section of GaN layers grown on i-SiC substrate, ED195 ($5 \times 5\ \mu m^2$, RMS=20 nm) and ED196 ($1 \times 1\ \mu m^2$, RMS=0.8 nm).

6.2.3 Structural Properties of GaN grown on n- and i-SiC Substrate

In order to compare the quality of GaN layers grown on n-SiC (Cree) and on insulating SiC (Sterling) substrates two samples were analyzed by X-ray diffraction, showing a similar surface morphology measured by AFM and optical microscope. The structure of the two measured samples ED132 and ED196, together with the Full Width at Half Maximum (FWHM) of the observed peaks is reported in table 6.3. For ED132 the observed FWHM

Sample	Structure	Substrate	FWHM $\omega - 2\theta$ scan	FWHM ω scan (rocking curve)
ED132	100 nm AlN / 500 nm GaN	n-SiC Cree	309 arcsec	322 arcsec
ED196	100 nm AlN / 1 μm GaN	i-SiC Sterling	527 arcsec	1268 arcsec

Table 6.3: FWHM of the ω and $\omega - 2\theta$ scans of GaN layers grown on different SiC substrates measured by XRD.

of the ω scan is quite good compared to data of GaN layers grown on 6H n-SiC by MBE reported in the literature [165, 167], while the $\omega - 2\theta$ scan is quite bad; anyway for this sample the buffer was not optimized and so higher values were expected. For ED196 the growth of both the AlN buffer and of the GaN was optimized by checking with AFM and therefore a better result was expected, considering also the very low roughness of the substrate: but as can be seen from fig. 6.12 the FWHM of the GaN peak is much larger. On the other hand while the peak of SiC is very narrow on ED132 (FWHM$= 54$ arcsec), it is quite broad on ED196 (FWHM$= 810$ arcsec). This strange result convinced us to perform a XRD also on an insulating SiC substrate alone (without MBE layers grown on it). The

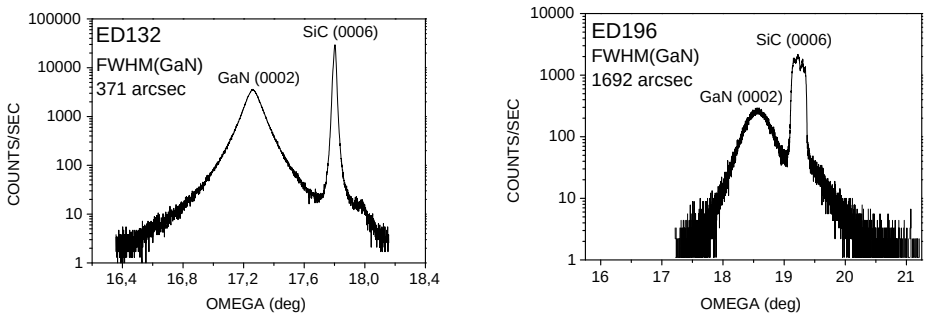

Figure 6.12: XRD rocking curve (ω-scan with wide open detector) of the ED132 and ED196. The peak of SiC is very wide (FWHM$= 810$ arcsec) for the Sterling substrate (ED196), while is reasonably narrow (FWHM$= 54$ arcsec) for the Cree substrate (ED132).

measurement confirmed that even though the surface is very flat, the bulk crystal quality of the substrate is quite bad, as can be seen in fig. 6.13.

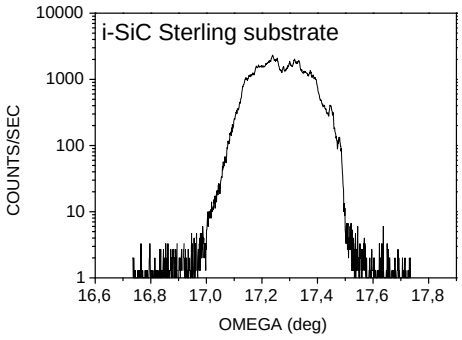

Figure 6.13: Rocking curve of an i-SiC Sterling sample, the same used as a substrate for ED196. The FWHM of the ω-scan was estimated to be ~ 650 arcsec.

6.2.4 Impurities in MBE Growth

In order to check the cleanliness of our MBE growth process an ex-situ Secondary Ions Mass Spectroscopy (SIMS) analysis was performed. A quantitative analysis of the impurities incorporated in the sample during growth is in principle difficult because of the lack of standards. To overcome this problem a MOCVD template (1 μm thick GaN layer grown by MOCVD on a SiC wafer) was used as a substrate[1]. The grown layer structure is displayed in figure 6.14. The MOCVD GaN layer is supposed to have a low concentration of impurities and therefore is a good reference to compare with the MBE layer grown on top.

The SIMS results are shown in fig. 6.15 (top). The abrupt steps in the signals of the GaN (83) and the AlN (41) at the AlN/AlGaN/GaN heterojunctions indicate sharp interfaces and less interdiffusion. The signal of AlN obviously decreases in passing from AlN to AlGaN and reaches the background level into the GaN layer; approaching the substrate the AlN signal increases again due to the interface GaN (MOCVD)/AlGaN graded (MOCVD)/SiC and remains high because AlN has the same atomic mass of some SiC isotope. The GaN signal remains constant at the GaN (MBE)/GaN (MOCVD) heterojunction, indicating a good interface. The signal of Oxygen is the same in MBE and MOCVD GaN layers, demonstrating that both process are run under the same "clean" conditions. Comparisons between the amount of oxygen into AlN, AlGaN, and GaN are not possible because the matrixes are different. In fact oxy-

[1]The MOCVD template was grown by Stacia Keller, University of California Santa Barbara, USA.

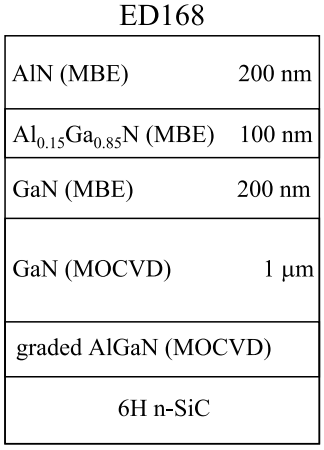

Figure 6.14: MBE layer structure grown on a MOCVD template (ED168) used for SIMS measurement. Detailed growth parameters are listed in the appendix B.

gen forms, in these matrixes, different bounds and this lead to different sputtering yields. The signal of carbon (CN) slightly decreases from the substrate to the MBE layers; this behavior is not clear. From fig. 6.15 (bottom) is possible to see that the signals of other possible impurities, such as Fe, Cr and Ti are almost no detectable. Fe and Cr have the same atomic mass (54) of Al_2, therefore it is not possible to distinguish between these elements.

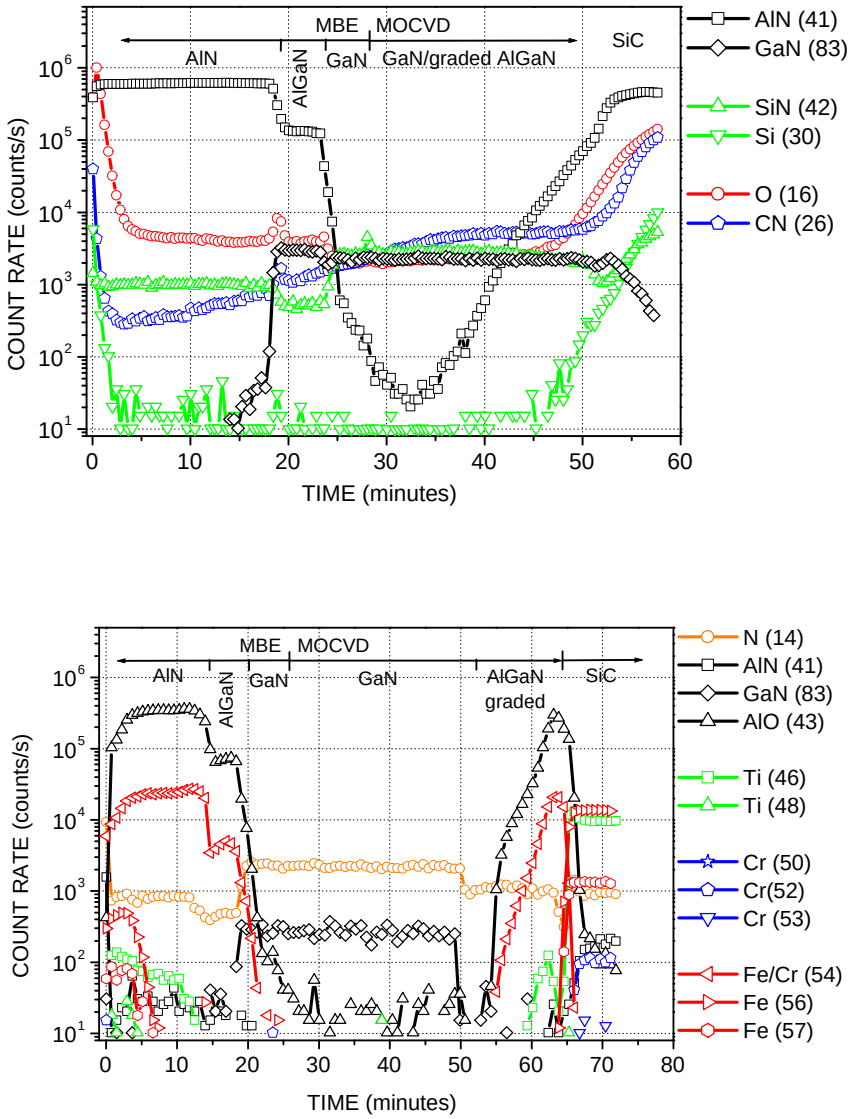

Figure 6.15: SIMS analysis of the sample ED168. The numbers reported in brackets in the legend are relative atomic masses. (top graph: Cs^+ ions, energy: 6 kV, current: 57 nA, normal incidence; bottom graph: $O_2{}^+$ ions, energy: 6 kV, current: 248 nA, normal incidence)

6.2.5 Unintentional Doping in MBE GaN Layers

In order to determine the carrier concentration of the bulk GaN grown within our system we performed a capacitance vs voltage measurement and we applied the model discussed in section 3.7. Figure 6.16 shows the layer structure of the measured sample, ED174. The last 20 nm of GaN were Si-doped to facilitate the formation of ohmic contacts. An array of

ED174

n-GaN	Si doped	20 nm
GaN		1 µm
AlN		100 nm
	6H i-SiC	

Figure 6.16: Layer structure of the grown sample characterized by C-V measurement. The growth parameters are listed in appendix B.

Schottky and ohmic contacts was realized by optical lithography, with the pattern shown in fig. 6.17. For the Schottky contact 25 nm of Ni and then 100 nm of Au were evaporated on the GaN.

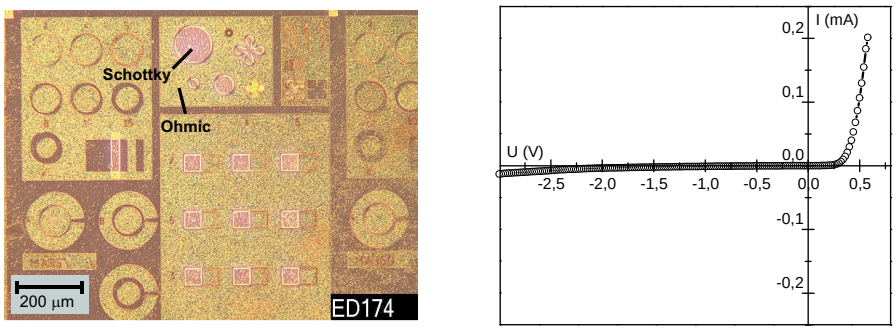

Figure 6.17: Contacts realized by optical lithography on the sample ED174 (left) and measured current-voltage characteristic of the Schottky diode (right).

For the ohmic contact the surface of the sample was first sputtered with Ar^+ ions to eliminate the oxide, then 35 nm Ti, 200 nm Al, 40 nm Ni, 50 nm Au were deposited and annealed at $900°C$ in N_2 flux for 30 seconds. The Schottky diode obtained shows the typical current vs voltage characteristic (fig. 6.17). It should be pointed out that the reverse current is quite high (100 μA at -5 V), probably because of the high number of defects (e.g. dislocations) in the MBE grown GaN.

The calculated carrier concentration profile obtained is shown in fig. 6.18. In the bulk the electron concentration is in the order of 2×10^{17} cm^{-3}, one order of magnitude higher than the best value reported in the literature for MBE GaN on SiC [167]. In the first 80 nm the electron concentration is higher, due to the 20 nm of Si-doped GaN on the top of the structure. The Si diffuses probably deeper into the structure during the growth.

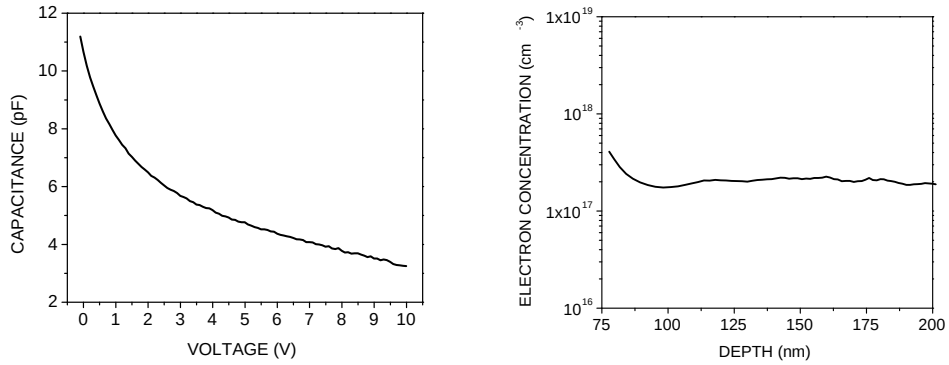

Figure 6.18: Measured capacitance-voltage characteristic of GaN grown on 6H i-SiC substrate (sample ED174) (left) and calculated carrier concentration profile (right). In the first about 80 nm the electron concentration is higher due to the Si-doping of the top of the structure, while in the bulk it is in the order of 2×10^{17} cm^{-3}.

6.2.6 Growth of a HEMT Structure

After having optimized the AlN buffer and the 1-2 μm thick GaN layer we have grown the 2DEG structure. The figure 6.19 shows the layer structure of grown samples on insulating SiC substrate with different Al composition in the $Al_XGa_{1-X}N$ barrier, ED198 and ED203. The growth parameters are listed in appendix B. In order to reduce the number of threading dislocations going through the 2DEG region a 5 nm thick AlN interlayer was inserted in the GaN. According to the studies in our group [141] this AlN interlayer seems to induce a bending of some dislocations, which can then interact with each other and annihilate. The AlN interlayer also induces a high electric field in the GaN layer on top due to the high polarization charge present at the AlN/GaN interface. Figure 6.20 shows the band

diagram of the grown layer structure calculated self-consistently using Schrödinger and Poisson equations [158]. The AlN interlayer causes a depletion of the lower part of the 300 nm thick GaN, which electrically isolates the 1.5 μm thick GaN below from the main 2DEG. The possible parallel GaN bulk channel is in this way suppressed. A parasitic effect due to the AlN interlayer is the formation of a parallel 2DEG underneath.

ED198	
GaN cap	5 nm
$Al_{0.27}Ga_{0.73}N$	25 nm
GaN	300 nm
AlN	5 nm
GaN	1.5 µm
AlN	100 nm
6H i-SiC	

ED203	
GaN cap	5 nm
AlN	23 nm
GaN	300 nm
AlN	5 nm
GaN	1.5 µm
AlN	100 nm
6H i-SiC	

Figure 6.19: Grown structure of the sample ED198 and ED203. The 2DEG is formed at the lower interface $Al_XGa_{1-X}N$/GaN. The 5 nm thick AlN interlayer was inserted to reduce the number of threading dislocations.

The Hall mobility and the sheet carrier concentration were measured on samples with van der Pauw contacts configuration in the temperature range of 4 to 300 K. The sample was cut in a 5×5 mm^2 square shape and four ohmic contacts were obtained in the corners by depositing the widely used layer system Ti/Al/Ni/Au (in our case with thicknesses 35 nm/200 nm/40 nm/50 nm) and by annealing it at 900°C for 30 s. As shown in fig. 6.21 the mobility of ED198 increases from 450 cm^2/Vs to 650 cm^2/Vs decreasing the temperature from 300 K to about 125 K, but then remains practically constant until 4 K. For the sample ED203 the mobility increases from 447 cm^2/Vs at room temperature up to 755 cm^2/Vs at 70 K and then remains also constant. This behavior corresponds to the expected one for a two dimensional electron gas [139, 171]. The maximum mobility (~ 650, 755 cm^2/Vs) is not very high [172]: this could be due to the still high number of threading dislocations and/or to the roughness of the interface, both leading to scattering of electrons. The fact that the mobility decreases with increasing electron concentration, from 1.5×10^{13} cm^{-2} (ED203) to 3.0×10^{13} cm^{-2} (ED198) (fig. 6.21), suggest that the scattering at the $Al_XGa_{1-X}N$/GaN interface plays an important role. In fact, at higher electron concentration the 2DEG is located closer to the interface. Slight increase of electron concentration with temperature is probably caused due to oxygen contamination in GaN layer.

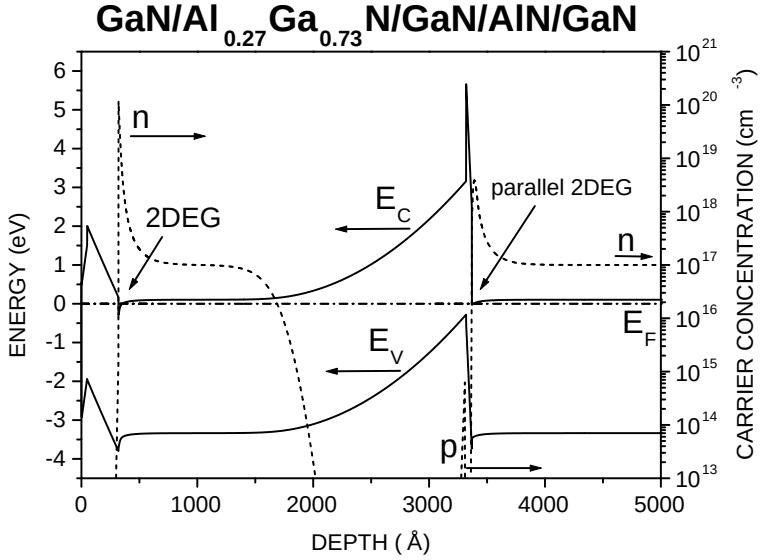

Figure 6.20: Simulation of the band scheme and carriers concentration of ($GaN/Al_{0.27}Ga_{0.73}N/GaN/AlN/GaN$) obtained from the Schrödinger-Poisson equation solver [158].

The sample with AlN barrier should lead to higher electron concentration in the 2DEG, as compared to the $Al_XGa_{1-X}N$ barrier. The Hall measurement showed opposite result. The higher electron concentration of the sample ED198 has not been understood yet.

Furthermore a qualitative analysis of the scattering is presented by comparing MBE with MOCVD grown samples. The samples have been chosen to have similar Al composition and thickness of the $Al_XGa_{1-X}N$ barrier: two of them are grown by MOCVD on sapphire in different laboratories[2], three of them are grown by MBE on conductive 6H SiC(0001) substrate in our group. The growth parameters are listed in the appendix B. The experimental results are shown in figure 6.22. The MBE samples show an increase of concentration with increasing temperature, attributed to parallel conduction either in the underlying GaN buffer layer or in the conductive SiC or both. Comparing this result to the MBE samples grown on insulating substrates (ED198, ED203, fig. 6.21) we can conclude, that the main contribution is caused by the conductive substrate. At low temperatures this contribution is freezed out and we can reasonably assume that the measured concentration is that of the 2DEG. Within the small variations in the heterostructure parameters, the 2DEG concentration compare well for all samples.

The MOCVD samples are device quality structures for HEMT application. The sum-

[2]The AlGaN/GaN heterostructures are from Cornell University (L. Eastman, CORN476) and from Stuttgart University (F. Scholz, BK2116)

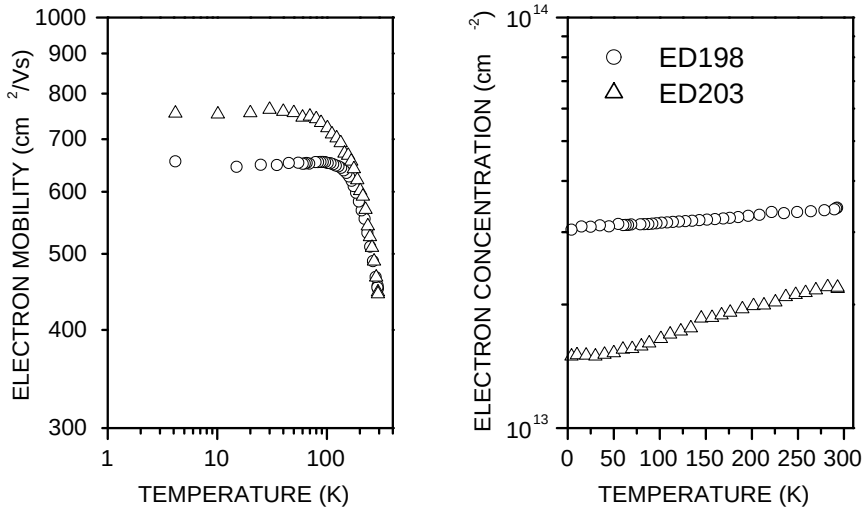

Figure 6.21: Temperature dependent Hall experiment data of AlGaN/GaN MBE structures grown on 6H i-SiC.

mary of the Hall data at low and room temperature are listed in tab. 6.4. In particular the 2DEG channel conductivity has been calculated, to compare the different samples in view of HEMT applications. Since the 2DEG MBE structures grown on conductive SiC substrate at room temperature show the anomalous behavior arising from a parallel conductive channel, they are not suited at this stage for high frequency HEMT application. For sake of comparison the low temperature values of the electron sheet and the room temperature mobilities have been used to calculate the conductivity. For the MBE samples grown on conductive SiC substrate, the measured value of the room temperature mobility value in presence of a bulk contribution is lower than the actual 2DEG mobility. After a systematic optimization of the different steps in our MBE process (from samples A172 to sample B65) a significant improvement has been achieved. Even though the high electric field regime in an operating HEMT device causes the electrons to move close to saturation velocity, still the low field mobility is a parameter which has to be maximized in non-ideal structures (defect material), in order to reach the predicted high saturation velocities.

Following analysis reported by Hsu and Walukiewicz [30] a qualitative description of some relevant 2DEG scattering mechanism has been considered in fig. 6.22. At high temperatures the mobility is limited by optical phonon scattering (op). Towards lower mobilities there is soon a clear deviation from experimental points. Since the optical phonon energy in GaN is 93 meV as compared to 37 meV in GaAs, the phonon scattering mechanism fits well at higher temperature. In order to compare our MBE samples with MOCVD ones we consider together several temperature independent scattering mechanism at low temperatures, namely alloy and dipole (dip) disorder, interface roughness (interf), dislo-

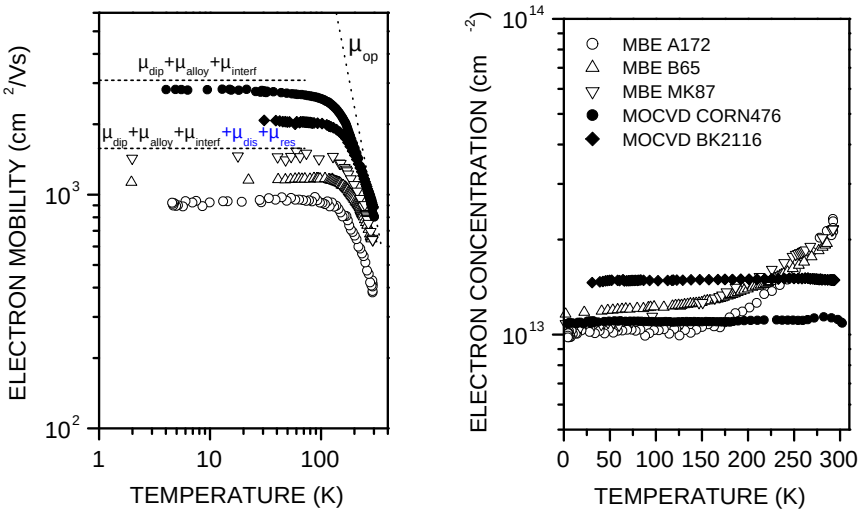

Figure 6.22: Temperature dependent Hall experiment data for AlGaN/GaN heterostructures. The MBE structures are grown on 6H n-SiC(0001) and two MOCVD samples on sapphire. The *dotted* lines are qualitative model estimations representing electron-scattering mechanism.

cation (dis) and residual (res) impurity scattering. Dipole scattering has been discussed by Jena *et al.* [50] and is described in the section 2.1.4. Since we expect that dipole, alloy and interface scattering are comparable in MOCVD and MBE structures, the lower mobility measured in these latter ones is mainly ascribed to a higher dislocation density. Also a possible influence of residual impurities is considered, in the case that the observed anomalous behavior of n_S towards room temperature should be assigned to impurities, like oxygen, in the MBE GaN buffer.

The samples grown on insulating SiC substrate (fig. 6.21) show lower low temperature mobilities than samples on conductive substrates, even if the i-SiC substrates show flat

AlGaN/GaN samples	$n_S \times 10^{13}$ (cm^{-2})		μ (cm^2/Vs)		σ_S (mS)
	20 K	300 K	20 K	300 K	
MBE A172	1.0	2.3	932	380	0.627
MBE B65	1.2	1.9	1155	648	1.246
MBE MK87	1.1	2.2	1465	641	1.130
MBE ED203	1.5	2.2	755	447	1.074
MOCVD BK2116	1.1	1.1	2821	802	1.413
MOCVD CORN476	1.5	1.5	2080	893	2.146

Table 6.4: Summary of the 2DEG Hall data in fi g. 6.21 and 6.22: sheet concentration n_S, mobility μ, conductivity $\sigma_S = e \cdot n_S(20\text{ K}) \cdot \mu\,(300\text{ K})$.

surfaces in comparison with the scratched surface of n-SiC (fig. 6.6). The reason are the poor structural properties of i-SiC (subsection 6.2.3), which results probably to high number of dislocations penetrating through the whole structure and lowering the carrier mobility.

In conclusion, for the optimization of the 2DEG conductivity in AlGaN/GaN heterostructures one should consider an as high as possible Al content in the barrier to increase the concentration. On other hand, the wave functions of the quasi-2DEG electrons penetrate more significantly the barrier at increasing electron concentrations (high x values) and this is expected to worsen mobility, because of the dipole scattering mechanism and the roughness of the interface. In fact, in AlGaN/GaN 2DEG structures there is always a disordered positive polarization charge with a density of the order 10^{13} C$\cdot$ cm^{-2} located at the GaN/AlGaN interface and a disordered distribution of dipoles in the AlGaN barrier, which is more sensed by electrons which penetrate more into the barrier.

This behavior is in contrast to what is known for classical modulation doped structures, where an increase of the 2DEG concentration also enhances the mobility, due to more efficient screening of the ionized impurities. It should be noted here, that in III-V modulation doped structures the carrier concentration in the 2DEG is increased by increasing the doping of the barrier layer and that a crucial parameter for achieving very high mobility is also the thickness of the spacer between the doped barrier and the electron channel. The spacer concept cannot help in reducing the Coulomb scattering due to polarization charges in nitride 2DEG heterostructures.

6.2.7 HEMT Device

The grown AlGaN/GaN heterostructure on insulating SiC substrate was used for HEMT device. The layer structure is shown in the figure 6.23. The grown structure does not contain the AlN interlayer, which seems to reduce the number of threading dislocations [141]. This sample had been processed before the measured structural properties showed unsatisfied results due to poor structural quality of the insulating substrate. A Linear HEMT

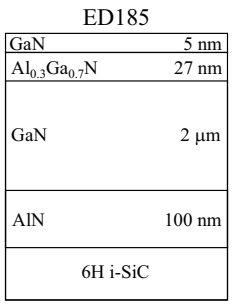

Figure 6.23: Grown structure on insulating SiC substrate of the sample ED185.

fabrication was used for the HEMT device processing (fig. 6.24). The ohmic contacts were

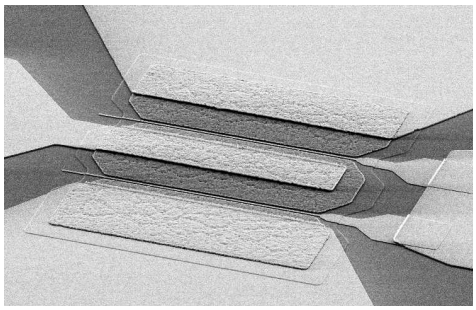

Figure 6.24: Linear HEMT used for device processing.

prepared using the planar optical lithography process. The sample was first degreased and cleaned. MESA etching of 200 nm was performed in order to restrict single HEMT devices from each other using electron cyclotron resonance reactive ion etching (ECR-RIE). For the ohmic contacts the surface of the sample was first sputtered with Ar^+ ions to eliminate the oxide, then 35 nm Ti, 200 nm Al, 40 nm Ni, 50 nm Au were deposited and annealed at $900°$C in N_2 flux for 30 seconds. The Schottky contacts for gate electrodes were patterned by electron beam lithography and prepared by evaporation of 25 nm of Ni and then 100 nm of Au. Finally the pads were prepared by metallization of a Ti and Au layer.

The DC measurements up to 15 V were performed using HP4155A semiconductor parameter analyzer on a HEMT structure with two gates, each of 0.3 μm in length and 50 μm in width, with a 3 μm source to drain spacing. Figure 6.25 (left) shows the DC

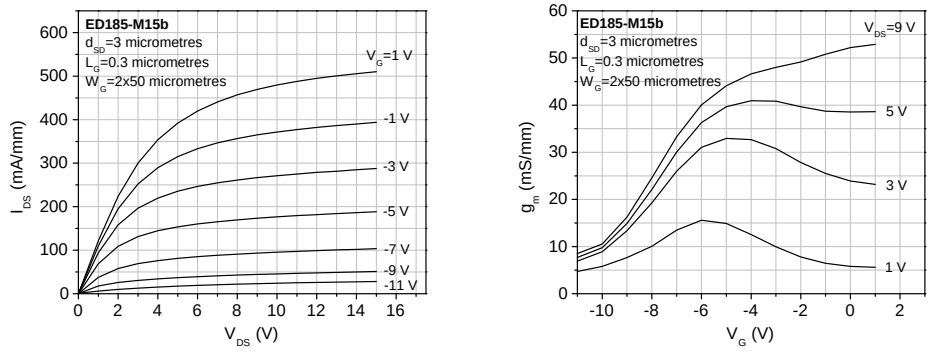

Figure 6.25: Output (left) and transfer (right) characteristics of a 0.3×50 μm AlGaN/GaN HEMT.

drain-source current I_{DS} dependence on the drain-source voltage V_{DS} at different gate voltage V_G. With increasing the gate voltage into the negative values, the channel is depleted of electrons and lower I_{DS} current flows. The channel is still not closed at relatively high gate voltage of -11 V indicating a parallel conductivity to the 2DEG channel. Figure 6.25 (right) displays the dependence of transconductance g_m on the gate voltage V_G at certain value of drain-source voltage V_{DS}. From the change of the g_m with decreasing the V_G we can see that the 2DEG is not confined very well. At higher drain-source voltages a conduction trough a bulk GaN layer is observed. This behavior is similar to a MESFET.

Small signal S-parameter measurements were carried out using an HP8510C network analyzer which can perform measurements in the range from 500 MHz to 110 GHz. Small signal RF measurements are shown in the figure 6.26. The short-circuit current gain h_{21} and unilateral power gain GU as a function of frequency was measured for a HEMT structure with gate length of 0.3 μm, gate width of 2×50 μm and source to drain spacing of 3 μm.
The unilateral power gain is defined as obtained power gain with compensation of retroactive capacitance from output toward the input by a lossless neutralization circuit. Current gain cutoff frequency f_T is the frequency at which the current gain is equal to unity. The maximum frequency of oscillation f_{max} is defined as frequency at unilateral power gain equal to unity [173].
The measured cutoff frequency f_T is 6.8 GHz. The unilateral gain exhibits 20 dB per decade decline and a maximum frequency of oscillation f_{max} of 15 GHz is reached.

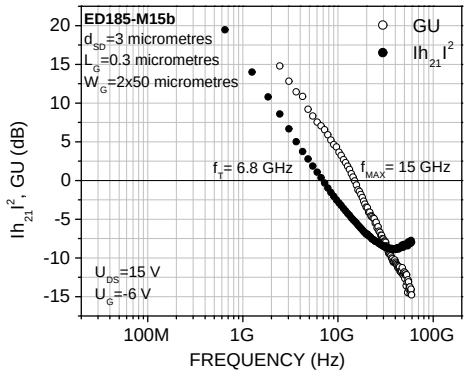

Figure 6.26: RF measurements of a 0.3×50 μm AlGaN/GaN HEMT.

The results of the HEMT properties on the sample ED185 does not show the best values compared to observed data in the literature. Sullivan *et al.* fabricated $Al_{0.2}Ga_{0.8}N$/GaN HEMT on insulating SiC substrate with a 0.7 μm gate length that reach

a unity gain frequency of 15 GHz and maximum frequency of oscillation 42 GHz [174]. $Al_{0.3}Ga_{0.7}N$/GaN HEMT structures grown on SiC with a gate length of 0.15 μm prepared by Moon *et al.* show cut-off frequency f_T of 85 GHz and rough estimated f_{max} approaching 140 GHz [175]. Javorka *et al.* reported on $Al_{0.23}Ga_{0.77}N$/GaN HEMTs on Si(111) with 0.5 μm gate length that exhibit a unity gain frequency of 32 GHz and maximum frequency of oscillation 27 GHz [176].
The DC measurements of ED185 show parallel conductivity to the 2DEG channel present in the structure. Probably due to the high number of dislocations[3] the background concentration of GaN buffer layer is high and provides parallel conduction. Fabrication of HEMT structure on samples grown on insulating SiC substrates with inserted interlayer promise to reach better device properties. Layer structure of such sample (MK210) is displayed in figure 6.27. A linear HEMT was fabricated with gate length of 0.5 μm, gate

MK210

GaN	5 nm
$Al_{0.15}Ga_{0.85}N$	27 nm
GaN	300 nm
AlN	5 nm
GaN	1.5 µm
AlN	100 nm
6H i-SiC	

Figure 6.27: Grown structure on insulating SiC substrate of the sample MK210.

width of 2×50 μm and source to drain spacing of 3 μm. The figure 6.28 (left) shows the DC drain-source current I_{DS} dependence on the drain-source voltage V_{DS} at different gate voltage V_G. A maximal I_{DS} current of 700 mA/mm at $V_G = 1$ V was reached. With increasing the negative gate voltage, the channel is depleted of electrons and lower I_{DS} current flows. The channel is closed at the gate voltage of approximately -6 V as could be also seen in the figure 6.28 (right) (right axis). The figure 6.28 (right) (left axis) displays the dependence of transconductance g_m on the gate voltage V_G at certain value of drain-source voltage V_{DS}. A maximal transconductance g_m of 122 mS/mm was reached. The frequency properties of the fabricated HEMT are displayed in the figure 6.29. A cut-off frequency f_T of 16.1 Hz and maximum frequency of oscillation f_{max} of 32.3 Hz were measured. The measured values of the sample MK210 compared to the sample ED185 show better properties. The inserted AlN interlayer of the sample MK210 seems to improve the HEMT device properties.

[3] see XRD measurements of GaN grown on i-SiC in subsection 6.2.3 for more details

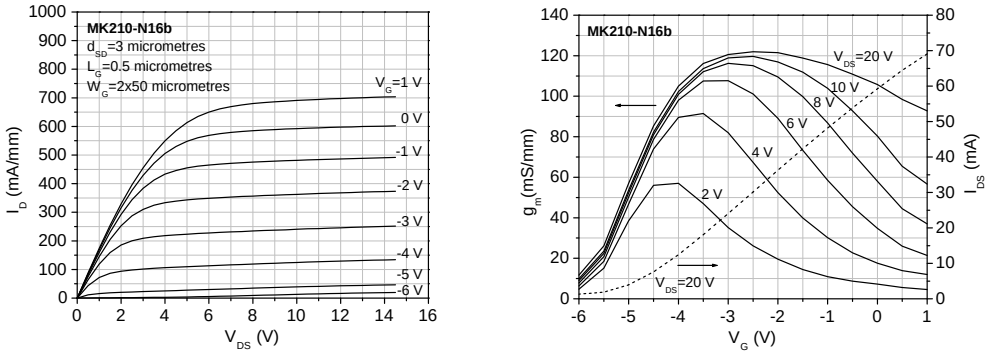

Figure 6.28: Output (left) and transfer (right) characteristics of a 0.5×50 μm AlGaN/GaN HEMT.

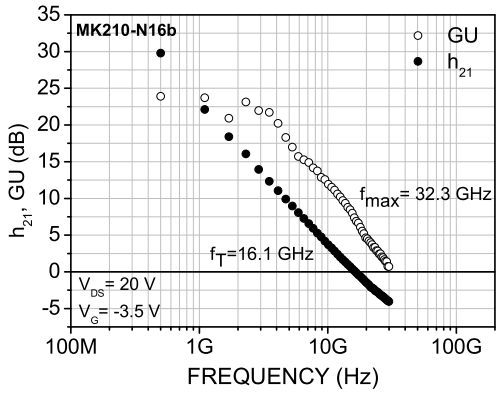

Figure 6.29: RF measurements of a 0.5×50 μm AlGaN/GaN HEMT.

6.3 Growth Optimization of Nitrides on Si Substrate

Silicon is an attractive substrate for GaN-based devices because of its physical properties, crystal quality, doping capability, thermal stability, low cost and well known Si technology (see section 2.2.1 for more details). To date, the quality of GaN epitaxial layers on silicon has been much poorer than that on sapphire or silicon carbide, due to large lattice constant (+17%) and thermal expansion coefficient (+54%) mismatch, and the tendency of silicon to form an amorphous silicon nitride layer when exposed to reactive nitrogen sources. Nevertheless, GaN devices have been already demonstrated on Si substrates including LEDs and HEMTs [67, 91].

In this section we first concentrate on the III-N MBE growth on p-Si(111) substrates (7-21 Ω·cm) and finally on the Hall effect characterization of 2DEG AlGaN/GaN heterostructure. The grown layers were characterized by optical microscope, AFM, SIMS and XRD measurement.

6.3.1 Substrate Preparation

The Si(111) substrates used for the epitaxial growth are p-type with a resistivity of $7 - 21\ \Omega \cdot \mathrm{cm}$ and a thickness of $350 - 400\ \mu\mathrm{m}$. Before starting the MBE growth it is necessary to remove the $\mathrm{SiO_2}$ that covers the surface of the substrate and the most common procedure is the Shiraki-method which consists of:

1. Wet chemical treatment to eliminate organic contaminants and $\mathrm{SiO_2}$.
2. Thin film oxide formation to protect the clean Si surface from contamination during processing before MBE growth.
3. Desorption of the thin oxide film under UHV at temperature around 800°C.

This method was proposed for the first time in 1986 by Y. Shiraki [177]. The very thin oxide film is removed as vaporized SiO, according to the following reaction:

$$\mathrm{Si} + \mathrm{SiO_2} \longrightarrow 2\mathrm{SiO} \uparrow$$

Several groups have adopted this method (usually referred to RCA procedure) in order to clean Si(111) for MBE growth: for example Si(111) substrates with resistivities from 1 to 400 Ω·cm were cleaned using RCA process and heated at 850°C for 20 min until a 7x7 reconstruction with Kikuchi lines appeared [178]. In another case to desorb the native oxide and volatile impurities, the substrate was outgassed at 900°C for 20-40 min. Within the range 800-900°C, the temperature ramp was kept low (10°C/min) to avoid formation of dislocations in silicon [179]. In our MBE apparatus the sample holder is able to heat the substrate approximately up to 800°C for short time (1-2 min). To reach this

temperature, the current of the heating resistance is already over the maximum. Auger spectra displayed in fig. 6.30 (1) show that silicon oxide is not removed completely from the substrate using only annealing in the MBE chamber.

Using Low Energy Electron Diffraction (LEED) no pattern was observed. Therefore

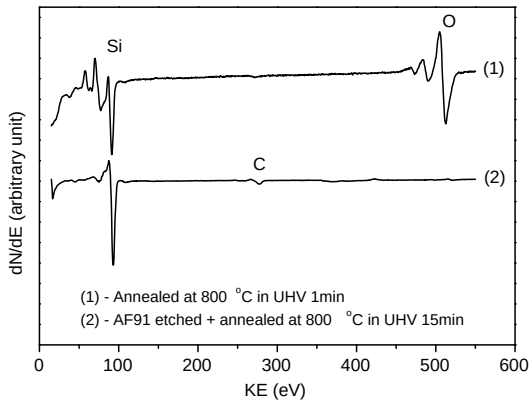

Figure 6.30: Comparison between Auger spectra of Si substrates cleaned in different ways (see text).

a dip in AF91 solution[4] was introduced in order to reduce the amount of SiO_2 on the surface. Then the sample was rapidly transferred in the MBE chamber.
The description of the used RCA cleaning procedure follows. After cleaning the substrate in Aceton and Propanol for 3 min in ultrasonic in order to remove the greasiness, subsequent steps were used:

1.	HNO_3	T= 80°C	3 min in ultrasonic
2.	DI H_2O	T= 25°C	
3.	AF91	T= 25°C	20 s in ultrasonic
4.	DI H_2O	T= 25°C	
5.	HCl + H_2O_2 + H_2O (5:3:3)	T= 80°C	3 min
6.	DI H_2O	T= 25°C	
7.	N_2 drying		

The cleaning steps 1-4 are repeated three times. At the end of the sixth step a thin oxide film (5-10 nm) is obtained on the surface, which protects the silicon surface from contam-

[4] AF91-09 is Ammonium fluoride etchant which consist of 91 parts by volume of ammonium fluoride solution (NH_4F) 40% and 9 parts by volume of hydrofluoric acid (HF) 50%. The etch rate of AF91 reactant for SiO_2 is $0.05\ \mu m/min$ at T=20°C.

inants and enables to store the substrates. Before the growth the oxide film has to be removed. We used a dip in AF91 solution for 10-30 seconds. Then the substrate was dipped in deionized H_2O, dried using N_2 and directly loaded into vacuum of the MBE chamber. After annealing at T=550°C for 10 hours to eliminate the organic impurities, the substrate was annealed up to 800°C for t=15 min. The Auger spectra displayed in figure 6.30 (2) show the almost complete removal of oxygen. LEED measurement revealed a (7×7) reconstruction image typical of clean Si(111) (fig. 6.31).

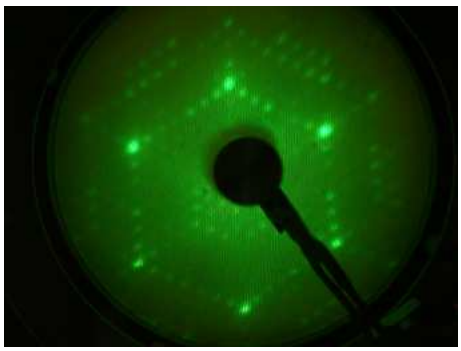

Figure 6.31: LEED image of a clean Si(111) surface. 7×7 reconstruction was observed.

6.3.2 GaN Layer Growth

To start GaN growth on a substrate (sapphire, SiC, Si) usually a nucleation layer is used in order to accommodate most of the lattice mismatch and orientate the GaN growth on the top of it [67]. An AlN nitride buffer layer is able to promote a bidimensional growth of GaN on the top of Si(111) and to reduce the density of cracks in the GaN film as demonstrated by Watanabe [180]. The improvement in the quality of the heteroepitaxial film is mainly due to two reasons: both the lattice and thermal mismatches between GaN and AlN are smaller than between GaN and Si(111) (table 2.5) and the (7×7) reconstructed Si(111) surface presents a high lattice order match to AlN. The large unit cell of Si(111) has several sites where extra AlN planes (*i.e.* edge dislocations) can be favorably displaced [181]. The 14Si:17AlN match shown in figure 6.32 results in +1.6% mismatch, small enough to support lattice-matched growth.

When a GaN layer is grown directly on the cleaned Si(111) surface, the formation of a thin amorphous layer was reported in the literature [179, 182], most probably Si_xN_y generated by reaction of the Si surface atoms with the active nitrogen. A way to prevent this and improving growth is to deposit first a few monolayers of Al and then to proceed with the epitaxy of a nucleation layer, in our case a 100 nm thick AlN at a substrate temperature of 770°C. The active nitrogen is provided by a RF-plasma source operating at 13.56 MHz, 350 W, 1 sccm. Two samples with different Al fluxes (BEP(Al)=1.4×10^{-7}

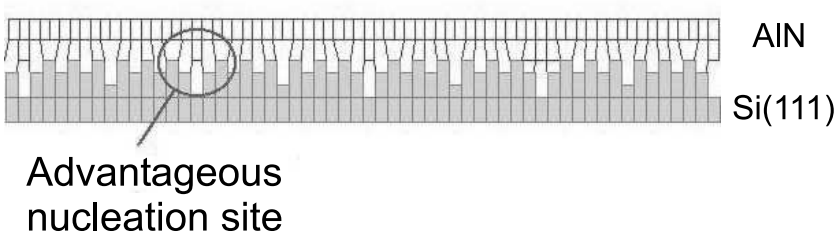

Figure 6.32: 17:14 lattice matching of a AlN on the (7×7) reconstructed surface of Si(111) [181].

and 1.0×10^{-7} mbar) were grown on a p-Si(111) substrate. The first (ED141) shows many Al droplets at the surface and the surface roughness measured by AFM is 3.93 nm on 5×5 μm^2 scan area. For the second sample (ED145), displayed in fig. 6.33 (a), the Al flux was adjusted to slightly Al rich conditions and shows flatter surface morphology. The RMS surface roughness measured by AFM is 1.79 nm on a 5×5 μm^2 area.

The next step was the growth of crack-free 1 μm thick GaN on AlN nucleation layer. Several samples were grown with different growth conditions (various Ga fluxes) at constant substrate temperature of 763°C, Plasma power source 450 W and Nitrogen flux 1sccm. The surface morphology was characterized by optical microscopy and AFM. The best result was achieved with BEP(Ga)=2.5×10^{-7} mbar (sample ED147). The surface roughness is 14.14 nm on a 5×5 μm^2 AFM image (fig. 6.33 (b)) and is about one order of magnitude larger than similar layers grown on SiC. The GaN (0002) reflex measured by X-ray diffraction shows in the ω scan a full width at half maximum (FWHM) of 2400 arcsec. By increasing the thickness of GaN, cracks form as observed with an optical microscope.

With the aim to provide a better lattice mismatch and thermal expansion mismatch for the subsequent growth of GaN an AlGaN buffer interlayer (100 nm of thickness) was

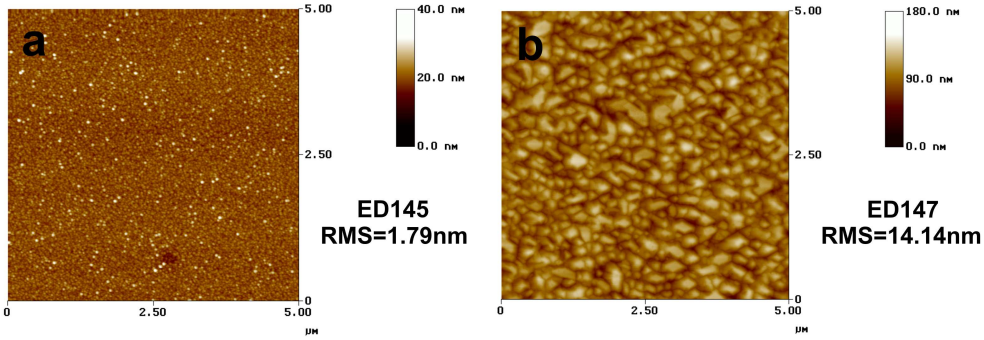

Figure 6.33: AFM images of III-N layers grown on Si(111) substrate:
(a) sample ED145: AlN(100 nm)/Si(111),
(b) sample ED147: GaN(500 nm)/AlN(100 nm)/Si(111).

grown on top of the AlN nucleation layer.
According to equation (2.35), the thermal stress is proportional to the difference between thermal expansion coefficients of the GaN layer and the underlying layer. If the tensile stress is lower, the quality of the GaN layer is improved and the crack density reduced. Significant improvement in the structural and optical properties of the GaN layer was also achieved. This result was shown for GaN grown by UHVCVD[5] [110], MBE [104] and MOCVD [183]. Marchand was able to grow a 200 nm thick GaN layer on Si(111) with a 800 nm graded $\mathrm{Al_XGa_{1-X}N}$ interlayer by MOCVD and found that the GaN layer on the top was under compressive strain instead of tensile strain [184]. This result is still not clearly explained in theory, however it is well accepted because the GaN film under compressive stress does not crack.
For the AlGaN interlayer growth the substrate temperature was set to $763°\mathrm{C}$, the Plasma source power to 450 W, the N flux to 1 sccm and the total metal flux to ($\mathrm{BEP(Al+Ga)} = 2.5 \times 10^{-7}\ \mathrm{mbar}$), that means slightly metal rich growth conditions. Several Al compositions were considered and the surface morphology slightly improves for higher Al contents. To the purpose of achieving optimum lattice match both to the AlN nucleation layer and to the GaN on top an intermediate composition (40%) was chosen (sample ED151). The surface roughness of the $\mathrm{Al_{0.4}Ga_{0.6}N}$ buffer is 2.17 nm (fig. 6.34 (a)).

Significant improvement in the surface morphology of $1\ \mu$m thick GaN layers grown on top was achieved in this way [104]. Figure 6.34 shows several GaN layers which were grown with different growth parameters (tab. 6.5): both the Ga flux and the substrate temperature play an important role. The same trend is obtained either by increasing the Ga flux or by decreasing the temperature in very tight window: $(3.0 \pm 0.2) \times 10^{-7}$ mbar, $(763 \pm 5)°\mathrm{C}$. In fact a temperature decrease corresponds to a lower Ga desorption from the surface. In general the Ga poor growth conditions lead to a rough surface with a lot of deep pits. The surface roughness is 15.3 nm (fig. 6.34 (b), sample ED158). An intermediate Ga supply improves the surface morphology up to a roughness of 1-2 nm (fig. 6.34 (c), sample ED160). The Ga rich growth conditions provide the best surface roughness of 0.88 nm (fig. 6.34 (d), sample ED156) and terraces are observed on the AFM picture indicating step-flow growth. The full width at half maximum of the (0002) GaN reflection in XRD is 1707 arcsec for the ω scan and 564 arcsec for the $\omega - 2\theta$ scan (fig. 6.36, 6.37 (a)). The measured data are significantly better than GaN grown directly on AlN nucleation layer.

Another improvement was tried using 100 nm thick graded AlGaN interlayer between the AlN nucleation layer and the GaN layer (sample ED166) [110, 184]. The Al composition x was changing linear from 1 to 0 during the growth of the $\mathrm{Al_XGa_{1-X}N}$ layer. The interlayer was grown under slightly metal rich and the GaN ($1\ \mu$m of thickness) under Ga rich growth conditions. The surface morphology shown in fig. 6.35 shows very flat

[5] UHVCVD - Ultra High Vacuum Chemical Vapour Deposition

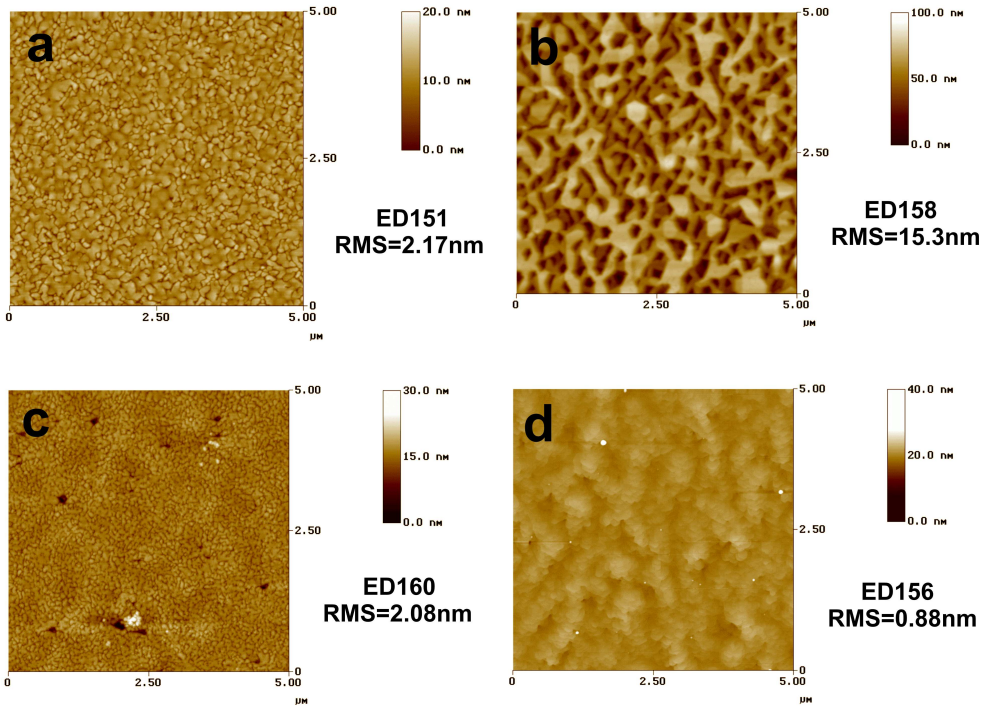

Figure 6.34: AFM images of $Al_{0.4}Ga_{0.6}N$/AlN layers grown on Si(111), rms=2.2 nm (a) and GaN/AlGaN/AlN layers grown on Si(111) with different growth conditions: Ga poor, rms=15.3 nm (b); intermediate Ga supply, rms=1.61 nm (c); Ga rich, rms=0.88 nm (d). The growth parameters are listed in appendix B.

surface with small Ga droplets (white points). The sample has Ga droplets on the surface as observed on optical micrographs. The surface roughness of 0.61 nm was measured. Figure 6.36 (b) shows the ω and figure 6.37 (b) the $\omega - 2\theta$ XRD pattern of GaN grown on AlGaN graded interlayer (sample ED166). An intense (0002) reflection of wurtzite GaN is clearly observed and the full width at half maximum value is 1530 arcsec for ω scan and

Sample name	BEP(Ga) (mbar)	T_{SUB} (°C)
ED158	3.0×10^{-7}	773°C
ED160	2.8×10^{-7}	763°C
ED156	3.0×10^{-7}	763°C

Table 6.5: Growth parameters of the 1 μm thick GaN layer of three samples grown on $Al_{0.4}Ga_{0.6}N(100\,nm)/AlN(100\,nm)/Si(111)$ resulting to different surface morphology (fi g. 6.34 (b)-(d)). The Plasma source power was set to 450 W and the N flux to 1 sccm for all samples.

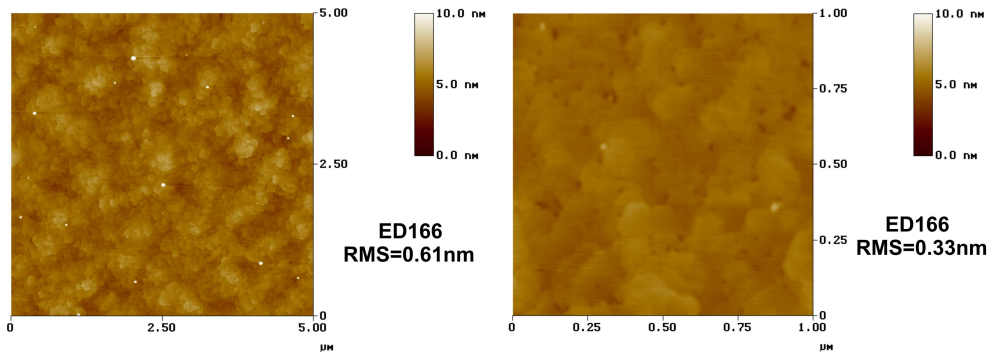

Figure 6.35: AFM image of the GaN(1 μm) layer grown on graded AlGaN(100 nm)/AlN(100 nm) buffer, rms=0.61 nm (sample ED166). 5×5 μm^2 and 1×1 μm^2 scan area is displayed on the left and right side, respectively.

558 arcsec for $\omega - 2\theta$ scan. A slight improvement is observed in the structural quality of the GaN grown on the AlGaN graded interlayer in the ω XRD-scan compared to the GaN grown on the $\mathrm{Al}_{0.4}\mathrm{Ga}_{0.6}\mathrm{N}$. The AFM images show similar surface morphology and also similar surface roughness.

Table 6.6 gives a summary of the best measured values achieved by using suitable growth parameters. The is observed GaN (0002) peak in XRD for ω and $\omega - 2\theta$ scan, and the RMS surface roughness measured by AFM are displayed. Clear improvement is observed using AlGaN or graded AlGaN interlayer. The differences between graded AlGaN and AlGaN with fixed Al composition are very small.

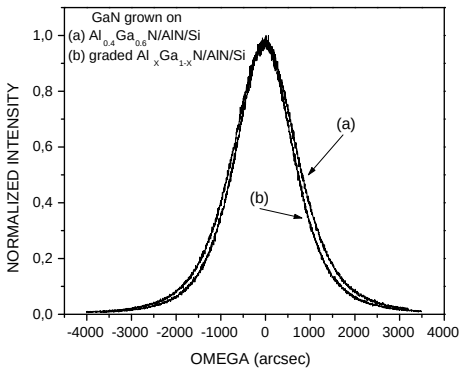

Figure 6.36: ω-rocking curve of the (0002) reflection of a GaN layer grown on the AlGaN/AlN buffer (ED156) (a) and on graded AlGaN/AlN buffer (ED166) (b).

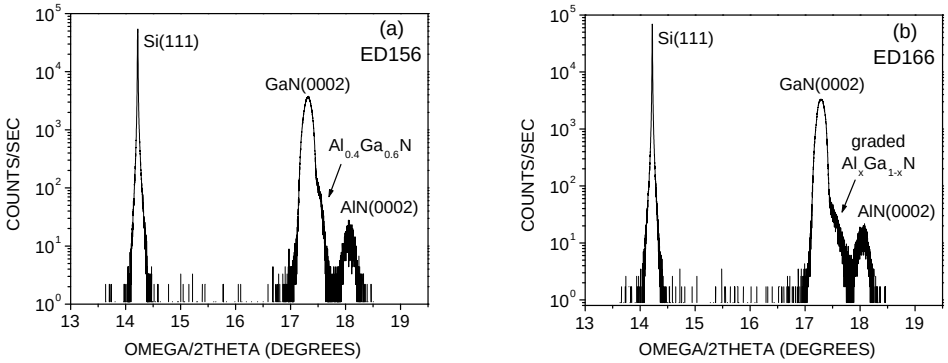

Figure 6.37: $\omega - 2\theta$ scan of a GaN layer grown on the AlGaN/AlN buffer (sample ED156) (a) and on graded AlGaN/AlN buffer (sample ED166) (b).
Three peaks can be seen: Si substrate peak, GaN (0002) reflection and AlN (0002) reflection. The right shoulder of the GaN peak corresponds to $\mathrm{Al_{0.4}Ga_{0.6}N}$ (a) and to graded $\mathrm{Al_XGa_{1-X}N}$ (b) interlayer.

Layer structure grown on Si(111)	FWHM of XRD ω rocking (0002) (arcsec)	FWHM of XRD $\omega - 2\theta$ rocking (0002) (arcsec)	RMS roughness (nm)
GaN/AlN	2400		14
GaN/AlGaN/AlN	1707	564	0.88
GaN/graded AlGaN/AlN	1548	560	0.61

Table 6.6: Surface and structural properties of a $1\ \mu$m thick GaN grown on Si(111) with different buffer layer structures. The surface roughness (rms) is measured on a $5 \times 5\ \mu\mathrm{m}^2$ scan area.

6.3.3 Diffusion and Impurities in MBE Growth

SIMS measurements have been performed on sample ED153 with a layer structure shown in figure 6.38 in order to get information about the presence of impurities during MBE growth and possible diffusion phenomena at the interface between the substrate and the layers grown on it. The measurements were done with primary ions of $\mathrm{Cs^+}$ and $\mathrm{O_2^+}$ with an energy 6 keV impinging on the sample along the normal direction to the sample surface. The primary ion beam had a diameter of 25 $\mu\mathrm{m}$. The measured SIMS results are shown in fig. 6.39.

It is not possible to compare the signals of the same atomic species in different layers, because AlGaN, AlN and Si(111) are forming different matrixes. Furthermore the sputtering time changes for different material systems, so the time axis of the SIMS plots is not proportional to the layer thickness (e.g. the sputtering rate of GaN is 2.5 times higher than the one of AlN). Finally Al and Ga can not be measured as atomic species because their

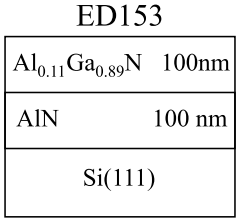

Figure 6.38: Layer structure of the sample ED153 used for SIMS analysis.

signals for SIMS equipment are too high, so AlN and GaN are measured.

Signal steps of Al(AlN) and Ga(GaN) at AlGaN/GaN/Si heterojuctions, shown in fig. 6.39 (a), indicate sharp interfaces. Ga reaches its background value in the AlN layer and Si(111) substrate, while Al falls to its background value of the SIMS equipment in Si(111). Impurity level of C and O, mostly present at the interfaces (AlGaN/AlN and AlN/Si), is quite low compared to GaN layer grown by MOCVD (ED168). The SIMS measurements of ED168 are shown in subsection 6.2.4.

The roughness at the interface AlN and Si(111) should be quite low (below 1 nm), so it is possible to extract data about diffusion phenomena. As can be seen from the figure 6.39 (b) Si diffuses into AlN because the Si signal is clearly leaking from the substrate into the AlN and the ratio among the three isotopes of SiO (45, 46, 47) is constant on both sides of the interface between AlN and Si(111). Concerning the diffusion of Al into Si no reliable conclusion can be drawn because there are not other Al isotopes to compare with and a set of reference Al-doped Si(111) samples was not provided.

Fig. 6.39 (c) shows that other impurities as Cr, Ti and Fe are almost absent.

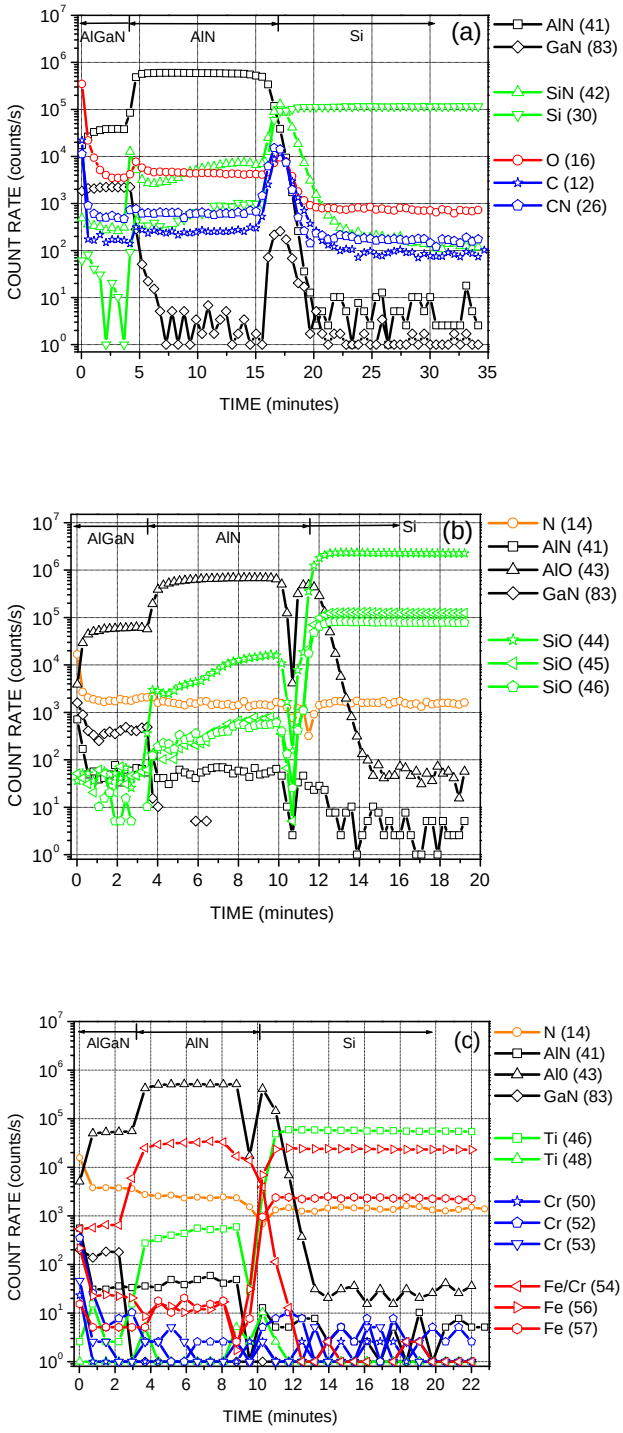

Figure 6.39: SIMS analysis of the sample ED153 ($Al_{0.11}Ga_{0.89}N(100\ nm)/AlN(100\ nm)/Si(111)$). The numbers reported in brackets in the legend are relative atomic masses.

6.3.4 Growth of a HEMT structure

The optimization of GaN growth on Si(111) was done in order to obtain a buffer suitable for the realization of a two dimensional electron gas structure for microelectronic applications (*i.e.* HEMTs). Therefore an $Al_{0.23}Ga_{0.77}N$ barrier and a GaN cap were grown on the same optimized layer structure as the sample ED156. The grown 2DEG heterostructure is shown in figure 6.40 (sample ED162).

ED162

GaN cap	8 nm
$Al_{0.23}Ga_{0.77}N$	25 nm
GaN	1 µm
$Al_{0.4}Ga_{0.6}N$	100 nm
AlN	100 nm
p-Si(111)	

Figure 6.40: Layer structure of the sample ED162 used for Hall effect measurement.

The Hall effect measurements were performed on van der Pauw samples ($5 \times 5\,\mathrm{mm}^2$). The ohmic contacts were prepared by metallic evaporation of Ti(35 nm)/Al(200 nm)/Ni(40 nm)/Au(50 nm) layers and subsequently annealed at $900^\circ\mathrm{C}$ for 30 min in N_2 flux. The measured temperature dependent Hall mobility and carrier concentration are displayed in figure 6.41.

By decreasing the temperature the mobility rises from $115\,\mathrm{cm}^2/\mathrm{Vs}$ at room temperature to the maximal value of $1869\,\mathrm{cm}^2/\mathrm{Vs}$ at about 55-60 K. Further cooling causes first a mobility decrease down to a minimum value of $47\,\mathrm{cm}^2/\mathrm{Vs}$ at 33 K and then the mobility increases again until it reaches the value of $447\,\mathrm{cm}^2/\mathrm{Vs}$ at 21 K, value which remains constant down to 4 K.
A corresponding strange behavior is observed for the carrier concentration: decreasing the temperature the two-dimensional carrier concentration slightly decreases from $1.8 \times 10^{14}\,\mathrm{cm}^{-2}$ at room temperature to the lowest value of $9.2 \times 10^{12}\,\mathrm{cm}^{-2}$ at 42 K. Decreasing further the temperature, the carrier concentration increases to the value of $1.23 \times 10^{14}\,\mathrm{cm}^{-2}$ at 33 K (the minimum of the mobility) and then decreases to $1.0 \times 10^{13}\,\mathrm{cm}^{-2}$ and remains constant in the range of 4-22 K. The Hall effect shows both n-type (below 35 K) and p-type (above 35 K) conductivity in sample ED162. These experiments indicate that more than one conductive channel is present in the heterostructure.

To understand better the conductivity behavior of the heterostructure, a selfconsistent Schrödinger-Poisson one dimensional band scheme calculation was performed, assuming

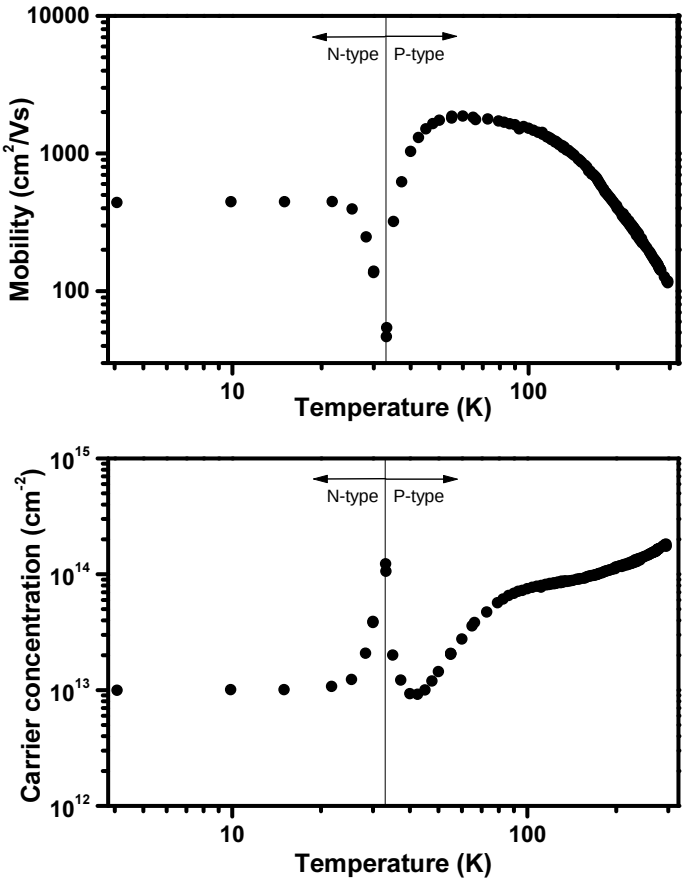

Figure 6.41: Temperature dependent Hall experiment data of AlGaN/GaN MBE structures grown on Si(111).

the structural parameters of the sample ED162. The donor background concentration of N_D=10^{17} cm^{-3} is assumed in all III-nitride layers, while for the p-Si(111) substrate (resistivity of 7-21 $\Omega \cdot \mathrm{cm}$) an acceptor doping concentration of N_A=10^{15} cm^{-3} is assumed. The surface potential of the GaN cap layer or $\mathrm{Al_XGa_{1-X}N}$ layers with various Al composition is known from X-ray spectroscopy (XPS) data shown in subsection 6.4.1 and is introduced here as a surface boundary condition. The influence of the cap layer turns out to be irrelevant for these calculations. Finally we assumed for the MBE grown structure a Ga-polarity and we introduced the polarization charges in the simulation as thin (1 Å) fully ionized doped layers according to the relation: $\sigma_{\mathrm{POL}} = N_D \cdot t$, where σ_{POL} is the polarization sheet charge density, N_D the bulk doping density, which represents the polarization charge and *t* the thickness of the layer [10]. In strained $\mathrm{Al_{0.25}Ga_{0.75}N}$ barrier layer both piezoelectric and spontaneous polarization are considered. In relaxed 100 nm thick AlN nucleation layer, $\mathrm{Al_{0.4}Ga_{0.6}N}$ and 1 μm GaN only spontaneous polarization is assumed [10].

Fig. 6.42 (a) shows the conduction band minimum (E_C), valence band maximum (E_V) and calculated carrier concentrations (n and p) along the heterostructure. A first two-dimensional electron gas (2DEG) is formed below the unintentionally doped $\mathrm{Al_{0.25}Ga_{0.75}N}$ barrier in the triangular GaN quantum well, due to the fixed positive polarization charges at the $\mathrm{Al_{0.25}Ga_{0.75}N/GaN}$ interface. Strong electric fields are also induced in the thin AlN nucleation layer and in the bottom part of the GaN layer. Due to the polarization charges at the $\mathrm{GaN/Al_{0.25}Ga_{0.75}N/AlN}$ interfaces, two dimensional hole gases (2DHGs) are formed with concentrations comparable to that of the 2DEG on top. Furthermore a second n-type channel is formed at the AlN/Si(111) interface. The result of the calculation might explain the complicated behavior measured in the Hall effect experiment if all conductivity channels contribute to the measured transport properties. From room temperature down to 35 K the main contribution is assumed to arise from the 2DHGs in the buffer-nucleation region of the structure. Additionally, the p-type substrate can also contribute to the conduction at higher temperatures. 1 μm thick GaN layer is not resistive enough to electrically insulate the active structure from parallel channels in the nucleation-substrate region. At lower temperatures, once freezing out of the carriers in the unintentionally doped GaN occurs, the conductivity of the 2DEG on top is measured. Our calculation shows that the AlN nucleation layer alone causes the presence of high concentration 2DHGs. Similar studies were reported also in literature [185].

P-type channel can be also formed at III-N/Si-substrate interface due to the diffusion phenomena as reported in the work of Calleja *et al.* [186]. Calleja studied the growth of GaN on Si(111) substrate by MBE and he found a strong diffusion of Ga into Si [186]. According to his results sample grown at around 660°C show n-type conductivity, while samples grown at around 720°C show p-type conductivity. For a given growth temperature, the longer the growth time, the higher the p-type conductivity. A further increase of the growth temperature to $770 \pm 10^{\circ}$C leaded to higher conductivity values, always p-type. Since Ga is a shallow acceptor in Si, at some 65 meV above the valence band, considering the activation energies from Hall measurements Calleja concluded that the Hall conductivity is dominated by a highly conductive p-type interface channel generated by Ga diffusion into the Si substrate. SIMS measurements revealed this diffusion process with onset temperatures around 600°C. Because Al behaves as an acceptor in Si and its diffusion coefficient is higher than that of Ga [187], a diffused p-type layer at the AlN/Si interface is also expected. Actually Hall data revealed that GaN layers grown on AlN/Si layers have p-type conductivity with an activation energy very close to that of the Al acceptors (57 meV) in Si[6]. From CV measurements Calleja and his group found a residual n-type concentration of 2×10^{17} cm^{-3} in GaN samples grown above 700°C [104].

The Schrödinger-Poisson one dimensional band scheme calculation does not take into account the diffusion effects. On other hand the p-type conductive layer in Si at AlN/Si

[6]Activation energies, diffusion coefficient and solubilities for Ga and Al in silicon can be found in Ref. [187]

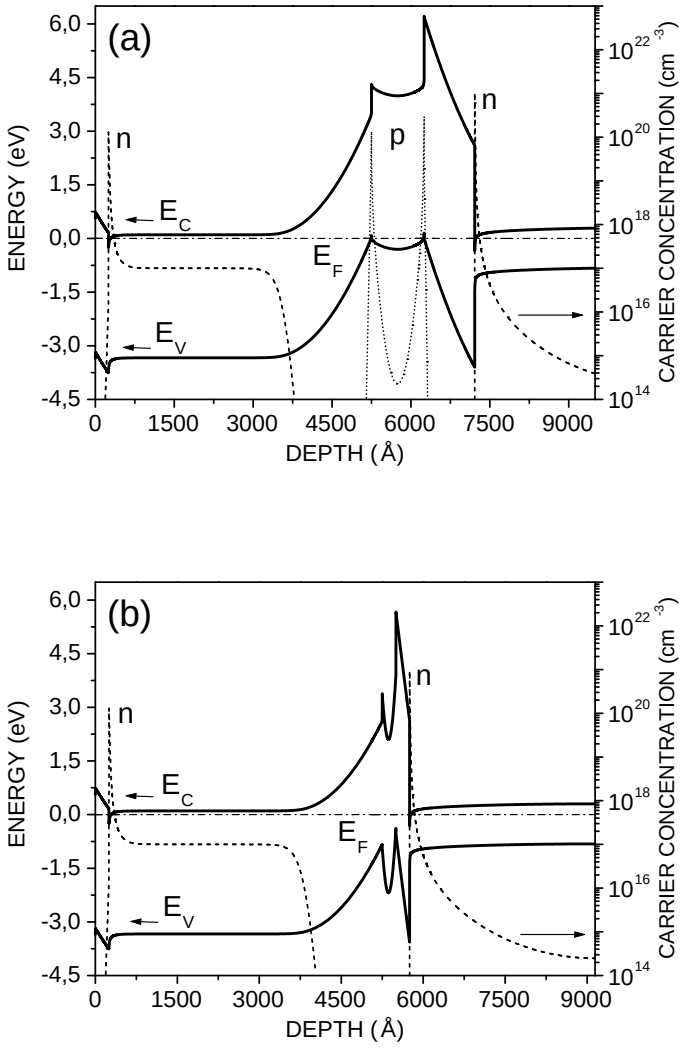

Figure 6.42: One dimensional band scheme calculation of the $Al_{0.25}Ga_{0.75}N/GaN/Al_{0.4}Ga_{0.6}N/AlN/Si$ heterostructure with:
(a) undoped $Al_{0.4}Ga_{0.6}N$(100 nm)/AlN(100 nm) buffer-nucleation layer,
(b) $Al_{0.4}Ga_{0.6}N$(25 nm, $N_D = 1 \times 10^{19}\ cm^{-3}$ doped)/AlN(25 nm, undoped) buffer-nucleation layer.

interface found by Calleja is also a possible reason of p-type conductivity observed by Hall effect measurements.

To avoid the two 2DHGs at the $\mathrm{GaN/Al_{0.4}Ga_{0.6}N}$ and $\mathrm{Al_{0.4}Ga_{0.6}N/AlN}$ interfaces evidenced by the Schrödinger-Poisson simulation (fig. 6.42 (a)), a reduction of the AlN and $\mathrm{Al_{0.4}Ga_{0.6}N}$ layer thickness and compensation doping of the $\mathrm{Al_{0.4}Ga_{0.6}N}$ interlayer can be considered. Several simulations were performed with different thickness of the AlN layer (100, 50, 25 nm) and doping concentration of the $\mathrm{Al_{0.4}Ga_{0.6}N}$ interlayer ($\mathrm{N_D} = 10^{18} - 10^{19}\ \mathrm{cm^{-3}}$). The best result was obtained for a thickness of 25 nm and a donor concentration of $\mathrm{N_D} = 1 \times 10^{19}\ \mathrm{cm^{-3}}$. The band diagram of such structure is shown in fig. 6.42 (b).

According to our knowledge of the recent literature only Semond *et al.* have been able to measure n-type 2DEG behaviour by Hall effect on a AlGaN/GaN HEMT structure grown on Si(111) by ammonia assisted MBE [188]. In order to avoid the parallel conductivity they have grown following structure GaN(1 μm)/AlN(250 nm)/GaN(250 nm)/AlN(50 nm)/Si(111). They have observed that the two AlN layers are useful in reducing the thermal stress in the GaN layer on the top and the 50 nm thick AlN layer is effective in stopping the diffusion of impurities coming from the substrate to the upper part of the structure. On the other hand the 250 nm thick AlN layer is helpful in reducing the density of the threading dislocations in the GaN film. Due to the low impurity content ($1 - 5 \times 10^{17}\ \mathrm{cm^{-3}}$ for C and O) and the relatively low dislocation density ($5 \times 10^{9}\ \mathrm{cm^{-2}}$), the free carriers background concentration is lowered to $5 \times 10^{15}\ \mathrm{cm^{-3}}$ and the $1\ \mu$m thick GaN layer behaves as an insulator between the two dimensional electron gas at the AlGaN/GaN interface and the bottom layers. The reduction of the electron background concentration in the GaN layer seems to be the key point for the realization of a AlGaN/GaN heterostructure on Si(111) suitable for HEMTs applications. As example Hall experiment data of $\mathrm{Al_{0.3}Ga_{0.7}N}$/GaN heterostructure grown on Si(111) substrate by MOCVD[7] displayed in figure 6.43 show clear 2DEG behavior without parallel channel effects.

The original contribution of our work is to point out the formation of 2DHG channels at the interfaces of the nucleation-buffer region. This also qualitatively explains both the high mobility and high concentrations measured in the Hall experiment. In fact the peak concentration of one 2DHG is $p \sim 10^{20}$ cm^{-3}, which means a sheet concentration on a 10 nm thick layer of $p_S \sim 10^{14}$ cm^{-2}, in good agreement with the experiment. Concerning the mobility, no experimental data are available to our knowledge for 2DHG. However theoretical calculations report on the expected 2DHG mobility values of e.g. 5080 cm^2/Vs at $p = 6 \times 10^{12}$ cm^{-2}, which are of the same order of our experimental results [189]. Additionally, the p-type conductivity can possibly also come from the p-type substrate and

[7]The sample F1449 was grown by AIXTRON AG.

from the p-type conductive layer which can be formed at nucleation/substrate interface due to the diffusion process of Al into the Si substrate during the growth [186].

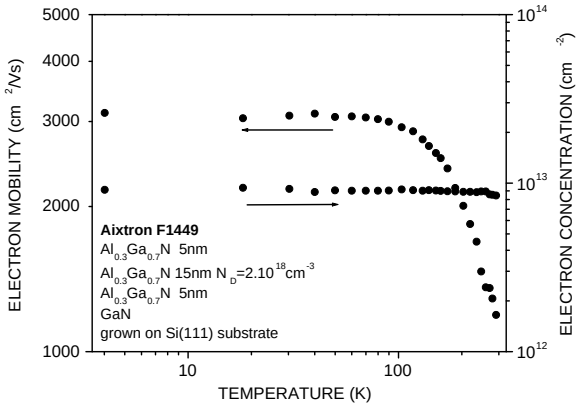

Figure 6.43: Temperature dependent Hall experiment data of $Al_{0.3}Ga_{0.7}N$/GaN MOCVD structure grown on Si(111) (sample F1149).

6.4 Surface and Interface Properties of AlGaN/GaN Heterostructures

The knowledge basis for the application of nitride heterostructures to advanced devices requires an understanding of the electronic properties of their surface and interfaces [161]. The Fermi energy (E_F) at the semiconductor surface relative to the semiconductor band edge (conduction band edge for n-type and valence band edge for p-type), that means the surface potential, has fundamental interest (electronic surface states) and technological relevance, especially for the performance of planar unipolar transistors (MOSFET, HEMTs). In this section we concentrate on the surface potential at GaN(0001), $\mathrm{Al_XGa_{1-X}N}$ alloys and passivated GaN surfaces.

6.4.1 Fermi Level Pinning at $\mathbf{Al_XGa_{1-X}N}$ Surfaces

The $\mathrm{Al_XGa_{1-X}N}$ layers of about 1 μm thickness (x=0.1, $0.3, 0.5, 0.75, 1$) were deposited directly on 6H n-SiC(0001)$_{Si}$ substrates under slightly metal-rich conditions and the GaN MBE layers were grown on top of a GaN template grown by MOCVD also on 6H n-SiC(0001)Si [190]. The active nitrogen is provided by a RF-plasma source operating at 13.56 MHz, 450 W, 1 sccm. The substrate temperature was 770°C during the growth of AlGaN layers and 763°C during the growth of GaN layers. For the GaN surface study the Ga beam equivalent pressure (BEP) is increased from nearly stochiometric conditions, slightly Ga-rich, 2.0×10^{-7} mbar (MK110) to 2.5×10^{-7} mbar (MK111). After deposition the samples were transferred *in-situ* into the XPS unit, where the photoemission spectra were measured with monochromatized Al-K$_\alpha$ radiation (hν=1486.6 eV) and with an overall energy resolution of 0.43 eV. AFM surface morphology characterization was performed on all samples. The Al concentration was determined by Rutherford Backscattering (RBS).

Fig. 6.44 shows the XPS spectra, in the energy range of the valence band, measured on as grown $\mathrm{Al_XGa_{1-X}N}$ layers with increasing Al content. The linear fit of the spectra in the energy region close to the valence band maximum (VBM), convoluted with a Gaussian corresponding to the experimental energy resolution, provides the energy position of the VBM relative E_F.

Let us first focus on some details of the energy dispersion curve of the valence band (VB). The energy width of the VB, about 8 eV, is essentially the same in the whole alloy range. This is in very good agreement with theory [191]. Besides the obvious opening of the gap in going from GaN (bottom) to AlN (top), also a change in the shape of the valence band is observed: by increasing the Al content the upper half of the VB broadens and correspondingly the intensity relative to the pronounced peak in the lower half decreases. Detailed calculations of the band structure and density of states (DOS) for the group-III nitrides [191] are taken here for the sake of discussion. The different hybridiza-

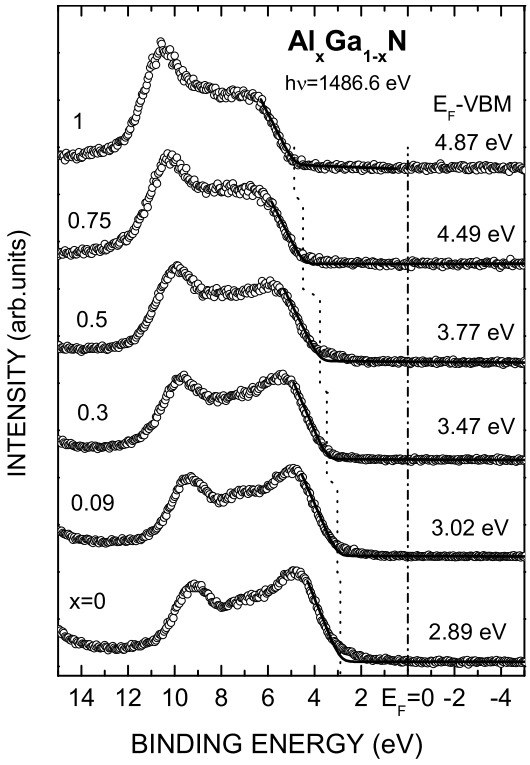

Figure 6.44: In-situ photoemission (XPS) valence band spectra of a series of $\mathrm{Al_XGa_{1-X}N}$ layers ($\sim$1 μm of thickness, x from 0 to 1.0). The energy distance between the Fermi level (BE=0) and the valence band maximum was determined by fi tting the measured spectra in a small region close to the VBM (continuous line).

tion between *d* and *p* states for the cations and nitrogen might be related to the differences observed in the experiment. In fact, the density maximum of N states of *p* symmetry is located in the upper half of the VB at the same energy as the Al *d* and *p* states, but they provide a stronger hybridization for AlN than for GaN. The stronger orbital overlap might be the reason for the broadening by increasing the Al content in the layer.

The Fermi level pinning, distance between Fermi level and Valence Band Maximum, increases at higher Al composition. The Fermi level at the surface is found in the upper part of the gap for the whole AlGaN alloy range and in the band scheme a depletion region is formed under the surface for a n-type semiconductor displayed in the fig. 6.45 (left). The measured Fermi level position at different Al concentration is summarized in the plot 6.45 (right). The band gap (E_G) and the surface potential increase at increasing Al composition.

In the MBE process the dependence of the surface morphology of GaN layers on the Ga/N ratio has recently been studied and a GaN growth diagram has been suggested, in

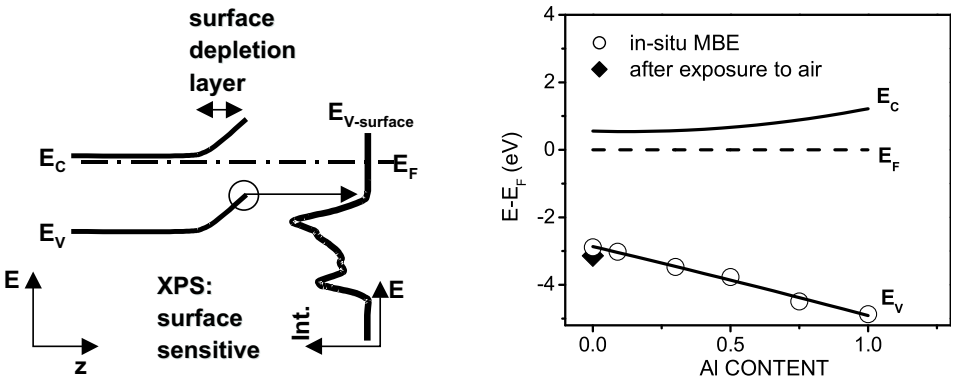

Figure 6.45: An depletion layer is formed under the n-type semiconductor surface due to the Fermi level pinning (left). Measured Fermi level pinning position of AlGaN at the surface displayed as function of Al content (right). The gap energy was added to the measured points using the following approximation $E_G(x) = (1-x) \cdot Eg(GaN) + x \cdot Eg(AlN)b \cdot x(1-x)$, where $b = (0.98 \pm 0.1)$ eV [192].

which three main regions are identified as a function of increasing Ga flux: N-stable, intermediate Ga-stable and Ga-droplets [164]. It is still unclear which regime between the intermediate Ga-stable and beginning of the Ga-droplets formation provides the optimum films and structures. Figure 6.46 shows the AFM images of the MOCVD template [190] and MBE layers grown with different Ga/N ratio on top of the MOCVD template. The surface of the sample MK110 (fig. 6.46b), which was grown under nearly stochiometric conditions is characterized by flat regions between small pit features. The surfaces of films grown under Ga-rich conditions close to the Ga-droplet regime (fig. 6.46c, sample MK111) had atomically flat surfaces with no pit features; the spiral hillocks are associated with the presence of pure screw or mixed dislocations.

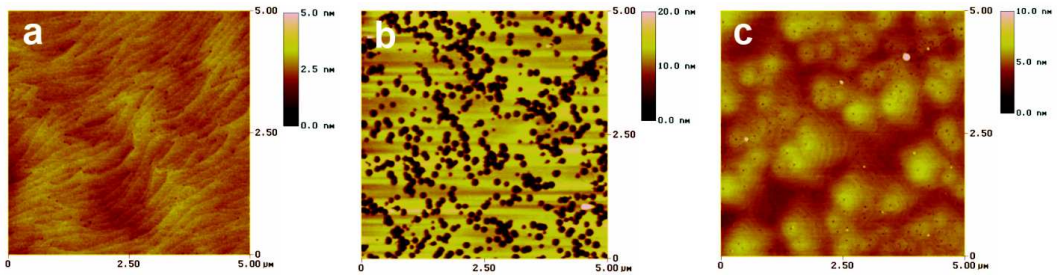

Figure 6.46: AFM images showing the surface morphology of GaN fi lms grown by MBE on the MOCVD template (a) using a Ga flux of: BEP(Ga)=2.0×10^{-7} mbar (sample MK110) (b) and BEP(Ga)= 2.5×10^{-7} mbar (sample MK111) (c).

The two MBE samples were investigated using Transmission Electron Microscopy (TEM) in order to see differences of the dislocation distribution between MBE and MOCVD growth. Figure 6.47 (left) shows cross-sectional bright-field TEM image of sample MK111 taken under two-beam imaging conditions with g=(0002) close to a $11\bar{2}0$ zone axis orientation of the specimen. The graded AlGaN/AlN interlayer separating the MOCVD GaN epilayer from the 6H n-SiC(0001) substrate is characterized by high density of dislocations which partly extend as threading into the GaN epilayer. A small number of this threading dislocations, indicated by the arrows, have nucleated approximately 300nm below the free surface, *i.e.* at that position along the 0001 growth direction where the MBE process was started. Figure 6.47 (right) shows cross-sectional bright-field micrograph of sample MK110 taken under two-beam imaging conditions with $g = (2\bar{2}00)$ close to a $11\bar{2}0$ zone axis orientation of the sample. Compared to figure 6.47 (left), the line directions of the threading segments penetrating the GaN layer are less uniformly distributed. Moreover, the free surface of the epilayer is characterized by a higher degree of roughening as expressed by trough-shaped undulations with a depth of about 30 nanometres.

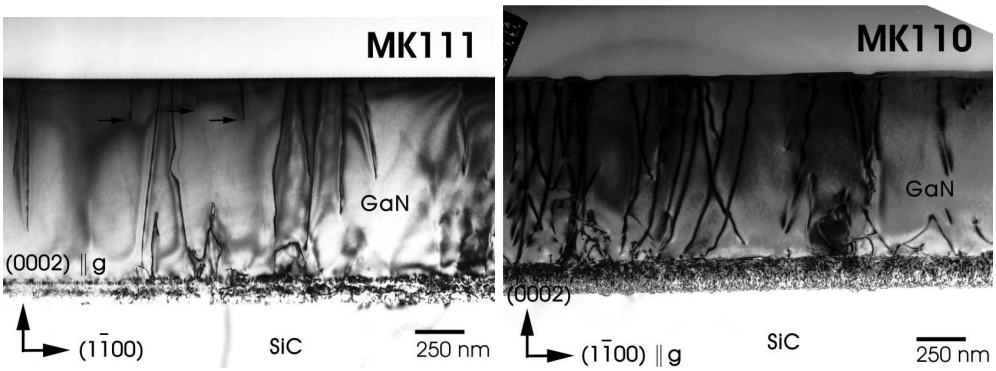

Figure 6.47: Cross-sectional bright-fi eld TEM image of sample MK111 (left) and of sample MK110 (right).

A recent scanning current-voltage microscopy (SIVM) study has pointed out that samples grown under Ga-rich conditions show three orders of magnitude higher reverse bias leakage compared with those grown under Ga-lean conditions [168]. The reverse bias leakage occurs predominantly at dislocations with a screw component. Furthermore, cross-sectional TEM images reveal microscopic Ga droplets at the surface terminations of pure screw dislocations in these samples. According to our study this is also correlated to different surface electronic properties.

Fig. 6.48 (left) shows the occupied density of states (DOS) at the GaN surface as measured by in-situ XPS. Zero binding energy corresponds to the Fermi energy. The linear fit of the spectra in the energy region close to the valence band maximum (VBM), convoluted with a Gaussian corresponding to the experimental energy resolution, pro-

vides the energy position of the VBM relative to E_F. The bottom spectrum (a) is that of the MOCVD template, after insertion into UHV and subsequent annealing. After MBE growth of GaN (300 nm of thickness) in the intermediate Ga-stable regime (b, MK110) almost the same XPS spectrum is measured, with the same Fermi-level pinning position ($E_F - E_{VBM} = 2.89$ eV). Quite differently appears the XPS spectrum of the sample grown under more Ga-rich conditions (c, MK111): an additional DOS feature at the Fermi level is superimposed to the typical GaN spectrum for which now the VBM occurs at $E_F - E_{VBM} = 1.65$ eV. Both samples have been exposed to air for at least 1 day and after reinsertion into UHV the XPS spectra have been measured again; the same spectrum is obtained for the two samples, MK110 and MK111 (fig. 6.48d), with $E_F - E_{VBM} = 3.14$ eV.

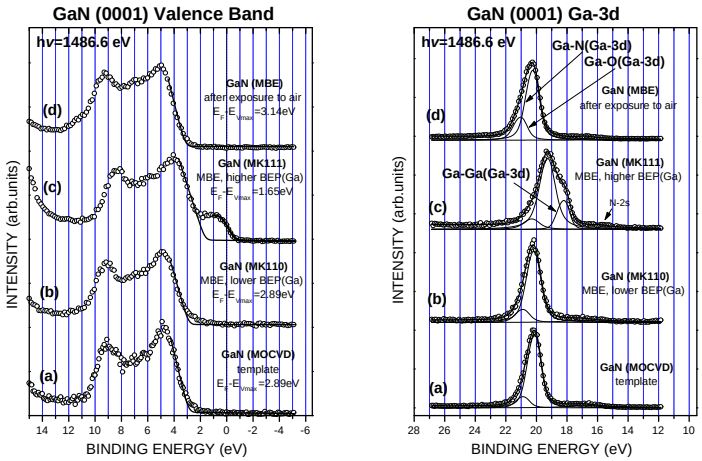

Figure 6.48: XPS spectra in the energy region of the valence band (left side) and of the Ga-3d core level (right side) measured at different GaN surfaces. (a) MOCVD template after UHV annealing at 770 °C, 10 min; MBE as grown surfaces (b) MK110: BEP(Ga)=2.0×10^{-7} mbar and (c) MK111: BEP(Ga)=2.5×10^{-7} mbar; (d) after exposure to air and reinsertion in UHV (see text). The solid lines represent the best fit close to the VBM region (left side), which provides the indicated VBM energy and the best fit of the Ga-3d core level (right side) decomposed in its single components.

The XPS results point out that also the surface electronic properties of GaN depend on MBE growth conditions. The Ga-lean sample (MK110) has the same electronic features as the GaN MOCVD template, even though the surface morphology looks quite different: atomically flat and with wide terraces for the template as compared with the pitted morphology of the MBE layer (fig. 6.46a,b). However the surface states which cause the pinning of the Fermi level must be of the same nature. On the other hand the spectra of the Ga-rich sample clearly indicate the formation of a metallic Ga surface: a clear Fermi edge in the density of occupied states and correspondingly a clear Ga-Ga component in

the fit of the Ga-3d core level (fig. 6.48c). In the presence of small Ga droplets at the surface of GaN a superposition of a metallic DOS with the GaN one would be expected, without any change in the band bending. The fact that both, the spectra in the VBM region as well as of the Ga-3d core levels, are shifted to lower binding energy suggests that the surface morphology of fig. 6.46c (MK111) is also associated with the formation of a thin metallic Ga layer covering the GaN surface. Therefore, instead of considering a changed surface potential an initial formation of a Ga/GaN Schottky barrier appears more adequate. After exposure to air the metallic features of sample MK111 disappeared and the same spectrum as for the Ga-lean sample was obtained. Furthermore the typical shoulder in the DOS close to the VBM of the template and sample MK110, always observed on the as grown surface, disappeared too. A similar behavior was observed after adsorption of air on low Al content surfaces (not shown here) and after adsorption of activated hydrogen on an AlN surface [193]. The exposure to the atmosphere causes a VBM shift of 0.2 eV to higher binding energies for the template and the Ga-lean sample (MK110), *i.e.* a lower surface potential. A fit of the Ga-3d core level shows two components: the Ga-N main one and a secondary component assigned to Ga-O as shown in fig. 6.48 (right). The Ga-O component, of low intensity at the freshly prepared surface obviously increases after exposure to air, which points to the formation of a thin Ga-oxide layer at the surface (fig. 6.48d (right side)). The measured $E_F - E_{VBM}$=3.14 eV is the one relevant for applications.

The measured surface band bending and the changes induced by adsorption of gaseous species and metallic layer infer the presence of surface states within the gap. The GaN MBE layer grown using Ga-lean growth conditions, MK110, compared to the template

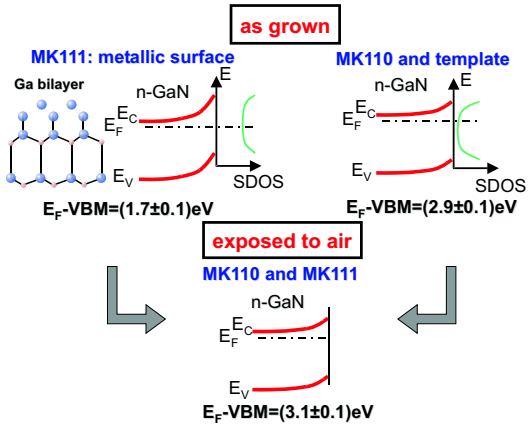

Figure 6.49: Band bending under the surface of as grown and air-exposed GaN MBE layers grown under different conditions. The values of the Fermi level pinning measured by XPS are displayed. The surface of the Ga-rich grown sample, MK111, have a Ga-adatom bilayer on the surface according to the theoretical investigations of Zywietz *et al.* [194].

shows the same surface potential and bend bending under the surface. The Ga-rich grown sample, MK111, results to larger upwards band bending and the surface states are more positively charged than the ones on template. We can imagine that the surface is covered by Ga-bilayer according to the theoretical studies of Zywietz *et al.* [194]. Since for the n-GaN the surface potential decreases after exposure to air, we can conclude that the surface states of the as grown surface are more negatively charged than the ones on the surface exposed to air. The band bending under the surface of the GaN MBE surfaces with measured surface potentials are summarized in figure 6.49.

6.4.2 Si_3N_4 Passivation

In this section, the issue of surface passivation is addressed, which turns out to be very important for HEMT device performance.
An approximately 3 nm thick Si_3N_4 layer was formed on an AlGaN surface by reactive deposition in the MBE chamber.
First, the formation of Si_3N_4 on a n-Si(100) surface was investigated, by reaction of activated nitrogen from the plasma source. Several experiments with different substrate temperature and reaction time were done. The attempts are summarized in the following table:

Sample name	Plasma source power (W)	N flux (sccm)	T_{SUB} (°C)	Time (min)	Si_3N_4 formation (yes/no)
MK92	450	1	27	10	no
MK93	450	1	150	5	no
MK93-1	450	1	150	+5	no
MK94	450	1	300	5	no
MK95	450	1	600	5	yes
MK95-1	450	1	600	+10	yes
MK96	450	1	700	10	yes
MK97	450	1	600	30	yes

The measured Si-*2p* core level peak by XPS of the samples listed in the table above are shown in the figure 6.50 (left panel). The reacted component of the Si-*2p* at higher binding energy with a chemical shift of 2.5 eV is the fingerprint of Si_3N_4 formation [195]. This Si_3N_4 component of the Si-*2p* core level at the binding energy of BE=102 eV starts to form at the substrate temperature of 600°C and 5 min of the Si(100) substrate reaction with the atomic nitrogen provided by RF plasma source operating at 450 W, 1 sccm. After 30 min at T_{SUB}=600°C the highest ratio between the Si_3N_4 component and Si-*2p* core level peak in the XPS spectra was reached. The XPS spectra are displayed in fig. 6.50 left graph at the top and in the right graph (a). The unreacted Si-*2p* component arises from the substrate. The thickness of the Si_3N_4 layer is estimated to be $\sim$3 nm.

Fig. 6.50d (right panel) shows the Ga-*3p* and Al-*2s* core level spectra of the as grown $Al_{0.25}Ga_{0.75}N$ 22 nm/GaN 1.6 μm/AlN 100 nm layer structure on the 6H n-SiC substrate (sample MK101). A fit of the Ga-*3p* peak evidences two components: a Ga-N main one and a further component, which is assigned to Ga-Ga metal bonds. This latter reflects the Ga-rich surface obtained for MBE optimum growth conditions.

Next the Si_3N_4 on top of the $Al_{0.25}Ga_{0.75}N$ layer (sample MK101) was deposited in two steps. First the sample was set vertically in front of a Si-wafer, which was heated up through current flow and Si was evaporated on the surface of the AlGaN layer. Subsequently the sample was moved down and set horizontally into the usual growth position. The reaction of the active nitrogen with the Si on the surface followed. The parameters for Si_3N_4 formation on top of an $Al_{0.25}Ga_{0.75}N$ 22 nm/GaN 1.6 μm/AlN 100 nm/6H-n-SiC heterostructure (sample MK101) in our MBE system is summarized in the following table:

Sample name	Effect	T_{Si} (°C)	T_{SUB} (°C)	Plasma source	Time (min)
MK101-1	Si evaporation	939	400	OFF	35
MK101-2	N reaction	-	600	450W/1sccm	30

Fig. 6.50b,c shows the measured XPS spectra. First step of the silicon nitride formation is

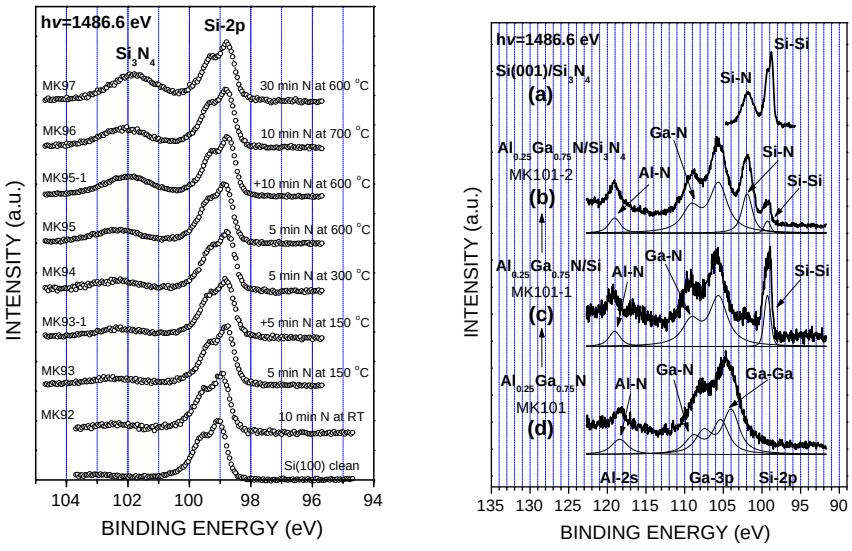

Figure 6.50: The formation of silicon nitride was optimized on Si(100) layer (left) and on AlGaN layer (right). The XPS spectra of Si-*2p* core level and Si_3N_4 reacted component are displayed on the left side. The right graph shows XPS spectra of (a) silicon nitride formed on a Si surface, (b) silicon nitride formed on the AlGaN layer, (c) Si evaporated on AlGaN layer and (d) clean AlGaN surface.

displayed in fig. 6.50c. Clear Si-*2p* peak is seen in the XPS spectra confirming the formation of thin Si layer on AlGaN surface. At the same time the metallic Ga-*3p* component disappears, leaving a clear Ga-N Ga-*3p* single component spectrum. The next step of the silicon nitride formation is shown in fig. 6.50b. The Si-*2p* chemically shifted component indicates the formation of Si_3N_4. Since the estimated silicon nitride thickness is $\leq$3 nm also photoelectrons from the underlying AlGaN layer are revealed.

A small shift (ΔBE$\leq +0.2$ eV) of the energy position of the Ga-*3p* Ga-N component after silicon nitride deposition is measured. The Fermi level at the interface is still found in the same energy range, as on the clean surface. The surface state distribution which pins E_F must be similar to that of the interface states formed at Si_3N_4/AlGaN.

Vetury *et al.* [133] reported a suppression of the current collapse of a AlGaN/GaN HEMT device (see also subsection 2.3.3) through surface passivation with a silicon nitride layer. The fact that the Fermi level does not change its position at the Si_3N_4/AlGaN interface as compared to the free surface preserves the charge balance across the structure and therefore the 2DEG concentration. Furthermore, the low conductivity of the passivation overlayer prevents the transfer of electrons from the gate to the interface layer and the formation of a virtual gate as in the case of the free surface.

Chapter 7

Conclusions

Aim of the work was to optimize the growth of III-nitrides on different substrates by molecular beam epitaxy in order to grow a AlGaN/GaN HEMT structure and to study the surface and interface properties which form the knowledge basis for understanding and improving the performance of AlGaN/GaN HEMTs.

The III-N growth was performed by molecular beam epitaxy with Galium, Aluminium, Silicon effusion cells and UNI-bulb RF-plasma source which provides the active nitrogen. The III-nitrides growth optimization was performed on insulating and conductive substrates. The optimized GaN buffer layer grown on insulating SiC substrate shows terraces on the surface indicating step flow growth with RMS roughness of 0.8 nm on $1 \times 1\ \mu\mathrm{m}^2$ area measured by AFM. Due to the poor structural properties of i-SiC substrates, it was possible to observe 2DEG behavior of AlGaN/GaN grown structures only after inserting an AlN interlayer into the GaN buffer layer. The interlayer induces the bending of threading dislocations and finally reduces the number of dislocations that penetrate trough the 2DEG region. The energy band scheme simulation by means of the self consistent Schrödinger-Poisson calculation of the grown 2DEG structure reveals a depletion layer above the interlayer which isolates the 2DEG from the bulk. A parasitic effect is a small parallel channel formed below the interlayer.
Hall effect measurements of the AlGaN/GaN heterostructure without interlayer grown on conductive substrate indicate a 2DEG behavior. Qualitative scattering mechanism was performed comparing our MBE samples grown on n-SiC with MOCVD high quality samples from different laboratories with similar Al content in the $\mathrm{Al_XGa_{1-X}N}$ barrier. Optical phonon scattering is dominating at high temperatures. Towards to low temperatures assuming similar dipole, alloy, interface scattering for both types of samples, the lower mobility of the MBE samples is ascribed to a higher dislocation density and residual impurities.
For the optimization of the 2DEG conductivity in AlGaN/GaN heterostructures, Al content in the barrier should be as high as possible in order to increase the electron concentration.

On other hand the wave functions of the electrons confined at the interface penetrate into the barrier for high n_S (high x values), that lowers the mobility due to the dipole, alloy disorder, interface roughness scattering.
Fabricated $Al_{0.3}Ga_{0.7}N$/GaN HEMT on insulating SiC substrate with a gate length of 0.3 μm shows unity gain frequency of 6.8 GHz and maximum frequency of oscillation 15 GHz.

The growth optimization of AlGaN/GaN heterostructure on Si substrate differs from the one on SiC substrate, especially due to the high lattice and thermal mismatch between the substrate and the GaN layer. The growth beginning has to be treated in different way, because of the possible silicon nitride formation on a clean Si surface. Significant improvement of the GaN structural quality and surface morphology was achieved inserting AlGaN interlayer between nucleation and buffer layer, which reduces the lattice and thermal mismatch between GaN and the substrate. Such grown GaN layer shows terraces on the surface indicating step flow growth. The surface roughness is 0.88 nm measured by AFM on 5×5 μm^2 scan area. The 2DEG structures characterized by temperature dependent Hall measurement show more than one conductive channels present in the structure and both types of conductivities. Similar anomalous behaviors are reported in the literature and different assumptions are discussed to clarify the origin of the p-type conduction. Using energy band scheme simulation of the whole layer structure by means of the self consistent Schrödinger-Poisson calculation reveals the possible p-type conduction in the 2DEG structure. Due to the polarization charges, strong induced electric fields in the AlGaN interlayer region bend the valence band maximum towards the Fermi level and cause formation of two dimensional hole gases.
Results of the calculation show possible reason for p-type conductivity observed in our structures additionally to already discussed p-type conductivities in literature. Indeed the 1 μm thick GaN layer is not resistive enough to electrically insulate the active structure from parallel channels in the nucleation-substrate region.

To improve the electrical properties of grown MBE 2DEG AlGaN/GaN heterostructures independent on substrate, it is necessary to reduce the background concentration of unintentionally doped nitride layers in order to make the parallel channel effects resulting from optimizing treatments of inserted interlayers ineffective. Thus can be achieved by compensation doping of grown GaN layers. Unfortunately, it was not possible in our MBE growing system due to the limited number of ports that do not allow to include a p-type doping source as Mg.
The electron mobility as a important parameter of the AlGaN/GaN nitride layer structure can be increased drastically by reducing the dislocation densities. For the growth on SiC substrate, its flat surface morphology is necessary to grow high quality GaN layers. The use of hydrogen treated SiC substrates (H_2^* etching should become a standard procedure) promises to improve the surface morphology of grown layers. A necessary further improvement in the growth of nitride based heterostructures on Si(111) substrate requires a complex engineering of the nucleation-buffer layer structure and insertion of AlN inter-

layer in order to compensate the tensile strain built-up during the growth of thick GaN layers.

All the difficulties resulting from the growth of III-nitrides on foreign substrates will be solved after GaN wafers as substrates become available.

The properties of AlGaN/GaN heterostructures were studied theoretically using energy band scheme simulation by means of self consistent Schrödinger-Poisson calculation.

Dramatic effect of polarization charge on the 2DEG formation at the AlGaN/GaN interface was found. No quantum well is formed at the heterojunction and no electron confinement results if no polarization and modulation doping is used. Introducing also the polarization charge into the calculation a triangular quantum well is formed and electrons are confined in quasi-2D electron gas. The polarization charge plays an important role in formation of 2DEG in AlGaN/GaN heterostructures.

The influence of surface states is included into the calculation by introducing the measured surface potential as a boundary condition. No quantum well is formed for low Al content in the barrier of an AlGaN/GaN heterostructure if no surface Fermi level pinning is assumed. Introducing the surface Fermi level pinning into the simulation, 2DEG is formed and higher electron concentrations are confined. These calculations together with the experimental results on electronic properties of AlGaN surfaces give some insight in the origin of 2DEG in unintentionally doped AlGaN/GaN heterostructures. We believe that an important role is played by electrically active surface states of the AlGaN, which are responsible for the surface Fermi level pinning. The lower value of surface Fermi level pinning found in the experiment corresponds to a lower value of electric field in AlGaN barrier and therefore to a positive charge of the surface states which partially screens the negative polarization charge. This positive charge of donor-like surface states arises from the transfer of electrons into the 2DEG.

The 2DEG concentration is less sensitive to the influence of Fermi level pinning at the surface for higher x values in $\mathrm{Al_XGa_{1-X}N}$ barrier due to the higher polarization charge, higher conduction band offset and hence better electron confinement in the AlGaN/GaN heterostructure.

With the aim of optimization of the AlGaN/GaN heterostructure several simulations with different Al content in the barrier, barrier thickness and doping were performed. Higher electron concentration at the AlGaN/GaN interface is reached using higher Al content due to the higher polarization charge at the AlGaN/GaN interface. The influence of barrier thickness is less significant. The doping in the barrier can increase the 2DEG concentration too, similar to the conventional AlGaAs/GaAs modulation doped heterostructures. High donor concentration, more than $10^{19}\,\mathrm{cm}^{-2}$, can lead to parallel channel formed in the AlGaN barrier depending on the barrier thickness. The higher electron concentration in the barrier can cause higher gate leakage current, higher pinch-off voltage and degradation of high frequency properties of HEMT devices. To

achieve high conductivity in the AlGaN/GaN HEMT heterostructures for high power applications according to the simulations, we suggest to grow AlGaN barrier layers with Al content between 0.25-0.40 and barrier thickness 30-20 nm in order to get high electron concentration in the 2DEG. Notice that high values of Al content reduce the critical thickness of the barrier and relaxation can occur. Thus drastically decrease the piezoelectric polarization charge and finally the 2DEG concentration. Additionally, high Al compositions cause high polarization charge at the interface and consequently reduce the mobility due to the dipole, alloy disorder, interface roughness and interface charge Coulomb scattering.

Surface and interface electronic properties of AlGaN, GaN layers were studied experimentally. The surface potential increases at higher Al composition of as-grown $Al_XGa_{1-X}N$ layer. The Fermi level at the surface is found in the upper half of the energy gap for whole AlGaN alloy range and in the band scheme an electron depletion region is formed under the surface for a n-type semiconductor. The measured surface potential of $Al_XGa_{1-X}N$ layers is used as a boundary condition for the energy band scheme simulation performed by self consistent Schrödinger-Poisson calculation.
Furthermore, we found that electronic surface properties of GaN layers do not depend from the surface morphology, but show dependence on the growth conditions and are the same for air exposed GaN samples independent from growth conditions.
The surface potential of a silicon nitride passivated AlGaN layer does not change compared to the free AlGaN surface. Thus preserves the charge balance across the structure and therefore the 2DEG concentration. Furthermore, the low conductivity of the passivation overlayer prevents the transfer of electrons from the gate to the interface layer and the formation of a virtual gate of a HEMT device as in the case of the free surface where the current collapse occurs.

Finally, we can conclude that studying the surface, interface and device electronic properties helps to understand better the physics and to improve the performance of a AlGaN/GaN heterostructure for HEMT applications. The provided theoretical and experimental work gives better insight view of the origin and of the properties of a 2DEG in AlGaN/GaN structure, and its dependence on other important parameters. To optimize the performance of AlGaN/GaN layer structure for HEMT applications it is essential to assume an interplay of surface, interface and device properties.

Chapter 8

Zusammenfassung

AlGaN/GaN MBE 2DEG Heterostrukturen: Wechselwirkung zwischen Oberflächen-, Grenzflächen- und Bauelemente-Eigenschaften

Das Ziel dieser Arbeit war die Optimierung des Wachstums von AlGaN/GaN HEMT Heterostrukturen auf verschiedenen Substraten mittels Molekularstrahlepitaxie und die Untersuchung der Oberflächen- und Grenzflächen-Eigenschaften der hergestellten III-Nitride Halbleiter, um die physikalischen Eigenschaften der HEMT Bauelemente zu verbessern.

Die Herstellung der Schichten erfolgte in einem MBE-System, das mit einer UNI-Bulb RF-Plasmaquelle zur Erzeugung von reaktiven atomarem Stickstoff aus N_2 sowie mit Effusionszellen zur Verdampfung von Gallium, Aluminium und Silizium ausgestattet ist. Es wurden Substrate aus SiC und Si eingesetzt. Für die Optimierung des Wachstums auf den SiC Substraten wurden die Wachstumsparameter der drei einzelnen Schichten der 2DEG-Struktur: AlN Nukleationsschicht, GaN Pufferschicht und AlGaN Barriere variiert. Bei der optimierten GaN Pufferschicht, die auf isolierenden SiC gewachsen ist, zeigen sich Terrassen auf der Oberfläche, was auf ein Step-flow Wachstum hindeutet. Die Rauhigkeit beträgt 0.8 nm auf einer 1×1 μm^2 großen Fläche. Die strukturellen Eigenschaften sind im Vergleich mit einer GaN Schicht, die auf leitendem SiC Substrat gewachsen ist, viel schlechter, obwohl die Oberflächenmorphologie des teueren isolierenden SiC Substrats viel besser ist. Der Grund dafür sind schlechtere strukturellen Eigenschaften des i-SiC Substrats, die sehr wahrscheinlich eine Auswirkung auf die gewachsene Schicht haben. Die 2DEG Struktur, die auf einem isolierenden SiC deponiert worden ist, zeigt in der Temperatur-abhängiger Hall-Effekt-Messung kein 2DEG-Verhalten. Erst nach Einführung einer zusätzlichen AlN Zwischenschicht in die GaN Pufferschicht wurde das Verhalten eines 2DEGs in der Hall-Effekt Messung beobachtet. Durch die Zwischenschicht wird die Krümmung der Pfaden-Versetzungen induziert und letztendlich führt dies

zur Verringerung der Zahl dieser Versetzungen. Anhand selbstkonsistenter Lösung der Schrödinger und Poisson Gleichung wurde die Simulation der Bänderschema der gewachsenen Heterostruktur durchgeführt. Oberhalb der AlN Zwischenschicht wird zusätzlich eine Verarmungszone gebildet, die das 2DEG von der GaN Bulk-Schicht elektrisch trennt. Ein negativer Effekt ist die Bildung eines kleinen parallelen Kanals unterhalb der Zwischenschicht.
Die optimierte AlGaN/GaN Heterostruktur, die auf leitenden SiC gewachsen ist, zeigt 2DEG Verhalten ohne zusätzlicher AlN Zwischenschicht in der GaN-Pufferschicht. Die Streuungsmechanismen der gewachsenen MBE Schichten wurden mit MOCVD Schichten qualitativ verglichen. Zu diesem Zweck wurden Proben mit ähnlichem Al Gehalt der $Al_XGa_{1-X}N$ Barriere gewählt. Streuung an optischen-polar Phononen dominiert bei hohen Temperaturen. Wenn man annimmt, dass bei niedrigen Temperaturen die Dipol-, Legierungs- und Rauhigkeits-Streuung für alle Proben ähnlich sind, kann die niedrigere Beweglichkeit der MBE Proben durch die Versetzungstreuung und die Streuung an ionisierten Störstellen verursacht werden (wenn die gemessene parallele Leitfähighkeit zu dem 2DEG durch Störstellen, wie Sauerstoff, in der MBE Pufferschicht gegeben ist).
Für die Optimierung der Leitfähighkeit eines 2DEGs in der AlGaN/GaN Heterostruktur sollte nach den durchgeführten Simulationen der Al Inhalt in der Barriere möglichst hoch sein, um eine hohe Elektronenkonzentration zu erreichen. Auf der anderen Seite dringen die Wellenfunktionen der Elektronen des 2DEGs für hohe Werte von n_S (hohes x) mehr in die Barriere ein und es kommt zur Verringerung der Beweglichkeit durch Dipole-, Legierung- und Rauhigkeit-Streuung.
Planares $Al_{0.3}Ga_{0.7}N$/GaN HEMT wurde auf einem isolierenden SiC Substrat mit einer Gate-Länge von 0.3 μm hergestellt. Bei dieser Gate-Länge wurde eine Grenzfrequenz von 6.8 GHz and eine maximale Schwingfrequenz von 15 GHz erreicht.

Die Optimierung des Wachstums der AlGaN/GaN Heterostruktur auf Si Substrat unterscheidet sich von der auf SiC. Eine dünne Siliziumnitrid Schicht kann sich auf der reinen Oberfläche des Siliziums bilden, wenn als erstes eine GaN Schicht gewachsen wird. Deshalb werden zuerst ein paar Monolagen von Al deponiert und dann wird eine AlN Schicht gewachsen. Der nächste Schritt ist die GaN Pufferschicht. Bedeutende Verbesserung der strukturellen Eigenschaften und Oberfächenmorphologie wurde mit Einführung einer AlGaN Zwischenschicht zwischen AlN Nukleationsschicht und GaN Pufferschicht erzielt. Die Zwichenschicht verringert die Gitterfehlanpassung und die Anpassung des thermischen Ausdehnungskoeffizienten zwischen der GaN Schicht und dem Substrat. Solche GaN Schichten zeigen Terrassen auf der Oberfläche, die auf Step-flow Modus des Wachstums hindeuten. Die mit AFM gemessene Rauhigkeit beträgt 0.88 nm auf einer 5×5 μm^2 großen Fläche. Nur geringfügige Verbesserung der strukturellen und der Oberflächen-Eigenschaften wurde mit einer gradierten $Al_XGa_{1-X}N$ Schicht als Zwischenschicht erzielt. Der letzte Schritt der Optimierung ist das Wachstum der AlGaN Barriere auf der GaN Pufferschicht. Die 2DEG Strukturen, die mit Temperatur-abhängiger Hall Effekt Messung charakterisiert wurden, zeigen mehr als ein leitender Kanal in der

Struktur mit beiden Typen, n und p, der Leitfähigkeit. Ähnliches Verhalten ist auch in der Literatur erwähnt und es werden verschiedene Ursachen zur Erklärung der p-Typ Leitfähigkeit diskutiert. Die Simulation der Bänderschema mittels selbstkonsistenter Lösung von Schrödinger und Poisson Gleichung der ganzen Heterostruktur wurde durchgeführt, um die Ursache des parallelen p-Kanals in der Probe aufzudecken. Die durch die Polarisationsladung induzierte starke elektrische Felder in der AlGaN Zwischenschicht verursachen die Krümmung des Valenzbandmaximums gegenüber dem Fermi-Niveau und führen zur Bildung einer zwei-dimensionalen Löchergase (2DHGs).
Das Ergebnis der Berechnung zeigt weitere mögliche Ursachen des p-Typs der Leitfähigkeit in unserer Struktur, zusätzlich zu den schon diskutierten p-Kanälen in der Literatur. In der Tat ist die 1 μm dicke GaN Schicht nicht ohmisch genug um die aktive Struktur von den parallelen Kanälen in dem Nukleationsschicht- und Substrat-Bereich elektrisch zu isolieren.

Die elektrischen Eigenschaften der deponierten MBE 2DEG AlGaN/GaN Heterostrukturen auf verschiedenen Substraten werden durch Reduzierung der Hintergrunddotierung der GaN Schichten verbessert, damit die von dem Optimierungsverfahren stammenden parallelen Effekte der Zwischenschichten unwirksam werden. Dies könnte durch Kompensationsdotierung der GaN Schichten erreicht werden. Bedauerlicherweise war dies in unserem MBE-System nicht möglich, weil die limitierte Anzahl der Zellenanschlüsse den Einbau einer p-Quelle, wie z.B. Mg, nicht erlaubt.
Die Elektronenbeweglichkeit kann durch Verringerung der Störstellenkonzentration drastisch erhöht werden. Für das Wachstum von hochwertigen III-N Halbleiter auf SiC Substraten ist die glatte Oberfläche des Substrates von sehr großer Wichtigkeit. Das Ätzen der SiC Substrate bei hoher Temperatur in der H_2^* Atmosphäre (sollte Standard-Reinigungsprozedur werden) verspricht die Oberflächenmorphologie zu verbessern. Erforderliche Verbesserung des III-N Wachstums auf Si Substraten fordert komplexes Studium der Nukleation-Puffer-Struktur, um die tensile Verspannung zu kompensieren, die sich während des Wachstums der dicken GaN Schicht bildet. Dies kann durch Einsetzen von AlN Zwischenschichten erreicht werden [67].

Alle Schwierigkeiten, die bei der Optimierung des III-Nitride Wachstums entstehen, könnten gelöst werden, in dem die GaN Wafers als Substrate verfügbar werden.

Die Eigenschaften der AlGaN/GaN Heterostrukturen wurden theoretisch mit der Simulation der Bänderschema mittels selbstkonsistenter Lösung von Schrödinger und Poisson Gleichung untersucht.
Der dramatische Effekt der Polarisationsladung auf die Bildung des 2DEGs an der AlGaN/GaN Grenzfläche wurde bestätigt. Es werden kein Quantentopf und kein 2DEG an dem Heteroübergang gebildet, wenn keine Polarisationsladung und Modulationsdotierung in die Simulation eingegeben ist. In der Tat, induziert die Verkrümmung der Bänder eine Verarmungszone über die AlGaN/GaN Grenzfläche. Wenn auch die Polarisationsladung in die Berechnung eingegeben wird, wird ein dreieckiger Quantentopf

gebildet und die Elektronen in dem quasi-2D Elektronengas gefangen. Demnach spielt die Polarisationsladung eine wichtige Rolle in der Bildung des 2DEGs in AlGaN/GaN Heterostrukturen.
Der Einfluss der Oberflächenzustände wurde auch in die Berechnung einbezogen, indem das gemessene Oberflächenpotential als Grenzflächenbedingung berücksichtigt ist. Es wird kein Quantentopf für kleine Al Inhalte der Barriere einer AlGaN/GaN Heterostruktur gebildet, wenn kein Fermi-Niveau-Pinning auf der Oberfläche definiert wird. Das durch Polarisationsladung induzierte hohe elektriche Feld führt in der Barriere zur Verarmungszone unterhalb der Oberfläche. Wenn auch das Fermi-Niveau-Pinning auf der Oberfläche in die Berechnung eingegeben wird, wird ein 2DEG gebildet und es werden grössere Elektronenkonzentrationen erreicht. Diese Berechnungen zusammen mit den experimentellen Ergebnissen der elektronischen Eigenschaften der AlGaN Oberfläche ermöglichen eine bessere Vorstellung der Herkunft der Elektronen des 2DEGs einer undotierten AlGaN/GaN Heterostruktur. Wir nehmen an, dass die elektronischen Oberflächenzustände der AlGaN Schicht eine wichtige Rolle spielen. Diese Zustände sind für das Fermi-Niveau-Pinning auf der Oberfläche verantwortlich. Der niedrigere Wert des Fermi-Niveau-Pinnings auf der Oberfläche, der experimentell bestimmt wurde, entspricht einem kleineren elektrischen Feld in der Barriere und deshalb einer positiven Ladung der Oberflächenzustände, die teilweise die negative Polarisationsladung kompensiert. Die positive Ladung der donatorartigen Zustände entsteht durch den Transfer der Elektronen von den Oberflächenzuständen in den 2DEG.
Die 2DEG Konzentration ist auf das Fermi-Niveau-Pinning auf der Oberfläche für höhere x Werte der $Al_XGa_{1-X}N$ Barriere weniger empfindlich. Der Grund dafür ist die grössere Polarisationsladung und Leitungsbanddiskontinuität bei höheren x Werten und deshalb die bessere Einsperrung (confinement) der Elektronen auf der Grenzfläche der AlGaN/GaN Heterostruktur.
Mit dem Ziel der Optimierung von AlGaN/GaN Heterostrukturen wurden mehrere Simulationen mit unterschiedlichen Al Inhalten in der Barriere, Dicken der Barriere und Dotierungen in der Barriere durchgeführt. Wegen der höheren Polarisationsladung wird eine höhere Elektronenkonzentration bei grösseren Werten von x in dem 2DEG auf der AlGaN/GaN Grenzfläche erreicht. Der Einfluss der Barrierendicke ist weniger signifikant. Die dickeren Barrieren führen zur stärkeren Verschiebung des dreieckigen Quantentopfes unterhalb des Fermi-Niveaus und daher werden höhere 2DEG Konzentrationen erreicht. Die Dotierung in der Barriere kann die 2DEG Konzentration auch erhöhen, ähnlich wie bei herkömmlichen AlGaAs/GaAs modulationsdotierten Heterostrukturen. Höhere Dotierungskonzentration, mehr als $10^{19}\,\mathrm{cm}^{-2}$, könnte auf der anderen Seite zur Bildung eines parallelen Kanals in der AlGaN Barriere führen. Dies kann zu höherem Gate-leakage-Strom, höherer pinch-off Spannung und zur Verschlechterung der Hochfrequenzeigenschaften eines HEMTs führen. Um eine hohe Leitfähigkeit in der AlGaN/GaN HEMT Heterostruktur für Hochleistungsapplikationen zu erreichen, sollte die AlGaN Barriere mit einem Al Inhalt zwischen 0.25-0.40 und mit einer

Dicke von 30-20 nm gewachsen werden, um eine grössere Elektronenkonzentrationen in dem 2DEG zu erreichen. Dabei ist zu beachten, dass bei höheren x Werten der $Al_XGa_{1-X}N$ Barriere die kritische Dicke der Barriere reduziert wird und eine Relaxation erfolgen kann. Dies kann drastisch die piezoelektrische Polarisationsladung und letztendlich die 2DEG Konzentration verringern. Zusätzlich, höhere Al Inhalte verursachen höhere piezoelektrische Polarisationsladung an der AlGaN/GaN Grenzfläche und infolgedessen wird die Elektronenbeweglichkeit durch Dipol-, Legierungs-, Rauhigkeits- und Grenzflächenladungs-Coulombstreuung reduziert.

Elektronische Oberflächen- und Grenzflächen-Eigenschaften der AlGaN und GaN Schichten wurden experimentell untersucht. Das Oberflächenpotential, das mit XPS *in-situ* gemessen wurde, vergrössert sich mit höherem Al Gehalt der $Al_XGa_{1-X}N$ Barriere. Das Fermi-Niveau auf der Oberfläche befindet sich für den ganzen Bereich der x Werte der $Al_XGa_{1-X}N$ Schicht in der oberen Hälfte des verbotenen Bandes. Im Bänderschema entsteht unterhalb der Oberfläche eine Verarmungszone für einen n-Typ Halbleiter. Das gemessene Oberflächenpotential wird als Grenzflächenbedingung für die Simulation der Bandstruktur benutzt.
Desweiteren wurde festgestellt, dass die elektronischen Oberflächeneigenschaften der GaN Schicht von den MBE Wachstumsbedingungen abhängig sind. Ga-arm gewachsene MBE Probe mit einer lochartigen Oberflächenmorphologie zeigt die selben elektronischen Eigenschaften wie eine typische MOCVD Probe, die eine glatte Oberfläche mit breiten Terrassen aufweist. Auf der anderen Seite eine Ga-reich gewachsene MBE Probe mit glatter Oberfläche, die mit spiralartigen Hügelchen bedeckt ist, deutet auf Bildung einer Ga-metallischer Oberfläche hin. Entsprechend der theoretischen Untersuchungen von Zywietz *et al.* [194] könnte man sich die Oberfläche so vorstellen, dass die mit einer Ga-Doppelschicht beendet wird. Die Verbiegung der Bänder unterhalb der Oberfläche hat sich in diesem Fall geändert. Anstelle des geänderten Oberflächepotentials denken wir, dass es sich hier mehr um eine Anfangsbildung von Ga/GaN Schottky Barriere handeln könnte. Nach der Exposition auf der Atmosphäre sind die metallischen Zustände verschwunden und die gleiche Verbiegung der Bänder, wie bei Ga-arm gewachsener MBE Probe, wurde festgestellt. Die Verbiegung der Bänder wurde nach dem Aufenthalt der GaN MBE Proben in der Atmosphäre verringert. Die experimentellen Ergebnisse zeigen, dass die elektronische Oberflächeneigenschaften der GaN Schichten nicht von der Oberflächenmorphologie abhängig sind, sondern von den Wachstumsbedingungen, und dass die elektronische Oberflächeneigenschaften der GaN Schichten nach der Exposition in der Atmosphäre gleich sind, unabhängig von den Wachstumsbedingungen.
Das Oberflächenpotential der passivierten AlGaN Schicht mit Siliziumnitrid ändert sich nicht im Bezug auf die freie AlGaN Oberfläche. Dies bewährt das Ladungsgleichgewicht in der Struktur und deshalb bleibt auch die 2DEG Konzentration unverändert. Außerdem wird der Elektronentransport von der Gate-Elektrode zu der Siliziumnitrid/Halbleiter Grenzfläche und die Bildung vom virtuellen Gate eines HEMTs durch die niedrige

Leitfähigkeit der Passivationsschicht verhindert, anders als im Fall der freien Oberfläche, wo der Kollaps des Stromes stattfinden kann.

Zum Schluss können wir zusammenfassen, dass mit der Untersuchung der Oberflächen-, Grenzflächen- und Bauelement-Eigenschaften einer AlGaN/GaN Heterostruktur für HEMT-Anwendung ein besseres Verständnis der physikalischen Abläufe erarbeitet wurde, mit dem die funktionellen Eigenschaften der 2DEG HEMT-Strukturen verbessert werden können. Die durchgeführten theoretischen und experimentellen Untersuchungen geben einen besseren Einblick in die Herkunft und Eigenschaften des 2DEGs einer AlGaN/GaN Heterostruktur und seine Abhängigkeit von anderen wichtigen Parametern. Zur Optimierung der Performance einer AlGaN/GaN Heterostruktur mit der Anwendung von HEMT-Bauelementen ist es notwendig die Wechselwirkung zwischen Oberflächen-, Grenzflächen- und Bauelement-Eigenschaften anzunehmen.

Appendix A

Hall Measurement Program Realization

A.1 Device Commands

The communication between the computer and the electronic instruments for Hall measurement is based on the RS-232 and IEEE-488 interface. All instruments on the bus connected to computer through IEEE-488 interface can be Talker, that transmits data onto the bus to other devices, and Listener, that receives data from other devices through the bus. The Bus Controller is the digital computer, which designates a function to perform to the device on the bus. In the serial communication the user is in charge all the time. The instrument can not initiate communication, determine which device should be transmitting at a given time or guarantee timing between messages. All of this is the responsibility of the user program. The queries and commands need to be properly format and transmit including terminators as one string. The user program has to be prepared to receive a response from the instrument immediately after sending query. Furthermore the program should guarantee that no other communication is started during the response of a query and for 50 ms after the last character of the command is transmitted or after the query operation completes. The communication should not initiate more than 20 times per second.

This section describes the addressed commands and queries used in the program to control the electronic instruments through the bus with personal computer.

Switch box

R	Reset instrument command
Input:	**R[term]**[1]
Description:	Sets switch box parameters to power-up settings.
[term]	Unknown string command
Input:	**[term]**
Returned:	Error!>
Description:	Error message, if unknown string command is used.
In	Control current command
Input:	**In[term]**
Format:	n=0: $I = 0$ A n=1: $I = k \times 10$ nA n=2: $I = k \times 100$ nA n=3: $I = k \times 1$ μA n=4: $I = k \times 10$ μA n=5: $I = k \times 100$ μA n=6: $I = k \times 1$ mA, if the input voltage from the oscillator $U_{OSC} = k \times 0.1$ V, where k is real number from 0 to 10.
Description:	Sets the current.
Example:	**I3[term]** means $I = 1$ μA, if $U_{OSC} = 0.1$ V
?I	Control current query
Input:	**?I[term]**
Returned:	?I n >
Format:	n=0..6: refer to the command description.
Description:	The returned string represents the adjusted current amplitude.
Example:	returned **?I** **6** > means $I = 1$ mA, if $U_{OSC} = 0.1$ V.
An	Control attenuation command
Input:	**An[term]**
Format:	n=0: $A = 0.001$ n=1: $A = 0.01$ n=2: $A = 0.1$
Description:	Sets the attenuation.
Example:	**A1[term]** means $A = 0.01$.
?A	Control attenuation query
Input:	**?A[term]**
Returned:	?A n >
Format:	n=0..2: refer to the command description.
Description:	The returned string represents the adjusted attenuation.
Example:	returned **?A** **2** > means $A = 0.1$.

[1] [term] - terminator character

Gn	Control gain command
Input:	**Gn[term]**
Format:	n=0: $G = 1$ n=1: $G = 10$ n=2: $G = 100$ n=3: $G = 200$ n=4: $G = 500$
Description:	Sets the attenuation.
Example:	**G3[term]** means $G = 200$.
?G	Control gain query
Input:	**?G[term]**
Returned:	?G n >
Format:	n=0..4: refer to the command description.
Description:	The returned string represents the adjusted gain.
Example:	returned **?G** **4** > means $G = 500$.
U+n	Control U+ pole command
Input:	**U+n[term]**
Format:	n=0: U+ pole is joined to contact "0" of sample A n=1: U+ pole is joined to contact "1" of sample A n=2: U+ pole is joined to contact "2" of sample A n=3: U+ pole is joined to contact "3" of sample A n=4: U+ pole is joined to contact "4" of sample B n=5: U+ pole is joined to contact "5" of sample B n=6: U+ pole is joined to contact "6" of sample B n=7: U+ pole is joined to contact "7" of sample B
Description:	Sets the U+ pole of the voltage signal to certain contact of the van der Pauw sample.
Example:	**U+1[term]** means U+ pole joins to contact "1" of sample A.
?U+	Control U+ pole query
Input:	**?U+[term]**
Returned:	?U+ n >
Format:	n=0..7: refer to the command description.
Description:	The returned string represents the contact of the van der Pauw sample, to which the U+ pole is connected.
Example:	returned **?U+** **5** > means U+ pole is joined to contact "5" of sample B.

U-n	Control U- pole command
Input:	**U-n[term]**
Format:	n=0: U- pole is joined to contact "0" of sample A n=1: U- pole is joined to contact "1" of sample A n=2: U- pole is joined to contact "2" of sample A n=3: U- pole is joined to contact "3" of sample A n=4: U- pole is joined to contact "4" of sample B n=5: U- pole is joined to contact "5" of sample B n=6: U- pole is joined to contact "6" of sample B n=7: U- pole is joined to contact "7" of sample B
Description:	Sets the U- pole of the voltage signal to certain contact of the van der Pauw sample.
Example:	**U-0[term]** means U- pole joins to contact "0" of sample A.
?U-	Control U- pole query
Input:	**?U-[term]**
Returned:	?U- n >
Format:	n=0..7: refer to the command description.
Description:	The returned string represents the contact of the van der Pauw sample, to which the U- pole is connected.
Example:	returned **?U-** **4** > means U- pole is joined to contact "4" of sample B.
I+n	Control I+ pole command
Input:	**I+n[term]**
Format:	n=0: I+ pole is joined to contact "0" of sample A n=1: I+ pole is joined to contact "1" of sample A n=2: I+ pole is joined to contact "2" of sample A n=3: I+ pole is joined to contact "3" of sample A n=4: I+ pole is joined to contact "4" of sample B n=5: I+ pole is joined to contact "5" of sample B n=6: I+ pole is joined to contact "6" of sample B n=7: I+ pole is joined to contact "7" of sample B
Description:	Sets the I+ pole of the current signal to certain contact of the van der Pauw sample.
Example:	**I+2[term]** means I+ pole joins to contact "2" of sample A.
?I+	Control I+ pole query
Input:	**?I+[term]**
Returned:	?I+ n >
Format:	n=0..7: refer to the command description.
Description:	The returned string represents the contact of the van der Pauw sample, to which the I+ pole is connected.
Example:	returned **?I+** **6** > means I+ pole is joined to contact "6" of sample B.

I-n	Control I- pole command
Input:	**I-n[term]**
Format:	n=0: I- pole is joined to contact "0" of sample A n=1: I- pole is joined to contact "1" of sample A n=2: I- pole is joined to contact "2" of sample A n=3: I- pole is joined to contact "3" of sample A n=4: I- pole is joined to contact "4" of sample B n=5: I- pole is joined to contact "5" of sample B n=6: I- pole is joined to contact "6" of sample B n=7: I- pole is joined to contact "7" of sample B
Description:	Sets the I- pole of the current signal to certain contact of the van der Pauw sample.
Example:	**I-3[term]** means I- pole joins to contact "3" of sample A.
?I-	Control I- pole query
Input:	**?I-[term]**
Returned:	?I- n >
Format:	n=0..7: refer to the command description.
Description:	The returned string represents the contact of the van der Pauw sample, to which the I- pole is connected.
Example:	returned **?I-** **7** > means I- pole is joined to contact "7" of sample B.

LakeShore Temperature controller 331

***RST**	Reset instrument command
Input:	***RST[term]**
Description:	Sets controller parameters to power-up settings.
CSET	Control loop parameter command
Input:	**CSET** <**loop**>,<**input**>,<**units**>, <**powerup enable**>,<**current/power**>**[term]**
Format:	<loop> Specifies which loop to configure: 1 or 2 <input> Specifies which input to control from: A or B. <units> Specifies the setpoint units. Valid entries: 1=kelvin, 2=Celsius, 3=sensor units. <powerup enable> Specifies whether the control loop is on or off after power-up, where 0=powerup enable off and 1=powerup enable on. <current/power> Specifies whether the heater output displays in current or power. Valid entries: 1=current or 2=power.
Example:	**CSET 1,A,1,1[term]** - Control Loop 1 controls off of input A with setpoint in kelvin.

INCRV	Input curve number command
Input:	**INCRV** <**input**>,<**curve number**>**[term]**
Format:	<input> Specifies which input to configure: A or B. <curve number> Specifies which curve the input uses. If specified curve parameters do not match the input, the curve number defaults to 0. Valid entries: 0=none, 1-20=standard curves, 21-41=user curves.
Description:	Specifies the curve an input uses for temperature conversion.
Example:	**INCRV A,23[term]** - Input A uses User curve 23 for temperature conversion.
INTYPE	Input type parameter command
Input:	**INTYPE** <**input**>,<**sensor type**>,<**compensation**>**[term]**
Format:	<input> Specifies which input to configure: A or B. <sensor type> Specifies input sensor type. Valid entries: 0=Silicon Diode 1=AlGaAs Diode 2=100Ω Platinum/250 3=100Ω Platinum/500 4=1000Ω Platinum 5=NTC RTD 6=Thermocouple 25 mV 7=Thermocouple 50 mV <compensation> Specifies input compensation, where 0=off and 1=on. Reversal for thermal EMF compensation if input is resistive, room compensation if input is thermocouple. Always 0 if input is a diode.
Example:	**INTYPE A,0,0[term]** - Sets input A sensor type to silicon diode.
KRDG?	Kelvin reading query
Input:	**KRDG?** <**input**>**[term]**
Format:	<input> Specifies which input to query: A or B.
Description:	Returns measured temperature.
SETP	Control setpoint command
Input:	**SETP** <**loop**>,<**value**>**[term]**
Format:	<loop> Specifies which loop to configure. <value> The value for setpoint (in whatever units the setpoint is using).
Description:	Sets the temperature setpoint for control loop.
Example:	**SETP 1,122.5[term]** - Control loop 1 setpoint is now 122.5 (based on its units).

IEEE-488 Interface Dynatrac 521 for Lock-In Dynatrac 501

DF	Data format command
Input:	**DFn**
Format:	n=0: ASCII data format n=1: BINARY data format
Description:	Sets data format to either ASCII or binary format for data transmission.
Example:	**DF0*OM1** - selects ASCII data format in burst output mode.
DM	Output data mode command
Input:	**DMn**
Format:	n=1: channel A n=2: channel B n=4: vectorsum - $\sqrt{\mathrm{A}^2 + \mathrm{B}^2}$ n=8: A+B n=16: A-B n=32: A/B n=64: phase - $\arctan(\mathrm{A}/\mathrm{B})$
Description:	Specifies the output parameters sent to the host for each measurement.
Example:	**DM69** - enables channel A, vectorsum $\sqrt{\mathrm{A}^2 + \mathrm{B}^2}$, phase $\arctan(\mathrm{A}/\mathrm{B})$ (1+4+64=69).
IN	Integration period command
Input:	**INn**
Format:	n=1..99999
Description:	Specifies number of periods for integration. Specifies the time as number of 50 Hz or 60 Hz cycles the 521 will generate the counted pulses from the counters.
Example:	**IN3000** - on a system with 50 Hz operation, this would result in one reading every minute (3000×20 ms=60 s).
OM	Output mode command
Input:	**OMn**
Format:	n=0: continuous output mode n=1: burst output mode
Description:	Specifies burst or continuous output. Selects between buffering of only single measurement (continuous mode) or buffering of 256 samples (burst mode) before the data can be read.
Example:	**OM1*DM3** - specifies burst output of channel data (A,B).
SR	Service request mask command
Input:	**SRn**
Format:	n=0: off n=1: overload input A n=2: overload input B n=4: data overrun n=8: data valid n=16: function completed
Description:	Selects sources for interrupt request. Enables or disables the specific service request (SRQ). An enabled SRQ source will generate a SRQ on the IEEE-488 bus as soon as it becomes active. A disabled source will always show its status in the serial poll register but without activating the SRQ line. SRQ is also indicated by a red front lamp.
Example:	**SR11** - produces a SRQ as soon as data is available or channel A or B runs into overload (8+1+2=11).

TB	Bus trigger command
Input:	**TBn**
Format:	n=0: bus trigger disabled n=1: bus trigger enabled
Description:	Enables or disables the bus trigger. The bus trigger (G.E.T. group execute trigger command) will start a new integration=A/D conversion.
Example:	**TB1*TI0** - enables the bus trigger and stops internal trigger.
TI	Internal trigger command
Input:	**TIn**
Format:	n=0: internal trigger disabled n=1: internal trigger enabled
Description:	Starts new integration period directly after the preceding period is completed. This ensures that not a single sample will be lost in measurement.
Example:	**TI1*TB0*TT0** - enables the internal trigger and disable of bus and TTL trigger.
TT	TTL trigger command
Input:	**TTn**
Format:	n=0: TTL trigger disabled n=1: TTL trigger enabled
Description:	Enables or disables the TTL trigger input on the DYNATRAC interface connector. The TTL trigger allows synchronizing the 521 integration periods to external events.
Example:	**TT1** - enables the TTL trigger. High to low transition on the TTL trigger input starts one analog to digital conversion/integration.
AA..AF	Analog output command
Input:	**AAaa.aaaaaa .. AFaa.aaaaaa**
Format:	$0 \leq aa.aaaaaa \leq 10$ V default: AA=00.000000 .. AF=00.000000
Description:	Sets the corresponding output to new level. The output is selected with the second character (A, B,..F) in the command. Floating point values are also accepted.
Example:	**AC5.25** - sets the output AC to an output voltage of 5.25 V. The resolution for the analog output is 15 bits (0.3 mV). After entering a new value into the interface, it can take to 160 ms before the level becomes active on the output. Negative voltages are ignored.
?xx	Setting single parameter query
Input:	**?xx**
Format:	xx represents the name of the command
Description:	Provides information on the current setting conditions. The "?" followed by the mnemonic of the parameter provides current setting information of the specifi c parameter
Example:	**?IN** - returns IN00030, for example.

?*	Setting all parameter query
Input:	**?***
Description:	Provides information of all current setting parameters.
Example:	returns output: AA00.464187*AB05.069430*AC00.333262...*ZA+00.000, for example. The total response is 220 characters large.

Varian Magnet

x	Magnetic field control command
Input:	**x[term]**
Format:	x=o: off x=n: normal magnetic field x=r: reverse magnetic field
Description:	Sets the magnetic field of the Varian magnet to either off or normal or reverse magnetic field.

A.2 Program Description

This section serves as a user manual for the Hall measurement program, "Measure VdP auto-user5.vi". First the electronic devices have to be turned on and set in remote control. The program window is shown in figure A.1 and is divided into several parts. After starting the program the user is asked to define the saving files for the measured data for sample A and B. In the **Parameters** part, several parameters have to be defined as *Sample name, Magnetic field*, if it is different from the default value of 0.5 T, *Sample thickness*, if bulk samples are characterized. Then the calculated 3D carrier concentration is given by dividing the measured 2D carrier concentration with the sample thickness. The voltage amplitude of the oscillator has to be also defined, if different value than default 0.1 V is used. The dialog boxes of *Current* and *gain* are indicators of set values in the switch box. The dialog boxes *Save file path A and B* show the saving file for sample A and B. If these files are defined, the indicators *Save A?* and *Save B?* light up. The measured data can be saved to the desired files by pressing the control button *Save Data*. Then the indicator *Data saved?* lights up.

The **Switch Box** enables to connect current source poles (I+, I-) and measured voltage poles (U+, U-) to the contacts of the sample A or B by pressing appropriate button. The connected points light up. The amplitude of the *Current* flowing through the sample, *Attenuation* and *Gain* of the differential amplifier can be also chosen. The current depends on the amplitude of the oscillator voltage according to following relation:

$$U_{OSC} = n \times 0.1\,V \qquad \triangleq \qquad I = n \times 10^{-x}\,A, \tag{A.1}$$

where $0 \leq n \leq 10$ and $x = 3, 4, ..8$. If the switch box does not respond, the reset button has to be pressed to initialize the switch box into power-up settings. Choosing the one of the 16 resistivities of the conductivity and Hall measurement in the enumerate control *Switch Box AUTO* and switching up the *Enable Switch box Manual settings* switch, it is possible to connect the corresponding current and voltage poles of the selected sample A or B (*Sample* switch). This is useful for checking the resistivity values for each resistivity configuration before starting the measurement cycle. According to this, the proper sensitivity range for Lock-In can be chosen.

In the part of the **Magnet**, forward and reverse magnetic induction can be set by pressing *B+* and *B-* control button, respectively.

The voltage from the sample contacted by U+, U- poles in the switch box is measured by **Lock-In**. The *Sensitivity* range, *Time constant* and *Phase* shift have to be defined by pressing the proper button. Time constant of 300 ms is a typical value, higher values are suitable for very noisy signals. The measured value is displayed as *Resistivity* in the dialog box after pressing the *Measure* button. The *Phase* of the signal is also shown. If the measured voltage is higher than selected sensitivity range, the *Overflow* indicator lights up. Pressing the *Auto scale* button, the range changes automatically according to the signal size.

The measured temperature is displayed in the **Temperature** part. Desired value for stabilizing the temperature by Temperature controller 331 can be defined in the *Setpoint* dialog box and sent to the device by pressing the *SET* button.

The Hall measurement cycle is started by pressing the *Hall Measure* button. Sample A or B can be measured by setting the *Sample* switch. If both samples are measured (multiple measurement mode), the *Measure both A & B sample* control button has to be in ON position. The measured resistivity values of the conductivity and Hall measurement, and

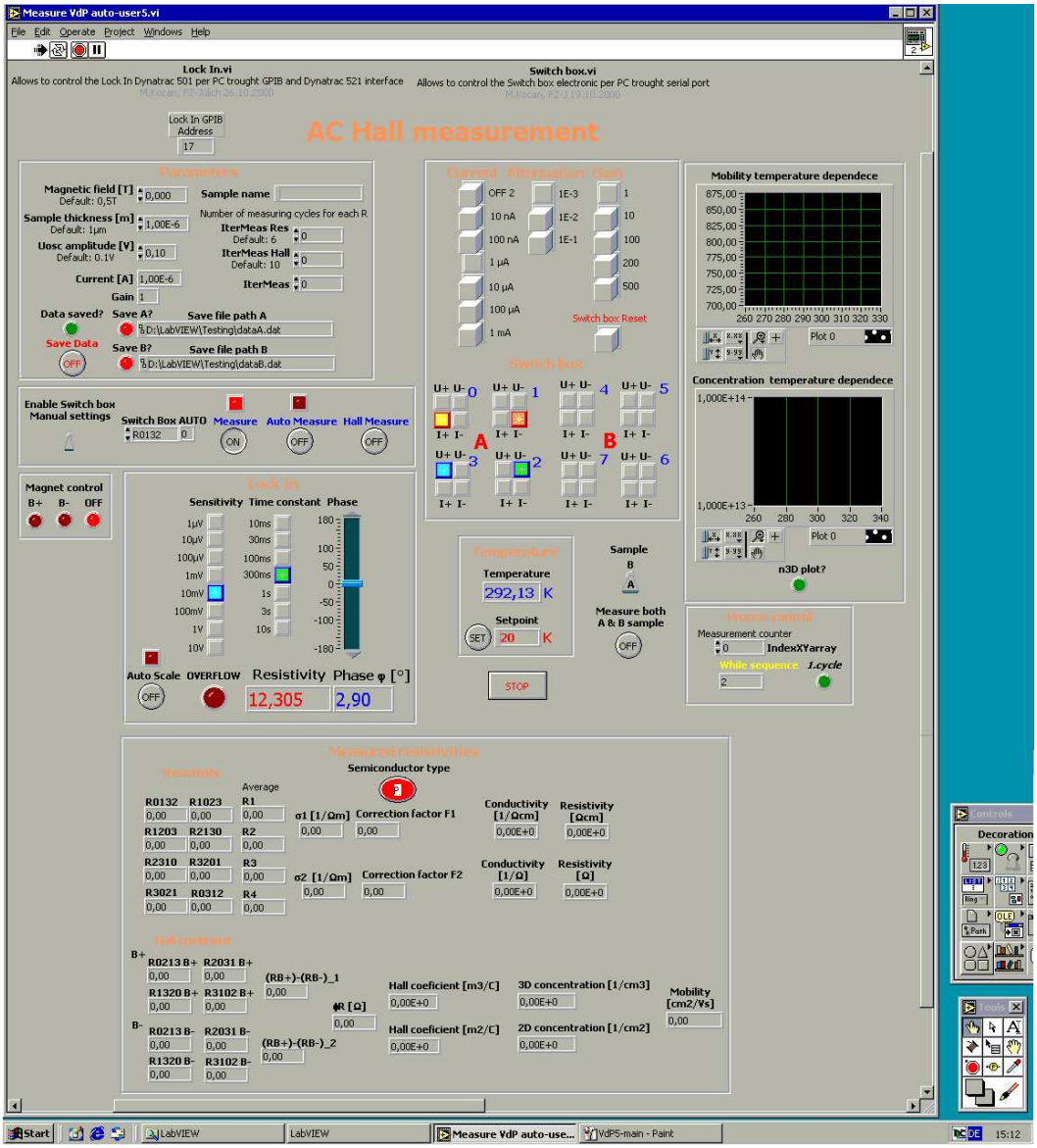

Figure A.1: Program window for Hall measurement.

calculated conductivity, carrier concentration and mobility are displayed in the apparent dialog boxes. More details about the calculation are described in the subsection 3.8.1. The carrier concentration and mobility as a function of temperature are displayed in graphs. The type of conductivity of the characterized semiconductor is also shown. The measurement cycle can be repeated, if instead of the *Hall Measure* button the *Auto Measure* button is pressed. The measurement process is indicated in the enumerated control *Switch Box AUTO*.

The given value in *IterMeasRes* and *IterMeasHall* control dialog for conductivity ($B = 0$) and Hall measurement ($B \neq 0$), respectively, defines the number of loop cycles, after which the measured resistivity is taken. The current value is displayed in *IterMeasRes* dialog. The default values are usually enough to get correct values measured by Lock-In.

All data must be saved before the program is stopped by pressing the *STOP* control button, otherwise all unsaved data will be lost.

Appendix B

Growth Parameters of MBE Samples

This chapter reports on growth parameters of all grown samples by MBE that has been mentioned in this work.

Structure **A172**	growth time	BEP_{Ga} (mbar)	BEP_{Al} (mbar)	N_2 power/flux	T_{SUB} (°C)	Thickness
$Al_{0.25}Ga_{0.75}N$	6’	4.5×10^{-7}	4.0×10^{-8}	350 W/3 sccm	885	30 nm
GaN	1h	5.2×10^{-7}		350 W/3 sccm	870	300 nm
$Al_{0.25}Ga_{0.75}N$	5’	4.5×10^{-7}	4.0×10^{-8}	350 W/3 sccm	885	25 nm
GaN	2.5h	5.2×10^{-7}		350 W/3 sccm	870	1 μm
AlN	13’		8.6×10^{-8}	350 W/2 sccm	700	26 nm
6H n-SiC(0001)$_{Si}$						

Structure **B65**	growth time	BEP_{Ga} (mbar)	BEP_{Al} (mbar)	N_2 power/flux	T_{SUB} (°C)	Thickness
$Al_{0.25}Ga_{0.75}N$	4’	6.55×10^{-7}	4.55×10^{-8}	450 W/1 sccm	763	18 nm
GaN	5h	7.0×10^{-7}		450 W/1 sccm	763	1.60 μm
AlN	25’		1.4×10^{-7}	350 W/1 sccm	770	100 nm
6H n-SiC(0001)$_{Si}$						

Structure **MK87**	growth time	BEP_{Ga} (mbar)	BEP_{Al} (mbar)	N_2 power/flux	T_{SUB} (°C)	Thickness
$Al_{0.25}Ga_{0.75}N$	4’	6.55×10^{-7}	4.55×10^{-8}	450 W/1 sccm	763	18 nm
GaN	5h	7.0×10^{-7}		450 W/1 sccm	763	1.60 μm
AlN	25’		1.4×10^{-7}	350 W/1 sccm	770	100 nm
6H n-SiC(0001)$_{Si}$						

Structure **MK92**	growth time	N_2 power/flux	T_{SUB} (°C)
N*	5’	450 W/1 sccm	27
n-Si(100) R$>$ 1000 Ω·cm			

Structure **MK93**	growth time	N_2 power/flux	T_{SUB} (°C)
N*	5'	450 W/1 sccm	150
n-Si(100) R> 1000 Ω·cm			

Structure **MK93-1**	growth time	N_2 power/flux	T_{SUB} (°C)
N*	5'	450 W/1 sccm	150
MK93			

Structure **MK94**	growth time	N_2 power/flux	T_{SUB} (°C)
N*	5'	450 W/1 sccm	300
n-Si(100) R> 1000 Ω·cm			

Structure **MK95**	growth time	N_2 power/flux	T_{SUB} (°C)
N*	5'	450 W/1 sccm	600
n-Si(100) R> 1000 Ω·cm			

Structure **MK95-1**	growth time	N_2 power/flux	T_{SUB} (°C)
N*	10'	450 W/1 sccm	600
MK95			

Structure **MK96**	growth time	N_2 power/flux	T_{SUB} (°C)
N*	10'	450 W/1 sccm	700
n-Si(100) R> 1000 Ω·cm			

Structure **MK97**	growth time	N_2 power/flux	T_{SUB} (°C)
N*	30'	450 W/1 sccm	600
n-Si(100) R> 1000 Ω·cm			

Structure **MK101**	growth time	BEP_{Ga} (mbar)	BEP_{Al} (mbar)	N_2 power/flux	T_{SUB} (°C)	Thickness
$Al_{0.25}Ga_{0.75}N$	4'1"	3.745×10^{-7}	4.55×10^{-8}	450 W/1 sccm	763	18 nm
GaN	5h	4.2×10^{-7}		450 W/1 sccm	763	1.6 μm
AlN	25'		1.4×10^{-7}	350 W/1 sccm	770	100 nm
6H n-SiC(0001)$_{Si}$						

Structure **MK101-1**	growth time	$T_{Si\ wafer}$ (°C)	N_2 power/flux	T_{SUB} (°C)
Si wafer	35'	939		400
MK101				

Structure **MK101-2**	growth time	$T_{Si\ wafer}$ (°C)	N_2 power/flux	T_{SUB} (°C)
N*	30'		450 W/1 sccm	600
MK101-1				

Structure **MK110**	growth time	BEP_{Ga} (mbar)	BEP_{Al} (mbar)	N_2 power/flux	T_{SUB} (°C)	Thickness
GaN	1h	2.0×10^{-7}		450 W/1 sccm	763	300 nm
GaN template 001025GA (MOCVD)						1 μm
AlGaN graded						
6H n-SiC(0001)$_{Si}$						

Structure **MK111**	growth time	BEP_{Ga} (mbar)	BEP_{Al} (mbar)	N_2 power/flux	T_{SUB} (°C)	Thickness
GaN	1h	2.5×10^{-7}		450 W/1 sccm	763	300 nm
GaN template 001025GA (MOCVD)						1 μm
AlGaN graded						
6H n-SiC(0001)$_{Si}$						

Structure **MK114**	growth time	BEP_{Ga} (mbar)	BEP_{Al} (mbar)	N_2 power/flux	T_{SUB} (°C)	Thickness
AlN	4h		1.0×10^{-7}	350 W/1 sccm	770	1 μm
6H n-SiC(0001)$_{Si}$						

Structure **MK115**	growth time	BEP_{Ga} (mbar)	BEP_{Al} (mbar)	N_2 power/flux	T_{SUB} (°C)	Thickness
$Al_{0.09}Ga_{0.91}N$	4h	1.8×10^{-7}	2.0×10^{-8}	450 W/1 sccm	763	1 μm
6H n-SiC(0001)$_{Si}$						

Structure **MK116**	growth time	BEP_{Ga} (mbar)	BEP_{Al} (mbar)	N_2 power/flux	T_{SUB} (°C)	Thickness
$Al_{0.3}Ga_{0.7}N$	4h	1.457×10^{-7}	5.43×10^{-8}	450 W/1 sccm	763	1 μm
6H n-SiC(0001)$_{Si}$						

Structure **MK117**	growth time	BEP_{Ga} (mbar)	BEP_{Al} (mbar)	N_2 power/flux	T_{SUB} (°C)	Thickness
$Al_{0.5}Ga_{0.5}N$	4h	1.166×10^{-7}	8.34×10^{-8}	450 W/1 sccm	763	1 μm
6H n-SiC(0001)$_{Si}$						

Structure **MK118**	growth time	BEP_{Ga} (mbar)	BEP_{Al} (mbar)	N_2 power/flux	T_{SUB} (°C)	Thickness
$Al_{0.75}Ga_{0.25}N$	4h	6.67×10^{-8}	1.333×10^{-7}	450 W/1 sccm	763	1 μm
6H n-SiC(0001)$_{Si}$						

Structure **ED130**	growth time	BEP_{Ga} (mbar)	BEP_{Al} (mbar)	N_2 power/flux	T_{SUB} (°C)	Thickness
GaN	1h35'	5.0×10^{-7}		450 W/1 sccm	763	590 nm
AlN	25'		1.4×10^{-7}	350 W/1 sccm	770	100 nm
6H n-SiC(0001)$_{Si}$						

Structure **ED131**	growth time	BEP_{Ga} (mbar)	BEP_{Al} (mbar)	N_2 power/flux	T_{SUB} (°C)	Thickness
GaN	1h35'	2.5×10^{-7}		450 W/1 sccm	763	588 nm
AlN	25'		1.4×10^{-7}	350 W/1 sccm	770	100 nm
6H n-SiC(0001)$_{Si}$						

Structure **ED132**	growth time	BEP_{Ga} (mbar)	BEP_{Al} (mbar)	N_2 power/flux	T_{SUB} (°C)	Thickness
GaN	1h35'	4.0×10^{-7}		450 W/1 sccm	763	548 nm
AlN	25'		1.4×10^{-7}	350 W/1 sccm	770	100 nm
6H n-SiC(0001)$_{Si}$						

Structure **ED133**	growth time	BEP_{Ga} (mbar)	BEP_{Al} (mbar)	N_2 power/flux	T_{SUB} (°C)	Thickness
GaN	1h35'	6.0×10^{-7}		450 W/1 sccm	763	584 nm
AlN	25'		1.4×10^{-7}	350 W/1 sccm	770	100 nm
6H n-SiC(0001)$_{Si}$						

Structure **ED134**	growth time	BEP_{Ga} (mbar)	BEP_{Al} (mbar)	N_2 power/flux	T_{SUB} (°C)	Thickness
GaN	1h35'	1.0×10^{-7}		450 W/1 sccm	763	468 nm
AlN	25'		1.4×10^{-7}	350 W/1 sccm	770	100 nm
6H n-SiC(0001)$_{Si}$						

Structure **ED135**	growth time	BEP_{Ga} (mbar)	BEP_{Al} (mbar)	N_2 power/flux	T_{SUB} (°C)	Thickness
GaN	1h35'	1.5×10^{-7}		450 W/1 sccm	763	585 nm
AlN	25'		1.4×10^{-7}	350 W/1 sccm	770	100 nm
6H n-SiC(0001)$_{Si}$						

Structure **ED136**	growth time	BEP_{Ga} (mbar)	BEP_{Al} (mbar)	N_2 power/flux	T_{SUB} (°C)	Thickness
GaN	1h35'	0.5×10^{-7}		450 W/1 sccm	763	299 nm
AlN	25'		1.4×10^{-7}	350 W/1 sccm	770	100 nm
6H n-SiC(0001)$_{Si}$						

Structure **ED137**	growth time	BEP_{Ga} (mbar)	BEP_{Al} (mbar)	N_2 power/flux	T_{SUB} (°C)	Thickness
$Al_{0.3}Ga_{0.7}N$	33'22"	2.045×10^{-7}	4.55×10^{-8}	450 W/1 sccm	763	150 nm
6H n-SiC(0001)$_{Si}$						

Structure **ED138**	growth time	BEP_{Ga} (mbar)	BEP_{Al} (mbar)	N_2 power/flux	T_{SUB} (°C)	Thickness
$Al_{0.23}Ga_{0.77}N$	33'21"	2.15×10^{-7}	3.5×10^{-8}	450 W/1 sccm	763	150 nm
6H n-SiC(0001)$_{Si}$						

Structure **ED141**	growth time	BEP_{Ga} (mbar)	BEP_{Al} (mbar)	N_2 power/flux	T_{SUB} (°C)	Thickness
AlN	25'		1.4×10^{-7}	350 W/1 sccm	770	100 nm
N*	11"			350 W/1 sccm	770	
Al	12"		1.0×10^{-7}		770	
p-Si(111) R$\sim 7 - 21$ Ω·cm						

Structure **ED145**	growth time	BEP_{Ga} (mbar)	BEP_{Al} (mbar)	N_2 power/flux	T_{SUB} (°C)	Thickness
AlN	25'		1.0×10^{-7}	350 W/1 sccm	770	100 nm
N*	11"			350 W/1 sccm	770	
Al	12"		1.0×10^{-7}		770	
p-Si(111) R$\sim 7 - 21$ Ω·cm						

Structure **ED147**	growth time	BEP_{Ga} (mbar)	BEP_{Al} (mbar)	N_2 power/flux	T_{SUB} (°C)	Thickness
GaN	3h10'	2.5×10^{-7}		450 W/1 sccm	763	1 μm
AlN	25'		1.0×10^{-7}	350 W/1 sccm	770	100 nm
N*	11"			350 W/1 sccm	770	
Al	12"		1.0×10^{-7}		770	
n-Si(111) R>3 kΩ· cm						

Structure **ED150**	growth time	BEP_{Ga} (mbar)	BEP_{Al} (mbar)	N_2 power/flux	T_{SUB} (°C)	Thickness
$Al_{0.12}Ga_{0.88}N$	22'	2.15×10^{-7}	3.5×10^{-8}	450 W/1 sccm	763	100 nm
N*	11"			350 W/1 sccm	770	
Al	12"		1.0×10^{-7}		770	
n-Si(111) R>3 kΩ· cm						

Structure **ED151**	growth time	BEP_{Ga} (mbar)	BEP_{Al} (mbar)	N_2 power/flux	T_{SUB} (°C)	Thickness
$Al_{0.4}Ga_{0.6}N$	22'	2.0×10^{-7}	5.0×10^{-8}	450 W/1 sccm	763	100 nm
AlN	25'		1.0×10^{-7}	350 W/1 sccm	770	100 nm
N*	11"			350 W/1 sccm	770	
Al	12"		1.0×10^{-7}		770	
p-Si(111) R$\sim 7 - 21$ Ω·cm						

Structure **ED153**	growth time	BEP_{Ga} (mbar)	BEP_{Al} (mbar)	N_2 power/flux	T_{SUB} (°C)	Thickness
$Al_{0.11}Ga_{0.89}N$	22’	2.3×10^{-7}	2.0×10^{-8}	450 W/1 sccm	763	100 nm
AlN	25’		1.0×10^{-7}	350 W/1 sccm	770	100 nm
N^*	11”			350 W/1 sccm	770	
Al	12”		1.0×10^{-7}		770	
p-Si(111) R$\sim 7-21$ Ω·cm						

Structure **ED155**	growth time	BEP_{Ga} (mbar)	BEP_{Al} (mbar)	N_2 power/flux	T_{SUB} (°C)	Thickness
$Al_{0.58}Ga_{0.42}N$	22’	1.7×10^{-7}	8.0×10^{-8}	450 W/1 sccm	763	100 nm
AlN	25’		1.0×10^{-7}	350 W/1 sccm	770	100 nm
N^*	11”			350 W/1 sccm	770	
Al	12”		1.0×10^{-7}		770	
p-Si(111) R$\sim 7-21$ Ω·cm						

Structure **ED156**	growth time	BEP_{Ga} (mbar)	BEP_{Al} (mbar)	N_2 power/flux	T_{SUB} (°C)	Thickness
GaN	3h10’	3.0×10^{-7}		450 W/1 sccm	763	1 μm
$Al_{0.4}Ga_{0.6}N$	22’	2.0×10^{-7}	5.0×10^{-8}	450 W/1 sccm	763	100 nm
AlN	25’		1.0×10^{-7}	350 W/1 sccm	770	100 nm
N^*	11”			350 W/1 sccm	770	
Al	12”		1.0×10^{-7}		770	
p-Si(111) R$\sim 7-21$ Ω·cm						

Structure **ED158**	growth time	BEP_{Ga} (mbar)	BEP_{Al} (mbar)	N_2 power/flux	T_{SUB} (°C)	Thickness
GaN	3h10’	3.0×10^{-7}		450 W/1 sccm	773	1 μm
$Al_{0.4}Ga_{0.6}N$	22’	2.0×10^{-7}	5.0×10^{-8}	450 W/1 sccm	773	100 nm
AlN	25’		1.0×10^{-7}	350 W/1 sccm	770	100 nm
N^*	11”			350 W/1 sccm	770	
Al	12”		1.0×10^{-7}		770	
p-Si(111) R$\sim 7-21$ Ω·cm						

Structure **ED160**	growth time	BEP_{Ga} (mbar)	BEP_{Al} (mbar)	N_2 power/flux	T_{SUB} (°C)	Thickness
GaN	3h10’	2.8×10^{-7}		450 W/1 sccm	763	1 μm
$Al_{0.4}Ga_{0.6}N$	22’	2.0×10^{-7}	5.0×10^{-8}	450 W/1 sccm	763	100 nm
AlN	25’		1.0×10^{-7}	350 W/1 sccm	770	100 nm
N^*	11”			350 W/1 sccm	770	
Al	12”		1.0×10^{-7}		770	
p-Si(111) R$\sim 7-21$ Ω·cm						

Structure **ED162**	growth time	BEP_{Ga} (mbar)	BEP_{Al} (mbar)	N_2 power/flux	T_{SUB} (°C)	Thickness
GaN	1'30"	2.8×10^{-7}		450 W/1 sccm	763	8 nm
$Al_{0.23}Ga_{0.77}N$	5'32"	2.15×10^{-7}	3.5×10^{-8}	450 W/1 sccm	763	25 nm
GaN	3h10'	3.0×10^{-7}		450 W/1 sccm	763	1 μm
$Al_{0.4}Ga_{0.6}N$	22'	2.0×10^{-7}	5.0×10^{-8}	450 W/1 sccm	763	100 nm
AlN	25'		1.0×10^{-7}	350 W/1 sccm	770	100 nm
N^*	11"			350 W/1 sccm	770	
Al	12"		1.0×10^{-7}		770	
p-Si(111) R$\sim 7-21$ Ω·cm						

Structure **ED166**	growth time	BEP_{Ga} (mbar)	BEP_{Al} (mbar)	N_2 power/flux	T_{SUB} (°C)	Thickness
GaN	3h10'	3.0×10^{-7}		450 W/1 sccm	763	1 μm
$Al_XGa_{1-X}N$ graded $x = 1 \mapsto 0$	22'33"	Ga:$1.5 \times 10^{-7} \mapsto 2.45 \times 10^{-7}$ Al:$1.0 \times 10^{-7} \mapsto 5.00 \times 10^{-9}$		450 W/1 sccm	763	100 nm
AlN	25'		1.0×10^{-7}	350 W/1 sccm	770	100 nm
N^*	11"			350 W/1 sccm	770	
Al	12"		1.0×10^{-7}		770	
p-Si(111) R$\sim 7-21$ Ω·cm						

Structure **ED168**	growth time	BEP_{Ga} (mbar)	BEP_{Al} (mbar)	N_2 power/flux	T_{SUB} (°C)	Thickness
AlN	49'		1.4×10^{-7}	350 W/1 sccm	770	200 nm
$Al_{0.27}Ga_{0.73}N$	22'	2.1×10^{-7}	0.4×10^{-7}	450 W/1 sccm	763	100 nm
GaN	38'	2.5×10^{-7}		450 W/1 sccm	763	200 nm
GaN template 001025GD (MOCVD)						1 μm
AlGaN graded						
6H n-SiC(0001)$_{Si}$						

Structure **ED174**	growth time	BEP_{Ga} (mbar)	BEP_{Al} (mbar)	N_2 power/flux	T_{SUB} (°C)	Thickness
n-GaN (Si-doped) $T_{Si} = 1200°C$	3'45"	2.25×10^{-7}		450 W/1 sccm	763	20nm
GaN	1h35'	2.25×10^{-7}		450 W/1 sccm	763	1μm
AlN	25'		1.4×10^{-7}	350 W/1 sccm	770	100nm
6H i-SiC(0001)$_{Si}$						

Structure **ED185**	growth time	BEP_{Ga} (mbar)	BEP_{Al} (mbar)	N_2 power/flux	T_{SUB} (°C)	Thickness
GaN	1'12"	2.0×10^{-7}		450 W/1 sccm	763	5 nm
$Al_{0.3}Ga_{0.7}N$	6'3"	1.55×10^{-7}	4.5×10^{-8}	450 W/1 sccm	763	27 nm
GaN	6h20'2"	2.0×10^{-7}		450 W/1 sccm	763	2 μm
AlN	25'		1.4×10^{-7}	350 W/1 sccm	770	100 nm
6H i-SiC(0001)$_{Si}$						

Structure **ED191**	growth time	BEP_{Ga} (mbar)	BEP_{Al} (mbar)	N_2 power/flux	T_{SUB} (°C)	Thickness
AlN	25'		1.4×10^{-7}	350 W/1 sccm	770	100 nm
6H i-SiC(0001)$_{Si}$						

Structure **ED194**	growth time	BEP_{Ga} (mbar)	BEP_{Al} (mbar)	N_2 power/flux	T_{SUB} (°C)	Thickness
AlN	25'		1.0×10^{-7}	350 W/1 sccm	770	100 nm
6H i-SiC(0001)$_{Si}$						

Structure **ED195**	growth time	BEP_{Ga} (mbar)	BEP_{Al} (mbar)	N_2 power/flux	T_{SUB} (°C)	Thickness
GaN	3h10'	2.0×10^{-7}		450 W/1 sccm	763	1 μm
AlN	25'		1.0×10^{-7}	350 W/1 sccm	770	100 nm
6H i-SiC(0001)$_{Si}$						

Structure **ED196**	growth time	BEP_{Ga} (mbar)	BEP_{Al} (mbar)	N_2 power/flux	T_{SUB} (°C)	Thickness
GaN	3h10'	2.2×10^{-7}		450 W/1 sccm	763	1 μm
AlN	25'		1.0×10^{-7}	350 W/1 sccm	770	100 nm
6H i-SiC(0001)$_{Si}$						

Structure **ED198**	growth time	BEP_{Ga} (mbar)	BEP_{Al} (mbar)	N_2 power/flux	T_{SUB} (°C)	Thickness
GaN	1'12"	2.0×10^{-7}		450 W/1 sccm	763	5 nm
$Al_{0.27}Ga_{0.73}N$	5'32"	1.6×10^{-7}	4.0×10^{-8}	450 W/1 sccm	763	25 nm
GaN	57'	2.05×10^{-7}		450 W/1 sccm	763	300 nm
AlN	1'13"		1.0×10^{-7}	350 W/1 sccm	770	5 nm
GaN	4h43'	2.05×10^{-7}		450 W/1 sccm	763	1.5 μm
AlN	25'		1.0×10^{-7}	350 W/1 sccm	770	100 nm
6H i-SiC(0001)$_{Si}$						

Structure **ED203**	growth time	BEP_{Ga} (mbar)	BEP_{Al} (mbar)	N_2 power/flux	T_{SUB} (°C)	Thickness
GaN	1'12"	2.0×10^{-7}		450 W/1 sccm	763	5 nm
AlN	5'30"		1.0×10^{-7}	450 W/1 sccm	763	23 nm
GaN	57'	2.05×10^{-7}		450 W/1 sccm	763	300 nm
AlN	1'13"		1.0×10^{-7}	350 W/1 sccm	770	5 nm
GaN	4h43'	2.05×10^{-7}		450 W/1 sccm	763	1.5 μm
AlN	25'		1.0×10^{-7}	350 W/1 sccm	770	100 nm
6H i-SiC(0001)$_{Si}$						

Structure **MK210**	growth time	BEP_{Ga} (mbar)	BEP_{Al} (mbar)	N_2 power/flux	T_{SUB} (°C)	Thickness
GaN	1'12"	2.0×10^{-7}		450 W/1 sccm	763	5 nm
$Al_{0.15}Ga_{0.85}N$	6'	1.75×10^{-7}	2.5×10^{-8}	450 W/1 sccm	763	27 nm
GaN	57'	2.1×10^{-7}		450 W/1 sccm	763	300 nm
AlN	1'13"		1.0×10^{-7}	350 W/1 sccm	770	5 nm
GaN	4h43'	2.1×10^{-7}		450 W/1 sccm	763	1.5 μm
AlN	25'		1.0×10^{-7}	350 W/1 sccm	770	100 nm
6H i-SiC(0001)$_{Si}$						

Appendix C

Physical Constants and Periodic Table of Elements

Quantity	Symbol	Value
Angstrom unit	Å	1 Å$= 10^{-8}$ cm$= 10^{-10}$ m
Planck constant	h	4.135×10^{-15} eVs$= 6.626 \times 10^{-34}$ Js
$h/2\pi$	$\hbar$	6.582×10^{-16} eVs$= 1.054 \times 10^{-34}$ Js
Speed of light in vacuum	c	2.997925×10^{8} m/s
Avogadro number	N	6.022×10^{23} mol^{-1}
Boltzmann constant	k	8.620×10^{-5} eV/K$= 1.381 \times 10^{-23}$ J/K
Electron charge	q	1.602×10^{-19} C
Electron rest mass	$m_\circ$	0.511003 MeV/c$^2 = 9.109 \times 10^{-31}$ kg
Electron volt	eV	1 eV$= 1.602 \times 10^{-19}$ J
Permeability of free space	$\mu_\circ$	1.257×10^{-6} H/m
Permittivity of free space	$\varepsilon_\circ$	8.850×10^{-12} F/m
Bohr radius	$a_0 = \hbar^2/me^2$	0.529177 Å
Bohr magneton	$\mu_B = e\hbar/2mc$	5.7884×10^{-5} eV/T
Wavelength of 1 eV quantum	λ	1.24 μm

PERIODIC TABLE OF THE ELEMENTS

http://www.ktf-split.hr/periodni/en/

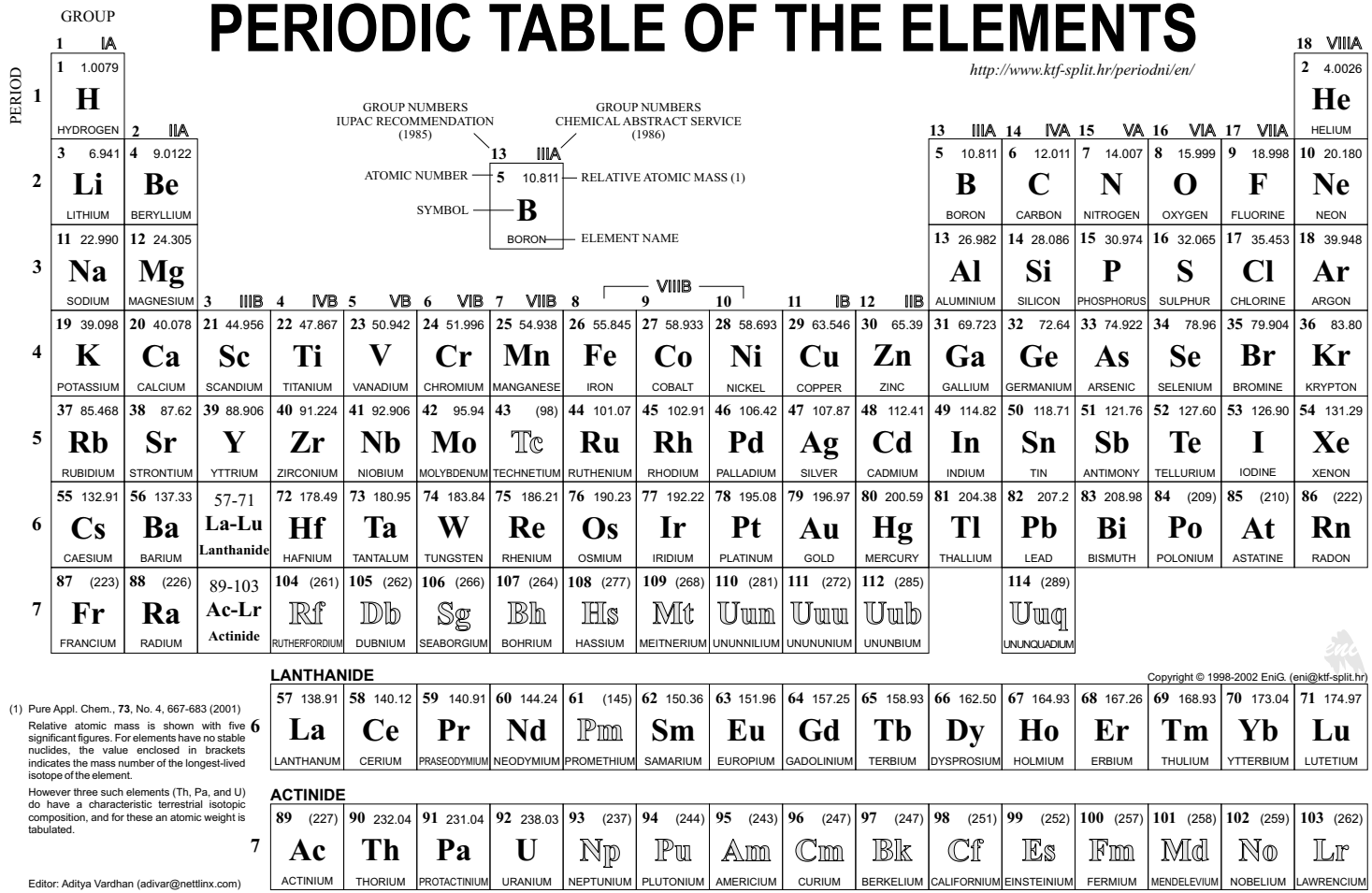

(1) Pure Appl. Chem., **73**, No. 4, 667-683 (2001)

Relative atomic mass is shown with five significant figures. For elements have no stable nuclides, the value enclosed in brackets indicates the mass number of the longest-lived isotope of the element.

However three such elements (Th, Pa, and U) do have a characteristic terrestrial isotopic composition, and for these an atomic weight is tabulated.

Editor: Aditya Vardhan (adivar@nettlinx.com)

List of Figures

List of Tables

Bibliography

[1] S. Nakamura and G. Fasol. *The Blue Laser Diode*. Springer-Verlag, Berlin, 1997. 343 pages.

[2] I. Akasaki and H. Amano. *Japanese Journal of Applied Physics*, 36:5393, 1997.

[3] T. Mikai, M. Yamada and S. Nakamura. *Japanese Journal of Applied Physics*, 38:3976, 1999.

[4] L. F. Eastman. Reports for the ONR Multidisciplinary University Research Initiative (MURI) for High Power, Linear, Broadband Solid State Amplifiers at http://www.iiiv.cornell.edu/www/schaff/muri/reports/. Technical report, 2001.

[5] L. F. Eastman, V. Tilak, V. Kaper, J. Smart, R. Thompson, B. Green, J. R. Shealy and T. Prunty. Progress in High-Power, High Frequency AlGaN/GaN HEMTs. *Physica Status Solidi A*, 194(2):433–438, 2002.

[6] H. Kroemer. The 2000 Nobel Physics Prize - Press Release and Nobel Lectures: http://www.nobel.se/physics/laureates/2000/;. See also H. Kroemer, *Surface Science* **132**, 543-576 (1983).

[7] V. Yu. Davydov, A. A. Klochikhin, V. V. Emtsev, S. V. Ivanov, V. V. Vekshin, F. Bechstedt, J. Furthmüller, H. Harina, A. V. Mudryi, A. Hashimoto, A. Yamamoto, J. Aderhold, J. Graul and E. E. Haller. Band Gap of InN and In-rich $In_xGa_{1-x}N$ alloys $(0.36 < x < 1)$. *Physica Status Solidi B*, 230(2):R4–R6, 2002.

[8] Ioffe Institute, http://www.ioffe.ru.

[9] http://ncsr.csci-va.com/properties.htm.

[10] O. Ambacher. Growth and applications of Group III-nitrides. *J.Phys.D: Appl. Phys.*, 31:2653–2710, 1998.

[11] V. Fiorentini F. Bernardini and D. Vanderbildt. Spontaneous polarization and piezoelectric constants of III-V nitrides. *Physical review B*, 56(16):R10 024–R10 027, 1997.

[12] K. Tsubouchi, K. Sugai and N. Mikoshiba. *IEEE Ultrason. Symp.*, 1:375, 1981.

[13] G. D. O′Clock and M. T. Duffy. *Applied Physics Letters*, 23:55, 1973.

[14] M. A. Littlejohn, J. R. Hauser and T. H. Glisson. *Applied Physics Letters*, 26:625, 1975.

[15] K. Shimada, T. Sota and K. Sizuki. *Journal of Applied Physics*, 84:4951, 1998.

[16] E. S. Hellman. The Polarity of GaN: a Critical Review. *MRS Internet Journal of Nitride Semiconductor Research*, 3(11):1–11, 1998.

[17] Sidney B. Lang. *Sourcebook of Pyroelectricity*. Gordon and Breach Science Publishers, Inc., New York, 1974.

[18] J. F. Nye. *Physical Properties of Crystals*. Osford University Press, 1957.

[19] R. M. Martin. *Physical Review B*, 9:1998–1999, 1974.

[20] R. Resta. *Review of Modern Physics*, 66:899–915, 1994.

[21] M. Posternak, A. Baldereschi, A. Catellani, R. Resta. *Physical Review Letters*, 64:1777–1780, 1990.

[22] O. Ambacher, B. Foutz and J. Smart. 2DEG induced by spontaneous and piezoelectric polarization in undoped and doped AlGaN/GaN heterostructures. *Journal of Applied Physics*, 87(1):334–344, January 2000.

[23] H. Lüth. *Surfaces and Interfaces of Solids*. Springer-Verlag, 1993.

[24] J. J. Harris, J. A. Pals and R. Woltjer. *Rep. Prog. Phys.*, 52:1217, 1989.

[25] B. R. Nag. *Electron transport in Compound Semiconductor*, volume 11 of *Solid States Science*. Springer Edition, 1980.

[26] W. Walukiewicz, L. Lagowski, L. Jastrzebski. M. Lichtensteiger and H. C. Gatos. *Journal of Applied Physics*, 50:899, 1979.

[27] M Shur, B. Gelmont and M. Asif Kahn. *J. Electr. Mat.*, 25:821, 1996.

[28] W. Walukiewicz. *in Semiconductor Interfaces and Microstructures*, page 1. World Scientific, Singapore, Z. C. Feng edition, 1992.

[29] H. L. Störmer, L. N. Pfeiffer, K. W. Baldwin and K. West. *Physical Review B*, 41:1278, 1990.

[30] L. Hsu and W. Walukiewicz. Electron mobility in $Al_XGa_{1-X}N$/GaN heterostructures. *Physical Review B*, 56(3):1520–1528, 1997.

[31] X. H. Wu, L. M. Brown, D. Kapolnek, S. Keller, B. Keller, S. P. DenBaars and J. S. Speck. *Journal of Applied Physics*, 80:3228, 1996.

[32] X. H. Wu, D. Kapolnek, E. J. Tarsa, B. Heying, S. Keller, B. P .Keller, U. K. Mishra, S. P. DenBaars and J. S. Speck. *Applied Physics Letters*, 68:1371, 1996.

[33] D. Jena, A. C. Gossard and U. K. Mishra. Dislocation scattering in a two-dimensional electron gas. *Applied Physics Letters*, 76(13):1707–1709, 2000.

[34] W. T. Read. *Philos. Mag.*, 45:775, 1954.

[35] F. A. Ponce. *MRS Bull.*, 22:51, 1997.

[36] X. H. Wu, P. Fini, E. J. Tarsa, B. Heying, S. Keller, U. K. Mishra, S. P. DenBaars and J. S. Speck. *Journal of Crystal Growth*, 189-190:232, 1998.

[37] D. Kapolnek, X. H. Wu, B. Heying, S. Keller, B. P .Keller, U. K. Mishra, S. P. DenBaars and J. S. Speck. *Applied Physics Letters*, 67:1541, 1995.

[38] H. M Ng, D Doppalapudi and T. D. Moustakas. The role of dislocation scattering in n-type GaN films. *Applied Physics Letters*, 73(6):821–823, 1998.

[39] N. G. Weimann and L. F. Eastman. Scattering of electrons at threading dislocations in GaN. *Journal of Applied Physics*, 83(7):3656–3659, 1998.

[40] J. S. Speck and S. J. Rosner. The role of threading dislocations in the physical properties of GaN and its alloys. *Physica B*, 273-274:24–32, 1999.

[41] X. H. Wu, C. R. Elsass, A. Abare, M. Mack, S. Keller, P. M. Petroff, J. S. Speck and S. J. Rosner. *Applied Physics Letters*, 72:692, 1998.

[42] C. R. Elsass, I. P. Smorchkova, B. Heying, E. Haus, P. Fini, K. Maranovski, J. P. Ibbetson, S. Keller, P. M. Petroff, S. P. DenBaars, U. K. Mishra and J. S. Speck. *Applied Physics Letters*, 74:3528, 1999.

[43] I. P. Smorchkova, C. R. Elsass, J. P. Ibbetson, R. Ventury, B. Heying, P. Fini, E. Haus, S. P. DenBaars, J. S. Speck and U. K. Mishra. Polarization induced charge and electron mobility in AlGaN/GaN heterostructures grown by plasma assisted molecular-beam epitaxy. *Journal of Applied Physics*, 86(8):4520–4526, 1999.

[44] T. S. Zheleva, O. H. Nam, M D. Bremser and R. F. Davis. *Applied Physics Letters*, 71:2472, 1997.

[45] R. Oberhuber, G. Zandler and P. Vogl. Mobility of two-dimensional electrons in AlGaN/GaN modulation-doped field-effect transistors. *Applied Physics Letters*, 73(6):818–820, 1998.

[46] D. L. Rode and D. K. Gaskills. *Applied Physics Letters*, 66:1972, 1995.

[47] J. G. Kim, A. C. Frenkel, H. Liu and R. M. Park. *Applied Physics Letters*, 65:91, 1994.

[48] D. C. Look and R. J. Molnar. *Applied Physics Letters*, 70:3377, 1997.

[49] J. Antoszewski, M. Gracey, J. M. Dell, L. Faraone, T. A. Fisher, G. Parish, Y.-F. Wu and U. K. Mishra. Scattering mechanism limiting two-dimensional electron gas mobility in $Al_{0.25}Ga_{0.75}N$ modulation-doped field-effect transistors. *Journal of Applied Physics*, 87(8):3900–3904, 2000.

[50] D. Jena, A. C. Gossard and U. K. Mishra. Dipole scattering in polarization induced III-V nitride two-dimensional electron gases. *Journal of Applied Physics*, 88(8):4734–4738, 2000.

[51] L. N. Pfeiffer, K. W. West, H. L. Stormer and K. W. Baldwin. *Applied Physics Letters*, 55:1888, 1989.

[52] P. Waltereit, O. Brandt, M. Ramsteiner, A. Trampert, H. T. Grahn, J. Meniger, M. Reiche, R. Uecker, P. Reiche and K. H. Ploog. *Physica Status Solidi A*, 180:133, 2000.

[53] L. Liu and J. H. Edgar. Substrates for gallium nitride epitaxy. *Materials Science and Engineering*, R37:61–127, 2002.

[54] F. A. Ponce. *Group III Nitride Semiconductor compounds*. Oxford University Press, Oxford, B. Gil edition, 1998. p. 123.

[55] L. T. Romano. *Properties, Processing and Applications of Gallium Nitride and Related Semiconductors*. INSPEC, The Institution of Electrical Engineers, Stevenage, UK, J. H. Edgar, S. S. Strite, I. Akasaki, H. Amano edition, 1999. p. 209.

[56] J. E. Northrup and L. T. Romano. *Properties, Processing and Applications of Gallium Nitride and Related Semiconductors*. INSPEC, The Institution of Electrical Engineers, Stevenage, UK, J. H. Edgar, S. S. Strite, I. Akasaki, H. Amano edition, 1999. p. 213.

[57] T. Siski, J. Jun, M. Leszczyski, H. Teisseyre, S. Strite, A. Rocket, A. Pelzmann, M. Kamp and K. J. Ebeling. *Journal of Applied Physics*, 84:1155, 1998.

[58] S. J. Rosner, E. C. Carr, M. J. Ludowise, G. Girolami and H. I. Ericson. *Applied Physics Letters*, 70:420, 1997.

[59] H. Amano, M. Iwaya, T. Kashima, M. Katsuragawa, I. Asaki, J. Han, S. Hearne, J. A. Floro, E. Chason and J. Figiel. *Japanees Journal of Applied Physics*, 37:L1540, 1998.

[60] B. Beaumont, Ph. Vennegures and P. Gibart. *Physica Status Solidi B*, 227:1, 2001.

[61] T. S. Zheleva, S. A. Smith, D. B. Thomson, K. J. Linthicum, P. Rajagopal and R. F. Davis. *J. Electron Mater.*, 28:L5, 1999.

[62] H. Lahreche, P. Vennegues, B. Beaumont and P. Gibart. *Journal of Crystal Growth*, 205:245, 1999.

[63] C. I. H. Ashby, C. C. Mitchell, J. Han, N. A. Missert, P. P. Provencio D. M. Vollstaed, G. M. Peake and L. Griego. *Applied Physics Letters*, 77:3233, 2000.

[64] T. Detchprohm, M. Yano, S. Sano, R. Nakamura, S. Mociduki, T. Nakamura, H. Amano and I. Akasaki. *Japanees Journal of Applied Physics*, 40:L16, 2001.

[65] Z. Q. Li, H. Chen, H. F. Liu, J. H. Li, L. Wan, S. Liu, Q. Huang and J. M. Zhou. *Journal of Crystal Growth*, 208:786, 2000.

[66] K. Onabe, J. Wu, R. Katayama, F. H. Zhao, A. Nagayama and Y. Shiraki. *Physica Status Solidi A*, 180:15, 2000.

[67] A. Krost and A. Dadgar. GaN-based devices on Si. *Physica Status Solidi A*, 194(2):361–375, 2002.

[68] W. E. Lee and K. P. D. Lagerlof. *J. Electron. Microsc. Technol*, 2:247, 1985.

[69] H. P. Maruskas and J. J. Tietjen. *Applied Physics Letters*, 15:327, 1969.

[70] E. V. Etzkorn and D. R. Clarke. *Journal of Applied Physics*, 89(2):1025, 2001.

[71] J. E. van Nostrand, J. Solomon, A. Saxler, Q. H. Xie, D. C. Reynolds and D. C. Look. *Journal of Applied Physics*, 87:8766, 2000.

[72] M. Stutzmann, O. Ambacher, M. Eickhoff, U. Karrer, A. Lima Pimenta, R. Neuberger, J. Schalwig, R. Dimitrov, P. J. Schuck and R. D. Grober. *Physica Status Solidi B*, 228:505, 2001.

[73] V. Daudin, J. L. Rouviere and M. Arlery. *Applied Physics Letters*, 69:2480, 1996.

[74] M. Seelmann-Eggebert, J. L. Weyher, H. Obloh, H. Zimmermann, A. Rar and S. Porowski. *Applied Physics Letters*, 71, 2635 1997.

[75] M. Sumiya, K. Yoshimura, T. Ito, K. Ohtsuka, S. Fuke, K. Mizuno, M. Yoshimoto, H. Koinuma, A. Ohtomo, M. Kawasaki. *Journal of Applied Physics*, 88:1158, 2000.

[76] D. Huang, P. Visconti, K. M. Jones, M. A. Reshchikov, F. Yun, A. A. Baski, T. King and H. Morkoç. *Applied Physics Letters*, 78:4145, 2001.

[77] N. W. Jeeps and T. F. Page. volume 7. Progress in Crystal Growth and Characterization, Pergamon Press, New York, P. Krishna edition, 1983. p. 259.

[78] H. Lahreche, M. Leroux, M. Laugt, M. Valle, V. Beaumont and P. Gibart. *Journal of Applied Physics*, 87:577, 2000.

[79] Q. Wahab, A. Ellison, A. Henry, E. Janzén, C. Hallin, J. Di Persio and R. Martinez. *Applied Physics Letters*, 76:2725, 2000.

[80] C. J. Antony, A. J. Pidduck and M. J. Uren. *Matter. Sci. Forum*, 264-268:367, 1998.

[81] Z. Y. Xie, C. H. Wei, L. Y. Li, Q. M. Yu and J. H. Edgar. *Journal of Crystal Growth*, 207:115, 2000.

[82] P. H. Yin, V. Saxena and A. J. Steckl. *Physica Status Solidi B*, 202:605, 1997.

[83] R. Lantier, A. Rizzi, D. Guggi, H. Lüth, B. Neubauer, S. Frabbni, G. Coli and R. Cingolani. *MRS Internet Journal of Nitride Semiconductor Research*, 4S1:G3.50, 1999.

[84] P. Ruterana, P. Vermaunt, G. Nouet, A. Salvador and H. Morkoç. *MRS Internet Journal of Nitride Semiconductor Research*, 2:42, 1997.

[85] K. H. Ploog, O. Brandt, R. Muralidharan, A. Thamm and P. Waltereit. *Journal of Vacuum Science Technology B*, 18(2290), 2000.

[86] C. F. Lin and H. C. Cheng. *Journal of Applied Physics*, 82:2378, 1997.

[87] W. Shan. *Applied Physics Letters*, 69:740, 1996.

[88] R. B. Capaz, H. Lim and J. D. Joannopolous. *Physical Review B*, 51(17):755, 1995.

[89] S. Ren and J. D. Dow. *Applied Physics Letters*, 69(2):251, 1996.

[90] S. Sasaki and T. Matsuoka. *Journal of Applied Physics*, 64(9):4531, 1988.

[91] A. Krost and A. Dadgar. *Materials Science and Engineering B*, 93:77–84, 2002.

[92] W. Weeks and R. Borges. *Compound Semiconductor*, November 2001.

[93] B. Yang, A. Trampert, O. Brandt, B. Jenichen and K. H. Ploog. *Journal of Applied Physics*, 83(7):3800, 1998.

[94] X. Zhang, S. J. Chua, Z. C. Feng, J. Chen and J. Lin. *Physica Status Solidi A*, 176:605, 1999.

[95] S. T. Kim, Y. J. Lee, S. H. Chung and D. S. Moon. *Semicond. Sci. Technol.*, 14:156, 1999.

[96] J. H. Boo, S. B. Lee, Y. S. Kim, J. T. Park, S. Yu and Y. Kim. *Physica Status Solidi A*, 176:711, 1999.

[97] V. Lebedev, J. Jinschek, U. Kaiser, B. Schoroter, W. Richter and J. Kraußlich. *Applied Physics Letters*, 76(15):2029, 2000.

[98] K. S. Stevens, M. Kinniburgh, A. F. Schwartzman, A. Ohtani and R. Beresford. *Applied Physics Letters*, 66(23):3179, 1995.

[99] A. Osinsky, S. Gangopadhyay, J. W. Wang, R. Gaska, D. Kuksenkov, H. Tempkin, I. K. Shmagin, Y. C. Chang, J. F. Muth and R. M. Kolbas. *Applied Physics Letters*, 72(5):551, 1998.

[100] S. Guha and N. A. Bojarczuk. *Applied Physics Letters*, 72(4):415, 1998.

[101] A. Strittmatter, A. Krost, M. Straburg, V. Turck, D. Bimberg, J. Blasing and J. Christen. *Applied Physics Letters*, 74(9):1242, 1999.

[102] S. A. Nikishin, N. N. Faleev, V. G. Antipov, S. Farncoeur, L. Grave de Peralta, G. A. Seryogin, H. Tempkin, T. I. Prokofyeva, M. Holtz and S. N. G. Chu. *Applied Physics Letters*, 75(14):2073, 1999.

[103] F. Semond, N. Grandjean, B. Damilano, S. Vezian, M. Leroux and J. Massies. *Applied Physics Letters*, 75(1):82–84, 1999.

[104] E. Calleja, M. A. Sánchez-García, F. J. Sánchez, F. Calle, F. B. Naranjo, E. Muñoz, S. I. Molina, A. M. Sánchez, F. J. Pacheco. *Journal of Crystal Growth*, 201/202:296–317, 1999.

[105] H. Ishikawa, K. Yamamoto, T. Egawa, T. Soga, T. Jimbo and M. Umeno. *Journal of Crystal Growth*, 189/190:178, 1998.

[106] W. Lee, S. W. Park and J. B. Yoo. *Physica Status Solidi A*, 176:583, 1999.

[107] H. P. D. Schenk, G. D. Kipshidze, V. B. Lebedev, S. Schokhovets, R. Goldhahn, J. Kraußlich, A. Fissel and Wo. Richter. *Journal of Crystal Growth*, 201/202:359, 1999.

[108] S. Zamir, B. Meyler, E. Zolotoyabko and J. Salzman. *Journal of Crystal Growth*, 218:181, 2000.

[109] M. W. Koch, R. Jothilingam, J. B. Posthill, and G. W. Wicks. A Study of Cracking in GaN grown on Si by MBE. *Journal of Electronic Materials*, 30(7):821–824, 2001.

[110] M. H. Kim, Y. G. Do, H. C. Kang, D. Y. Noh and S. J. Park. *Applied Physics Letters*, 79(17):2713–2715, 2001.

[111] H. Marchand, L. Zhao, N. Zhang, B. Moran, R. Coffie, U. K. Mishra, J. S. Speck, S. P. Den Baars and J. A. Freitas. *Journal of Applied Physics*, 89:7846, 2001.

[112] E. Feltin, B. Beaumont, M. Laügt, P. De Mierry, P. Wennéguès, H. Lahrèche, M. Leroux and P. Gilbart. *Applied Physics Letters*, 79:3230, 2001.

[113] M. Kim, Y. Bang, N. Park, C. Choi, T. Seong and S. Park. *Applied Physics Letters*, 78:2858, 2001.

[114] N. Grandjean F. Semond, P. Lorenzini and J. Massies. *Applied Physics Letters*, 78(3):335–337, 2001.

[115] L. Zhao, H. Marchand, P. Fini, S. P. Denbaars, U. K. Mishra and J. S. Speck. *MRS Internet Journal of Nitride Semiconductor Research*, 5S1:W3.3, 2000.

[116] G. Kamler, J. Zachara, S. Podsiadlo, L. Adamowicz and W. Gebicky. *Journal of Crystal Growth*, 212:39, 2000.

[117] J. W. Kolis, S. Wilcenski and R. A. Laudise. *Mater. Res. Soc. Symp. Proc.*, 495:367, 1998.

[118] M. Yano, M. Okamoto, Y. K. Yap, M. Yoshimura, Y. Mori and T. Sasaki. *Diamond Relat. Mater*, 9:512, 2000.

[119] M. A. Herman and H. Sitter. *Molecular Beam Epitaxy*. Springer-Verlag, 1989.

[120] A. Rizzi, R. Lantier, F. Monti, H. Lüth, F. Della Sala, A. Di Carlo and P. Lugli. *Journal of Vacuum Science Technology B* , 17:1674–1681, 1999.

[121] J. E. Northrup, R. Di Felice and J. Neugebauer. *Physical Review B*, 55:13878, 1997.

[122] W. Schottky. *Phys. Z.*, 41:570, 1940.

[123] V. Heine. *Physical Review*, 138 A:1689, 1965.

[124] J. Tersoff. *Physical Review Letters*, 52:465, 1984.

[125] W. Mönch. *Rep. Prog. Phys.*, 53:221–278, 1990.

[126] U. Karrer, O. Ambacher and M. Stutzmann. *Applied Physics Letters*, 77:2012, 2000.

[127] W. Mönch. *Journal of Vacuum Science Technology B*, 17:1867, 1999.

[128] A. Rizzi and H. Lüth. Comment on "Influence of crystal polarity on the properties of Pt/GaN Schottky diodes" [Appl. Phys. Lett. **77**, 2012 (2000)]. *Applied Physics Letters*, 80(3):530–531, 2002.

[129] A. R. Smith, R. F. Feenstra, D. W. Greve, M. S. Shin, M. Skowronski, J. Neugebauer and J. E. Northrup. *Journal of Vacuum Science Technology B*, 16:2242–2249, 1998.

[130] O. Ambacher *et al.* Two-dimensional electron gases induced by spontaneous and piezoelectric polarization charges in N- and Ga- face AlGaN/GaN heterostructures. *Journal of Applied Physics*, 85:3222–3233, 1999.

[131] J. P. Ibbetson *et al.* Polarization effects, surface states, and the source of electrons in AlGaN/GaN heterostructure field effect transistors. *Applied Physics Letters*, 77:250–252, 2000.

[132] R. Vetury *et al.* Polarization induced 2DEG in MBE grown AlGaN/GaN HFETs: On the origin, DC and RF characterization. *in Proc. Materials Research Soc. Symp.*, 622:T2.5.

[133] R. Vetury, N. Q. Zhang, S. Keller and U. K. Mishra. The Impact of Surface States on the DC and RF Characteristics of AlGaN/GaN HFETs. *IEEE Transactions on Electron Devices*, 48(3):560–566, 2001.

[134] Y. F. Wu *et al.* GaN-based FET's for microwave amplification. *IEICE Trans. Electron.*, E82-C:1895–1905, 1999.

[135] E. Kohn *et al.* Large signal frequency dispersion of AlGaN/GaN heterostructure field effect transistor. *Electronics Letters.*, 35:1022–1024, 1999.

[136] C. Nguyen, N. X. Nguyen and D. E. Grider. Drain current compresion in GaN MODFET's under large-signal modulation at microwave frequencies. *Electronics Letters*, 35:1380–1382, 1999.

[137] L. F. Eastmen. Results, potential and challenges of high power GaN-based transistors. *Physica Status Solidi A*, 176:175–178, 1999.

[138] T. Mizutani, Y. Ohno, M. Akita, S. Kishimoto and K. Maezawa. Current Collapse in AlGaN/GaN HEMTs Investigated by Electrical and Optical Characterizations. *Physica Status Solidi A*, 194(2):447–451, 2002.

[139] H. Lüth. *Surfaces and Interfaces of Solid Materials*. Springer-Verlag, 1998.

[140] M. S. Rogalski and S. B. Palmer. *Solid State Physics*. Gordon and Breach Science Publishers, 2000.

[141] Roberta Lantier. *GaN/AlGaN Heterostructures: MBE Growth, Electronic Properties and Polarization Fields*. PhD thesis, Fakultät für Mathematik, Informatik und Naturwissenschaft der Rheinisch-Westfälischen Technischen Hochschule (RWTH), Aachen, 2000. Done at Institut für Schicht- und Ionentechnik, Forschungszentrum Jülich GmbH.

[142] S. H. Fner. *Photoelectron Spectroscopy*. Springer Verlag, Berlin, 1996.

[143] P. Y. Yu and M. Cardona. *Fundamentals of Semiconductors*. Springer Verlag, Berlin, 1996.

[144] C. N. Berglund and W. E. Spicer. *Physical Review A*, 136:1030, 1964.

[145] M. P. Seha and W. A. Dench. *Surface and Interface Analysis*, 1:2, 1979.

[146] N. J. Shevchik. *Physical Review B*, 16:3428, 1977.

[147] N. J. Shevchik. *Journal Physics C: Solide State Physics*, 10:L555, 1977.

[148] E. A. Kraut, R. W. Grant and J. R. Waldrop. *Physical Review B*, 28:1965, 1983.

[149] K. Horn. *Surface Science*, 269/270:938, 1992.

[150] W. Schottky. *Naturwiss.*, 26:843, 1938.

[151] J. Tersoff. *Physical Review*, 30:4874, 1984.

[152] J. Tersoff. *Physical Review B*, 32:6968, 1985.

[153] J. Tersoff. *Surface Science*, 168:275, 1986.

[154] J. Tersoff. *Physical Review Letters*, 56:2755, 1986.

[155] E. H. Hall. *American Journal of Mathematics*, 2, 1879.

[156] L. J. van der Pauw. A method of measuring Specific Resistivity and Hall Effect of Discs of Arbitrary Shape. Philips Research Reports, 1958. p. 13.

[157] Dirk Dörner. Herstellung und Charakterisierung von AlGaN/GaN 2DEG-Heterostructuren für HEMT-Anwendungen. Master's thesis, Fakultät für Mathematik, Informatik und Naturwissenschaft der Rheinisch-Westfälischen Technischen Hochschule (RWTH), Aachen, Germany, 2001. Done at Institut für Schicht- und Ionentechnik, Forschungszentrum Jülich GmbH, Germany.

[158] The simulation package "1D Poisson/Schrödinger" has been downloaded from http:/www.nd.edu/∼ gsnider/; further reference in I-H. Tan, G. L. Snider, L. D. Chang and E. L. Hu, *Journal of Applied Physics* **68**, pp. 4071-4076 (1990).

[159] G. Zandler, J. A. Majewski and P. Vogl. *Journal of Vacuum Science Technology B*, 17:1617, 1999.

[160] E. T. Yu, G. J. Sullivan, P. M. Asbeck, C. D. Wang, D. Qiao and S. S. Lau. *Applied Physics Letters*, 71:2794, 1997.

[161] A. Rizzi and H. Lüth. III-V semiconductor interface properties as a knowledge basis for modern heterostructure devices. *Applied Physics A, Material Science and Processing*, (75):69–77, 2002.

[162] I. P. Smorchkova, C. R. Elsass, J. P. Ibbetson, R. Ventury, B. Heying, P. Fini, E. Haus, S. P. DenBaars, J. S. Speck and U. K. Mishra. Polarization-induced charge and electron mobility in AlGaN/GaN heterostructures grown by plasma-assisted molecular-beam epitaxy. *Journal of applied physics*, 86(8):4520–4526, 1999.

[163] B. Shen, T. Someya and Y. Arakawa. *Applied Physics Letters*, 76:2746–2748, 2000.

[164] B. Heying, R. Averbeck, L. F. Chen and E. Haus. Control of GaN surface morphologies using plasma assisted MBE. *Journal of Applied Physics*, 88(4):1855–1860, 2000.

[165] C. Lee and V. Ramachandran and A. Sagar and R. Feenstra. Properties of GaN Epitaxial Layers Grown on 6H-SiC(0001) by Plasma-Assisted MBE. *Journal of Electronic Material*, 30(3):162–169, 2001.

[166] C. R. Elsass, C. Poblenz and B. Heying. Influence of Ga flux on the growth and electron transport properties of AlGaN/GaN heterostructures grown by plasma assisted MBE. *Journal of Crystal Growth*, (233):709–716, 2001.

[167] O. Brandt, R. Muralidharan and A. Thamm. Key issues for the growth of high quality heterostructures on SiC. *Applied Surface Science*, (175-176):429–427, 2001.

[168] J. W. P. Hsu, M. J. Manfra, S. N. G. Chu, C. H. Chen, L. N. Pfeiffer and R. J. Molnar. *Applied Physics Letters*, 78(25):3980, 2001.

[169] T. Kampen V. van Elsbergen and W. Mönch. Surface analysis of 6H-SiC. *Surface Science*, (365):443–452, 1996.

[170] R. Kaplan and T. Parrill. Reduction of SiC surface oxides by a Ga molecular beam: LEED and electron spectroscopy studies. *Surface Science*, (165):L45–L52, 1986.

[171] C. T. Foxon, J. J. Harris, D. Hilton, J. Hewitt and C. Roberts. Optimization of (Al,Ga)As/GaAs two-dimensional electron gas structures for low carrier densities and ultrahigh mobilities at low temperatures. *Semicond. Sci. Technology*, 4:582–582, 1989.

[172] M. J. Manfra, N. G. Weimann, J. W. P. Hsu, L. N. Pfeiffer and K. W. West. High mobility AlGaN/GaN heterostructures grown by plasma-assisted molecular beam epitaxy on semi-insulating GaN templates prepared by hydride vapor phase epitaxy. *Journal of Applied Physics*, 92(1):338–345, 2002.

[173] K. Schimpf. *Herstellung und Charakterisierung von sub-μm InGaAs/InP High Electron Mobility Transistoren*. PhD thesis, Fakultät für Mathematik, Informatik und Naturwissenschaft der Rheinisch-Westfälischen Technischen Hochschule (RWTH), Aachen, Germany, 1998. Done at Institut für Schicht- und Ionentechnik, Forschungszentrum Jülich GmbH, Germany.

[174] G. J. Sullivan, J. A. Higgins, M. Y. Chen, J. W. Yang, Q. Chen, R. L. Pierson and B. T. McDermott. High power RF operation of AlGaN/GaN HEMTs grown on insulating silicon carbide substrates. *Electronics Letters*, 34(9), April 1998.

[175] J. S. Moon, M. Micovic, P. Janke, P. Hashimoto, W.-S. Wong, R. D. Widman, L. McCray, A. Kurdoghlian and C. Nquyen. GaN/AlGaN HEMTs operating at 20 GHz with continuous-wave power density>6 W/mm. *Electronics Letters*, 37(8), April 2001.

[176] P. Javorka, A. Alam, A. Fox, M. Marso, M. Heuken and P. Kordoš. GaN/AlGaN HEMTs on silicon substrates with f_T of 32/20 GHz and f_{max} of 27/22 GHz for 0.5/0.7 μm gate length. *Electronics Letters*, 38(6), March 2002.

[177] Y. Shiraki and A. Ishizaka. *J. Electrochemical Science and Technology*, 133(4):666–671, 1986.

[178] E. Calleja, M. A. Sanches-Garcia, E. Monroy, F. J. Sanches, E. Munoz, A. Sanz-Hervas, C. Villar and M. Aguilar. *Journal of Applied Physics*, 9(82):4681, 1997.

[179] K. S. Stevens, A. Ohtani, M. Kinniburgh, R. Beresford. *Applied Physics Letters*, 65(3):321, 1994.

[180] A. Watanabe, T. Takeuchi, K. Hirosawa, H. Amano, K. Hiramatsu and I. Akasaki. *Journal of Crystal Growth*, 128:391–396, 1993.

[181] E. S. Hellman, D. N. E. Buchanan and C. H. Chen. Nucleation of AlN on the (7×7) Reconstructed Silicon (111) Surface. *MRS Internet Journal of Nitride Semiconductor Research*, 3(43):1–5, 1998.

[182] A. Ohtani, K. S. Stevens ans R. Beresford. *Applied Physics Letters*, 65:61, 1994.

[183] H. Ishikawa, G. Y. Zhao, N. Nakada, T. Egawa, T. Soga, T. Jimbo and M. Umeno. *Physica Status Solidi A*, 176:599, 1999.

[184] H. Marchand, L. Zhao, N. Zhang, B. Moran, R. Coffie, U. K. Mishra, J. S. Speck and S. P. Den Baars. *Journal of Applied Physics*, 89(12), 2001.

[185] B. Jogai. Parasitic Hole Channels in AlGaN/GaN Heterojunctions Structures. *Physica Status Solidi A*, 233(3):506–518, 2002.

[186] E. Calleja, M. A. Sanchez-Garcia, D. Basak, F. J. Sanchez, F. Calle, P. Youinou and E. Munoz. Effect of Ga/Si interdiffusion on optical and transport properties of GaN layers grown on Si(111) by MBE. *Physical Review B*, 58(3):1550–1559, 1998.

[187] A. G. Milnes. *Deep impuririties in Semiconductors*. Wiley, 1973.

[188] F. Semond, Y. Cordier, N. Grandjean, F. Natali, B. Damilano, S. Vezian and J. Massies. Molecular Beam Epitaxy of group-III nitrides on Si substrates: Growth, Properties and Devices Applications. . *Physica Status Solidi A*, 188(2):501–510, 2001.

[189] L. Hsu and W. Walukiewicz. Theoretical transport studies of p-type gan/algan modulation-doped heterostructures. *Applied Physics Letters*, 74(17):2405, 1999.

[190] MOCVD GaN template on SiC(0001) grown by Stacia Keller *et al.*, University California Santa Barbara, USA.

[191] K. Lawniczak-Jablonska, T. Suski, I. Gorczyca, N. E. Christensen, K. E. Attenkofer, R. C. C. Perera, E. M. Gullikson, J. H. Underwood, D. L. Ederer, Z. Liliental Weber. *Physical Review B*, 61:16623–16632, 2000.

[192] N. Teofilov, L. Kirste, M. Kočan, A. Rizzi, H. Lüth, K. Thonke, D. Ebling, R. Sauer, K. Benz. *Proceedings of the 26th ICPS, Edinburgh*, 2002. in press.

[193] A. Rizzi, R. Lantier and H. Lüth. *Physica Status Solidi A*, 177:165, 2000.

[194] T. Zywietz, J. Neugebauer and M. Scheffler. Adatom diffusion at GaN(0001) and $(000\overline{1})$ surfaces. *Apllied Physics Letters*, 73(4):487–489, 1998.

[195] C. H. F. Peden, J. W. Rogers, N. D. Shinn, K. B. Kidd and K. L. Tsang. Thermally grown Si_3N_4 thin films on Si(100): Surface and interfacial composition. *Physical Review B*, 47(23):15622–15629, 1993.

Acknowledgements

I would like to thank by heart all the people that helped and supported me in realizing this work. My particular thanks go to:

- Prof. Dr. H. Lüth for his enormous enthusiasm in the scientific research towards new ideas, friendly atmosphere and for the opportunity to work at the Institut für Schichten und Grenzflächen 1 in Forschungszentrum Jülich;
- Prof. Dr.-Ing. R. Waser for kindly accepting to referee this work;
- Prof. Dr. Angela Rizzi for the possibility to do PhD work in her group and for many interesting scientific discussions;
- Prof. Dr. P. Kordoš and Prof. Dr. D. Donoval for the opportunity to join the research group in Forschungszentrum Jülich;
- Dipl.-Ing. Marco Bertelli for his valuable help in life, job, for many interesting discussions in various fields and for his very nice personality that made the stay in Jülich very pleasant;
- Dipl.-Phys. Enrico Donà for his very good collaboration, fruitful suggestions and discussions within the researched field, and for his friendly attitude;
- Dipl.-Phys. Dirk Dörner for the very friendly, pleasant and partly funny collaboration and for his help in private life;
- Klaus Wambach for his engagement in solving technical problems in MBE laboratory and for his help to overcome the difficulties at the beginning of the stay;
- Dipl.-Ing. A. Mück for the professional performing of SIMS measurements;
- Dr. M. Grimm for several XRD measurements;
- Dr. H. L. Bay for many RBS measurements;
- S. Bunte for perfect cutting of samples;
- Dipl.-Ing. A. Steffen, J. Zillikens and J. Müller, as well as all other co-workes of the cleanroom for their help with processing of the samples;

- Priv.-Doz. Dr. Thomas Schäpers for his help with magneto-transport measurements and with solving of technical problems with measurement equipment;
- D. Meertens, Dr. K. Tillmann and Dr. M. Luysberg for TEM measurements;
- Dr. S. Keller for growing of templates;
- Dipl.-Ing. Peter Javorka for the fabrication of devices and help in living in Germany, and Dipl.-Ing. Martin Mikulics for his moral support and comprehension;
- Dr. Michael Goryll, Dr. Michael Indlekofer for the kindly collaboration;
- Dipl.-Ing. Juraj Bernát for the great help with the computer and with the LaTeX;
- Dr. O. Mayrock for useful discussions about the simulation of III-Nitrides;
- Prof. Dr. T. Hashizume and Dr. J. Neugebauer for fruitful discussions about the surface properties;
- Irene Schumacher for her help in the administrative issue and for her very nice personality;
- R. Otto and his co-workers of the Elektronik Werkstatt for the technical support of electronic devices;
- Dr. Raffaella Calarco, Dipl.-Ing. Simone Montanari, Dipl.-Ing. Claudio Varini, Dipl.-Phys. Frank Macherey, Dipl.-Phys. Oliver Zimmermann, Dipl.-Phys. Jürgen Stock, Dr. Jörg Malindretos, Dr. Vitaliy Guzenko, Herbert Kertz, Dipl.-Phys. Nikolas Thillosen, Dr. Pavel Vagner, Dr. Roman Adam, Karl Nicoll, Dr. S. Vitusevych, Dr. Mike Lepsa, Dipl.-Phys. Mike Wolter, Dipl.-Ing. Serhiy Danylyuk and all other people from Forschungszentrum for their kindness that made the stay very pleasant;
- Dipl.-Ing. Aleš Havránek, Prof. Peter Stahmann, Dr. Diego Kienle, Ulrike Finger, Karin Maschke-Neuss, Kumar Majumder Arup for their friendly attitude within the Karate-verein Jülich e.V.;
- Jutta Zillikens for her kindness and very nice accommodation;
- Sergey N. Pron'kin, Sergey Grudinin, Yuriko and Yoshi Maeda, Diane Barrier, Andrij Fomenko and other that make the life in Jülich nice;
- Martina Mičková for her permanent moral support, patience and help in every difficulty;
- my parents, my brothers: Marek and Peter, all my relatives and Tomáš Ogrodník for their help in life and for their constant standing on my side during the time of the PhD work;

as well as all other not namely mentioned people for their versatile support and their kindness.

Curriculum vitae

Personal data

Name	Martin Kočan
E-mail	martin_kocan@yahoo.com
Date of birth	29.09.1975 in Bratislava, Slovakia

Education

1982-1990	Primary school Sokolikova in Bratislava, Slovakia
1990-1994	High school Jura Hronca, Bratislava, Slovakia Graduated in subjects: Slovak Language and Literature, English, German and Mathematics
1994-1998	Slovak Technical University in Bratislava, Slovakia Faculty of Electrotechnical Engineering and Information Technology BACHELOR OF SCIENCE Discipline - Electronics Final exam - Semiconductor structures
1998-2000	Slovak Technical University in Bratislava, Slovakia Faculty of Electrotechnical Engineering and Information Technology MASTER OF SCIENCE Discipline - Electronics Study branch - Microelectronics Masters thesis - "MQW photodetector of infrared radiation"
2000-2003	PhD study in the Institut für Schichten und Grenzflächen (ISG-1) of the Forschungzentrum Jülich in the group of Mr. Prof. H. Lüth PhD thesis - "AlGaN/GaN MBE 2DEG Heterostructures: Interplay between Surface-, Interface- and Device-Properties" PhD exam at the Fakultät für Elektrotechnik und Informationstechnik der Rheinisch-Westfälischen Technischen Hochschule Aachen